Charles University

Faculty of Science

Study programme: Geology

Mgr. Petra Holá

Metamorphism of gabbroic rocks of Teplá-Barrandian Unit

Metamorfóza gabroidních hornich tepelsko-barrandienské jednotky

Doctoral thesis

Supervisor: Mgr. Martin Racek Ph.D.

Advisor: doc. RNDr. Petr Jeřábek Ph.D.

Prague, 2024

Declaration

I declare that this thesis is a result of my own work and that I have cited all the resources and literatuře. Neither this thesis nor its substantial part has been submitted to fulfill requirements for any other academic degree. The results of the thesis are my own work ort he product of collaboration with other members of the research team.

Prohlášení

Prohlašuji, že jsem závěrečnou práci vypracovala samostatně a že jsem uvedla všechny použité informační zdroje a literaturu. Tato práce ani její podstatná část nebyla předložena k získání jiného nebo obdobného druhu vysokoškolské kvalifikace. Výsledky práce jsou produktem mé vlastní práce ve výzkumném týmu.

In Prague/ V Praze Mgr. Petra Holá

Acknowledgments:

This work was financially supported by Grand Agency of Charless University in Prague (n.1767318) to Petra Holá; by the Czech National Grant Agency (13–16315S to P. Štípská and O. Lexa) and by the Institute of Geology of the Czech Academy of Sciences institutional support RVO67985831 to Martin Svojtka and Lukáš Ackerman.

Here I wanted to thank to all the people who have contributed to the articles related to this thesis. František Veselovský from the Czech Geological Survey is thanked for zircon and titanite separation and J. Ďurišová from the Institute of Geology of the Czech Academy of Sciences for providing ICP-MS measurements, Gerlinde Habler from the University of Vienna for EBSD measurements.

I would like to thank to my supervisor Martin Racek for his guidance and patience during all these years. More importantly I want to say that I am really glad that you are my supervisor. I also thank to my konzultant Petr Jeřábek for assigning me Martin as a supervisor and for his plate-tectonic contribution. Huge thanks belong to co-authors of my second article Lukáš Ackerman and especcially Martin Svojtka for their help with the manuscript, kindness, and moral support to see the light at the end of the tunnel. I also thank to Drahu Seemanová for kind advice with paperwork and cheerful conversations and Tatiana Lariková with the help during preparation of my first confference presentation (lecture). Another big thank belongs to my colleagues and friends (most of them currently working at Czech Geological Survey) for moral support and general advice. Among them I want to highlight Vítek Peřestý who has stuck with me since our master study to keep me company during the field work, and also to disscuss the TBU evolution, Terka Zelinková for her sense of humor that was the important part of the final stages of my Ph.D. and also Josef Klomínský for his advice and pleasant company at the office.

However, the biggest thank is to my amazing family for their patience and support during all of the Ph.D. difficulties!

Concept of the thesis

This thesis is written as a monograph. The publication where the candidate is a first author (Jašarová et al., 2016) characterize samples from one of the two studied areas, for this thesis the sample collection was extended with samples from the second studied area. Their detailed decsribtion below is part of the second publication where the candidate is also the first author. The other publications are focused on detailed study of selected processes observed in the studied metagabbros such as breakdown of ilmenite (Racek and Holá, in rev) and magmatic labradorite (Holá et al. in prep). The decomposition of magmatic plagioclase brings useful information about re-equilibration, that can be applied for evolution of the studied area thus it is included as a separate chapter in the thesis. On the other hand, the late alteration of the metagabbros probably connected to the exhumation processs is not characterized in detail in the thesis, however the article demonstrating ilmenite breakdown and subsequent formation of Ti-bearing sulfides during later alteration of the gabbros is not included in the thesis.

List of related publications:

***P. Jašarová**, M. Racek, P. Jeřábek, F. V. Holub (2016).* Metamorphic reactions and textural changes in coronitic metagabbros from the Teplá Crystalline and Mariánské Lázně complexes*, Bohemian Massif. Journal of Geosciences, 61, 193-216.*

Author's contribution: 90%

***P. Holá**, M. Racek, P. Jeřábek, M. Svojtka, L. Ackerman, V. Špilar (prepared for submit to Lithos during March 2024):* Zircon in different textural positions as an important indicator for multi-stage evolution of metagabbroic rocks: insights from the Western part of the Teplá-Barrandian Unit, Bohemian Massif

Author's contribution: 75%

P. Holá, *P. Jeřábek, M. Racek, G. Habler (in prep for Journal of Structural Geology):* Features related to destabilization of magmatic labradorite with increasing metamorphic grade of metagabbros from the west of the Teplá-Barrandian Unit, Bohemian Massif

Author's contribution: 85%

M. Racek and ***P. Holá*** *(in rev):* Formation of Ti-bearing sulphides related to ilmenite breakdown in metagabbros (Teplá-Barrandian Domain, Bohemian Massif*). Neues Jahrbuch für Mineralogie – Abhandlungen*

Author's contribution: 20%

I declare that the information on the percentage of the student's contribution and involvement in the aforementioned research papers is an accurate representation.

Mgr. Martin Racek Ph.D.

Conference contributions:

***P. Jašarová**, M. Racek, P. Jeřábek, F. V. Holub, T. Larikova:* Metamorphic reactions and textural changes in coronitic metagabbros from the Teplá Crystalline and Mariánské Lázně complexes, Bohemian Massif (lecture). *14th Meeting of the Central European Tectonic Studies Groups (CETEG), Predná Hora, Slovakia (April, 2016)*

***P. Jašarová**, M. Racek P. Jeřábek*: Metagabbros from western part of the Teplá-Barrandian Unit (Bohemian Massif) and its significance for evolution of the area (poster). *15th Meeting of the Central European Tectonic Studies Groups (CETEG) Zánka, Hungary (April, 2017)*

***P. Holá**, M. Racek P. Jeřábek*, *G. Habler*: Exsolutions of two plagioclases in the magmatic labradorite, evidence from the coronitic metagabbro from the west of the Teplá-Barrandian Unit, Bohemian Massif (lecture). *17th Meeting of the Central European Tectonic Studies Groups (CETEG) Rozdrojovice, Czech Republic (April, 2019)*

***P. Holá**, M. Racek P. Jeřábek*, *G. Habler*: Features related to destabilization of magmatic labradorite with increasing metamorphic grade of metagabbros from the west of the Teplá-Barrandian Unit, Bohemian Massif (poster), postponed thus presented in *18th Meeting of the Central European Tectonic Studies Groups (CETEG), Terchová – Vrátna, Slovakia (2021).*

***P. Holá**, M. Racek P. Jeřábek*, *M. Svotka, L. Ackerman:* Geochronological, geochemical, and petrological constrains on magmatic and metamorphic evolution of the metagabbros from the Western part of the Teplá-Barrandian Unit, Bohemian Massif (lecture) *18th Meeting of the Central European Tectonic Studies Groups (CETEG), Terchová – Vrátna, Slovakia (2021).*

Abstract

In the thesis I focuse on petrographic, geochronological and geochemical characterization of gabbroic rocks to provide constrains on the Cambro-Ordovician and Variscan evolution of the Teplá-Barrandian Unit in Bohemian Massif situated in Central Europe. The studied rocks occur in two areas of interest in the western margin of the Teplá-Barrandian: (1) along the contact of the Teplá Crystalline and Mariánské Lázně Complexes in the north-western part of the TBU, (2) in area between the Domažlice Crystalline Complex and Kdyně-Neukirchen Massif (KNM) in the south-western part of the Teplá-Barrandian Unit. Detailed petrological study together with U–Pb dating of representative samples allow to characterize three events (I–III) defined by different textural position of analyses zircon and titanite grains. The oldest (Cambrian) event I is recorded in isolated metamictized matrix-hosted grains that yield similar mean age of c. 500–510 Ma in both areas. The second Cambro-Ordovician event II was connected with formation of tiny zircon grains forming rim around ilmenite at ~480–490 Ma due to diffusion reaction of ilmenite and surrounding silicate matrix enabled by increase of temperature. The youngest (Variscan) event III is associated with the formation of zircon corona around baddeleyite at ca. 360–380 Ma. Similar age (c. 370 Ma) was also obtained for titanite grains forming corona around ilmenite and/or rutile indicating metamorphic re-equilibration. Major/trace element and Sr–Nd isotopic compositions imply that gabbroic rocks formed from two consecutive melt batches that undergone different evolution. First magma represented by samples from Neukirchen-Kdyně Massif was emplaced at c. 510 Ma and underwent fractional crystallization and crystal accumulation, while the second one represented by samples from the Teplá Crystalline and Mariánské Lázně Complexes and Domažlice Crystalline Complex intruded c. 10 My later is characterized by significant influence of assimilation of adjacent sedimentary rocks.

Consequently, all the gabbroic bodies were collectively metamorphosed and exhumed during Variscan orogenesis. Metamorphism led to destabilization of primary mineral assemblage that resulted in formation of single or multiple coronas at the contact of plagioclase with the other primary minerals such as olivine or orthopyroxene and to decomposition and subsequent recrystallization of primary plagioclase. The P–T conditions calculated for garnet corona in TCC-MLC samples show an increase in metamorphic grade from eats-southeast (~600±50°C; 10±1.5 kbar) to west-northwest (~700±50°C; 13.5±1.5 kbar), which corresponds to previously reported Variscan metamorphic field gradient in this area. Across the studied samples we can demonstrate progressive breakdown of magmatic labradorite and its effect on plagioclase recrystallization. In initial phases plagioclase breakdown occur in domains located at marginal parts of the large grains, where the original grain is replaced by a mixture formed by thin elongated lamellae of anorthite-bytownite (An83-91) with apparent random orientation enclosed within oligoclase-andesine (An27-48) matrix and accompanied by crystallization of small spinel and corundum grains. With ongoing metamorphism, the breakdown of labradorite occur in the whole volume of the plagioclase grains and subsequent recrystallization started on previously exoluted lamellae. Additionally, the formation of spinel and corundum is interpreted due to variable diffusion rates of Ca and Al from the plagioclase during the corona formation.

Český abstrakt

V této disertační práci se zabývám petrologickou, geochronologickou a geochemickou charakteristikou gabroidních hornin v kontextu kambro-ordovického a variského vývoje tepelsko-barrandienské jednotky, která je součástí Českého masivu. Studované horniny se vyskytují ve dvou zájmových oblastech podél západního okraje tepelsko-barrandienské jednotky: 1. oblast se nachází na kontaktu tepelského krystalinika a mariánsko-lázeňského komplexu a 2. zájmová oblast zabírá jiho-západní cíp tepelsko-barrandienské jednotky a táhne se z neukirchen-kdyňského masivu přes domažlické krystalinikum. Na základě detailní petrologické charakteristiky kombinované s datováním metodou uran-olovo aplikované na zirkony a monazity byly definovány tři etapy (I-III) vývoje gabbroidních hornin, kdy každá etapa je spojena s jinou texturní pozicí datovaného zirkonu, případně titanitu. Nejstarší událost I je kambrického stáří, v tomto případě byly průměrné věky c. 500–510 Ma stanoveny pro velká izolovaná zrna zirkonů nacházejících se v matrix. Druhá datovaná II událost ukazuje kambro-ordovické stáří (~480–490 Ma) a je spojena s výskytem malých zrnek zirkonu lemujících ilmenit. Vznik těchto malých zrnek tvořících lem kolem ilmenitu je výsledkem difúzní reakce mezi ilmenitem a okolní silikátovou matrix, kdy mobilita zirkonia je umožněna zvýšením teploty. Nejmladší událost (III) je spjatá se zirkony tvořícími koronu kolem původního baddeleyitu, který je ve výsledku patrný pouze v malých reliktech. Stáří těchto zirkonů je ca. 360–380 Ma, srovnatelné variské stáří c. 370 Ma bylo stanoveno i pro titanity, které se ve vzorcích vyskytují ve formě koron kolem ilmenitu a/nebo rutilu, což indikuje jejich vznik spojený s re-ekvilibrací. Na základě obsahu hlavních a stopových prvků a také izotopových poměrů Sr a Nd ve studovaných horninách bylo možné určit, že gabbroidní horniny pocházejí ze dvou různých porcí magmatu, které byly formovány jinými procesy. První porce magmatu zahrnující vzorky z neukirchen-kdyňského

masivu byla vmístěna před c. 510 Ma a probíhala v něm rozsáhlá frakční krystalizace a akumulace. Druhá porce magmatu, kam patří vzorky z tepelského krystalinika, mariánsko-lázeňského komplexu a domažlického krystalinika, je o c. 10 Ma mladší a vykazuje známky vyššího podílu asimilované materiálu z okolních metasedimentárních hornin. Následně byly během variské orogeneze gabroidních horniny metamorfovány a exhumovány. Metamorfóza se ve studovaných vzorcích projevila destabilizací primárních minerálních fází, které vyústilo ve vytvoření koronitických sekvencí mezi mafickými minerály (např. olivínem a/nebo ortopyroxem) a plagioklasem a také rozpadem a následnou rekrystalizací primárního plagioklasu. Teplotně-tlakové podmínky vypočítané pro granátovou koronu vyskytující se ve vzorcích z tepelského krystalinika a mariánsko-lázeňského komplexu ukazují nárůst stupně metamorfózy směrem od jiho-východu (~600±50°C; 10±1.5 kbar) na severo-západ (~700±50°C; 13.5±1.5 kbar), což je v souladu s variskou metamorfní charakteristikou této oblasti. Rozpad a následná rekrystalizace magmatického plagioklasu je ve vzorcích charakterizována ve třech stádiích. V první stadiu dochází k rozpadu primárního labradoritu jen v určitých doménách koncentrovaných na okrajích velkých zrn, kde je labradorit nahrazen směsí podlouhlých lamel anortit-bytownitového složení (An83-91) bez viditelné přednostní orientace v oligoklas-andezínové matrix. V těchto rozpadových zónách se také vyskytují drobná zrnka korundu a spinelu. S narůstajícím stupněm metamorfózy je rozpad labradoritu pozorován v celém objemu plagioklasových zrn což vede k následné rekrystalizaci primárního plagioklasu iniciované na již odmíšených lamelách. Krystalizace spinelu a korundu v rozpadových zónách plagioklasu je pravděpodobně způsobena rozdílnou mírou difúze Ca a Al z plagiokla

Content

1. INTRODUCTION

Bohemian Massif belongs to the European Variscan orogenic belt which was formed during Devonian and Carboniferous convergence (e.g. Matte et al., Schulmann et al., 2014). The associated deformation and high-temperature, high-pressure metamorphism (e.g. Colett et al., 2022) affected major part of the Bohemian Massif with exception of the Teplá-Barrandian Unit which represents almost undeformed fragment of Neoproterozoic basement (e.g. Zulauf et al., 1997; Dörr et al., 2002; Drost et al., 2004). Thus, this unit provides a great opportunity to get some information about pre-Variscan history that includes Neoproterozoic convergence followed by Cambro-Ordovician rifting and subsequent opening of the Rheic ocean (e.g. von Raumer & Stampfli 2008; Nance et al., 2010). So far a number of studies has been focused on history of the formation of Neoproterozoic accretionary wedge (e.g. Hajná et al., 2017; Hajná et al., 2018; Žák et al., 2020) occupying the major part the Teplá-Barrandian Unit or sedimentary basins (e.g. Mašek, 2000; Dörr et al., 2002; Drost et al., 2004; Drost et al., 2008) and volcano-sedimentary sequences (e.g. Waldhausrová et al., 1971; Mašek, 2000; Sláma et al., 2008). However, evolution of the western part of Teplá-Barrandian Unit which was affected by Cadomian (e.g. Kreutzer et al., 1989; Zulauf et al., 1997) and Variscan (e.g. Zulauf et al., 1997; Peřestý et al., 2017) metamorphism is still matter of debate. Moreover, most of the data characterizing the evolution of the western part of the Teplá-Barrandian Unit were obtained from completely re-equilibrated metasedimentary rocks or granitic plutons. Thus, there is lack of information from other lithologies.

Since the gabbroic rocks are commonly spared from complete reworking during metamorphism, this kind of lithology often capture the complete evolution from preserved

magmatic stage to metamorphic re-equilibration which makes it the best candidate for studying areas that underwent a polyphase evolution. Moreover, gabbroic rocks commonly contain interesting and quite unique features such as decomposition of magmatic plagioclase (Jašarová et al., 2016), corona textures (e.g. Larikova, 2000 Gallien et al., 2012;) and most importantly zircon coronas around ilmenite and baddeleyite (e.g. Salnikova et al., 2022). These phenomena are in literature commonly used for demonstration of prograde metamorphism from gabbro to granulite transition as well as the evidence for destabilization of mineral phases during post-magmatic cooling.

1.1 Aims of the study

The aim of this study is to characterize and compare the metagabbro bodies located in two studied areas: 1) along the contact of Teplá Crystalline and Mariánské Lázně Complexes; 2) across the Neukirchen-Kdyně Massif and Domažlice Crystalline Complex. So far, these two areas have been investigated separately, however the gabbroic rocks show a lot of similarities in both studied areas which imply to a possibility that they share common evolution. Moreover, in studied rocks interesting features mentioned above were observed thus there is also an opportunity to investigate zircon in different textural positions, decomposition of magmatic plagioclase or even corona sequences developed around primary minerals and shed some light to the processes of its formation. So in this work the multidisciplinary approach was chosen to be the most promising. The combination of detailed petrology with accent to relationships among mineral phases such as zircon, ilmenite, rutile and titanite and U–Pb zircon and titanite dating would provide information about timing of the regional events recorded in metagabbros and also contstrains for crystallization of zircon in different textural positions. Moreover, the results of geochemistry

bring some information about magma source of the studied metagabbros, do they originate from the same magma or are there different magma sources for each area? Based on these results it sloud be possible to reconstruct the evolution of the magmatic phase recorded in the samples. Since the studied samples underwent variable degree of re-equilibration manifested by corona formation and plagioclase recrystallization, a calculation of P–T conditions together with calculation of diffusion coefficients will provide some characteristics for corona formation process. Additionally, the process of decomposition of magmatic plagioclase (labradorite) into bytownite-anorthite lamellae within andesine-oligoclase matrix investigated by electron backscattered diffraction (EBSD) mesurements of crystallographic orientation will bring answers if the decomposition is an exsolution origin or the result of complete recrystallization.

1.2 Current state of knowledge

1.2.1 Geological setting

Bohemian Massif is part of the European Variscan Orogenic belt (e.g. Matte et al., 1990; Shulmann et al., 2014) which was formed due to Late-Paleozoic convergence of the Gondwana and Laurussia continents resulting in closure of the Rheic ocean (e.g. Nance et al., 2012; Collett et al., 2020). Variscan Orogenic Belt forms the major part of the western and central Europe. It consists of three major zones reflecting their different structural position in the orogen, from Moldanubian zone representing the orogenic root to Saxothuringian and Rhenohercynian. Following this distribution there are four main units defined in Bohemian Massif: Saxothuringian, Moldanubian, Teplá-Barrandian and Brunovistulian Unit. The Teplá-Barrandian Unit represents well preserved fragment of

Cadomian basement and Brunovistulian Unit can be characterized by volcanic-arc related granitoids which were underthrust below the Moldanubian Unit (e.g. Schulmann et al., 2009).

1.2.1.1 Teplá-Barranian Unit (TBU)

The Teplá-Barrandian Unit (Fig.1) is itrerpreted to be a part of the Cadomian-Avalonian Belt on the active northern Gondwana margin (e.g. Linnemann et al., 2004). In the Bohemian Massif this TBU represents an orogenic suprastructure where the pre-Variscan evolution is well preserved. Major part of the TBU is formed by the Blovice Accretionary Complex (BAC). This complex document the Neoproterozoic–Cambrian evolution including change of geotectoic regime from Pacific-type subduction to passive margin and to opening of the Rheic ocean (e.g. Dörr et al., 2002; Drost et al., 2004; Hajná et al., 2017; Hajná et al., 2018; Ackerman et al., 2019; Žák et al., 2020). The Blovice Accretionarry Complex can be divided into two domains, the first one lying in the nort-west is interpreted to reflect rapid accretion and the second one located in the south-east characterize slow accretion (Žák et al., 2020). During the Cambrian a number of plutons of variable composition were emplaced into BAC (e.g. Zulauf et al., 1997; Dörr et al., 1998; Dörr et al., 2002, Venera et al., 2000). According to recent study by Syahputra et al. (2003) the hot plutonism was the driving force of Cambro-Ordovician rifting event. Furthermore, the extensional regime resulted to passive margin that lasted until Mid-Devonian when the TBU was incorporated to Variscan Orogenic Belt. The Variscan metamorphic overprint in TBU associated with deformation is relatively low grade except for its northwestern part (Teplá Crystalline Complex, Fig.1).

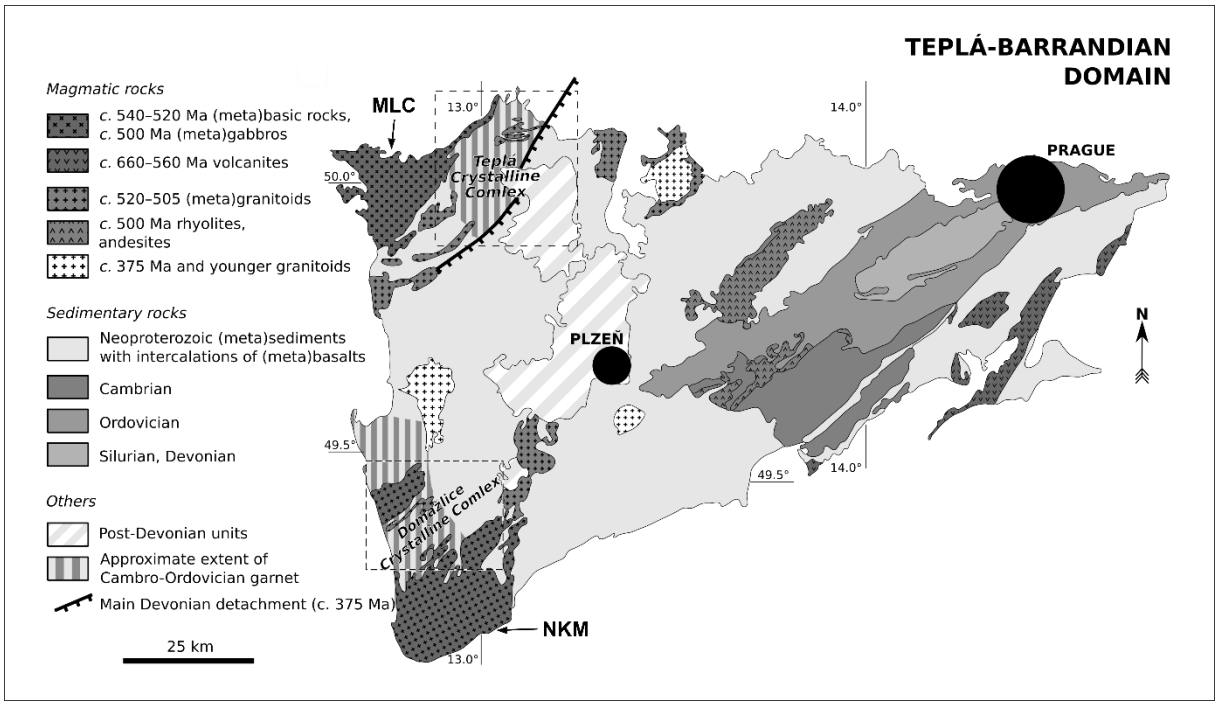

Fig. 1 Simplified geological map of the TBU according to Peřestý et al. (2017) based on Žák et al., (2012)

1.2.1.2 Teplá Crystalline and Mariánské Lázně Complexes

The Teplá Crystalline Complex (TCC; Fig. 2b) is composed of phyllites to micaschists with maximum depositional age of 533 ± 8 Ma (Žák et al., 2020). Two metamorphic events were distinguished in TCC. The younger event corresponds to Variscan Barrovian metamorphism (Cháb a Žáček, 1994; Žáček, 1994; Peřestý et al., 2017) reaching 8 kbar at 600°C between 387-373 Ma (U-Pb monazite Peřestý et al., 2017; Timmermann et al., 2006). The older metamorphic event, reaching 3–6 kbar and ~ 550–650 °C at ~ 485 Ma, indicates low pressure-high temperature metamorphism related to Cambro-Ordovician rifting during opening of the Rheic ocean (Peřestý et al., 2017). This event is associated with emplacement of several granitic plutons transformed to orthogneiss during Variscan (Dörr et al., 1998).

The metamorphism further increases towards NW in the Mariánské Lázně Complex (MLC; Fig. 1, Fig. 2b) that is dominated by amphibolite with lenses of eclogite and HP granulite, and serpentinite. U–Pb zircon dating of eclogite revealed Cadomian protolith age (~560–535 Ma; Timmermann et al., 2004). The protolith of MLC eclogites and amphibolites had been associated with N-MORB and E-MORB sources (e.g. Beard et al., 1995; Timmermann et al., 2004) although recent work of Collett et al. (2022) suggested supra-subduction geochemical signature for most eclogites and MORB source for amphibolites. Garnet dating and U-Pb ages suggest that eclogite facies conditions of 16–25 kbar and 640–715 °C (Jelínek et al., 1997; Štědrá, 2001; Faryad, 2012; Collett et al., 2018) had been reached at ~390 Ma, while granulite facies overprint of ~14-18 kbar and >800 °C occurred between 385-375 Ma (Timmermann et al., 2004; Collett et al., 2018). MLC had been exhumed from below TCC along a large-scale detachment shear zone affecting both units by ~370 Ma (Fig.1) Ar-Ar Dallmeyer and Urban, 1998; Peřestý et al., 2020).

Several small isolated metagabbro bodies with late Cambrian protolith age (c. 500 Ma, e.g. Beard et al., 1995; Timmermann et al., 2004; Timmermann et al., 2006) occur in both TCC and MLC near the contact between the two complexes (Fig. 2b). These rocks show generally well-preserved magmatic mineral assemblage surrounded by metamorphic corona sequences (e.g. Štědrá et al., 2002; Jašarová et al., 2016). The metagabbros have subalkaline character following the tholeiitic trend with major and trace element compositions similar to the E-MORB (e.g. Beard et al., 1995; Štědrá et al., 2002; Jašarová et al., 2016). Significant Variscan reequilibration of metagabbro records peak P-T conditions of ~600–730 °C and 8–13 kbar (Štědrá, 2001; Faryad, 2012) with westward increasing degree of metamorphism across the TCC-MLC contact from 600 °C and 10 kbar in east-southeast to 700 °C and 13.5 kbar in the west (Jašarová et al. 2016).

1.2.1.3 Domažlice Crystalline Complex and Kdyně-Neukirchen Massif

The Domažlice Crystalline Complex (DCC, Fig. 2b) is formed by micaschist, phyllite, paragneiss, with maximum depositional age of 526 +5/-7 Ma (Žák et al., 2020), and minor amphibolite. DCC was affected by Barrovian metamorphism with increasing PT conditions from ENE to WSW (Vejnar 1966, 1982; Zulauf, 1997b). For garnet isograde, the PT conditions were estimated to 400–500 °C and 6 kbar (Helferich et al., 1995, Zulauf, 1997a). The metamorphic record in staurolite and kyanite zone was overprinted by low-pressure and high-temperature mineral assemblages including sillimanite associated with intrusion of lower Cambrian granitoid plutons providing zircon U–Pb ages of ~523 Ma (Zulauf, 1997a), however recent geochronological work of V. Peřestý (pers. com.) revealed Ordovician U–Pb monazite ages suggesting more complicated metamorphic evolution. Several mafic bodies belonging to the Poběžovice Massif (Fig. 2b), have composition of norites (orthopyroxene-gabbro, Vejnar, 1986).

The Neukirchen-Kdyně Massif (NKM, Fig. 2b) is a mafic to intermediate igneous complex situated in the south-western part of TBU. According to Vejnar (1986), the NKM represents layered intrusion with transitional boundaries among the layers, where the lowest part is represented by Orlovice gabbroic rocks while middle and upper part is built by diorites. The mafic bodies occur in Orlovice area are represented by gabbro and ferrodiorite are commonly surrounded by uralitized gabronorites of cumulative character with corona texture around olivine (Vejnar, 1986). Most of the Kdyně Massif plutons show similar age of intrusion c. 523 Ma (U–Pb zircon dating; Bues et al., 2002, Dörr et al., 2002). Miethig et al. (1997) and Svobodová (1999) corroborated that the differences in Sr–Nd composition among the rocks of NKM can be explained by contamination of parental magmas by lower crust material. Bues et al. (2002) assumed that during Cambrian times, felsic and intermediate plutons

intruded at upper crustal levels whereas intermediate to mafic magmas were emplaced into deeper crust.

1.2.2 Different textural position of zircon

In studied samples the zircon occurs in different textural positions: as large grains in the matrix, as tiny grains forming a rim around ilmenite, and it also occurs in corona consuming former baddelleyite. The thin rim of zircon surrounding ilmenite is observed in plutonic and metamorphic rocks and its origin has been quite discussed topic with an uncertain answer. Morisset and Scoates (2008) described thin rims of zircon at the contact of ilmenite with plagioclase or biotite in unmetamorphosed anorthosite suites in Grenville (Canada). The authors discuss several possible mechanisms of its formation, and they suggest formation during slow cooling, additionally they also point out that zircon rims can be commonly observed in slowly cooled plutonic rocks derived from ferrobasaltic magmas. On the other hand, Bingen et al. (2001) studied granulites and eclogites from Bergen Arcs and they assumed forming the rim in two phases – exsolution of baddeleyite from magmatic ilmenite following the increase SiO_2 activity during granulite-facies metamorphism which resulted in forming the zircons. Development of zircon rims during metamorphism is also proposed by Sláma et al. (2007). Austrheim et al. (2008) studied zircon coronas around ilmenite to get constrains for metamorphic and metasomatic reactions, based on the results they imply that zircon rim must have been already present before metamorphism. The complex reconstruction of process of formation zircon coronas at the expense of baddeleyite in gabbroic rocks was provided by Beckman and Möller (2018). Results of recent study by Salnikova et al. (2022) also corroborate formation of zircon at the expense of baddeleyite

during metamorphism and additionally the authors connect development of zircon corona with formation of multiple corona sequence between olivine and plagioclase.

1.2.3 Corona formation processes

Representative samples characterized below preserve magmatic texture and the contact of mafic minerals with adjacent plagioclase is marked by the development of corona layers. This phenomenon was described from gabbroic rocks worldwide e.g. in troctolitic gabbros (Gallien et al., 2012) and metagabbros (Cruciani et al., 2008) from Argentina, in gabbros from Grenvillian orogeny in Canada (Cox and Indares, 1999), in troctolitic gabbro from Norway (e.g. Joesten, 1986; Haas et al., 2002), in metagabbros from Adirondack mountains in North America (Whitney and McLelland, 1973) and also in gabbro-norites from Belomorian belt in Baltic sheald (Russia). Although the coronitic texture was quite popular topic among the authors since the 1970s (e.g. Whitney and McLelland, 1973; Joesten, 1986), thus several possible scenarios of its formation have been invoked so far. While Whitney and McLelland (1973) interpreted corona formation by simultaneous subsolidus reaction during slow cooling (post-magmatic stage), Joesten (1986) suggested the development of corona sequence is due to successive reactions during magmatic stage of crystallization. Based on recent studies three major interpretations can be outlined. First group of authors (e.g. Cox and Indares, 1999; Larikova and Zaraisky, 2009; Schorn et al., 2016) argue, that coronitic texture indicates prograde metamorphism and gabbro-to-eclogite transition. On the other hand, second group of authors (e.g. Cruciani et al., 2008; Gallien et al., 2012) imply the formation of corona sequences during cooling from granulite facies condition during its post-magmatic metamorphism. The third interpretation can be represented by Haas et al. (2002)

who concluded that coronas between olivine and plagioclase in gabbro from Norway were formed during a multi-stage, late-magmatic process.

1.2.4 Destabilization of magmatic plagioclase

Another interesting feature observed in our samples is decomposition and subsequent recrystallization of intermediate plagioclase to bytownite-anorthite lamellae with random orientation in oligoclase-andesine matrix. In previous works like Grove et al. (1983) or Spear (1980) the occurrence of andesine/bytownite coexisting with oligoclase was described as consequence of immiscibility gap in plagioclase, andesine and bytownite in this case are considered as a stable equilibrium assemblage. Characteristics of plagioclase lamellae in dependence of composition range is described in Smith and Brown (1988). Similar texture (randomly oriented lamellae of albitic and anorthitic plagioclase) is in recent studies commonly associated with gabbro to eclogite transition (e.g Santini-Rideout et al., 2007; Proyer and Postl, 2010; Schörn and Diener, 2016). The process of recrystallization of plagioclase to zoisite and its subsequent replacement by new plagioclase was already described by O'Brien et al. (1999) from Zone of Erbensdorf-Vohenstraus which has similar characteristics as MLC. Additionally, the decomposition of intermediate plagioclase is accompanied by occurrence of small corundum and spinel grains. The presence of other mineral phases enclosed in plagioclase is commonly known as "clouding" and it was described by Poldervaard and Gilkey (1953) or Goldsmith (1982).

2. RESULTS

2.1 Sampling strategy

In order to evaluate emplacement and evolution of gabbroic rocks along the western margin of the TBU (Fig. 2b), representative samples were collected from the two above-described areas. In the north-western part of TBU, the metagabbro samples were collected near the TCC and MLC boundary (Fig. 2b); sample PJ 5 in TCC, samples PJ 7, PJ 8, VP 46 along the contact between the two complexes, and samples PJ 6, PJ 9 in MLC. In the south-western part of TBU, the collected samples correspond to gabbroic rocks from south-eastern part of the NKM (Orlovice area) and from the Poběžovice Massif in DCC (Fig. 2b). The central part of NKM is represented by gabbro samples PJ 12A, PJ 12B, PJ 13 of the Orlovice area (Fig. 2b). These gabbro bodies are enveloped by ferrodiorite represented by sample PJ 14. Additional chemical analyses of samples from this area were included into our dataset; samples 06OH1B, 06OH2, 06OH3A, 06OH4B, 06OH5B, 06OH6B, 06OH7B, 06OHBK1B, 06OHBK2A represent gabbros from the Orlovice area, samples 06MB1, 06MB2, 06MB3 represent adjacent transition between metagabbros and ferrodiorites, and samples 06OH9, 06OH10B, 06OH11, 06OH13 represent ferrodiorite. Three metagabbro samples were collected from body surrounded by granodiorites near Kdyně, samples PJ 15 and PJ 22 and sample DK 17 surrounded by amphibolites of the NKM, represented by sample DK-L. Two metagabbro samples PJ 20, PJ 21 were collected in the Poběžovice Massif (Fig. 2b).

Sample	N	E	area	rock	Primary minerals assemblage
PJ 12A	**49.328032**	**13.085924**	**Orlovice (Orlovice hill)**	**metagabbro**	**Pl - Ol - Ilm**
PJ 12B	**49.326871**	**13.084658**	**Orlovice (Orlovice hill)**	**metagabbro**	**Pl - Ol - Cpx - Opx - Ilm**
06OH1B	49.324852	13.084736	Orlovice (Orlovice hill)	metagabbro	
06OH2	49.326265	13.082118	Orlovice (Orlovice hill)	metagabbro	
06OH3A	49.325845	13.092074	Orlovice (Orlovice hill)	metagabbro	
06OH4B	49.327160	13.092117	Orlovice (Orlovice hill)	metagabbro	
06OH5B	49.327985	13.094129	Orlovice (Orlovice hill)	metagabbro	
06OH6B	49.331455	13.086096	Orlovice (Orlovice hill)	metagabbro	
06OH7B	49.331269	13.090293	Orlovice (Orlovice hill)	metagabbro	
PJ 13	**49.333801**	**13.096041**	**Orlovice (Havranice hill)**	**metagabbro**	**Pl - Cpx - Am - Bt - Ilm**
06HBK1B	49.332497	13.109739	Orlovice (Havranice hill)	metagabbro	
06HBK2A	49.330944	13.108859	Orlovice (Havranice hill)	metagabbro	
06MB1	49.336003	13.068692	Orlovice (Můstek hill)	metagabbro	
06MB2	49.336967	13.061160	Orlovice (Můstek hill)	metagabbro	
06MB3	49.335779	13.058006	Orlovice (Můstek hill)	metagabbro	
PJ 14	**49.349478**	**13.063425**	**Orlovice (Ostrý hill)**	**ferrodiorite**	**Pl - Ol - Cpx Ilm**
06OH9	49.349127	13.063648	Orlovice (Ostrý hill)	ferrodiorite	
06OH10B	49.349602	13.063380	Orlovice (Ostrý hill)	ferrodiorite	
06OH11	49.349074	13.061706	Orlovice (Ostrý hill)	ferrodiorite	
06OH13	49.348571	13.063122	Orlovice (Ostrý hill)	ferrodiorite	
PJ 15	**49.386278**	**13.072395**	**Kdyně**	**metagabbro**	**Pl - Am - Bt - Ilm - Qtz**
PJ 22	**49.387696**	**13.055604**	**Kdyně**	**metagabbro**	**Pl - Ol - Cpx - Opx - Ilm**
DK 17	**49.391761**	**12.965632**	**Kdyně-Domažlice**	**metagabbro**	**Pl - Am - Bt - Ilm - Ap**
DK-L	**49.402876**	**12.973185**	**Kdyně-Domažlice**	**amphibolite**	**Pl - Am - Bt - Ilm**
PJ 20	**49.497122**	**12.844182**	**Poběžovice**	**metagabbro**	**Pl - Cpx - Am - Bt - Ilm**
DK 13	**49.510198**	**12.910095**	**Poběžovice**	**metagabbro**	**Pl - Cpx - Opx - Am - Ilm**

Tab. 1 Sample localities with their geographic coordinates

Samples used for petrologic describtion below with primary mineral assemblage are bold

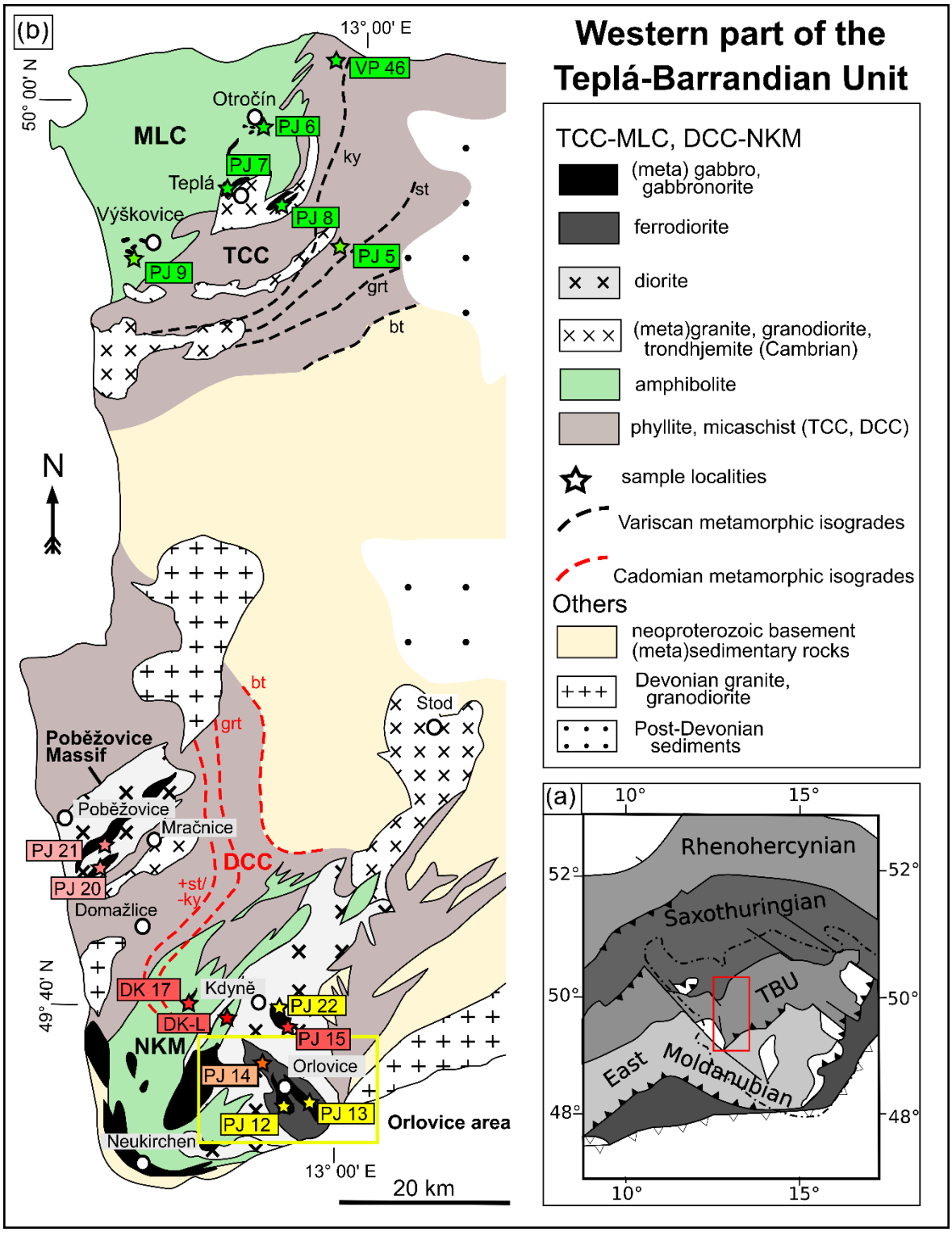

Fig. 2 Geological map of the western part of the TBU

(a) Bottom left corner location of Teplá-Barrandian Unit (TBD) in European Variscides; (b) Map of the studied areas is simplified from the Geological map of the Czech Republic 1: 500 000 (Cháb et al., 2007). Variscan metamorhic isograde after Peřestý et al. (2020), Cadomian metamorphic isograde after Zulauf et al. (1997).

2.2 Methodology

Composition of the minerals was determined at the laboratory of electron microscopy at the Institute of Petrology and Structural Geology (Charles University in Prague) using an electron probe micro analyser (EMPA) with field emission gun (FEG) electron source JXA-8530F by Jeol, equipped with 5 wave dispersive spectrometers (WDS). Quantitative analyses were acquired with an acceleration voltage of 15 kV and a probe current of 1.5 nA, compositional maps showing elemental distribution were acquired at 15 kV and 7 nA. Chemical composition of amphiboles was estimated following classification by Leake et al. (1997), the ratio X_{Mg} was calculated as $X_{Mg} = Mg/(Fe^{2+}+Fe^{3+}+Mg)$. Chemical composition of main rock-forming minerals is illustrated in figure 5, representative analyses of the samples are listed in table 2 and 3 with mineral abbreviations according to Kretz (1983).

An Element 2 high-resolution sector field mass spectrometer (Thermo Scientific) coupled with a 193 nm ArF Analyte Excite excimer laser ablation system (Teledyne/Cetac) laser ablation system at the Institute of Geology of the Czech Academy of Sciences in Prague was used to acquire the Pb/U isotopic ratios in zircon grains. The laser was fired at a repetition rate of 5 Hz, using a spot size of 25 μm and a fluence of c. 3.5 J/cm2. Acquisitions for all measured samples consisted of a 15 s measurement of blank followed by U and Pb signals from zircons for another 35 s. The total of 420 mass scans data were acquired in time resolved – peak jumping - pulse counting / analog mode with one point measured per mass peak for ^{204}Pb, ^{206}Pb, ^{207}Pb, ^{208}Pb, ^{232}Th, ^{235}U, and ^{238}U. Due to a non-linear transition between the counting and analogue acquisition modes of the ICP-MS instrument, the raw data were pre-processed using a purpose-made Excel macro. As a result, the intensities of ^{238}U were left unchanged, if measured in a counting mode, and recalculated from ^{235}U intensities, if the ^{238}U was acquired in analogue mode. The Hg impurities in the carrier He gas were reduced by using in-house made gold-coated sand trap. No common Pb correction

was applied to the data due to the high Hg contamination of the commercially available He carrier gas, which precludes accurate correction of the interfering ^{204}Hg on the very small signal of ^{204}Pb (common lead). The in-house glass-signal homogenizer, design inspired by Tunheng and Hirata (2004) was used for mixing all the gases and aerosol resulting in smooth, spike-free signal. The signal was tuned for maximum sensitivity of Pb and U, Th/U ratio close to unity and low oxide level, commonly below 0.2 %. Elemental fractionation and instrumental mass bias were corrected by normalization of internal natural zircon reference material 91500 (1065.4 ± 0.3 Ma, Wiedenbeck et al. 1995). Zircon reference materials Plešovice (337.1 ± 0.4 Ma; Sláma et al. 2008) and GJ-1 (^{207}Pb/^{206}Pb age of 608.5 ± 0.4 Ma, Jackson et al. 2004; ^{206}Pb/^{238}U weighted mean age of 602.7 ± 0.5 Ma, Kylander-Clark et al. 2013) and were periodically analysed during the measurement for quality control during four different analytical sessions correspond well and are less than 1.1 % accurate within the published reference values. Raw data reduction and age calculations, including corrections for baseline, instrumental drift, mass bias and down-hole were carried out off-line using the Iolite program (v. 3.5; Paton et al. 2011) with the VizualAge utility (Petrus and Kamber 2012). For the data presented here, blank intensities and instrumental bias were interpolated using an automatic spline function while down-hole inter-element fractionation was corrected using an exponential function (Paton et al. 2011). The U–Pb isotopic ages shown in concordia diagrams and age distributions of weight mean were generated using the ISOPLOT R program (Vermeesch 2018) and histograms with the Density Plotter 8.5 (Vermeesch, 2012). Discordance (%) limit for concordant population of the studied samples (Electronic Supplementary Material Table 1) was taken 5% and were calculated as follows: D<1Ga=[1((206Pb/238U) ⁄ (207Pb/235U))] × 100, this was due to worse accuracy of 207Pb/206Pb ages of younger zircons; analyses that were more than discordant were discarded for interpretations. Age errors are quoted at 2 sigma confidence levels.

Compared to zircons, common-Pb (non-radiogenic or initial) titanites have generally low uranium concentration and have a significant proportion of common-Pb that is inherited during crystallization. In contrast to non-radiogenic, radiogenic Pb is added to the common Pb after crystallization due to the decay of U and Th and contains only three isotopes (^{206}Pb, ^{207}Pb, and ^{208}Pb), which occur in variable proportions as a function of the Th/U-ratio and age (Kohn, 2017). The common Pb intercept of the isochron can be anchored to some nominal values or a common approach is to use ^{204}Pb based total U–Pb isochron method with Stacey and Kramers (1975) terrestrial Pb evolution model for correction of Pb. Unfortunately, in our case, ^{204}Pb-based common Pb correction is not appropriate practice, because measures ^{204}Pb are not with sufficient precision and accuracy due to the presence of an isobaric interference with ^{204}Hg (in He carrier gas). And also, ^{204}Pb requires the longest dwell times during ICP-MS measuring, which reduces the precision of the other lead's four naturally occurring isotopes. Thus, for data interpretation, we used regression of uncorrected izotope data on a Tera–Wasserburg total Pb plot (^{238}U/^{206}Pb vs. ^{207}Pb/ ^{206}Pb; Fig.12), where the initial 207Pb/206Pb is calculated as the y-intercept. For the measuring routine, we used the same analytical approach as for zircon isotope measuring. Data were acquired by single 20 μm spot analyses bracketed by internal natural zircon reference materials: 91500 (Wiedenbeck et al., 1995) and Plešovice (Sláma et al., 2008) and also titanite standards MKED-1 and KHAN (1517 ± 5 Ma and 521 ± 3 Ma, respectively; Sun et al., 2012). Finally, we have used just titanite in-house standards to minimize fractionation corrections and matrix effects (Sun et al., 2012), and these are less than 4.4 % accurate within the above-published reference values.

Chemical analyses of major and trace elements in the representative samples were carried out in order to characterize their petrogenesis. Pulverized and homogenized samples were analysed in the Bureau Veritas Mineral Laboratories (Vancouver, Canada) using the ICP–

OES method (major elements) and the ICP–MS (trace elements) methods. The obtained results were processed using the GCDkit software package (Janoušek et al., 2006) and are plotted in figures 10–12. Additionally, Sr–Nd isotopic compositions were determined at the Institute of Geology of the Czech Academy of Sciences.

2.3 Petrology and mineral chemistry

Most of the collected samples display well preserved magmatic textures, thus this primary mineral assemblage is described as M_1. Later-stage re-equilibrating process resulting in development of corona sequences at the contact of mafic minerals with plagioclase, replacement of mafic minerals by amphibole, and also break down of magmatic plagioclase. Minerals formed during these processes are assigned to M_2 mineral assemblage. Representative samples from both studied areas were selected for detailed description below. Samples from TCC-MLC area are charactrerized in Figures 3–8, composition of main rock-forming minerals is demonstrated in Tables 2–3. Samples from DCC-NKM area are demonstrated in Figures 9–17 and mineral analyses are summarized in Table 3 (M_1 minerals), Table 4 (M_2 minerals).

2.3.1 TCC-MLC samples

Samples in this area were collected from 6 localities and the representative samples were selected to characterize the typical lithotype for each locality. Based on geographic position, the samples were divided into 3 groups: 1) metagabbros from the TCC; 2) metagabbros collected along the contact of TCC with MLC; 3) metagabbros from bodied located in MLC (Fig. 2b).

Samples collected from TCC and MLC show similarities in metamorphic changes, which resulted in corona sequences terminated by garnet layer and advanced stage of breakdown of M_1 plagioclase. Two out of three samples collected along the contact of TCC and MLC are olivine-bearing metagabbros with undecomposed M_1 plagioclase (VP 46) or early stage of plagioclase breakdown (PJ 8).

2.3.1.1 Sample from TCC area

Sample PJ 5b (Fig. 2b) has well preserved magmatic texture defined by large aggregates of clinopyroxene and amphibole within plagioclase grains (Fig. 3a). Primary mineral assemblage consists of plagioclase – clinopyroxene – amphibole – biotite – ilmenite. Large M_1 plagioclase grains preserve its original shape with twinning, commonly it has a composition of andesine-labradorite ($An_{49–54}$), however the contact with garnet or amphibole is characterized slightly increased Na content accompanied by decrease of Ca content visible in compositional maps (Fig. 3g, i). Clinopyroxene of composition of diopside (Tab. 2) with X_{Mg} = 0.75–0.76 and jadeite content 2,5–4 % is observed in the central parts of the aggregates with amphibole, and it also commonly contains small (<10 μm) inclusions of amphibole. M_1 amphibole occurs with clinopyroxene in polycrystalline aggregates and its composition corresponds to pargasite-edenite with X_{Mg} = 0.51–0.58 (Tab. 2). Locally, in these aggregates, grains of albitic plagioclase occur between amphibole and clinopyroxene grains. Biotite (Tab. 3) is usually present in association with ilmenite.

M_2 mineral assemblage consisting of amphibole – garnet – titanite – plagioclase is connected to formation of coronas at the contact of M_1 mafic minerals with M_1 plagioclase ad also by break down of M_1 plagioclase. M_2 amphibole (Tab. 3) of magnesiohornblende composition with X_{Mg} = 0.59–0.67 commonly form corona enveloping

clinopyroxene and/or M_1 amphibole at the contact with M_1 plagioclase, this type of corona shows compositional zonation defined by increase of X_{Mg} towards plagioclase accompanied by decrease of Na content (0.33→0.26 apfu), K content (0.14→0.08 apfu), Al content (1.7→1.3 apfu; Fig. 3i) a Ti content (0.16→0.10 apfu). Garnet is typically observed as terminated layer of corona sequences at the contact with plagioclase, its composition is predominantly represented by almandine component (52–58%), followed by similar amount of pyrope (16–22%) and grossular (18–22%) and only minor representation of spessartine (2–6%, Fig. 4d). Garnet grains commonly contain small (1–40 μm) inclusions of amphibole, quartz and kyanite (Fig. 3c). Based on analysed profiles across the garnet layer it is possible to characterize asymmetric zonation defined from the central part (Alm = 56%; Py = 22%; Grs = 18%; Spess = 3%; X_{Mg} = 0.28) by more significant change in composition at the contact with M_2 amphibole (Alm = 54%; Py = 18%; Grs = 20%; Spess = 4%; X_{Mg} = 0.25) compared to (Alm = 53%; Py = 21%; Grs = 22%; Spess = 2%; X_{Mg} = 0.28) at the contact with M_1 plagioclase, however Ca content is higher at the contact with M_1 plagioclase (Fig. 3h). Ilmenite is usually surrounded by tiny (<10 μm) zircon grains forming a rim. Titanite is locally present forming corona around ilmenite (Fig. 3b). The second significant feature connected to metamorphic re-equillibration is break down of magmatic labradorite to bytownite (An_{85}) lamellae within andesine matrix (An_{45}; Fig.3d). Additionally, M_2 mineral assemblage includes actinolite, prehnite, albite and epidote (Fig.3e).

Sample PJ 5

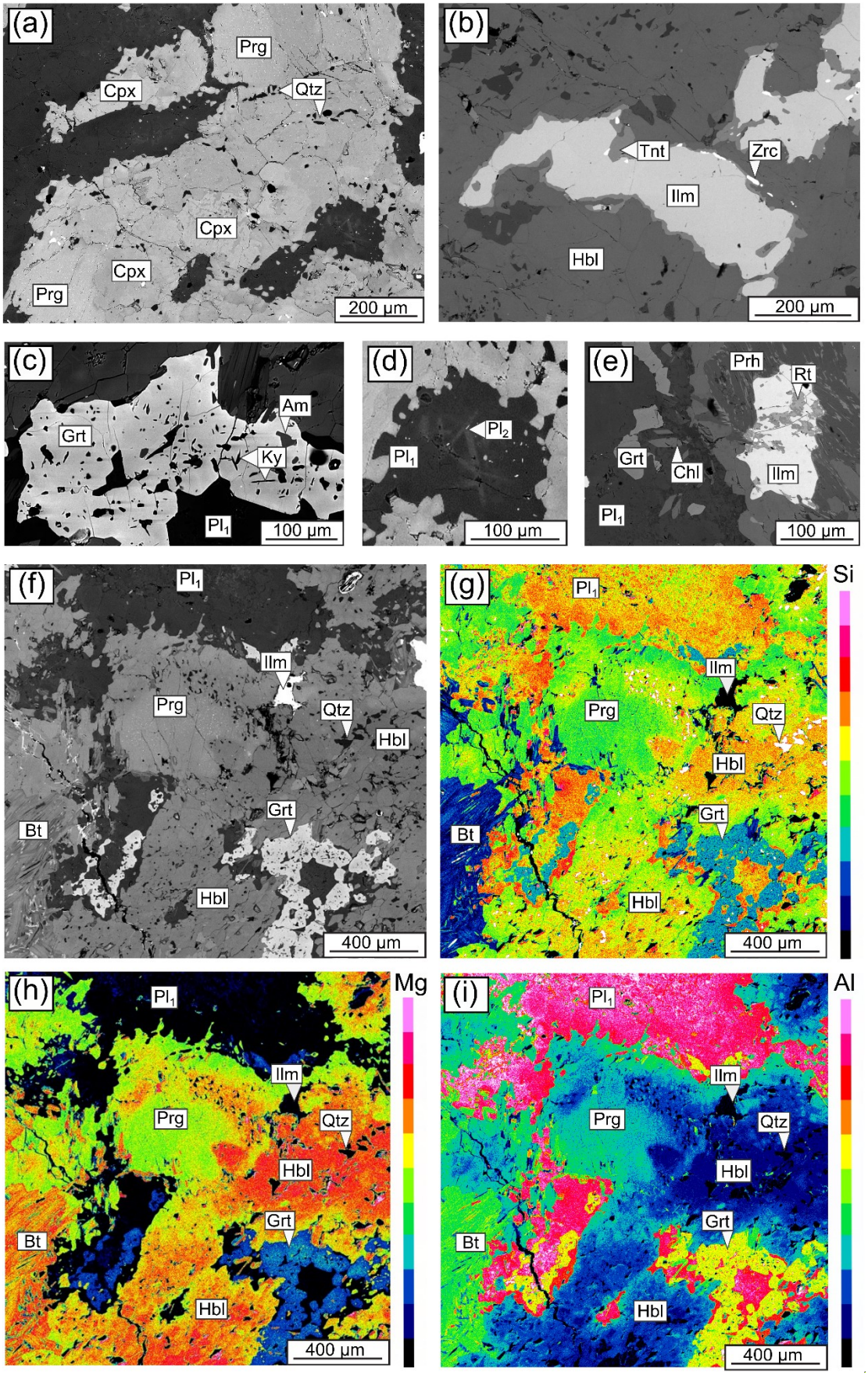

Fig. 3 Backscattered electron (BSE) images characterizing texture of the sample PJ 5

(a) Polycrystalline agreaggate of clinopyroxene and amphibole; (b) ilmenite grain with surrounded by titanite and small grains of zircon; (c) detail of garnet corona with its inclusions; (d) lammelae of anorthite in andesine matrix; (e) rutile in association with ilmenite; (f) BSE picture of area used for compositional map; (g) compositional map demonstrating distribution of Si, Mg (h) and Al (i) in minerals

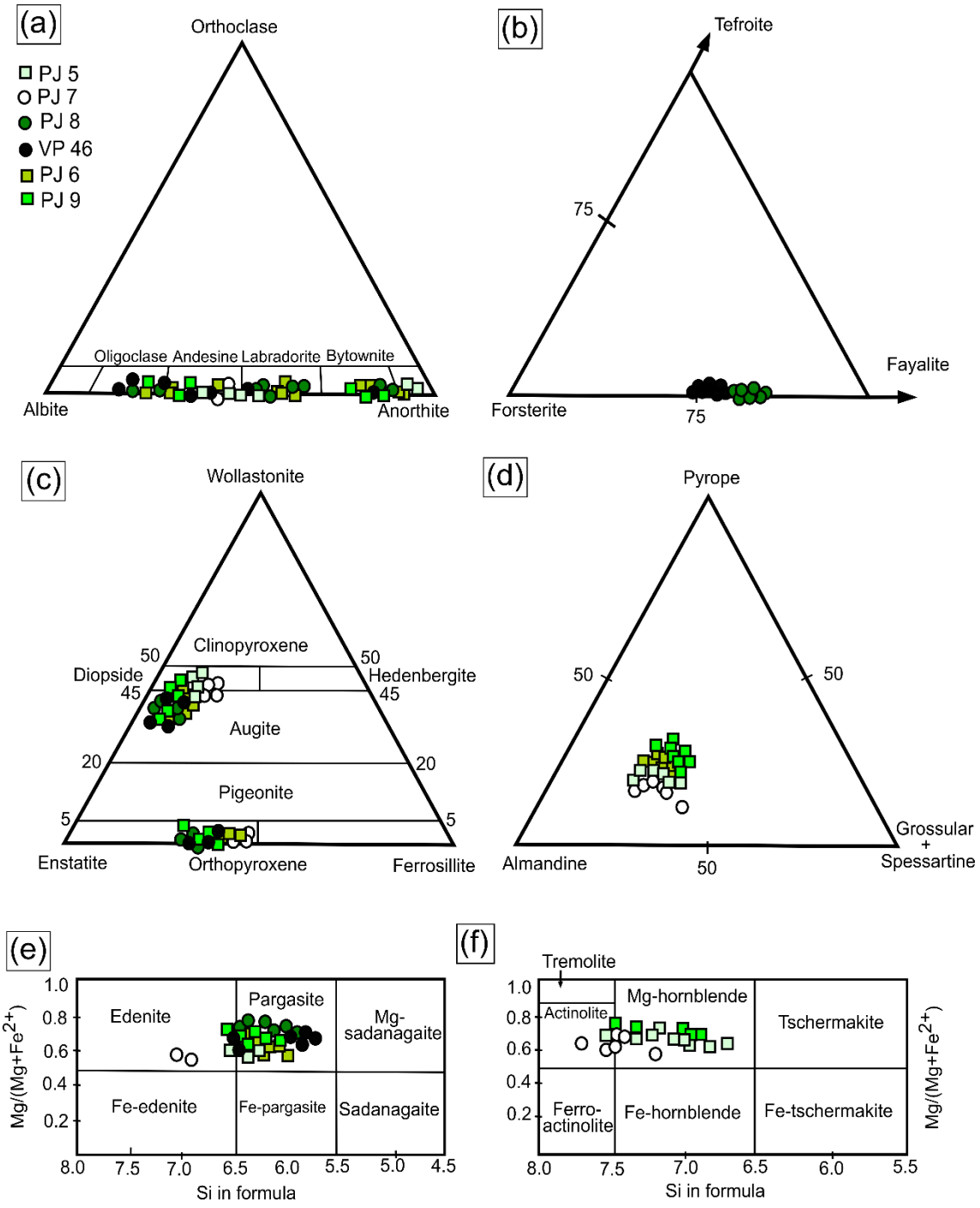

Fig. 4 Diagrams demonstrating composition of the main rock-forming minerals of representative samples described above.

(a) plagioclase; (b) olivine; (c) pyroxenes after Morimoto (1988); (d) garnet composition; (e), (f) amphibole after Leake et al. (1997).

unit	TCC			TCC-MLC							MLC			
sample	**PJ 5**			**PJ 8**				**VP 46**			**PJ 6**			**PJ 9**
mineral	Cpx	Am	Bt	Ol	Pl	Cpx	Opx	Am	Spl	Bt	Opx	Cpx	Am	Am
SiO_2	53.24	44.02	36.77	37.24	50.58	52.00	55.12	44.21	0.18	39.37	52.13	52.1	42.28	46.51
TiO_2	0.16	1.62	4.06	b.d	b.d	0.83	0.08	2.93	0.86	2.42	0.13	0.36	1.59	1.93
Cr_2O_3	0.37	0.28	b.d	b.d	b.d	0.65	b.d	0.59	26.08	b.d	b.d	b.d	b.d	b.d
Al_2O_3	1.36	11.35	15.11	b.d	31.50	3.05	0.43	10.88	20.88	14.95	0.97	2.39	13.12	9.61
FeO	7.66	14.32	16.73	30.00	b.d	5.93	16.08	9.70	46.35	7.48	24.84	8.83	14.44	9.89
MnO	0.31	0.18	b.d	0.30	b.d	0.16	0.51	0.20	0.47	b.d	0.69	0.26	0.16	0.09
MgO	13.42	10.94	12.96	32.30	b.d	15.35	26.50	14.18	3.03	20.70	20.09	12.68	11.56	14.96
CaO	23.14	11.76	0.07	b.d	14.05	20.45	1.06	11.06	b.d	b.d	0.53	22.07	11.12	11.38
Na_2O	0.50	1.38	0.16	b.d	3.54	1.13	b.d	2.99	b.d	0.83	b.d	0.72	2.45	1.87
K_2O	b.d	0.83	9.70	b.d	b.d	b.d	b.d	0.92	b.d	9.21	b.d	0.00	0.64	0.58
V_2O_5	b.d	b.d	b.d	b.d	b.d	b.d	b.d	b.d	0.58	b.d	b.d	b.d	b.d	b.d
Cl	b.d	b.d	b.d	b.d	b.d	b.d	b.d	b.d	b.d	0.05	b.d	b.d	b.d	b.d
ZnO	b.d	b.d	b.d	b.d	b.d	b.d	b.d	b.d	0.93	b.d	b.d	b.d	b.d	b.d
total	100.16	96.68	95.56	99.84	99.66	99.54	99.78	97.66	99.36	95.01	99.38	99.41	97.36	96.82
cat/O	4/6	13+A/23	16/22	3/4	5/8	4/6	4/6	13+A/23	3/4	16/22	4/6	4/6	13+A/23	13+A/23
Si	1.98	6.56	5.67	1.01	2.31	1.91	2.00	6.45	0.01	5.74	1.98	1.95	6.22	6.72
Ti	0.00	0.18	0.47	0.00	0.00	0.02	0.00	0.32	0.02	0.25	0.00	0.01	0.18	0.21
Cr	0.01	0.03	0.00	0.00	0.00	0.02	0.00	0.07	0.68	0.00	0.00	0.00	2.27	1.64
Al	0.06	1.99	2.75	0.00	1.69	0.13	0.02	1.87	0.81	2.55	0.04	0.11	0.00	0.00
Fe^{2+}	0.24	1.77	2.16	0.68	0.00	0.12	0.49	1.18	0.87	0.92	0.79	0.26	1.73	1.17
Fe^{3+}	0.00	0.02	0.00	0.00	0.00	0.06	0.00	0.01	0.41	0.00	0.00	0.02	0.07	0.04
Mn	0.01	0.02	0.00	0.01	0.00	0.00	0.02	0.02	0.01	0.00	0.02	0.01	0.02	0.01
Mg	0.74	2.43	0.00	1.30	0.00	0.84	1.43	3.08	0.00	0.02	1.14	0.71	2.53	3.22
Ca	0.92	1.88	2.98	0.00	0.69	0.81	0.04	1.73	0.15	4.58	0.02	0.89	1.75	1.76
Na	0.04	0.40	0.01	0.00	0.31	0.08	0.00	0.85	0.00	0.00	0.00	0.05	0.70	0.52
K	0.00	0.16	0.05	0.00	0.00	0.00	0.00	0.17	0.00	0.20	0.00	0.00	0.12	0.11
V	0.00	0.00	0.00	0.00	0.00	0.00	0.00	0.00	0.01	1.74	0.00	0.00	0.00	0.00
Cl	0.00	0.00	0.00	0.00	0.00	0.00	0.00	0.00	0.00	0.01	0.00	0.00	0.00	0.00
Zn	0.00	0.00	0.00	0.00	0.00	0.00	0.00	0.00	0.02	0.00	0.00	0.00	0.00	0.00
XMg	0.76	0.58	0.58	0.66		0.82	0.75	0.72	0.14	0.83	0.59	0.72	0.58	0.73

Tab. 2 Representative analyses characterizing M1 minerals in samples from TCC-MLC area *cat/O - number of cations / oxides in formula unit, A = Ca+Na+K; b.d. - below detection limit. Amphiboles were calculated after Leake et al. (1997)*

	TCC			TCC-MLC							MLC						
sample	**PJ 5**			**PJ 7**				**VP 46**			**PJ 6**			**PJ 9**			
mineral	Pl	Pl	Am	Am (Pl)	Am (Opx)	Cm	Opx	Opx	Grt (Am)	Grt core	Grt (Pl)	Spl	Cpx	Opx	Am	Pl rim	Pl core
SiO2	46.54	56.49	48.32	42.11	51.19	54.44	55.55	55.82	37.56	38.83	38.9	0.12	53.96	54.41	48.54	43.84	59.21
TiO2	b.d.	b.d.	0.95	0.33	0.15	b.d.	0.13	b.d.	b.d.	b.d.	b.d.	b.d.	0.09	b.d.	0.84	b.d.	b.d.
Cr2O3	b.d.	b.d.	0.28	b.d.	b.d.	b.d.	b.d.	b.d.	b.d.	b.d.	b.d.	b.d.	b.d.	b.d.	0.42	b.d.	b.d.
Al2O3	34.06	27.61	7.76	14.07	4.23	0.44	0.6	1.03	21.13	21.86	21.99	61.63	0.98	0.86	7.53	35.57	25.55
FeO	b.d.	b.d.	12.72	16.28	14.09	22.51	16.95	14.66	25.67	23.99	23.61	22.16	5.59	17.38	8.42	b.d.	0.11
MnO	b.d.	b.d.	0.22	0.12	0.29	0.40	0.36	0.32	0.89	0.54	0.66	b.d.	0.09	0.23	0.13	b.d.	b.d.
MgO	b.d.	b.d.	13.38	9.31	14.70	17.80	26.80	28.09	5.68	6.36	5.97	13.08	15.29	26.05	16.38	b.d.	b.d.
CaO	17.24	9.61	12.06	11.78	10.86	0.83	0.39	0.19	7.61	8.47	9.38	0.27	23.47	0.16	12.04	19.48	7.42
Na2O	1.80	6.04	0.91	0.96	0.31	b.d.	b.d.	b.d.	b.d.	b.d.	b.d.	b.d.	0.45	b.d.	1.38	0.65	7.47
K2O	b.d.	0.14	0.43	1.26	0.19	b.d.	b.d.	b.d.	b.d.	b.d.	b.d.	b.d.	b.d.	b.d.	0.27	b.d.	0.06
ZnO	b.d.	b.d.	b.d.	b.d.	b.d.	b.d.	b.d.	b.d.	b.d.	b.d.	b.d.	0.37	b.d.	b.d.	b.d.	b.d.	b.d.
total	99.64	99.89	97.03	96.22	96.01	96.42	100.78	100.11	98.54	100.1	100.50	97.63	99.92	99.09	95.95	99.54	99.82
cat/O	5/8	5/8	13+A/23	13+A/23	13+A/23	13+A/23	4/6	4/6	8/12	8/12	8/12	3/4	4/6	4/6	13+A/23	5/8	5/8
Si	2.14	2.54	7.04	6.75	7.51	7.03	2.00	2.00	2.97	3.00	2.99	0.01	1.98	1.99	7.02	2.03	2.65
Ti	0.00	0.00	0.10	0.04	0.02	0.00	0.00	0.00	0.00	0.00	0.00	0.00	0.00	0.00	0.09	0.00	0.00
Cr	0.00	0.00	0.03	0.00	0.00	0.00	0.00	0.00	0.00	0.00	0.00	0.00	0.00	0.00	0.05	0.00	0.00
Al	1.85	1.46	1.33	1.78	0.49	0.07	0.03	0.04	1.97	1.99	1.99	1.95	0.04	0.04	1.28	1.94	1.35
Fe2+	0.00	0.00	1.53	2.18	1.66	2.13	0.51	0.44	1.59	1.53	1.49	0.67	0.16	0.53	0.99	0.00	0.00
Fe3+	0.00	0.00	0.03	0.00	0.10	0.64	0.00	0.00	0.10	0.02	0.03	0.03	0.01	0.00	0.03	0.00	0.00
Mn	0.00	0.00	0.03	0.02	0.04	0.04	0.01	0.01	0.06	0.04	0.04	0.00	0.00	0.01	0.02	0.00	0.00
Mg	0.00	0.00	2.91	2.23	3.22	3.43	1.44	1.50	0.67	0.73	0.68	0.00	0.84	1.42	3.53	0.00	0.00
Ca	0.85	0.46	1.88	2.02	1.71	0.11	0.02	0.01	0.64	0.70	0.77	0.28	0.92	0.01	1.86	0.97	0.36
Na	0.16	0.53	0.26	0.30	0.09	0.00	0.00	0.00	0.00	0.00	0.00	0.01	0.03	0.00	0.39	0.06	0.65
K	0.00	0.01	0.08	0.26	0.04	0.00	0.00	0.00	0.00	0.00	0.00	0.00	0.00	0.00	0.05	0.00	0.00
Zn	0.00	0.00	0.00	0.00	0.00	0.00	0.00	0.00	0.00	0.00	0.00	0.05	0.00	0.00	0.00	0.00	0.00
XMg			0.65	0.50	0.65	0.55	0.74	0.77	0.28	0.32	0.31	0.29	0.83	0.73	0.78		
Endm																	
An	84.00	46.00						Py	21.10	24.20	22.50				An	94.00	35.00
Ab	16.00	53.00						Alm	50.40	50.50	49.00				Ab	6.00	64.00
Or	0.00	1.00						Grs	20.40	23.10	25.40				Or	0.00	1.00
								Spess	1.90	1.20	1.40						

Tab. 3 Representative analyses characterizing M2 minerals in samples from TCC-MLC area

cat/O - number of cations / oxides in formula unit, A = Ca+Na+K; b.d. - below detection limit. Amphiboles were calculated after Leake et al. (1997

2.3.1.2 Samples from contact of TCC and MLC

Sample PJ 7 was collected from gabbroic body situated at the east from the village Teplá (Fig. 2b). At the locality there are present several lithotypes from coarse-grained gabbropegmatite to fine-grained gabbro. Selected sample represents coarse-grained metagabbro with higher amount of plagioclase and ilmenite compared to other selected samples. Primary magmatic assemblage consists of plagioclase – clinopyroxene – orthopyroxene – biotite – ilmenite and quartz. Texture is characterized by clinopyroxene, orthopyroxene and ilmenite aggregates surrounded by large grains of plagioclase (up to 5 mm large, Fig. 5a). Although M_1 plagioclase is completely broke down to acidic and sodic plagioclases, its original twinning is still recognizable. The composition of the M_1 plagioclase was estimated from analysed area (15 μm in diameter) as labradorite (An_{60}). M_1 clinopyroxene occurs as large grains (up to 2 mm size) and it commonly contain exsolutions of orthopyroxene and ilmenite inclusions. Its composition varies between diopside and augite (Fig. 4c) with X_{Mg} = 0.67 and jadeite content 2.3–2.7%. Orthopyroxene of enstatite composition (Fig. 4c) with X_{Mg} = 0.51–0.56 form large grains of similar size as clinopyroxene and these grains show slight compositional zonation defined by decrease of X_{Mg} towards rim from 0.55 in central part to 0.52 at the marginal part. In M_1 orthopyroxene ilmenite and amphibole inclusion are observed as well as clinopyroxene exsolutions. Biotite is commonly associated with ilmenite, its X_{Mg} = 0.22 is noticeably lower compared to other investigated samples. Ilmenite form grains up to 2 mm size which are enveloped by tiny grains of zircon forming thin rim (Fig. 5b), inside of ilmenite grains there are enclosed small grains of pyrrhotine.

M_2 minerals such as plagioclase – amphibole – garnet, are connected to the decomposition of M_1 plagioclase and formation of three types of corona sequences at the contact of magic minerals and plagioclase. Ilmenite is in places surrounded by garnet corona, which commonly contain inclusions of amphibole, quartz, kyanite, in addition carbonate was

observed here. Composition of garnet consists of almandine component (55–59%), grossular component (18–28%), pyrope component (15–17%) and spessartine (3–4%, Fig. 4d). This type of corona shows slightly asymmetric compositional zonation defined from central part (Alm = 51%; Py = 14%; Grs = 28%; Spess = 3%; X_{Mg} = 0.21) by increase of X_{Mg}, almandine, pyrope and spessartine components accompanied by decrease of grossular content towards rims. Asymmetry of zonation is demonstrated by more significant change in composition at the contact with ilmenite (Alm = 58%; Py = 15%; Grs = 18%; Spess = 4%; X_{Mg} = 0.20) compared to the contact with plagioclase (Alm = 56%; Py = 17%; Grs = 21%; Spess = 4%; X_{Mg} = 0.22). Between clinopyroxene and plagioclase the double amphibole (Tab.3) corona is formed (Fig. 4c). The M_1 clinopyroxene is surrounded by symplectitic layer of amphibole and quartz followed by monomineral amphibole corona at the contact with plagioclase. Composition of amphibole in symplectite corresponds to actinolite, however there is a compositional zonation characterized by decrease of X_{Mg} accompanied by increase of Al, Ca, and alkali content towards monomineralic layer (X_{Mg} = 0.65→0.61; Al = 0.49→0.94 apfu; Ca = 1.78→1.90 apfu; Na = 0.09→0.20 apfu; K = 0.04→0.09 apfu). Following amphibole corona show strong compositional zonation defined by transition from magnesiohornblende at the contact with symplectite to edenite at the contact with plagioclase (X_{Mg} = 0.60→0.51; Al = 0.98→1.78 apfu; Ca = 1.95→2.02 apfu; Na = 0.18→0.30 apfu; K = 0.11→0.25 apfu; Fig. 5i). Occasionally, this corona sequence is terminated by garnet layer at the contact with plagioclase, in this case, the garnet layer has a similar character as the garnet observed around illmenite. Between M_1 orthopyroxene and M_1 plagioclase the multiple corona sequence is formed. At the contact with orthopyroxene layer of cummingtonite (X_{Mg} = 0.55; Fig. 5d; Tab.3) is developed, followed by symplectite of quartz and amphibole (actinolite to magnesiohornblende with X_{Mg} = 0.65). The sequence continues with amphibole layer which composition change from magnesiohornblende to edenite and the whole sequence is terminated by garnet zone formed at the contact with M_1

plagioclase. Garnet contains inclusions of amphibole, quartz and kyanite. Garnet in this corona sequence has the similar character as the garnet around ilmenite, thus in composition it has major representation of almandine content (51–59%), grossular (19–28%), pyrope (16–17%) and minor spessartine content (3–4%). It also show asymmetry in compositional zonation characterized from the central part (Alm = 51%; Py = 16%; Grs = 28%; Spess = 3%; X_{Mg} = 0.23) by increase of almandine, spessartine and decrease of grossular content, while the more significant change is observed in direction to M_1 orthopyroxene (Alm = 59%; Py = 16%; Grs = 19%; Spess = 4%; X_{Mg} = 0.21) compared to the contact with M_1 plagioclase (Alm = 54%; Py = 17%; Grs = 23%; Spess = 3%; X_{Mg} = 0.24). The X_{Mg} and pyrope content continuously increase towards M_1 plagioclase. M_2 mineral assemblage is also connected to the breakdown of M_1 plagioclase, which is in the sample completely decomposed to small bytownite grains (An_{80}) in andesine matrix (An_{41-50}), within these M_2 plagioclases tiny (<1 μm) lamellar grains of ilmenite are present as well as biotite, amphibole, and quartz (Fig. 5e). It is important to note that in this sample, zircon was not observed.

Sample PJ 7

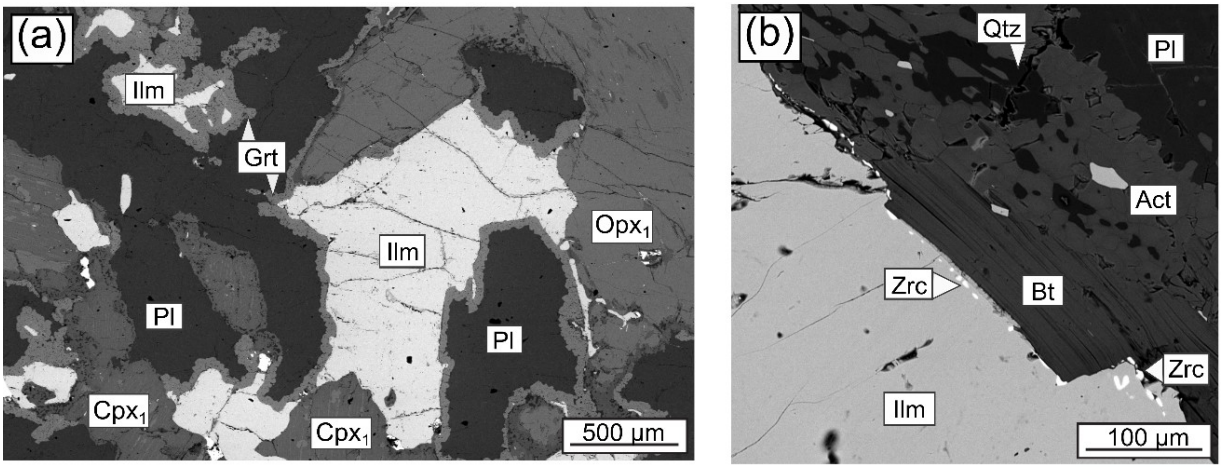

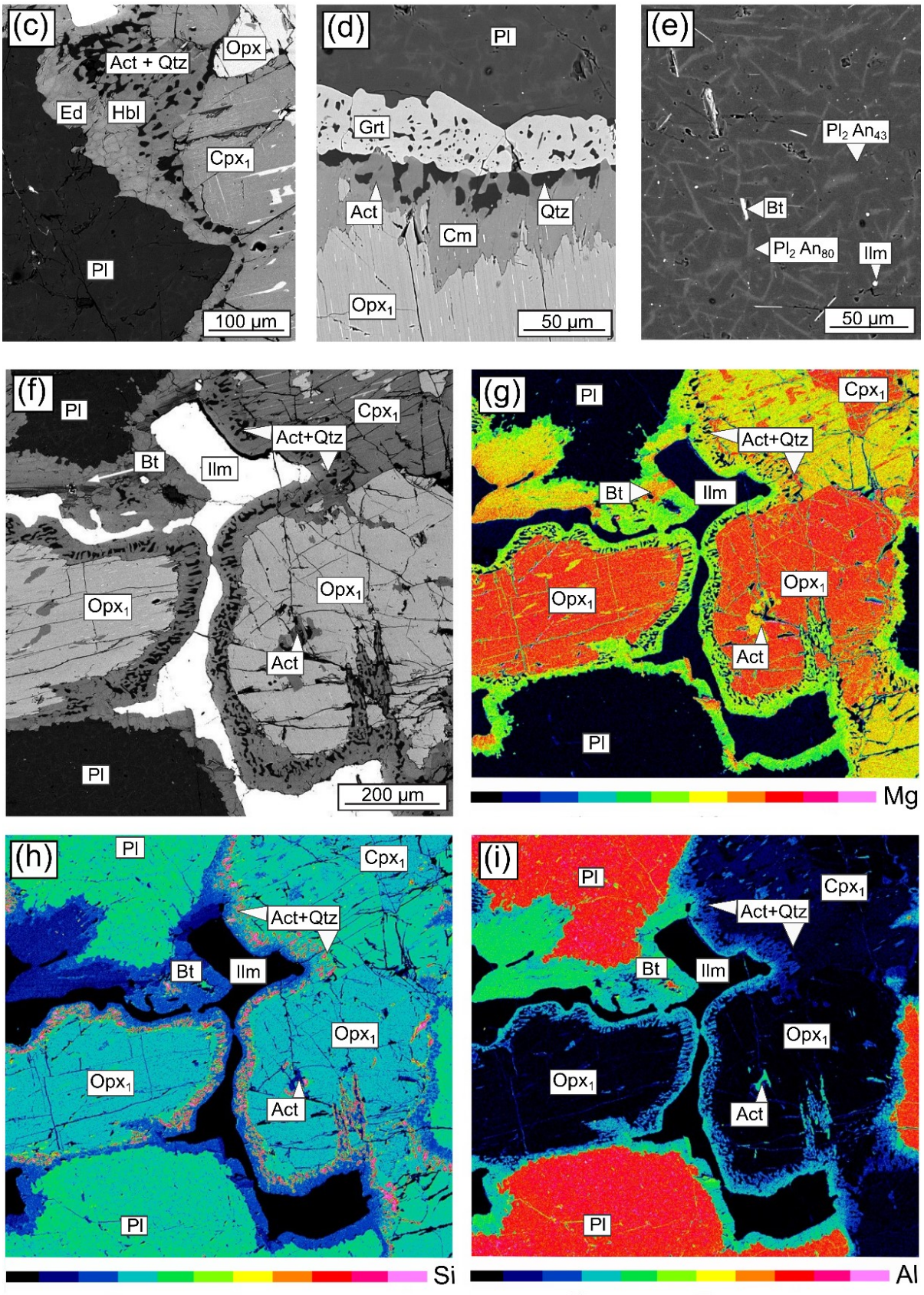

Fig. 5 BSE images characterizing texture of sample PJ 7

(a) Polycrystalline agreaggate of clinopyroxene, orthopyroxene and ilmenite; (b) ilmenite grain with small grains of zircon; (c) detail ofamphibole corona between clinopyroxene and plagioclase; (d) detail of corona sequence between orthopyroxene and plagioclase; (e) detail of decomposed M_1 plagiclase; (f) BSE picture of area used for compositional map; (g) compositional map demonstrating distribution of Mg, Si (h) and Al (i) in minerals

Sample PJ 8 was collected from the locality called Ovčí Dvůr located south-east from the village Teplá (Fig. 2b), where the small medium-grained metagabbro body is surrounded by deformed orthogneiss. M_1 mineral assemblage consists of olivine – plagioclase – clinopyroxene – orthopyroxene – amphibole – biotite – ilmenite – Cr-spinel. The texture is characterized by large clinopyroxene grains accompanied by olivine grains and occasionally biotite within plagioclase. Olivine grains of forsterite composition ($Fo_{65–72}$; X_{Mg} = 0.65–0.71; Tab.2) commonly occur with fractures filled by amphibole serpentinite, and olivine crystals also contain inclusions of Cr- spinel or pyrrhotite. M1 plagioclase occurs as large grains up to 8 mm size it has well visible twinning and a labradorite composition ($An_{56–69}$; Tab.2). M_1 clinopyroxene form grains up to 5 mm large, which enclose olivine, ilmenite and apatite grains, small inclusions of spinel and pyrrhotite are also present here. The composition of M_1 clinopyroxene corresponds to augite with X_{Mg} = 0.81–0.86 and jadeite content 2–5% Tab.2). M_1 orthopyroxene of enstatite composition with X_{Mg} = 0.74–0.75 (Tab.2) is occasionally observed in association with M_1 amphibole at the marginal part of the clinopyroxene grains (Fig. 6a) and it occasionally contains inclusions of spinel, pyrrhotite and apatite. M_1 amphibole is predominantly present in marginal parts of the clinopyroxene aggregates, and it is rimmed by tiny grains of ilmenite, which also form inclusions in M_1 amphibole together with apatite and pyrite. The composition of amphibole varies between pargasite and edenite (Fig. 4e) with Ti content (0.30–0.36 apfu) and constant X_{Mg} = 0.76–0.77. Biotite and ilmenite grains of similar size (<1 mm) commonly occur in association with each other. Biotite of phlogopite composition

(X_{Mg} = 0.79–0.81) contain higher amount of Ti (1.81–2.05 apfu) compared to other studied samples. Ilmenite forms grains up to 0.5 mm size (Fig. 6b). In addition, Cr-spinel (Cr = 1.04–1.14 apfu, Zn = 0.04–0.05 apfu, Mg = 0.28–0.32 apfu) is locally present in some parts of ilmenite grains (Fig. 6b).

M_2 mineral assemblage consists of orthopyroxene – amphibole – spinel observed in corona sequences, and plagioclase which is present in small domains of decomposed M_1 plagioclase. M_1 clinopyroxene is commonly enveloped by layer of M_2 amphibole at the contact with M_1 plagioclase. Between olivine or biotite and plagioclase a multiple corona is developed, it consists of orthopyroxene layer at the contact with olivine, followed by amphibole layer at the contact with M_1 plagioclase. Locally, in amphibole corona the plagioclase and spinel symplectites are observed at the contact with plagioclase, in these marginal parts of amphibole layer spinel inclusion accompanied by corundum grains (up to 20 μm long; Fig. 6c) are present. Composition of M_2 orthopyroxene generally corresponds to enstatite with X_{Mg} = 0.70–0.74, which is slightly lower than the X_{Mg} of M_1 orthopyroxene, however this corona shows compositional zonation characterized by increase of Al and minor decrease of X_{Mg} towards amphibole layer (Al = 0.02→0.05 apfu; X_{Mg} = 0.73→0.72; Fig 6f). M_2 amphibole is represented by pargasite (X_{Mg} = 0.71–0.73) with slightly lower X_{Mg} compared to its M_1 equivalent. The decomposition of M_1 plagioclase occur only in small domains predominantly located in the marginal part of the large grains or at the contact with amphibole corona. The breakdown of M_1 labradorite is characterized by presence of two plagioclases: anorthite (An_{92}) form lamellae in oligoclase ($An_{24–29}$) matrix accompanied by tiny grains of spinel (up to 2μm) and corundum (<1 μm) grains are observed (Fig. 6c). Commonly it is possible to find a systematics in orientation of corundum and spinel grains with respect to the crystallographic orientation of hosted plagioclase. It is important to note that only zircon observed in the sample is thin of zircon (<5 μm) around ilmenite (Fig. 6b).

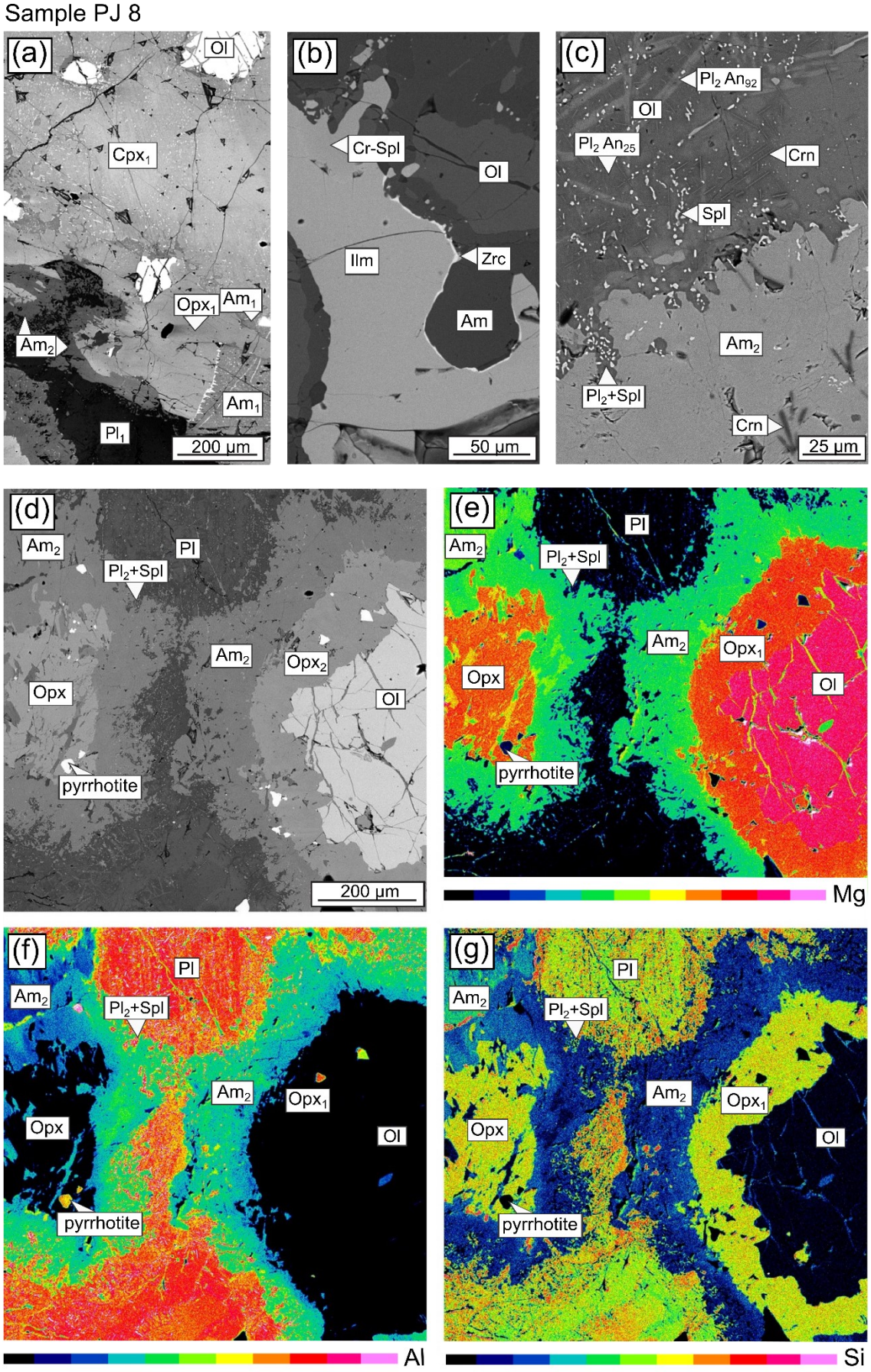

Fig. 6 BSE images characterizing texture of sample PJ 8

(a) Polycrystalline agreaggate of clinopyroxene, orthopyroxene and amphibole; (b) ilmenite grain with small grains of zircon froming thin rim and accompanied by Cr-spinel; (c) detail of anorthite lamellae in andesine matrix together with spnel and corundum grains; (d) BSE picture of area used for compositional map; (e) compositional map demonstrating distribution of Mg, Al (g) and Si (g) in minerals

Sample VP 46 was collected from small metagabbro body located at the contact of Teplá Crystalline and Mariánské-Lázně Complexes (Fig. 2b). In the texture of medium-grained sample, olivine, clinopyroxene and plagioclase grains are dominant. M_1 minerals are represented by olivine – plagioclase – clinopyroxene – orthopyroxene – amphibole – biotite – ilmenite and Cr-spinel (Fig. 7a). Olivine form grains up to 3mm large, which are commonly fractures. These fractures are filled by amphibole and serpentinite. Occasionally, tiny lamellar inclusions (<1 μm) filled with amphibole and magnetite are observed in olivine. The olivine composition (forsterite with X_{Mg} = 0.70–0.75, Fig. 4b) is relatively uniform, however individual grains show compositional variability in Mg content (Fig. 7e). M_1 plagioclase occurs as grains up to 5 mm large with noticeable twinning. Although plagioclase do not show any signs of decomposition, within the grains there are characterized sectors of different composition in range from oligoclase ($An_{18–25}$), andesine ($An_{34–45}$) to labradorite (An_{53}; Fig. 4a). Large grains (up to 1 mm size) of M_1 clinopyroxene often enclose crystals of Cr-spinel and pyrrhotite. Its composition varies between diopside and augite (Fig. 4c) with X_{Mg} = 0.77–0.80 and jadeite content 3–7 mol %. However, the clinopyroxene grains demonstrate strong compositional zonation characterized from Cr-rich central part of the grains (Cr = 0.04 apfu, Na = 0.07 apfu, Al = 0.18 apfu, Ti = 0.03 apfu, Ca = 0.77 apfu, X_{Mg} = 0.80 apfu) by decrease of Cr, Na, Ca, X_{Mg} accompanied by increase of Ti and Al content towards the contact with plagioclase (Cr = 0.01 apfu, Na = 0.05 apfu, Al = 0.24 apfu, Ti = 0.05 apfu, Ca = 0.76 apfu , X_{Mg} = 0.77 apfu), and by decrease of Cr, Na, Al, Ti, X_{Mg} accompanied by increase of Ca content towards the contact with M_1 amphibole (Cr = 0.01 apfu, Na = 0.04 apfu, Al = 0.06 apfu, Ti = 0.01 apfu, Ca = 0.80 apfu,

X_{Mg} = 0.79 apfu, Fig. 7f, g). M_1 orthopyroxene of enstatite composition with X_{Mg} = 0.70–0.78 is rarely observed among the olivine and biotite grains, it occasionally contains ilmenite and spinel inclusions. M_1 amphibole is locally present in association with M_1 clinopyroxene. Although, it has a composition of pargasite-edenite Fig. če; Tab.2), the individual gains show compositional zonation defined from the central part by decrease of Ti, Al, Na contents accompanied by increase of Cr content and X_{Mg} towards rims (Ti = 0.58→0.32 apfu, Al = 1.99→1.87 apfu, Na = 0.92→0.85 apfu, Cr = 0.05→0.07 apfu, X_{Mg} = 0.70→0.72). Biotite form grains up to 0.5 mm in size, which predominantly occur among olivine grains. Its composition corresponds to flogopite with X_{Mg} = 0.80–0.85 and has a highly variable Ti content (0.75–3.04 apfu; Tab.2). Ilmenite in this sample is commonly associated with magnetite and Cr-spinel (Cr = 0.63–0.91 apfu). Magnetite and Cr-spinel (Tab. 2) are observed also as lamellas in ilmenite. At the marginal parts of ilmenite grains Cr-spinel and small zircon grain occurs (Fig. 7c).

M_2 mineral assemblage orthopyroxene – amphibole – spinel is related to formation of corona sequences around olivine and biotite. At the contact between olivine and plagioclase double corona of orthopyroxene and amphibole is developed (Fig. 7b, d). M_1 orthopyroxene forming layer adjacent to olivine has a composition of enstatite (X_{Mg} = 0.76–0.78; Tab.2). The M_2 orthopyroxene layer is followed by corona of M_2 amphibole (pargasite with X_{Mg} = 0.74–0.79), which is alternating with orthopyroxene and spinel symplectite. Biotite is enveloped by similar symplectite corona of orthopyroxene and spinel, which is alternated by amphibole corona at the contact with plagioclase (Fig. 7b). At the marginal parts of ilmenite, the symplectite-like texture is observed, it is formed by tiny grains of ilmenite and spinel. In this area zircon is also present (Fig. 7c).

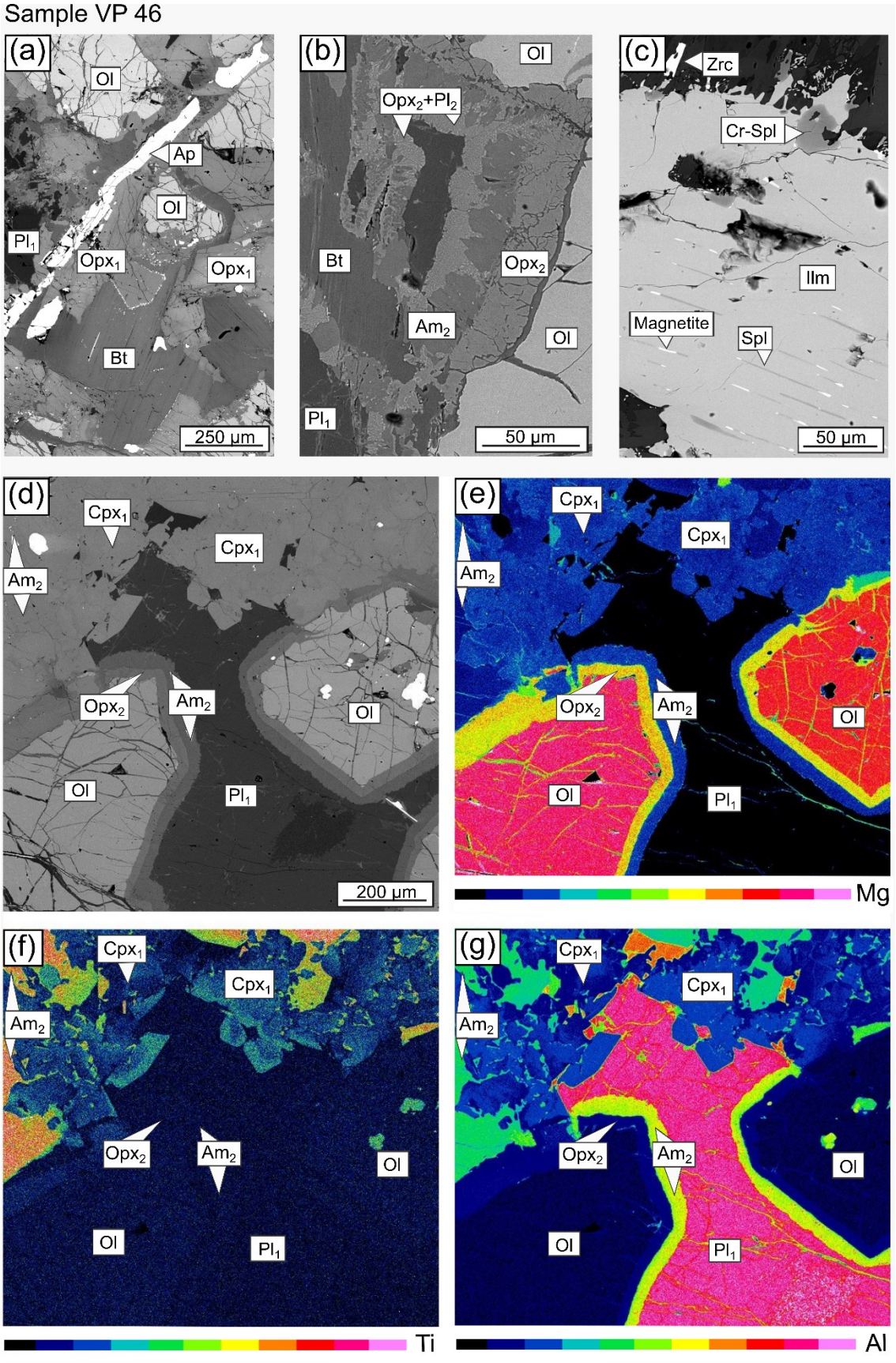

Fig. 7 BSE images characterizing texture of sample VP 46

(a) Polycrystalline agreaggate of olivine, orthopyroxene and biotite; (b)detail of corona sequence between olivine and plagioclase; (c) ilmenite grain with inclusions of magnethite and spinel lamellae and zircon and Rc-sninel; (d) BSE picture of area used for compositional map; (e) compositional map demonstrating distribution of Mg, Ti (g) and Al (g) in minerals

2.3.1.3 Samples from MLC area

Sample PJ 6f was collected from small metagabbro body surrounded by garnet bearing amphibolite near the village Otročín (Fig. 2b). Texture is characterized by large grains (up to 3 mm) grains of plagioclase accompanied by clinopyroxene, orthopyroxene and amphibole. M_1 mineral assemblage is defined by plagioclase – orthopyroxene – clinopyroxene – amphibole – biotite – ilmenite (Fig. 8b). Although, M_1 plagioclase of labradorite composition ($An_{65–67}$) still preserves its original shape with twinning, in detail small lamellas of basic plagioclase (assigned to M_2) can be observed. Thus, the original composition is preserved only in some relicts. Clinopyroxene occurs as large grains up to 2 mm in size and it commonly contains orthopyroxene lamellas and ilmenite inclusion, which form chains of tiny grains (<1 μm), or lamellas restricted with respect to the crystallographic properties of the clinopyroxene (Fig. 8c). The composition of M_1 clinopyroxene corresponds to augite with X_{Mg} = 0.71–0.82 and jadeite content 5–7 % (Fig. 4c, Tab. 2). Orthopyroxene is observed as large grains of similar size as clinopyroxene, and it is also commonly present in the central parts of the large grains of clinopyroxene or M_1 amphibole (Fig. 8a). The M_1 orthopyroxene has consistent composition of enstatite with X_{Mg} = 0.57–0.59 (Fig. 4c; Tab. 2). M_1 amphibole of brown colour form grains up to 0.5 mm size and its composition corresponds to pargasite with X_{Mg} = 0.58–0.65 (Tab. 2). Biotite is predominantly observed in association with ilmenite, which affects its variable Ti content which increase towards ilmenite from 0.24 apfu to 0.55 apfu at the contact with ilmenite accompanied by minor change in X_{Mg} = 0.62–0.68. On the other hand, ilmenite grains (up to 1

mm large) are commonly surrounded by small zircon grains (<10 μm), or by uniform zircon rim.

M_2 minerals are typically represented by orthopyroxene – amphibole – garnet – plagioclase. These minerals are associated with corona formation processes including formation of symplectites (amphibole-plagioclase, orthopyroxene-plagioclase) and breakdown of M_1 plagioclase. M_1 amphibole is usually surrounded by amphibole-plagioclase and orthopyroxene-plagioclase symplectite at the contact with M_1 plagioclase (Fig. 8a). M_1 clinopyroxene occurs either with corona of M_2 amphibole or with amphibole-plagioclase and orthopyroxene-plagioclase symplectite at the contact with plagioclase. The same mineral association is also observed around orthopyroxene. Composition of M_2 amphibole (pargasite; X_{Mg} = 0.54–0.58) and M_2 orthopyroxene (enstatite with X_{Mg} = 0.56–0.58) is very similar to the composition of their M_1 equivalents with slightly lower X_{Mg} values. Locally corona .3sequence of M_1 amphibole around orthopyroxene or biotite is followed by garnet layer. Garnet contains a large amount of inclusion of amphibole, clinopyroxene, ilmenite and kyanite. Garnet composition is represented by 50% of almandine component, 20–26% of pyrope and grossular with minor representation of spessartine 1–2% (Fig. 8d, Tab. 3). From analysed profiles across the garnet layer, slightly asymmetric compositional zonation can be characterized from the central part (Alm = 51%; Py = 24%; Grs = 23%; Spess = 1%; X_{Mg} = 0.32) by decrease of almandine, pyrope component and X_{Mg} value towards rims (Fig. 8d). Asymmetry of the zonation is defined by more significant decrease of the pyrope component at the contact with amphibole (Alm = 50%; Py = 21%; Grs = 20%; Spess = 2%; X_{Mg} = 0.28) compared to (Alm = 49%; Py = 23%; Grs = 25%; Spess = 1%; X_{Mg} = 0.31) composition at the contact with plagioclase (Tab. 3). Additionally, from amphibole to plagioclase continuously increase grossular component accompanied by decrease of spessartine. Breakdown of the M_1 plagioclase is observed predominantly at the central parts of the large grains (Fig. 8c, f), where former labradorite is

replaced by bytownite-anorthite (An_{83-91}) lamellas within oligoclase-andesine (An_{28-47}) matrix. In these domains, small grains of spinel (<30 µm; Tab. 3) are also present.

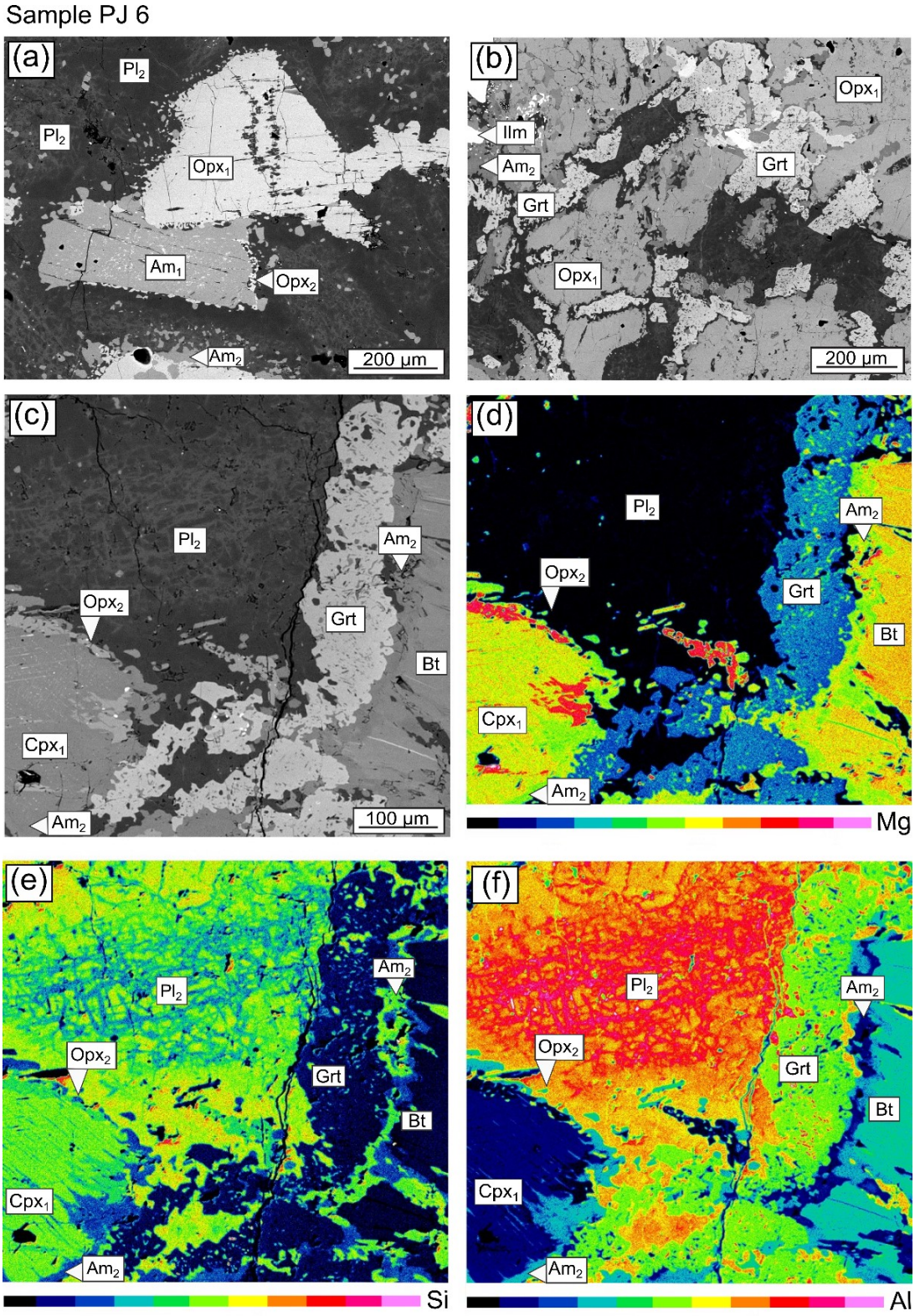

Fig. 8 BSE images characterizing texture of sample PJ 6

(a) Orthopyroxene and amphibole grains; (b)characteristic texture where orthopyroxene is enveloped by garnet corona; (c) BSE picture of area used for compositional map; (d) compositional map demonstrating distribution of Mg, Si (e) and Al (f) in minerals

Sample PJ 9 was collected from the marginal part of an old quarry situated near the village Výškovice (Fig.2b). The metagabbro body is surrounded by amphibolite. A coarse-grained sample with macroscopically visible garnet coronas around pyroxenes and amphiboles was selected for detailed description. M_1 mineral assemblage is represented by plagioclase – clinopyroxene – orthopyroxene – amphibole – biotite – ilmenite. The texture is characterized by large clinopyroxene (Fig. 9a) and orthopyroxene grains within plagioclase. Although M_1 plagioclase still preserves its original shape, in detail it is completely recrystallized. Clinopyroxene form grains up to 3 mm large, which contain orthopyroxene exsolution and inclusions of amphibole. Its composition varies between diopside and augite (Fig. 4c) with X_{Mg} = 0.79–0.80 and jadeite content 8–10%, however some of the grains show slight compositional zonation defined by decrease of Ti and Cr towards rim (Ti = 0.01→0.006 apfu, Cr = 0.015→0.011 apfu). Orthopyroxene of enstatite composition with X_{Mg} = 0,67–0,73 (Fig. 4c) contains exsolutions of clinopyroxene and inclusions of amphibole, apatite, and rutile. M_1 amphibole commonly occur in association with M_1 orthopyroxene, the inclusions of clinopyroxene, rutile and apatite are also present here. It has a composition of pargasite-edenite with X_{Mg} = 0.70–0.73 (Fig. 4e; Tab. 2). Biotite is rarely observed close to ilmenite. In this sample ilmenite has a minor representation compared to other studied samples, it occurs in association with rutile and zircon (Fig. 9b).

The M_2 mineral assemblage containing clinopyroxene – orthopyroxene – amphibole – garnet – plagioclase – rutile is connected to corona forming processes accompanied by plagioclase recrystallization. At the contact of mafic mineral and plagioclase several types of coronas were observed. M_1 clinopyroxene is commonly enveloped by corona of M_2 amphibole.

This amphibole layer shows compositional zonation defined by transition from magnesiohornblende (close to clinopyroxene) to edenite at the contact with plagioclase (X_{Mg} = 0.78→0.68; Ti = 0.09→0.17 apfu; Na = 0.39→0.67 apfu; K = 0.05→0.14 apfu; Fig. 4f, Tab 3). The multiple corona sequence is developed between M_1 orthopyroxene and the large plagioclase grains. This corona consists of 4 layers that are described in direction from M_1 orthopyroxene (Fig. 9e). The first layer at the contact with M_1 orthopyroxene is layer of small grains of M_2 amphibole (magnesiohornblende with X_{Mg} = 0.75–0.83; Tab. 3) and M_2 clinopyroxene (augite-diopside with X_{Mg} = 0.82–0.84; Tab. 3). This layer it typically followed by symplectitic corona of M_2 orthopyroxene (enstatite with X_{Mg} = 0.67–0.73; Tab. 3) and M_2 plagioclase (andesine, $An_{30–46}$). This symplectite layer is followed by zone of M_2 plagioclase which separates it from following garnet corona. Plagioclase zone (Fig. 9e, h) show strong compositional zonation characterized by transition from oligoclase (at the contact with symplectite) to labradorite at the contact with garnet ($An_{25→68}$). Following garnet corona contains inclusions of plagioclase, quartz, amphibole and kyanite. The garnet composition corresponds predominantly to almandine (39–48%) with pyrope (29–34%) and grossular (18–26%) content and minor representation of spessartine (1–2%; Fig. 4c, Tab. 3). Analysed profiles across the garnet layer show compositional zonation characterized from the central part (Alm = 41%; Py = 29%; Grs = 26%; Spess = 1%; X_{Mg} = 0.40) by decrease of grossular content accompanied by increase of pyrope content towards rims. On the other hand, almandine and spessartine content continuously decrease from the M_1 orthopyroxene side (Alm = 48%; Py = 31%; Grs = 18%; Spess = 2%; X_{Mg} = 0.41) towards M_1 plagoclase (Alm = 40%; Py = 35%; Grs = 22%; Spess = 1%; X_{Mg} = 0.46), in this direction X_{Mg} continuously increases. During metamorphism former M_1 plagioclase was affected by deformation, which resulted in its recrystallization to mixture of fine-grained clusters (Fig. 9c). The small grains of newly formed plagioclase show compositional zonation defined by increase of anorthite content from the

central parts towards rims ($An_{35\rightarrow94\%}$; Tab. 3). In these recrystallized domains small grains of spinel, corundum and kyanite are present, occasionally there are also present tiny grains of biotite and epidote. In pressure shadows of plagioclase matrix or plagioclase grains enclosed in clinopyroxene, breakdown of labradorite to bytownite-anorthite lamellae ($An_{79–94}$) in oligoclase-andesine matrix ($An_{35–46}$) can be observed (Fig. 9d). In addition, rutile replacing ilmenite is assigned to M_2 mineral assemblage.

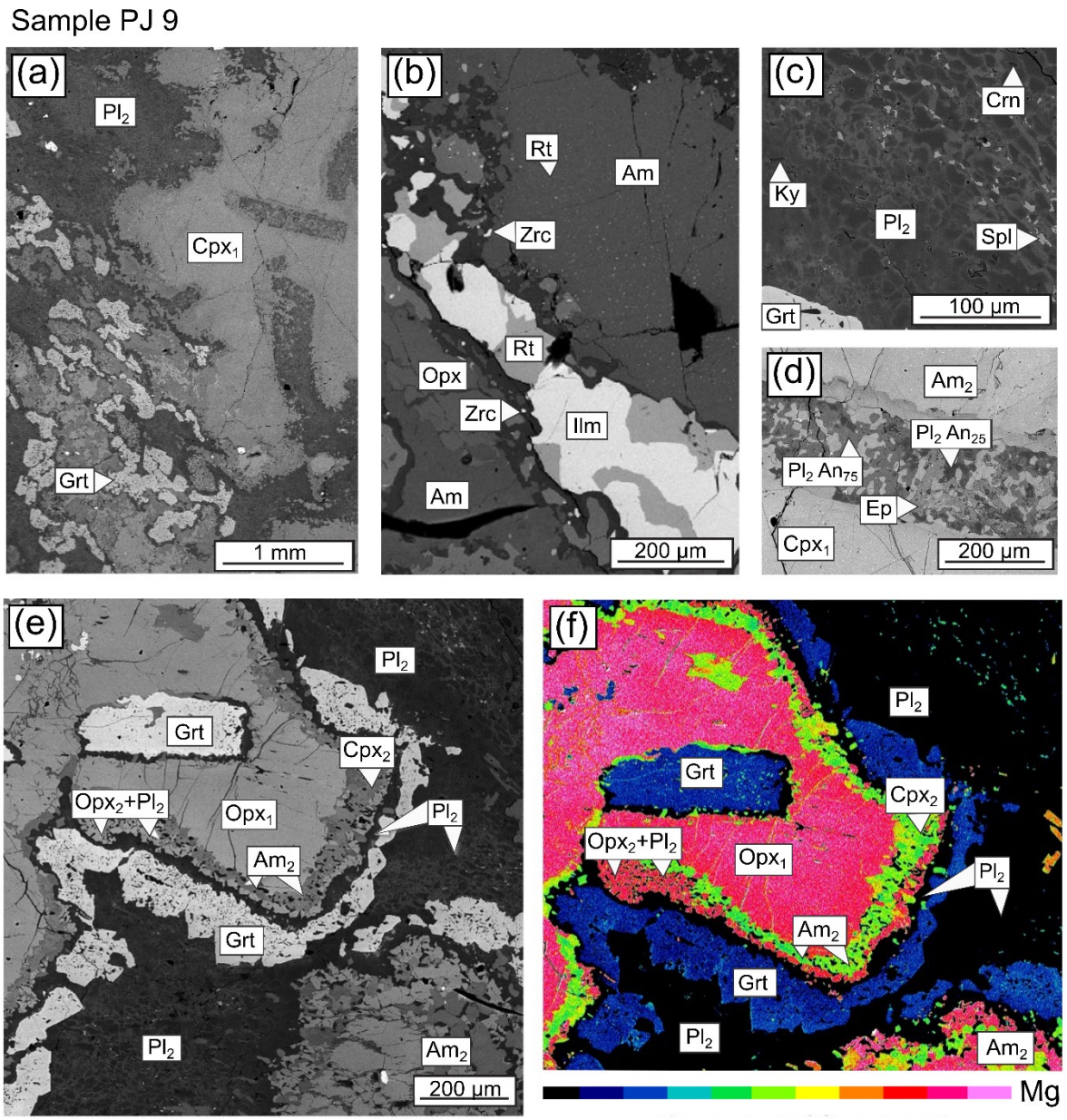

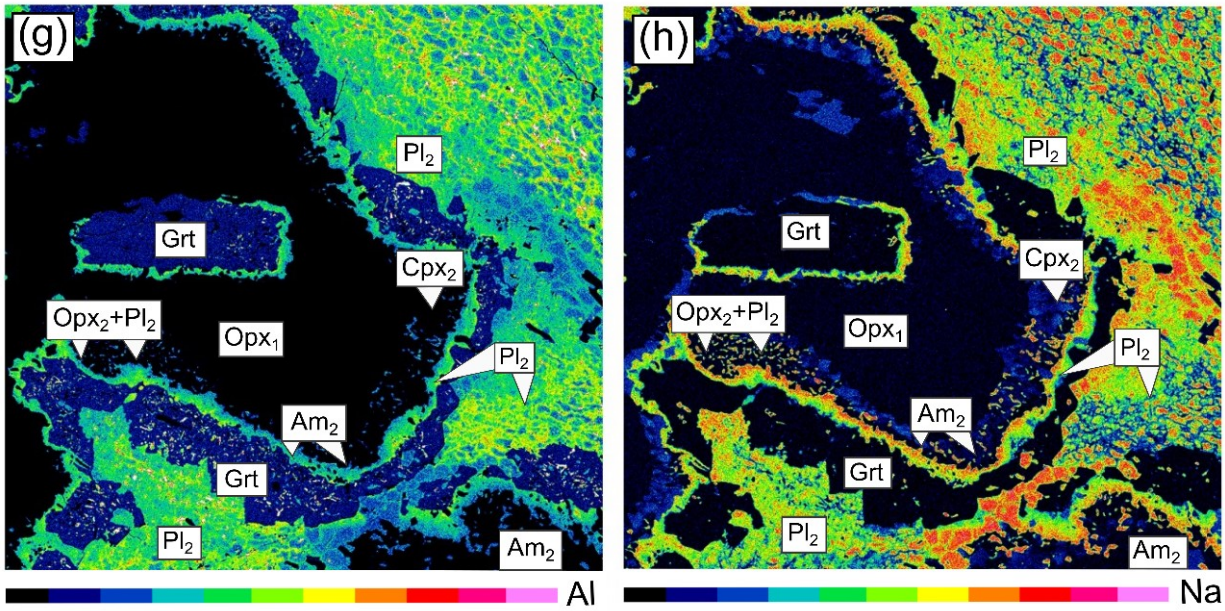

Fig. 9 BSE images characterizing texture of sample PJ 9

(a) Large grain of clinopyroxene enclosing formerplagioclase; (b) ilmenite grain in association with rutile and small grains of zircon froming thin rim; (c) detail of fine-grained clusters of zoned plagioclase grains together with spinel, corundum and kyanite grains; (d) detail of fromer M_1 plagioclase replaced by mixture of acidic and sodic M_2 plagioclase and epidote (d) BSE picture of area used for compositional map; (e) compositional map demonstrating distribution of Mg, Al (g) and Na (g) in minerals

2.3.2 DCC-NKM samples

Second area of interest is situated in the southwestern corner of TBU (Fig. 2b). Large gabbro bodies lie in the central part of Kdyně Massiv (near Orlovice village) here they are enveloped by gabbronorites, occasionally bodies of ferrodiorite are present here. Smaller bodies were sampled within Domažlice Crystalline Complex and Kdyně Massiv and the last group of samples was collected from area of Poběžovice Massiv. Well preseved magmatic texture defined by olivine grains, accompanied by pyroxene grains within plagioclase matrix, is typical for metagabbros and ferrodiorites of the Orlovice area, but it is also observed in two samples collected from Kdyně (PJ 22) and Poběžovice area (DK 13). Metagabbros and amphibolite

located around Kdyně or within Domažlice Crystalline complex commonly show higher degree of metamorphic changes compared to samples from Orlovice area, the magmatic texture is not generally well preserved (with exception of sample PJ 22) and it is defined predominantly by amphibole and plagioclase grains. Representative samples from all 3 areas were selected for detailed description below. All characteristics are demonstrated in Figures 10–20 and mineral analyses are in Table 4 (M_1 minerals), Table 5 (M_2 minerals).

2.3.2. 1 Samples collected from Orlovice area

Locality PJ 12 is situated in the southern part of the Orlovice metagabbro body (Fig. 3b). Two samples, A and B, were chosen from this locality as representative to characterize evolution of corona textures. Both samples show well preserved magmatic texture with olivine and pyroxene grains surrounded by plagioclase matrix. M_1 mineral assemblage consists of plagioclase, olivine, ilmenite, orthopyroxene ± clinopyroxene. M_2 mineral assemblage is represented by amphibole, clinopyroxene ± titanite ± orthopyroxene ± spinel which form coronas around olivine, clinopyroxene and ilmenite.

In the sample PJ 12B, the most common mineral of M_1 assemblage is plagioclase with composition of An_{81-83} (Fig. 11a; Tab. 4). Plagioclase grains show compositional zoning characterized by decrease of Na and increase of Ca in margins (Fig. 10a, d, f). Within the plagioclase matrix, olivine forms crystals up to 5 mm large commonly crossed with fractures, which are filled with amphibole and/or sulphides (Fig. 10a, d). Composition of olivine is quite homogeneous ($Fo_{50–53}$; Fig. 11b; Tab. 4) without systematic compositional zoning. Clinopyroxene occurs as 0.X mm size crystals commonly containing orthopyroxene lamellae (Fig. 10b, d). Its composition corresponds to the diopside-augite transition with X_{Mg} = 0.71–0.75 and jadeite content about 2 mol % (Fig. 11d; Tab. 4). Orthopyroxene with composition of $En_{59–60}$ and X_{Mg} = 0.63–0.64 (Fig. 11d; Tab. 4) is less frequent than clinopyroxene in this sample

and it reaches similar size as clinopyroxene (Fig.10a). M_1 mineral assemblage also involves ilmenite (Fig. 10a, b).

M_2 mineral assemblage is characterized by its textural position connected to the corona sequences around M_1 minerals. This mineral assemblage includes amphibole, orthopyroxene, and spinel. Olivine is commonly surrounded by multiple corona sequence, in direction from olivine to plagioclase it starts with layer of cummingtonite alternating with calcic amphibole (actinolite with X_{Mg} = 0.88–0.90; Si = 7.09–7.59 apfu, Fig. 10c, e; Fig. 11e; Tab. 5) which is followed by a layer of amphibole (pargasite with X_{Mg} = 0.65–0.66; Si = 6.12–6.16 apfu; Fig. 10c; Fig. 11d; Tab. 5) associated with spinel (Fig. 10a,c, d). M_1 orthopyroxene is surrounded by amphibole corona with compositional zonation characterized by change in composition from pargasite to actinolite. Clinopyroxene is rarely surrounded by an amphibole corona like the one observed around orthopyroxene, but usually, it observed without any corona. No signs transformation of M_1 ilmenite into rutile or titanite are observed in this sample as well as no zircon grains are present here.

Sample PJ 12 B

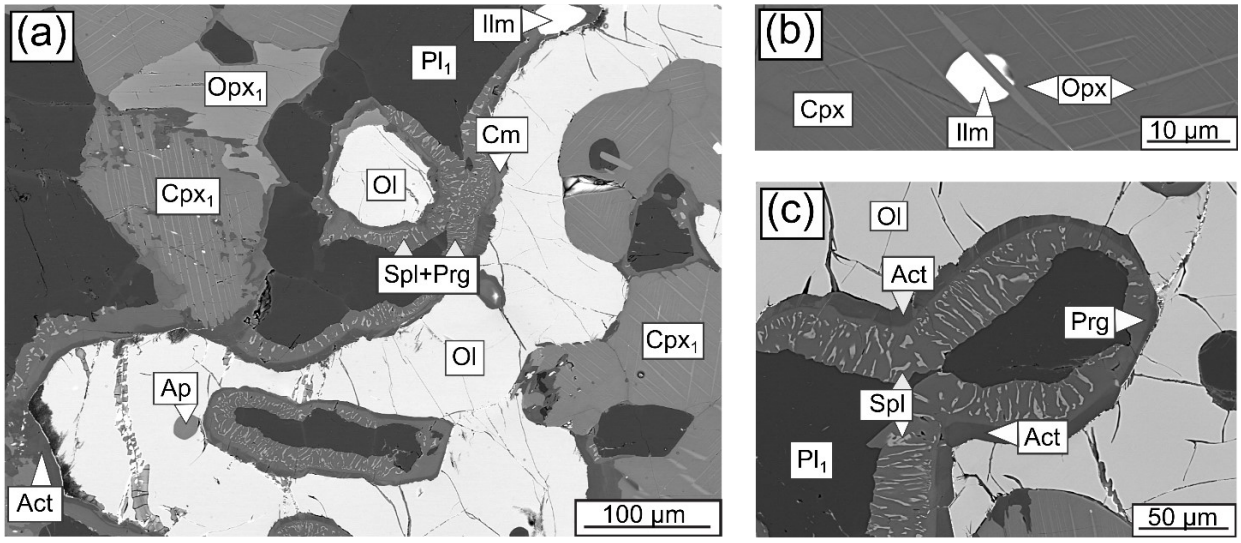

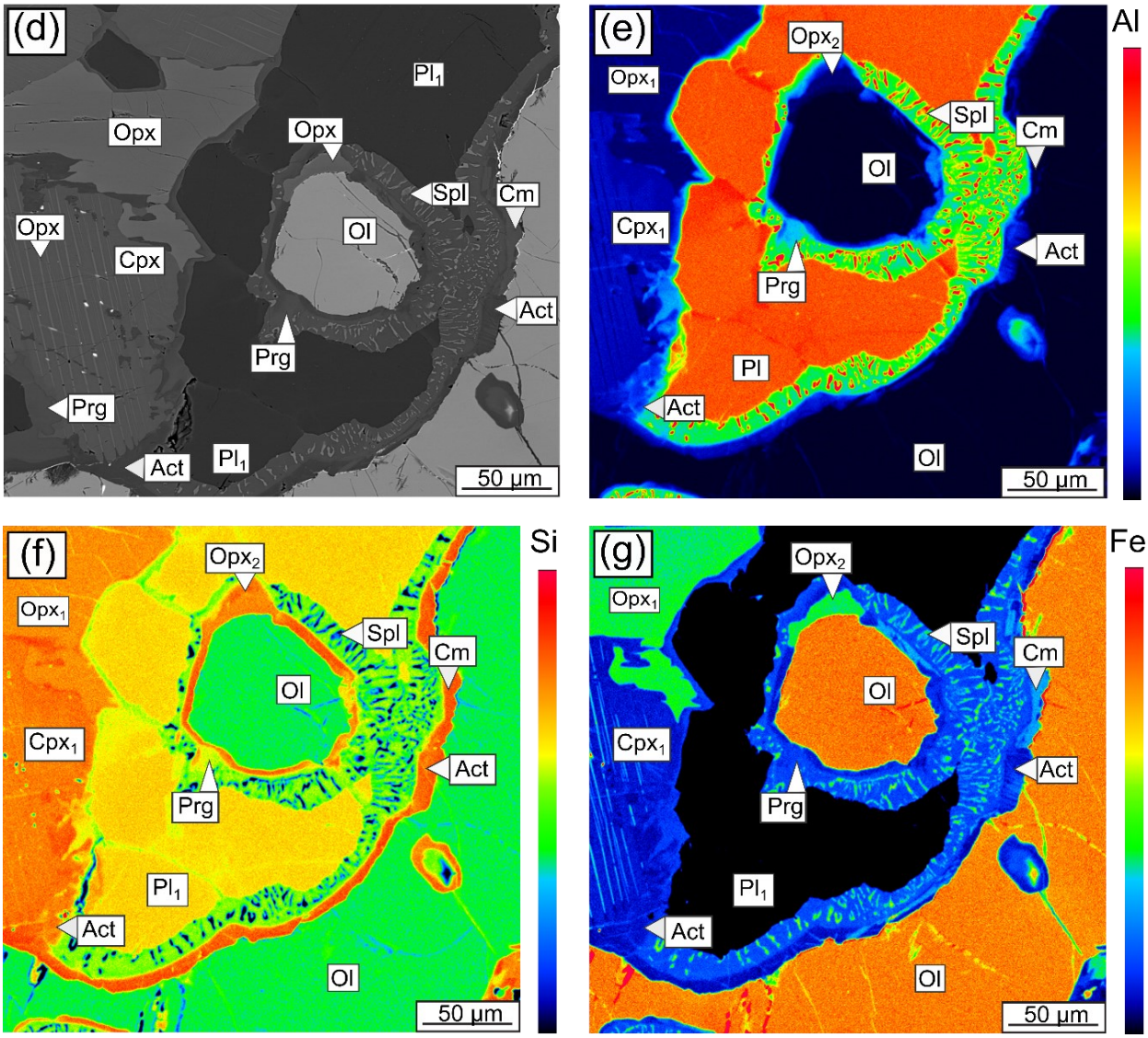

Fig. 10 BSE pictures and compositional maps characterizing mineral assemblage of the sample PJ 12B.

(a) polycrystalline aggregate consisting of clinopyroxene, orthopyroxene and olivine in plagioclase matrix; (b) detail of orthopyroxene exsolution cutting ilmenite inclusion in clinopyroxene grain; (c) detail of corona sequence enveloping olivine; (d) BSE picture of analysed area; (e) compositional map demonstrating distribution of Al, Si (f) and Fe (g) in minerals

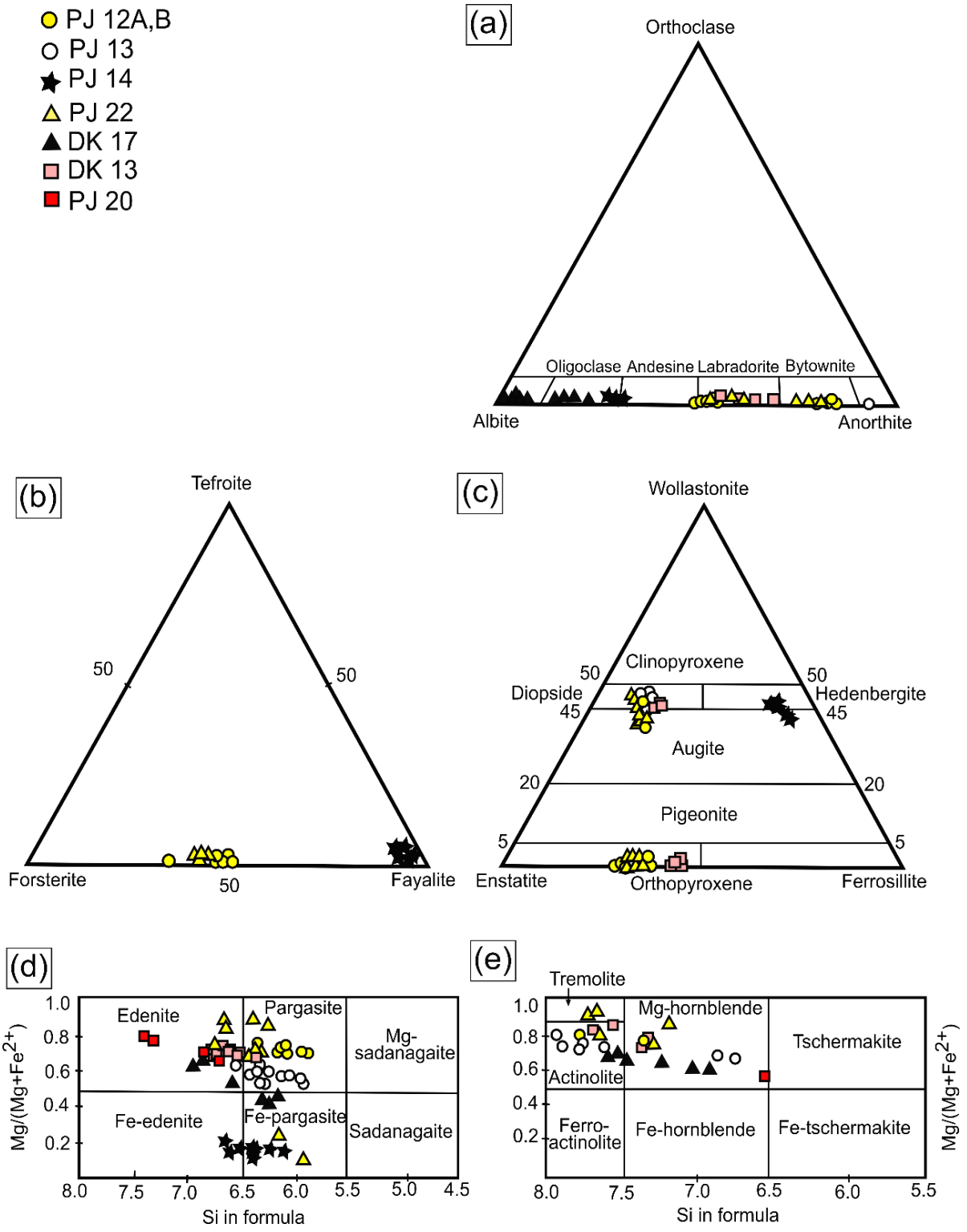

Fig. 11 Diagrams demonstrating composition of the main rock-forming minerals of representative samples described above.

(a) plagioclase; (b) olivine; (c) pyroxenes after Morimoto (1988); (d) amphibole after Leake et al. (1997).

sample	**PJ 12B**				**PJ 12A**		**PJ 13**		**PJ 14**		
mineral	ol-56	pl-61	opx-60	cpx-64	ol-18	pl-36	pl-31	cpx-23	ol-46	pl-09	px-42
SiO_2	35.25	48.10	52.88	51.32	37.05	47.76	55.05	51.60	29.72	61.65	48.58
TiO_2	0.02	b.d.	0.28	0.93	0.01	0.02	0.03	0.66	b.d.	b.d.	0.39
Cr_2O_3	0.01	0.05	0.04	0.03	b.d.	b.d.	0.06	0.10	0.04	0.01	b.d.
Al_2O_3	0.01	33.62	1.51	2.84	b.d.	32.85	28.36	2.58	b.d.	24.12	0.87
FeO	40.06	0.25	22.17	10.65	31.18	0.25	0.06	8.89	67.62	0.20	27.41
MnO	0.78	0.01	0.63	0.38	0.46	b.d.	b.d.	0.29	1.49	b.d.	0.61
MgO	24.02	b.d.	21.51	14.64	31.42	b.d.	0.01	13.79	1.53	0.01	2.85
CaO	0.06	17.69	1.12	19.93	b.d.	15.42	11.35	21.66	0.02	5.65	20.25
Na_2O	b.d.	2.04	b.d.	0.24	b.d.	2.19	5.19	0.40	0.03	7.95	0.20
K_2O	b.d.	b.d.	b.d.	b.d.	b.d.	0.02	0.03	b.d.	b.d.	0.25	b.d.
Cl	b.d.	b.d.	b.d.	b.d.	b.d.	b.d.	b.d.	b.d.	b.d.	b.d.	b.d.
Total	100.21	101.75	100.14	100.96	100.11	98.50	100.14	99.96	100.46	99.84	101.15
cat/O	3/4	5/8	4/6	4/6	3/4	5/8	5/8	4/6	3/4	5/8	4/6
Si	1.00	2.17	1.97	1.90	1.01	2.22	2.48	1.92	0.99	2.75	1.95
Ti	0.00	0.00	0.01	0.03	0.00	0.00	0.00	0.02	0.00	0.00	0.01
Cr	0.00	0.00	0.00	0.00	0.00	0.00	0.00	0.00	0.00	0.00	0.00
Al	0.00	1.79	0.07	0.12	0.00	1.80	1.51	0.11	0.00	1.27	0.04
Fe^{2+}	0.00	0.01	0.00	0.05	0.00	0.00	0.00	0.03	0.00	0.00	0.05
Fe^{3+}	0.95	0.00	0.69	0.28	0.71	0.01	0.00	0.24	1.89	0.01	0.87
Mn	0.02	0.00	0.02	0.01	0.01	0.00	0.00	0.01	0.04	0.00	0.02
Mg	1.02	0.00	1.20	0.81	1.27	0.00	0.00	0.77	0.08	0.00	0.17
Ca	0.00	0.85	0.04	0.79	0.00	0.77	0.55	0.86	0.00	0.27	0.87
Na	0.00	0.18	0.00	0.02	0.00	0.20	0.45	0.03	0.00	0.69	0.02
K	0.00	0.00	0.00	0.00	0.00	0.00	0.00	0.00	0.00	0.01	0.00
Cl	0.00	0.00	0.00	0.00	0.00	0.00	0.00	0.00	0.00	0.00	0.00
xMg	0.51		0.63	0.71	0.64			0.73	0.04		0.16
An		82.80				79.50	54.60			27.80	
Ab		17.20				20.40	45.20			70.70	
Kž		0.00				1.00	0.20			1.50	

Tab. 4 Representative analyses characterizing M1 minerals in samples from DCC-NKM area

cat/O - number of cations / oxides in formula unit, A = Ca+Na+K; b.d. - below detection limit. Amphiboles were calculated after Leake et al. (1997).

M_1 mineral assemblage in the **sample PJ 12A** is represented by plagioclase, olivine, and ilmenite (Fig. 12a). Plagioclase (labradorite) has relatively consistent composition of An_{50-51} with no sign of compositional zonation of the grains (Fig. 11a, Tab. 4). Olivine (Fo_{64}; Fig. 11b; Tab. 4) grains up to 2 mm size are extensively fractured, along these fractures is observed rim of sulfides accompanied by amphibole filling the rupture (Fig.12a).

M_2 minerals form complicated corona sequences around M1 minerals, which are dominant in this sample. At the contact between olivine and plagioclase, multilayer corona was developed (Fig. 12c,d), towards plagioclase it is represented by layer of cummingtonite (X_{Mg} = 0.70–0.73; Si = 6.90–6.95 apfu; Tab. 5) alternating with orthopyroxene (En_{67-70} with X_{Mg} = 0.69–0.71), surrounded by mixture of amphibole (pargasite with X_{Mg} = 0.64–0.68; Si = 5.90–6.09 apfu; Fig. 11d), sodic gedrite (X_{Mg} = 0.62–0.63; Si = 5.01–6.35 apfu; Na = 0.60–0.75 apfu; Tab. 5) and spinel, commonly all sequence is terminated by amphibole (pargasite with X_{Mg} = 0.61–0.64; Si = 5.72–6.35 apfu; Tab. 5) and plagioclase symplectite, in this zone biotite occur in places. M_2 plagioclase of bytownite composition (An_{80}) occur only at the contact of M_1 plagioclase and in association with calcic amphibole (Fig. 12d, e, f, g). Ilmenite is in places enveloped by double corona, consists of zone with mixture of pargasitic amphibole, sodic gedrite and spinel, which is followed by symplectite of M_2 plagioclase with pargasitic amphibole, composition of minerals in this corona lie in the same range as corresponding layer in corona sequence around olivine. Accessory minerals are represented only by apatit, no zircon occurs here. It is also important to note, that this sample do not show transformation of M_1 ilmenite into rutile or titanite.

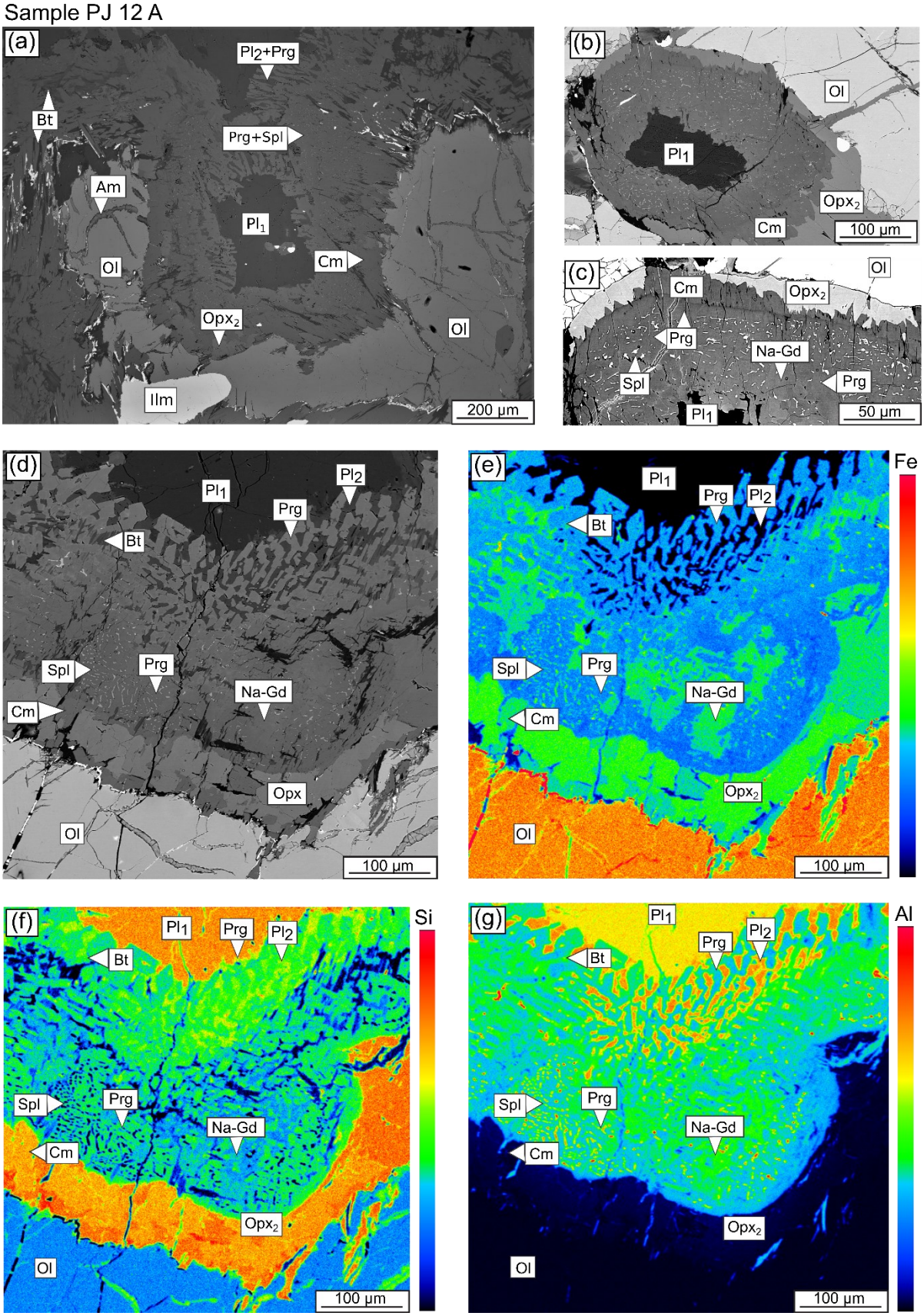

Fig. 12 BSE pictures and compositional maps characterizing mineral assemblage of the sample PJ 12A.

(a) characteristic texture defined by olivine grains surrounded by wide corona sequence; (b) detail of coronas around olivine; (c) closer detail of the orthopyroxene corona alternating with cummingtonite layer followed by symplectite of pargasitic amphibole and spinel alternating with sodic gedrite; (d) BSE picture of analysed area and compositional maps characterizing distribution of Fe (f), Si (g) and Al (h) among mineral phases.

Sample PJ 13 was collected from different part of Orlovice area (from Havranice body, Fig. 3b). Metagabbro of this locality suffered by uralitization, and magmatic texture also show extensive breakdown of primary minerals (predominantly clinopyroxene, Fig. 13a, d). M_1 mineral assemblage contains plagioclase – clinopyroxene – amphibole – biotite – ilmenite. Plagioclase of labradorite composition $An_{52–55}$ (Fig. 11a; Tab. 4) forms large grains up to 2 mm size which do not show any textural or compositional changes (except fracturing). Clinopyroxene (diopside with X_{Mg} = 0.73–0.76 and Jd content 3–4 mol %; Tab. 4) can be observed only in relicts (Fig. 13a). Biotite occasionally occur in aggregates of relict clinopyroxene and calcic amphibole (Fig. 13b). M1 amphibole in this sample is defined pargasite (X_{Mg} = 0.51–0.58; Si = 6.31–6.38 apfu and Ti content 0.25–0.43 apfu) present as single grains or as a part of former amphibole-clinopyroxene aggregates.

As M_2 minerals are defined plagioclase and amphibole (Fig. 11d, e; Tab. 5), which commonly occur in corona sequences around primary minerals. Calcic amphibole of composition actinolite (X_{Mg} = 0.71–0.79; Si = 7.79–7.95 apfu) form at the expense of clinopyroxene and it is dominant in central parts of amphibole-clinopyroxene aggregates, where it is accompanied by ilmenite inclusions. The most complex corona sequence is observed around clinopyroxene (eventually replaced by actinolite). Towards plagioclase clinopyroxene in enveloped by layer of amphibole (pargasite with X_{Mg} = 0.56–0.58; Si = 5.72–6.35 apfu and Ti content 0.07–0.08 apfu) which in places show compositional zonation in Mg and Ti content (Fig. 4). Corona of pargasitic amphibole is followed by layer of amphibole with compositional zoning demonstrated in Fig. 13c characterized by transition from magnesiohornblende (X_{Mg} =

0.65–0.66; Si = 6.76–6.87 apfu) at the contact with pargasitic layer to edenite (X_{Mg} = 0.53–0.61; Si = 6.07–6.54 apfu) and the sequence is terminated by pargasite-plagioclase symplectite (pargasite with X_{Mg} = 0.51–0.52; Si = 5.95–5.96 apfu). Ilmenite is commonly observed with double corona consisting of amphibole zone (pargasite with X_{Mg} = 0.58–0.63; Si = 6.26–6.44 apfu and Ti content 0.21–0.31 apfu) followed by zone of pargasitic amphibole-plagioclase symplectite at the contact with M_1 plagioclase (Fig. 13i). Both layers in places show weak compositional zoning demonstrated in compositional maps (Fig. 13c). Accessory mineral in this sample is zircon, which occur in association with ilmenite where it is present as inclusion or it form tiny tiny (<15 μm) grains forming a rim at the contact with ilmenite.

Sample PJ 13 C

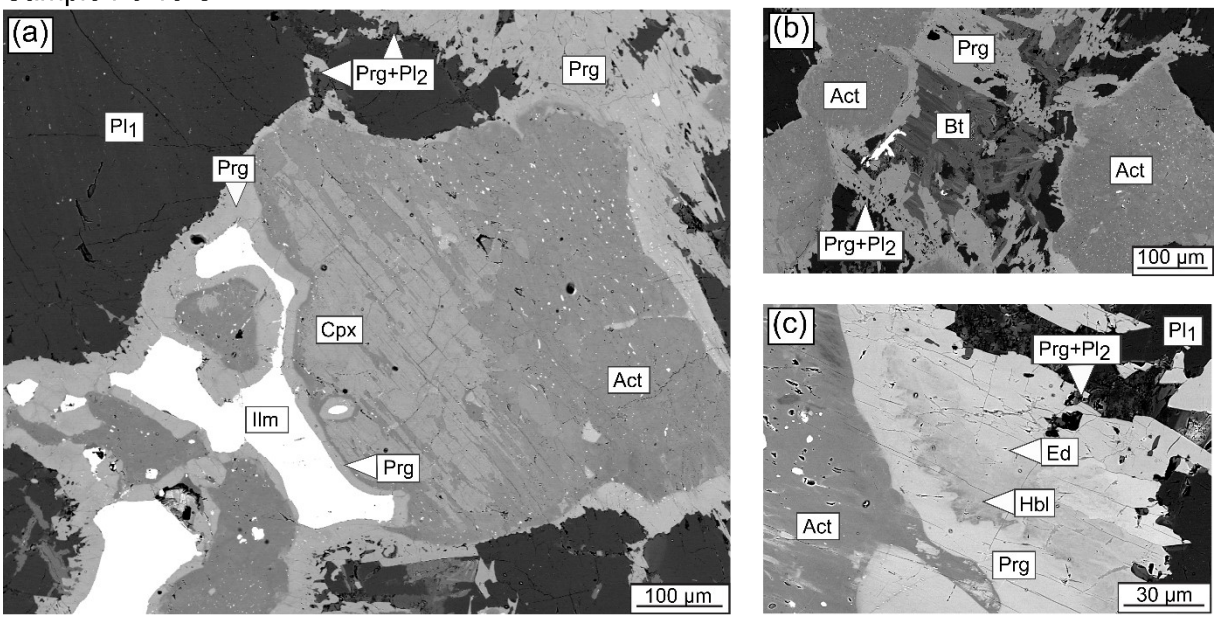

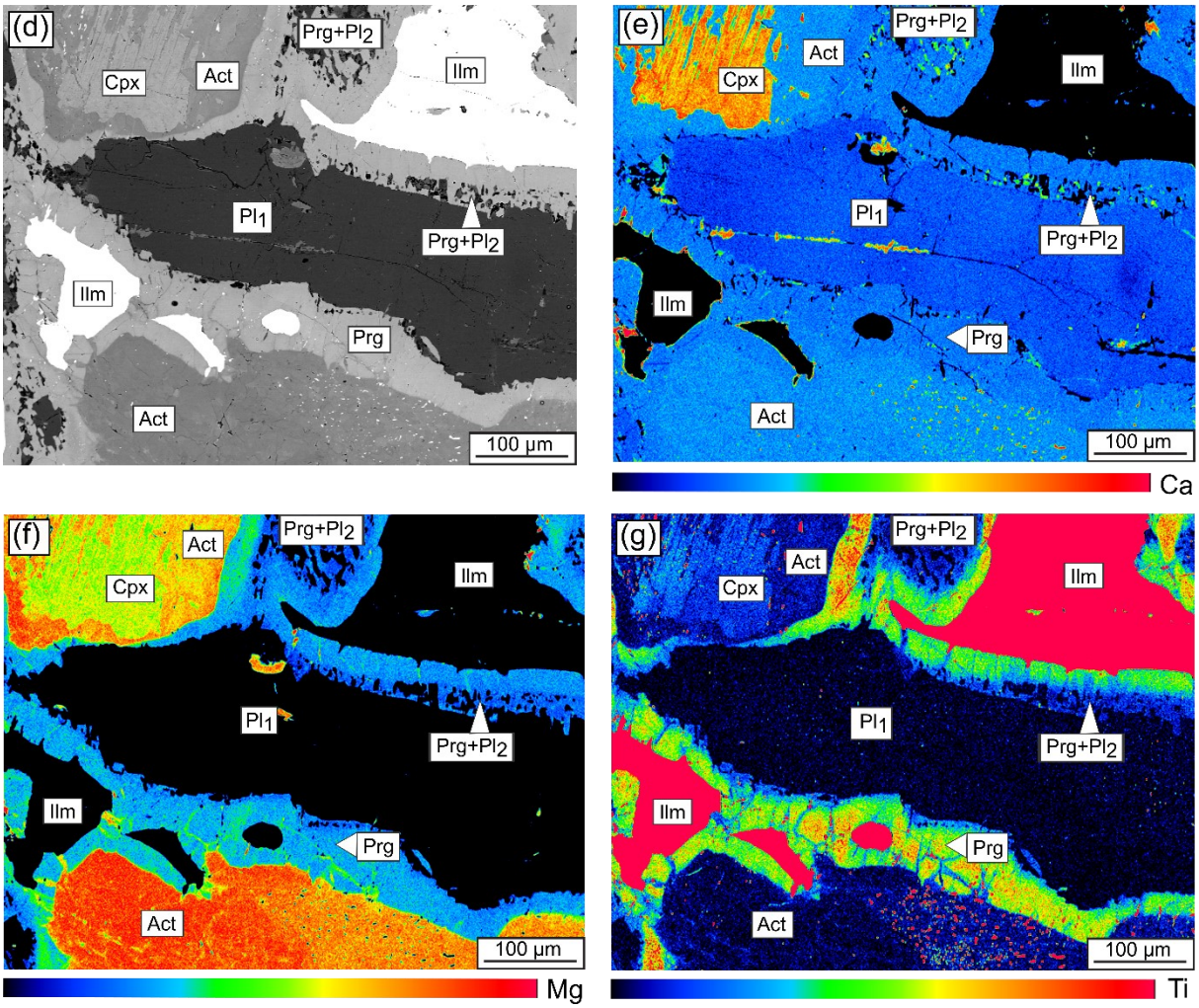

Fig. 13 BSE pictures and compositional maps characterizing mineral assemblage of the sample PJ 13C.

(a) primary magmatic texture defined by large clinopyroxene grains consumed by actinolititic amphibole, ilmenite and plagioclase with amphibole coronas; (b) detail of biotite grains occurring between pargasitic amphibole and Pl_2 symplectite; (c) detail of amphibole corona with strong compositional zonation; (d) BSE picture of analysed area and compositional maps characterizing Ca (e), Mg (f) and Ti (g) content in the minerals

Sample PJ 14 was taken from ferrodiorite body located between Orlovice and Chodská Lhota which encloses Orlovice and Havranice body (Fig. 3b). The M_1 mineral assemblage consists of plagioclase - olivine – clinopyroxene – ilmenite (Fig. 14a). Large grains of acidic plagioclase (An_{28-30}) and Fe-rich olivine (Fa_{94-95}) are commonly filled with fractures and show

no compositional zoning (Fig. 11a, b; Tab. 4). Clinopyroxene occurs in association with olivine and together with ilmenite it forms large aggregates. Clinopyroxene (hegenbergite with X_{Mg} = 0.14–0.17 and Jd content up to 2 mol %; Fig. 11d; Tab. 4) grains are often full of orthopyroxene exsolutions (Fig. 14b). Ilmenite is commonly observed in association with apatite and zircon grains which both show strong zonation. This sample contains large amount of accessory minerals such as zircon and apatite forming crystals up to 100 μm in size. Although some of the zircon grains appear to be spatially associated with ilmenite, there are no tiny zircon grains forming a rim around ilmenite as described in other samples.

M_2 mineral assemblage is represented by corona forming minerals two types of amphiboles – ferropargasitic amphibole and cummingtonite (Tab. 5). Olivine grains are enveloped by double corona consists of cummnigtonite layer (X_{Mg} = 0.15–0.18; Si = 7.88–7.95 apfu; Tab. 5) followed by ferropargasitic layer (ferropargasite to ferroendenite with X_{Mg} = 0.10–0.15 and Si content 6.10–6.60 apfu, Tab. 5) which show increase of Ti content from cummingtonite to plagioclase (0.06→0.12 apfu), occasionally amphibole of ferrohornblende composition (X_{Mg} = 0.15) was observed at the contact with cummingtonite (Fig. 14c, d, f). Clinopyroxene is commonly surrounded by double corona of pargasitic amphibole-quartz symplectite which continues by monomineral layer of pargasitic amphibole at the contact with plagioclase (Fig. 14a). Occasionally, clinopyroxene occur with no corona. Corona of pargasitic amphibole is locally observed also around ilmenite. No signs of ilmenite transformation into rutile or titanite was observed.

Sample PJ 14

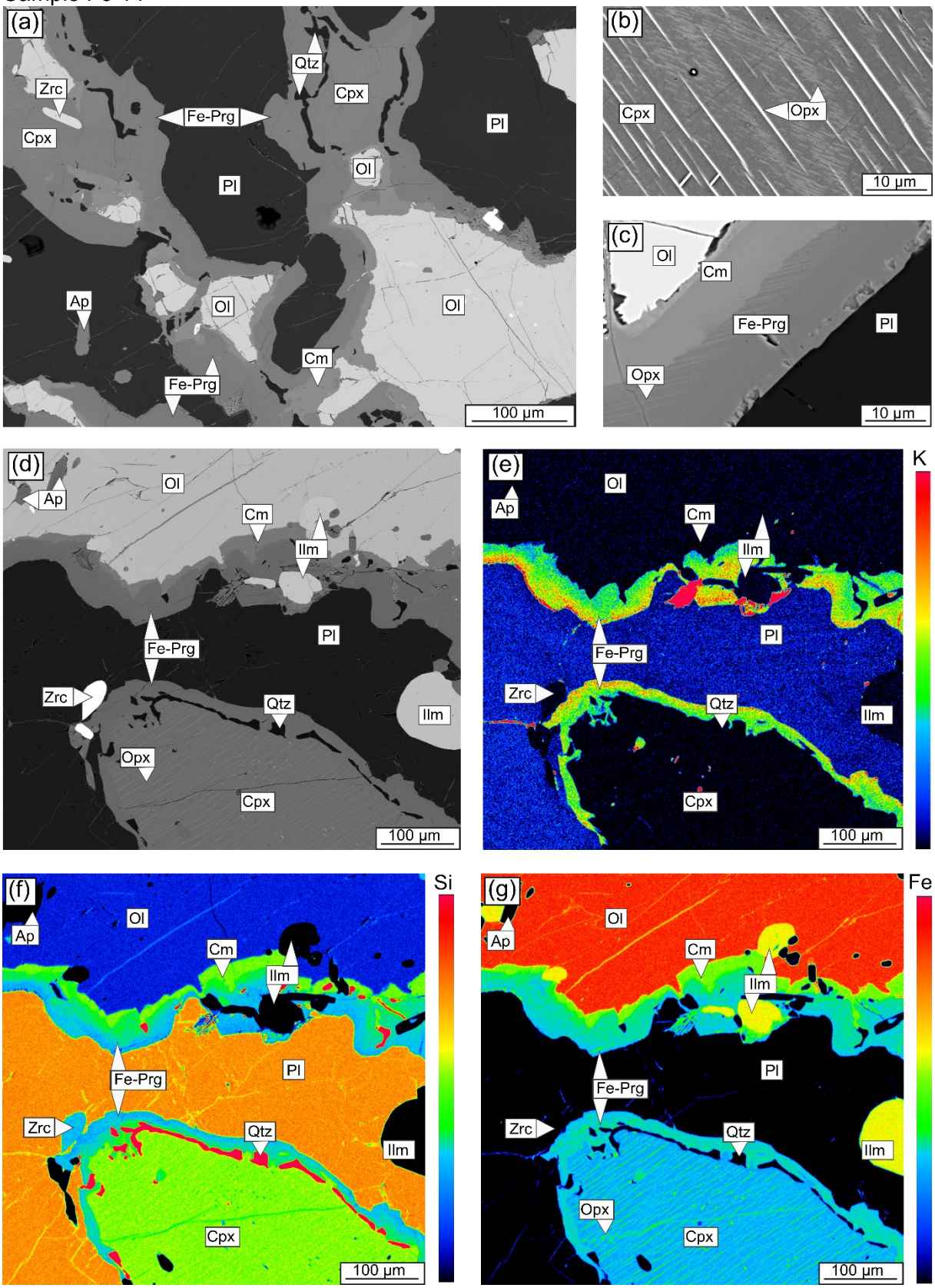

Fig. 14 BSE image demonstrating characteristic texture of the sample PJ 14

(a) characteristic texture defined by olivine grains surrounded by wide corona sequence; (b) detail of coronas around olivine; (c) closer detail of the orthopyroxene corona alternating with cummingtonite layer followed by symplectite of pargasitic amphibole and spinel alternating with sodic gedrite; (d) BSE picture of analysed area and compositional maps characterizing distribution of Fe (f), Si (g) and Al (h) among mineral phases.

2.3.2.2 Samples from Kdyně and DCC area

Sample PJ 15 originate from small diorite body western from Branišov. M_1 minerals are represented by plagioclase – amphibole – biotite – ilmenite and quartz (Fig. 15). Plagioclase grains show weak compositional zonation in andesine composition (An_{36-40}) with higher Ca content at the marginal parts. Among plagioclases, quartz grains are observed. Amphibole (ferroedenite with X_{Mg} = 0.43–0.50 and Si = 7.19–7.26 apfu) usually form aggregates together with biotite (X_{Mg} = 0.37 and Ti content 0.55–0.56 apfu), ilmenite and quartz. Biotite grains are in places rimmed by biotite-plagioclase symplectite.

M_2 mineral assemblage includes only titanite, which is in places observed enveloping ilmenite.

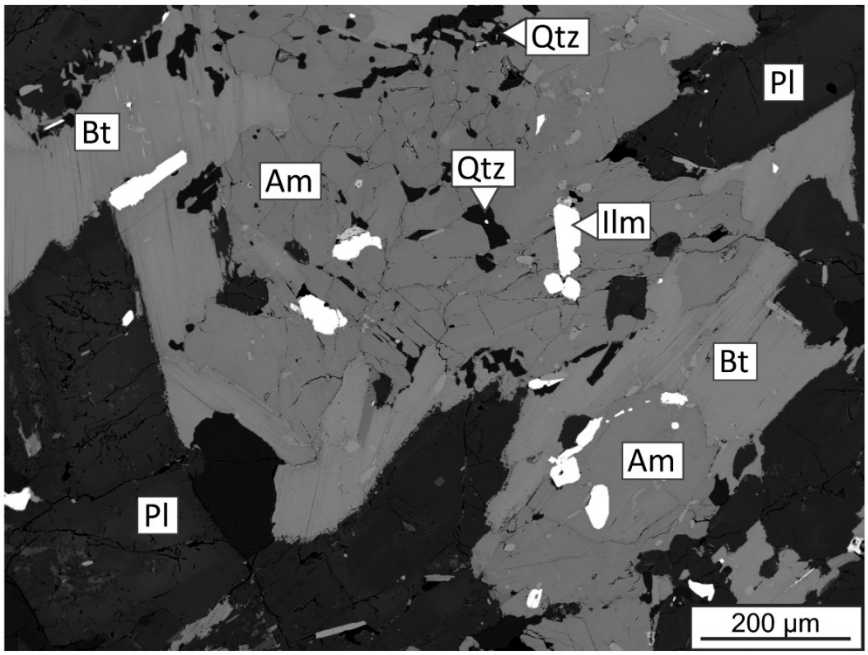

Fig. 15 BSE image demontrating characteristic texture of the sample PJ 15

Sample PJ 22 has very similar texture as sample PJ 14 and its mineral characteristic is comparable to the sample PJ 12. M_1 mineral assemblage consists of plagioclase – olivine – clinopyroxene – orthopyroxene – ilmenite. Plagioclase has a composition of labradorite (An_{54-61}), in places it contains tiny ilmenite inclusions. Olivine grains together with clinopyroxene, orthopyroxene and ilmenite commonly form large aggregate in plagioclase matrix (Fig. 16a) Olivine ($Fo_{56–57}$) contains fractures which are filled amphibole or iron sulfides. Clinopyroxene (diopside to augite with X_{Mg} = 0.75–0.81 and jadeite content up to 2 mol %) grains are commonly full of orthopyroxene exsolutions and ilmenite inclusions. Orthopyroxene (En_{60-63} with X_{Mg} = 0.64–0.68) grains are commonly fractured but in contrast to clinopyroxene, it occurs with no inclusions. The large grains show slight compositional zonation characterized from the central part by decrease Mg content and increase Fe content (Mg = 1.30→1.22 apfu; Fe = 0.60→0.68 apfu) towards rims. Isolated zircon grains are locally observed.

M_2 mineral assemblage is represented by plagioclase – amphibole – orthopyroxene – biotite, which form corona sequences at the contact of M_1 mafic minerals with M_1 plagioclase. Coronas enveloping olivine usually consist of orthopyroxene layer (En_{62-67} with X_{Mg} = 0.65–0.68) which is followed by layer of pargasitic amphibole (pargasite; X_{Mg} = 0.71–0.73, Si = 6.19–6.35 apfu) with incorporate biotite grains (X_{Mg} = 0.73–0.75 and Ti content 0.1–0.2 apfu), in places this corona of pargasitic amphibole is alternating with biotite grains and M_2 plagioclase, which together with orthopyroxene form symplectite-like texture (Fig. 16b, d). Between olivine and orthopyroxene layer thin (up tu X μm size) rim of cummingtonite is observed. M_2 plagioclase of bytownite composition (An_{75-83}) is present at the direct contact of olivine and the endmember of corona sequence. Orthopyroxene is commonly surrounded by single layer of pargasitic amphibole (pargasite; X_{Mg} = 0.71–0.73, Si = 6.19–6.35 apfu) with weak compositional zonation defined by edenite composition (X_{Mg} = 0.75, Si = 6.87 apfu) in

the central part of the layer (Fig. 16e). Clinopyroxene is in one place observed with corona of ferropargasite (X_{Mg} = 0.09–0.26, Si = 5.94–6.16 apfu; Fig. 16c). Additionally, actinolitic amphibole of variable composition (magnesiohornblende, actinolite and tremolite; X_{Mg} = 0.68–0.78, Si = 6.87–7.61 apfu) occur predominantly at the expense of clinopyroxene and epidote was also locally present.

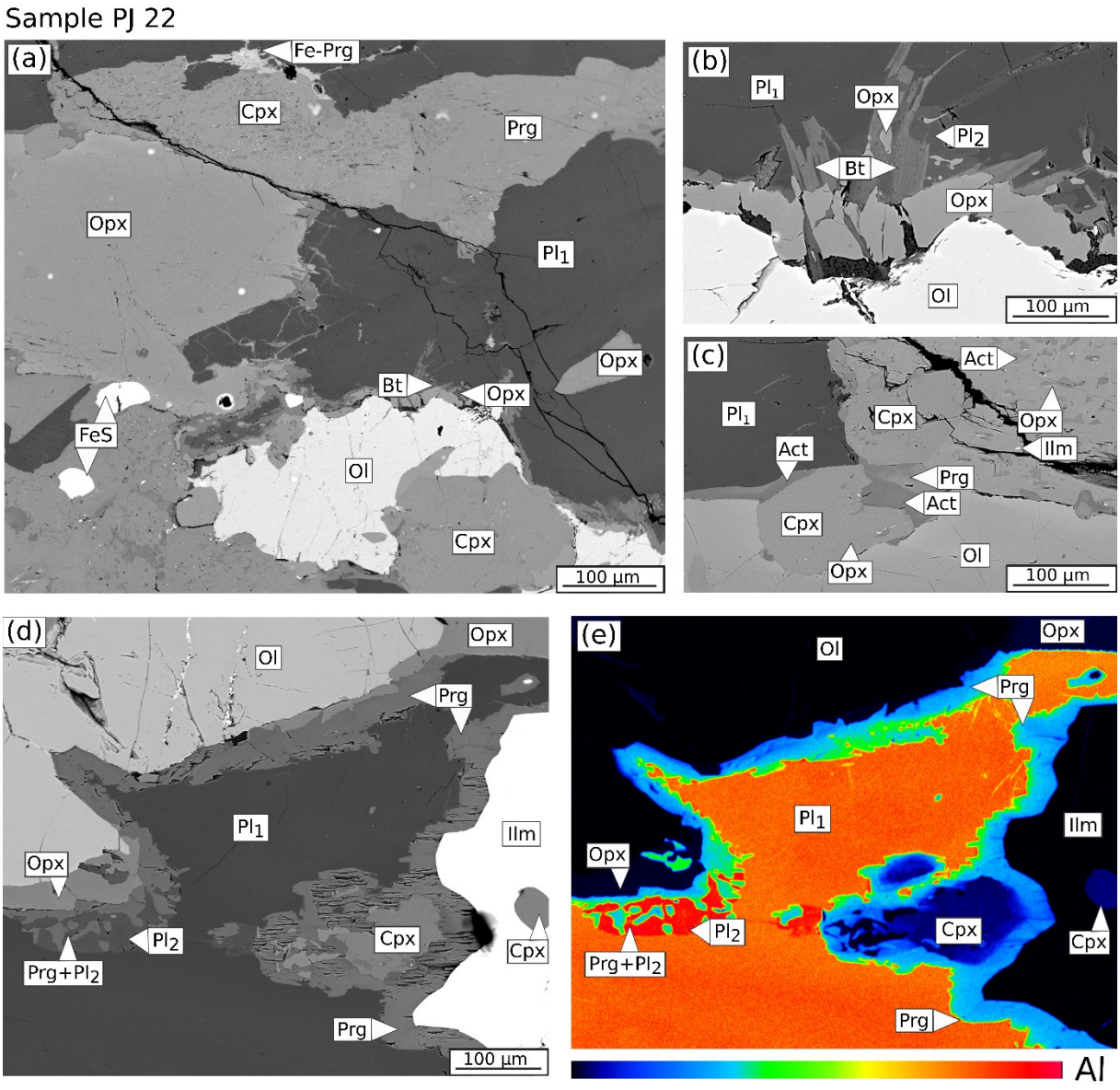

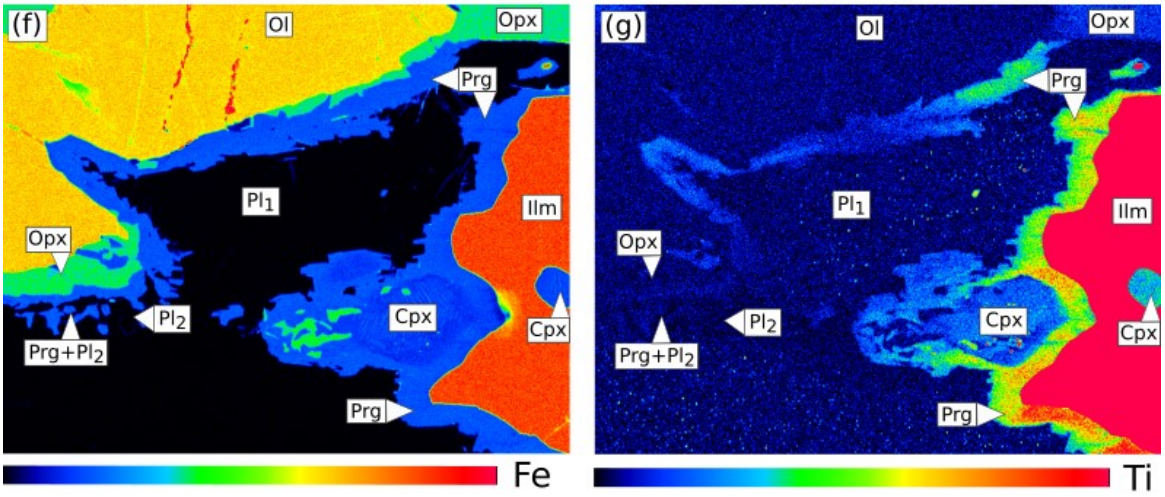

Fig. 16 BSE image of characterizing texture of sample PJ 22

(a) characteristic texture defined by olivine grains surrounded by wide corona sequence; (b) detail of coronas around olivine; (c) closer detail of the orthopyroxene corona alternating with cummingtonite layer followed by symplectite of pargasitic amphibole and spinel alternating with sodic gedrite; (d) BSE picture of analysed area and compositional maps characterizing distribution of Fe (f), Si (g) and Al (h) among mineral phases.

Sample DK 17 was collected in small quarry near the village Mrákov. Several varieties of gabbros were observed in the locality, for further description coarse-grained one was used. Typical texture is demonstrated in Fig 17a. Due to extensive recrystallization of M_1 minerals only ilmenite could be assigned to M_1 assemblage. M_2 assemblage is represented by amphibole of variable composition (Fig. 11d, e; Tab. 5). In detail most of the amphibole grains in the aggregates show significant compositional zonation (Fig. 17b) marked by compositional zoning with actinolite cores (X_{Mg} = 0.62–0.63, Si = 7.53–7.56 apfu; Ti = 0.01–0.02 apfu) through magnesiohornblende to edenite (X_{Mg} = 0.53–0.60; Si = 6.61–6.82 apfu; Ti = 0.02–0.07 apfu) occasionally ferropargasite (X_{Mg} = 0.41–0.42; Si = 6.17–6.31 apfu; Ti = 0.06–0.07 apfu) rims. To M_2 mineral assemblage rutile and titanite are also assigned, both occur in corona sequence enveloping ilmenite (Ilm1; Fig. 17a). Rutile is observed at direct contact with ilmenite and titanite forms second layer or fill the fractures between ilmenite and rutile. Titanite (Tnt1) layer

is usually dominant, and it is formed at the expense of ilmenite (and/or rutile). In the marginal part of the titanite corona ilmenite (Ilm2) is observed ant it is also again followed by titanite (Tnt2) grains (Fig. 17a). There are some differences in ilmenite composition, Ilm 1 (Mn = 2.13-2.18 apfu; Mg = 0.21–0.26 apfu; Zn = 0.06–0.14 apfu; Ca = 0.10–0.25 apfu) show lower Mn content and higher Mg and Zn content compared to Ilm 2 (Mn = 2.30–2.43 apfu; Mg = 0.10–0.21 apfu; Zn = 0–0.02 apfu; Ca = 0.37–0.55 apfu), the most significant difference is in Ca content, which is higher in Ilm 2. On the other hand, compositions of Tnt 1 ad Tnt 2 show only minor difference in Mn content where Ilm 1 has Mn = 0.01-0.03 apfu and Ilm 2 Mn = 0.03-0.04 apfu. Occasionally small grains of zircon are present at the outer rim of corona sequence, in places zircon occur forming a thin corona around small grains (up to 3 μm size) of baddeleyite (Fig. 17c). In places, chlorite replacing former biotite occur, occasionally accompanied by K-feldspar grains. Recrystallization of M_1 plagioclase is observed in domains with concentrated deformation (Fig. 17d). Newly formed albitic plagioclase show zonation show several varieties of zonation between An_{24} and An_1.

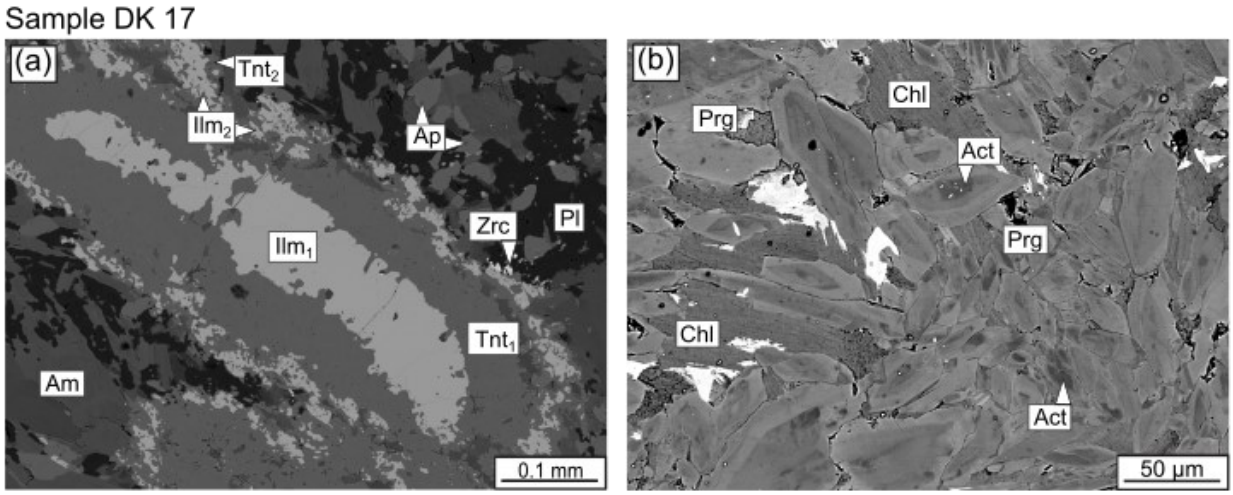

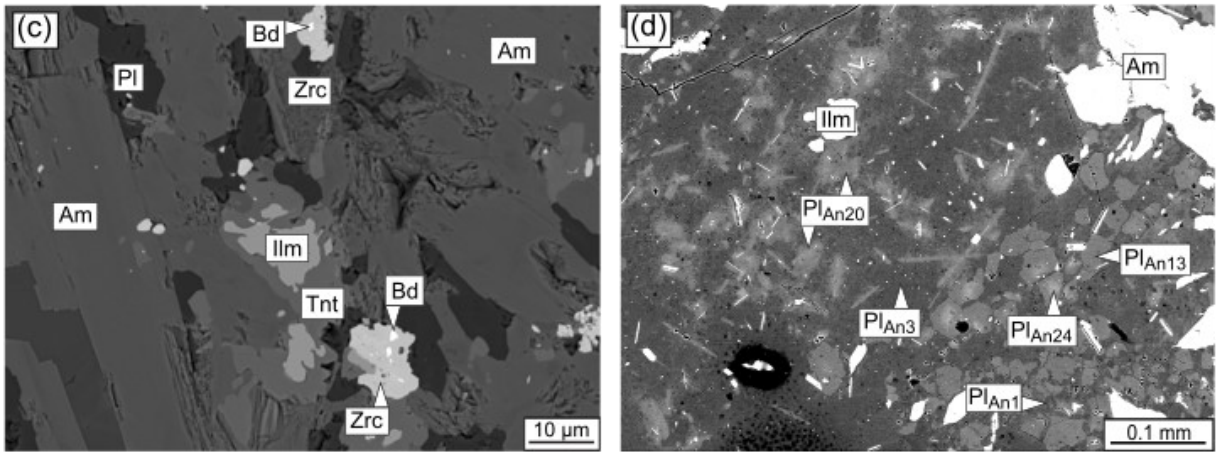

Fig. 17 BSE image demonstrating textural relatioships of the minerals in the sample DK 17

(a) ilmenite grain surrounded by dominant corona of titanite 1, followed by second ilmenite layer and titanite 2 layer; (b) detail of zoned amphibole grains from the central part of the amphibole aggregate (c) detail of tiny baddeleyite grains surrounded by zircon; (d) detail of recrystallization of plagioclase in domain affected by deformation

Sample DK-L is fine-grained amphibolite picked-up in the open quarry near Tisová village. This sample has very fine-grained texture (Fig. 18d). M_1 mafic minerals represented by amphibole – biotite and ilmenite form grains up to 0.08 mm size in plagioclase matrix. Plagioclase occur as a mixture of small grains which in places show zoning from acidic plagioclase in the central part to the intermediate or calcic plagioclase at the marginal parts. Occasionally ilmenite was observed with thin rim (up to 1 µm size) of zircon.

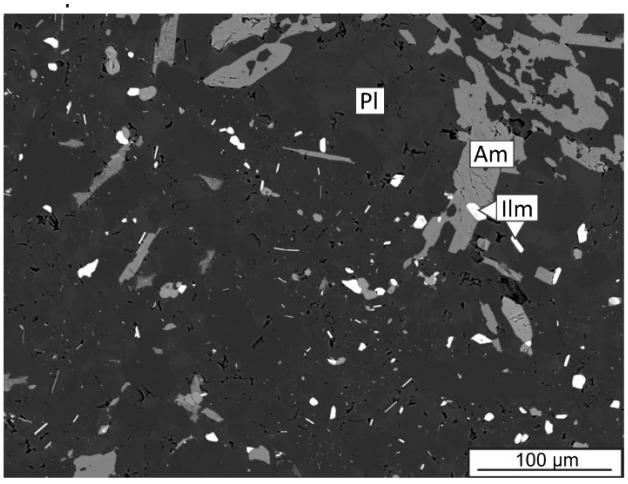

Fig. 18 BSE image characterizing typical texture of the sample DK-L

2.3.2.3 Samples collected from Poběžovice Massif

Sample PJ 20 is gabbro-amphibolite collected from mafic body located northwest from the village Otov. Magmatic minerals are extensively reworked due to metamorphic overprint, thus only ilmenite is assigned to M_1 mineral assemblage (Fig. 19a). The texture is characterized by amphibole aggregates enclosing quartz locally also accompanied by ilmenite and biotite grains within plagioclase matrix (Fig. 19d). Plagioclase matrix is generally formed by small grains of andesine (An_{31-43}), in places relicts of labradorite (An_{52}) can be observed in central parts of the grains. Amphibole in aggregates has a composition of magnesiohornblende (X_{Mg} = 0.57–0.66; Si = 6.73–7.39 apfu; Tab. 5) and it show compositional zoning generally characterized by decrease of Ti content towards plagioclase (from 0.15 to 0.03 apfu), in the central parts of the aggregates edenite (X_{Mg} = 0.59–0.65; Si = 6.58 apfu) can be observed (Fig. 19b). Amphibole grains commonly contain inclusion of ilmenite, quartz and in places clinopyroxene relicts are observed (Fig. 19c). Titanite is typically observed as corona around ilmenite which in places reach width of 100 μm. Tiny zircon grains forming a thin rim between ilmenite and titanite corona is commonly present. Rutile occurs along the ilmenite grains and at the contact with titanite, occasionally it appears to be consumed by titanite (Fig. 19a). Muscovite and epidote are observed in small domains inside plagioclase grains. In places, chlorite forms at the expense of former amphibole. In this sample accessory minerals are represented by Ti-bearing sulfides, which formation due to ilmenite break down is characterized in separate publication (Racek and Holá in rev).

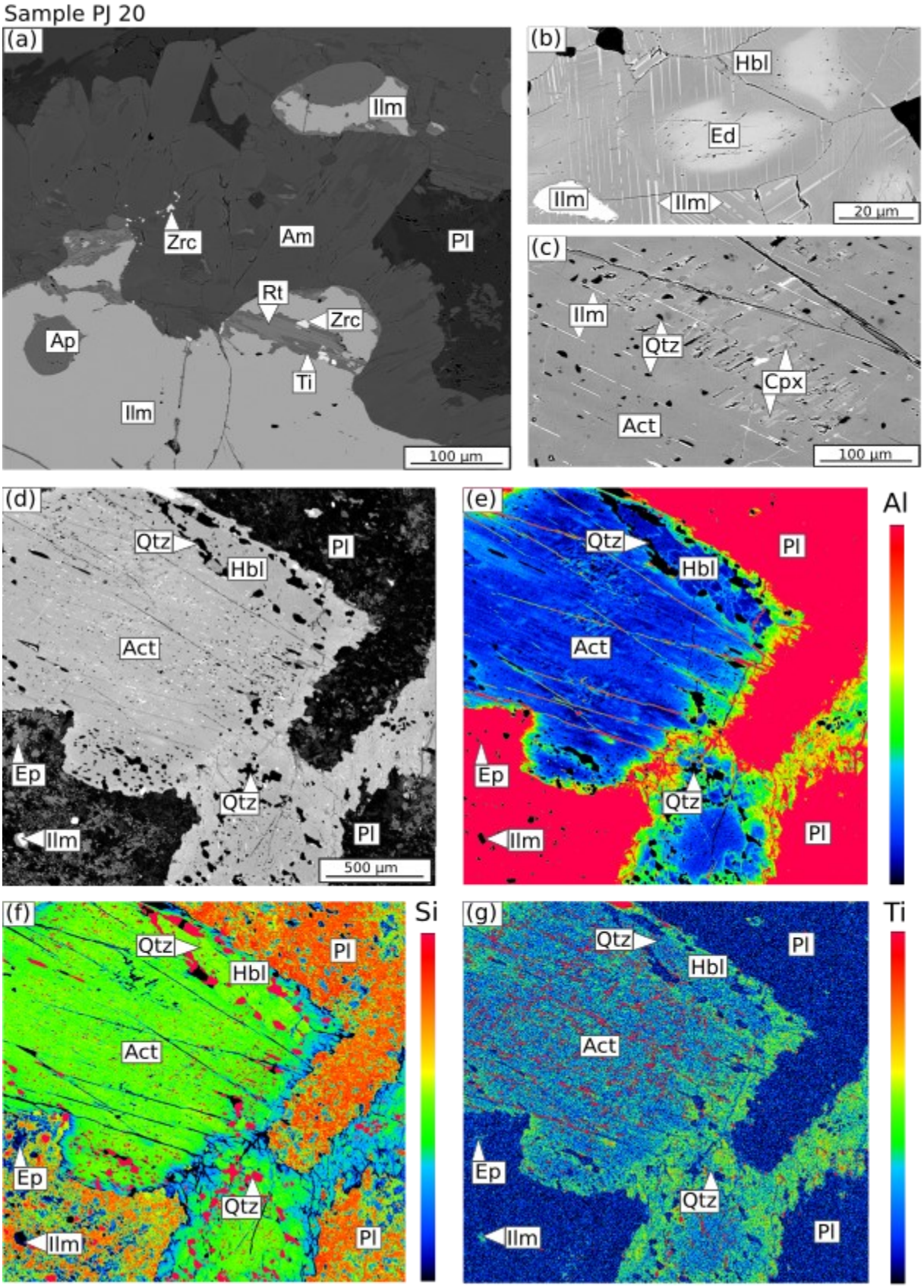

Fig. 19 BSE pictures and compositional maps characterizing mineral assemblage of the sample PJ 20.

(a) ilmenite grain with zircon rim and it is in places replaced by rutile and titanite; (b) detail of zoned amphibole grains from the central part of the amphibole aggregate; (c) relict of former clinopyroxene in amphibole aggregate; (d) BSE picture of analysed area and compositional maps characterizing distribution of Al (e), Si (f) and Ti (g) in mineral phases.

Sample DK 13 is fine-grained metagabbro collected from small, isolated body north-east from Meclov. This sample show well preserved magmatic texture defined by M_1 minerals plagioclase – orthopyroxene – clinopyroxene – amphibole – ilmenite (Fig. 20a). Plagioclase of labradorite composition ($An_{53–69}$) forms grains up to 400 μm size, occasionally inclusions of ilmenite and amphibole are observed here (Fig. 20b). Orthopyroxene (enstatite with X_{Mg} = 0.56–0.59) occur as a part of large aggregates, individual grains are fractured, it also contains needle shaped inclusions of ilmenite, which show preferent orientation. Clinopyroxene (diopside with X_{Mg} = 0.72–0.74 and jadeite content up to 2 mol %) occasionally occurs in association with M_1 orthopyroxene and M_1 amphibole. M_1 amphibole (Fig. 20a) forms major part of the aggregates and is has a composition of pargasite-edenite (X_{Mg} = 0.59–0.65, Ti content 0.23–0.38 apfu). Ilmenite is occasionally observed with thin rim of zircon grains.

M_2 mineral assemblage is represented by M_2 amphibole, which forms double corona around orthopyroxene or single layer corona around M_1 amphibole. In places orthopyroxene occurs with thin corona sequence (up to 10 μm each layer) of cummingtonite (X_{Mg} = 0.58), which is followed by M_2 amphibole layer of magnesiohornblende-actinolite composition with X_{Mg} = 0.69–0.74, which show weak compositional zonation and variable Ti content (0.04–0.2 apfu). The layer of actinolitic M_2 amphibole is observed also around M_1 amphibole.

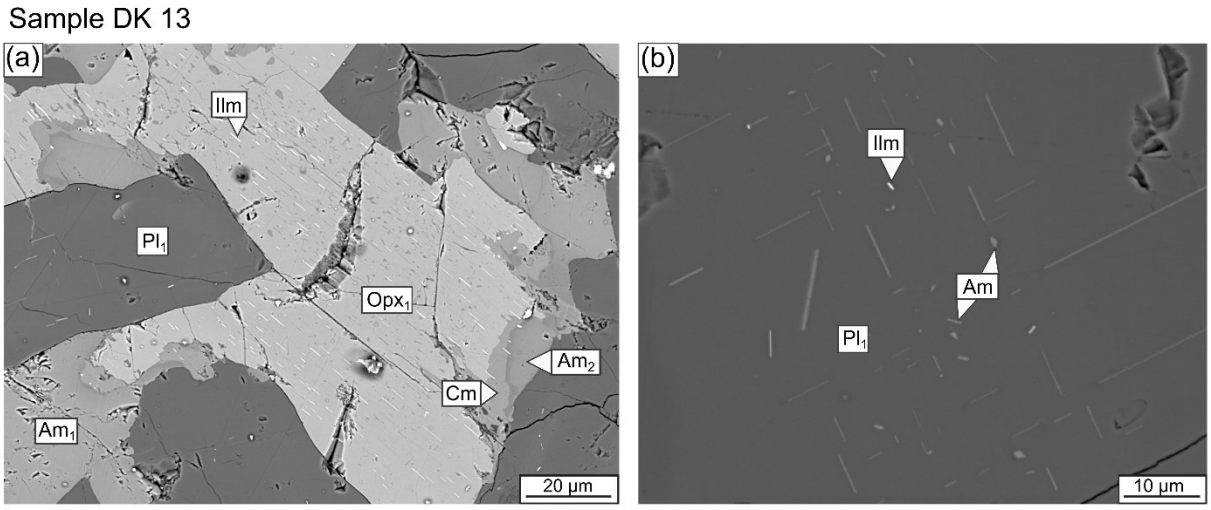

Fig. 20 BSE image of texture typical for sample DK 13

(a) M_1 orthopyroxene surrounded by layer of cummingtonite followed by M_2 amphibole; (b) detail of M1 plagioclase with amphibole and ilmenite inclusions

2.4 Geochronology

2.4.1 U-Pb zircon dating

In this study, representative samples from five localities (PJ 6, PJ 9, PJ 14, PJ 22, and DK-L; Fig. 2b) were used to acquire the zircon Pb/U isotopic ratios using the laser ablation ICP-MS technique. The results are summarized in Figures 21–28. For the U–Pb zircon data, see Appendix.

Two studied samples (PJ 6, PJ 9 described above) come from the contact of the Mariánské-Lázně (MLC) and Teplá Crystalline Complexes (TCC) and three samples (PJ 14, PJ 22 and DK-L) from the Domažlice Crystalline Complex (DCC) and Kdyně Massif (NKM). Across the samples from both areas, zircon grains were observed in different textural positions (Fig. 21). While the majority of zircons occur as isolated individual grains in matrix (Fig. 21a),

then also form small grains (usually up to 10 μm difficult to analyze; Fig. 21b) forming thin rims around ilmenite. Additionally, the zircons are also occasionally present in the form of corona enveloping baddeleyite (also the corona is mostly too thin to analyse, Fig. 21c). In some cases, the baddeleyite is almost completely consumed and it is present only as a relict surrounded by a cluster of tiny zircon grains (Fig. 21d). For better understanding of the relationship between the obtained age and zircon textural position, U-Pb zircon analyses were acquired on separated grains as well as those in-situ from thin sections (see below).

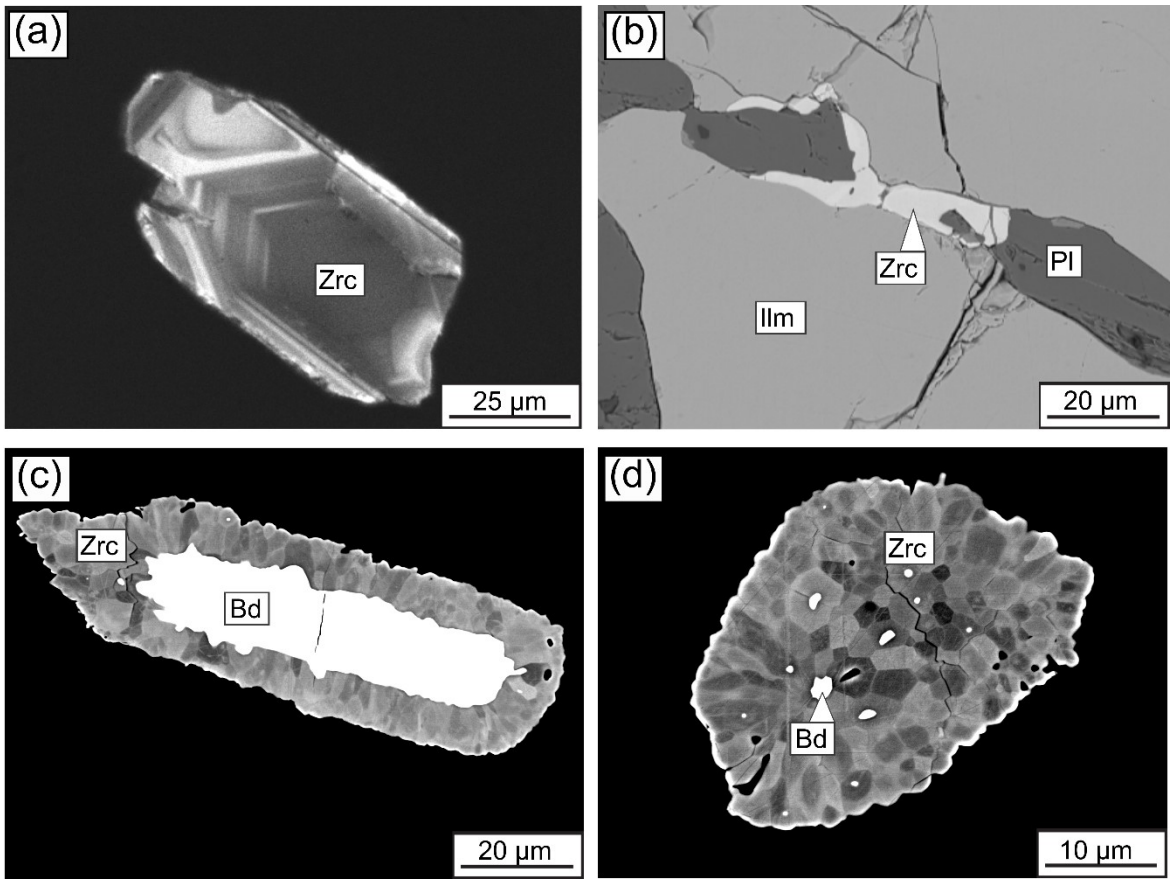

Fig. 21 Different textural position of the zircon grains

(a) Large isolated grain in the matrix; (b) tiny grains forming a rim around ilmenite; (c) Cathodoluminescence (CL) image of zircon corona around baddelleiyte; (d) CL image of newly formed zircon with baddeleyite relicts

2.4.1.1TCC-MLC samples

Zircon grains separated from the coarse-grained metagabbro **PJ6** within MLC show rather prismatic and stubby euhedral shape (or their fragments), mostly 150 to 400 μm long and light cream to tan-coloured. In CL images, these zircons exhibit polygonal zoning (Fig. 22b), mostly faint regular/oscillatory zonation which is generally weak. A lot of grains show detectable unzoned inner CL-dark parts with convolute zoning resulted from metamictization (Fig. 22d, e) alteration of zircons which have lost their radiogenic Pb. The range of the Th/U ratios (Appendix) spans from ~0.4 to 1.7 and higher content of U (usually >1000 ppm) compared to other zircons (usually lower hundreds of ppm) correspond to a higher degree of metamictization. A total of 33 analyses reveals a wider array of ages ranging from *c.* 483 Ma to *c*. 515 Ma with a maximum at *c*. 502 Ma and also a distinct age of *c*. 550 Ma. Partial Pb loss probably caused this continuously expanded age spectrum and it seems that unzoned recrystallized domains give concordant or slightly discordant ages. In detail, the dominant cluster of ages splits internally into two subgroups (Fig. 22a). The 5 younger analyses yield a concordia age of *c.* 487 ± 4 Ma, which recalculated as the weighted mean gives an age of *c.* 485 ± 4 Ma. The remaining 28 analyses constitute a concordia age of *c.* 505 Ma ± 4 Ma of all dates corresponding to *c.* 502 ± 4 Ma as a weighted mean (Fig. 22a). The analyses coming from the zircon core and rim overlap within their 2-sigma error.

Dating of zircons from **PJ 6 thin-section** reveals two age clusters. The younger one yielded an isolated age of *c.* 362 Ma coming from fine-grained aggregate exhibiting composite resorbed zircon in CL images (Fig. 22e). This zircon aggregate represents the advanced stage of zircon corona, where the zircon nearly completely replaced baddeleyite (Fig. 21d). The second age cluster associated with the zircon grains forming a rim around ilmenite, constitute a single concordia age of 484 ± 4 Ma (2σ; 3 analyses; Fig. 22). These grains typically show chaotic polygonal zonation in CL-images (Fig. 22f).

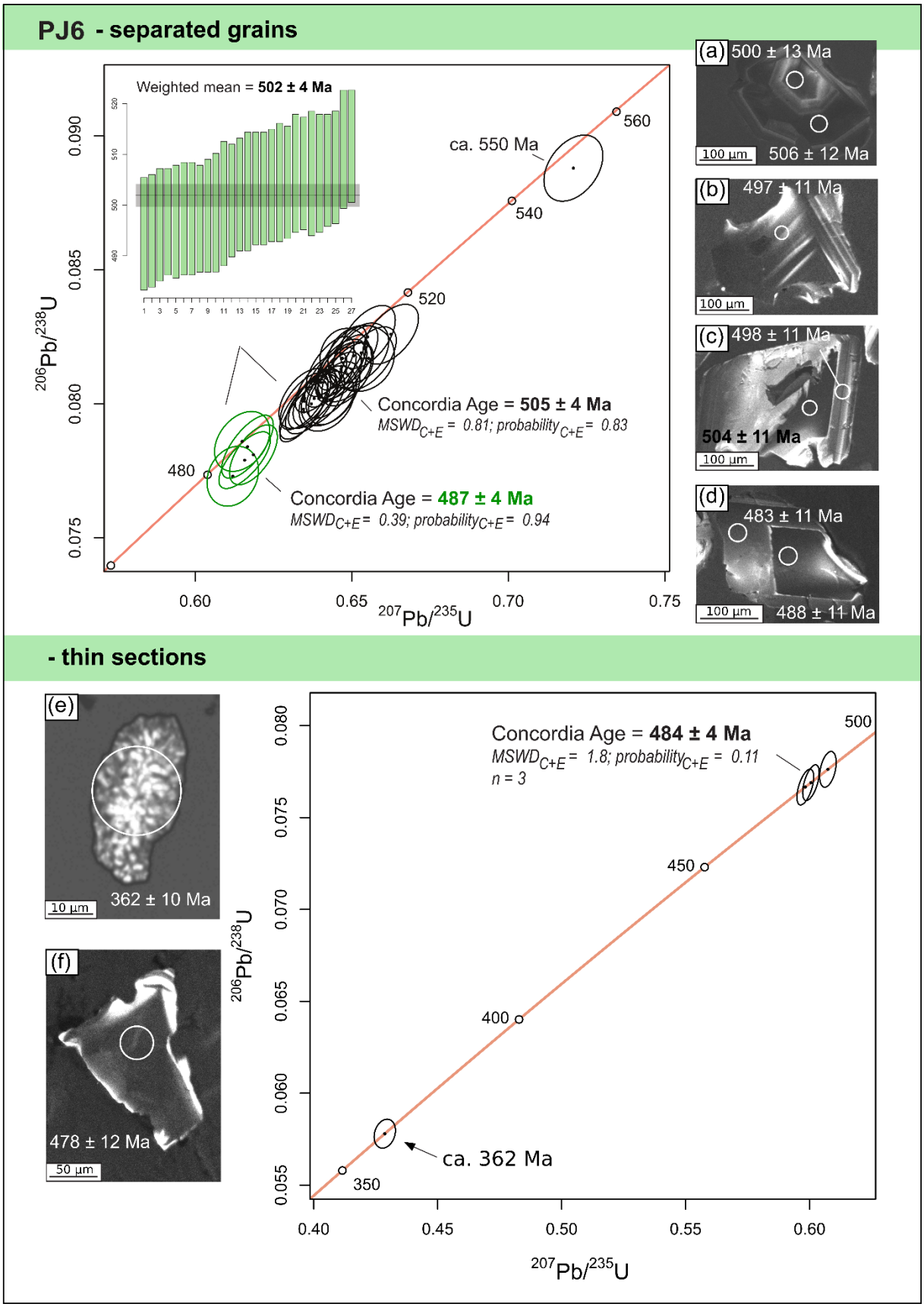

Fig. 22 Results of U-Pb zircon dating from sample PJ 6.

(a); (b) CL image of polygonal zoning in the zircon grains; (c); (d) CL image of zircons with characteristic dark unzoned core; (e) CL image of small-grain aggregates exhibiting composite resorbed zircon (f) CL image of zircon with chaotic polygonal zonation. Weighted mean in upper left corner is calculated for two groups of analyses (c. 487 Ma; c. 505 Ma). ICP-MS analyses spots (25 μm) are marked with concordant $^{206}Pb/^{238}U$ ages ± 2 σ uncertainties.

Zircon populations in separates of the coarse-grained MLC metagabbro **PJ9** (Fig. 23) contain shapes that vary from long prismatic euhedral crystals to isometric or fragmented grains, mostly 200 to 400 μm long, all being brown or dark brown. Cathodoluminescence images show similar internal textures as in the sample PJ6 with recrystallization and faded metamict textures of zircons. A regular polygonal zoning with completely dark zones is typical. Bright and grey high-CL areas are also common, mostly with regular/oscillatory (Fig. 23a) and sector zoning (Fig. 23b). A total of 49 analyses of variously metamict zircons show a widespread in ages ranging from *c.* 499 Ma to *c*. 510 Ma with a weighted mean of *c*. 502 Ma and one younger analysis of c. 464 Ma (Fig. 23). Similarly to sample PJ6, the internal CL structures could be interpreted to result from incomplete recrystallization accompanied by partial loss of radiogenic Pb. The Th/U ratio of the analysed zircons varies from ~0.4 to 1.9 (Appendix), with no systematics reflecting elevated U content (>1000 ppm) and thus higher Th/U ratio, as described in the sample PJ6.

Dated zircon grains from the **PJ9** thin-section are similar to those in the PJ6 thin-section in terms of CL-internal structure and age distributions. The concordia diagram shows an isolated young peak of *c.* 381 Ma (2σ, 1 analysis), followed by a concordia age of 480 ± 4 Ma (2σ; 4 analyses) as well as a peak of *c.* 503 Ma (Fig. 23). All of these ages were also obtained for zircons forming a rim around ilmenite. The youngest age is associated with resorbed zircon aggregate (preserving only tiny relics of former baddeleyite; Fig. 23d) marked by disturbed "cauliflower" CL signature, while internal textures of the rest of the zircon grains show wider zones with local appearance of of recrystallized domains (Fig. 23e).

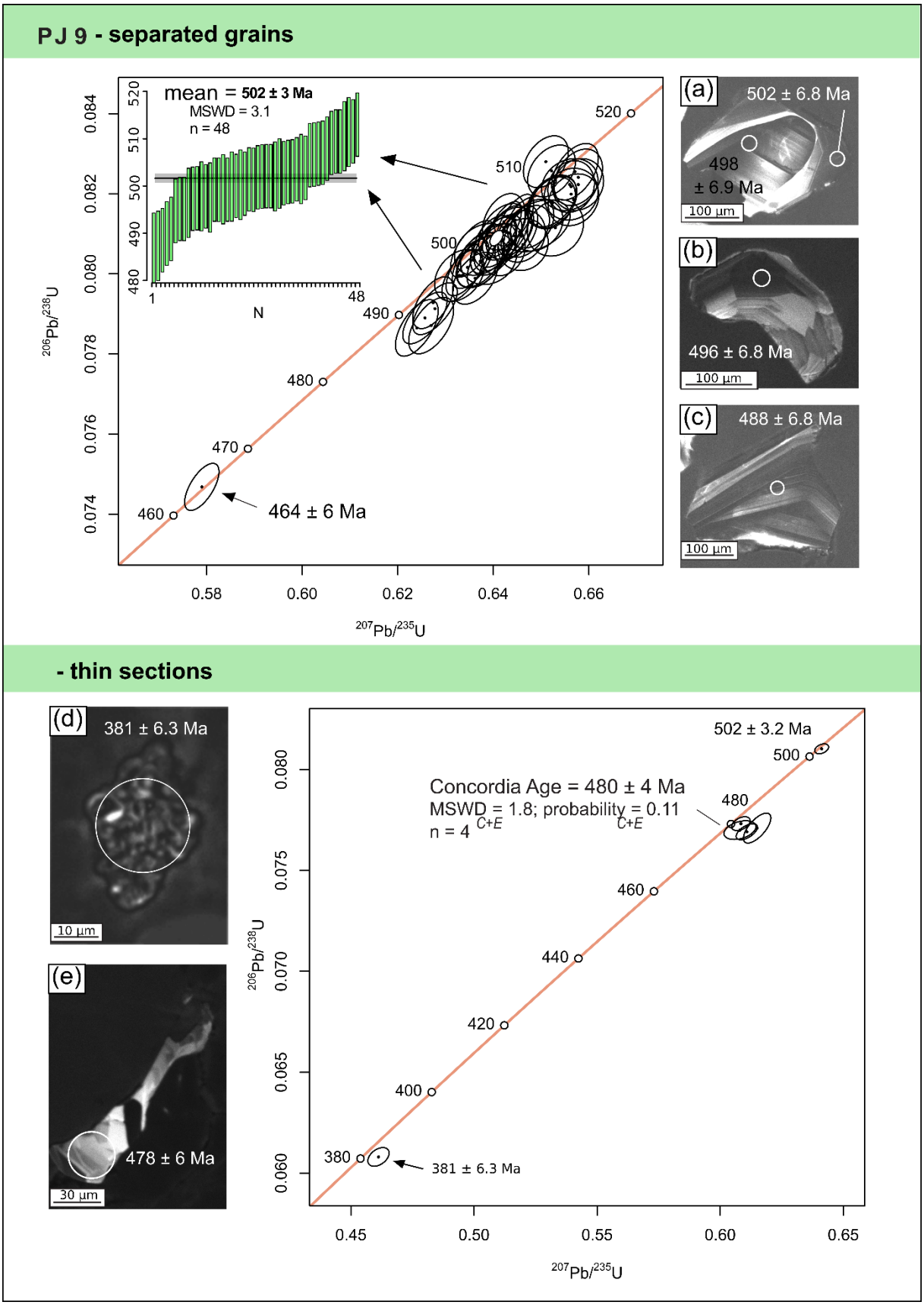

Fig. 23 Results of U-Pb zircon dating from sample PJ 9.

(a) CL image of polygonal zoning in the zircon grains; sector zoning in zircon grains is demonstrated in CL images (b); (c); (d) CL image of small-grain aggregates of zircon with possible relicts of baddeleyite; (e) CL image of zircon observed as rim around apatite. Weighted mean in upper left corner is calculated for large group of analyses. ICP-MS analyses spots (25 µm) are marked with concordant $^{206}Pb/^{238}U$ ages ± 2 σ uncertainties.

2.4.1.2 DCC-KM samples

Zircons separated from the sample **PJ14** (ferrodiorite, NKM) exhibit a variety of shapes and CL zoning patterns. The shapes vary from long-prismatic euhedral grains to stubby or fragmented crystals with lengths of 150 to 300 µm. The zircon grains often show low CL luminescence in their inner parts, frequently with relict dark unzoned cores (Fig. 24a, b) reflecting U-rich metamict domains (>1000 ppm U, Appendix), and wider high-CL rims with low-U growth zones. Some zircons affected by recrystallization show intense faded or blurred domains with an oscillatory/regular zoning preserved only as ghost areas in the crystals (Fig. 24c). A total of 41 analyses revealed a relatively wide spread of ages between *c.* 495 Ma and 527 Ma, which provided a mean age of *c.* 507 Ma and age maxima at peaks of *c.* 501, 512, and 522 Ma (Fig. 24). Younger ages of *c*. 500–495 Ma were systematically obtained from U rich cores (usually >1000 ppm). Isolated analysis of one zircon grain gave an age of *c.* 542 Ma. The studied sample shows relatively uniform Th/U ratio of 0.2–0.7 (Appendix).

Zircons in the **PJ14** thin-sections are similar to those identified in separates revealing low-CL luminescence in the inner parts and brighter, high-CL polygonal zoning in zircon rims (Fig. 24d, e). The largest cluster of ages predominantly from low-CL cores provided a mean age of 485 ± 5 Ma (2σ; 12 analyses), generally brighter high-CL zones show distinct peak with a concordia age of 510 ± 4 Ma (2σ; 3 analyses) as well as a minor peak of age ~520 Ma (Fig. 24).

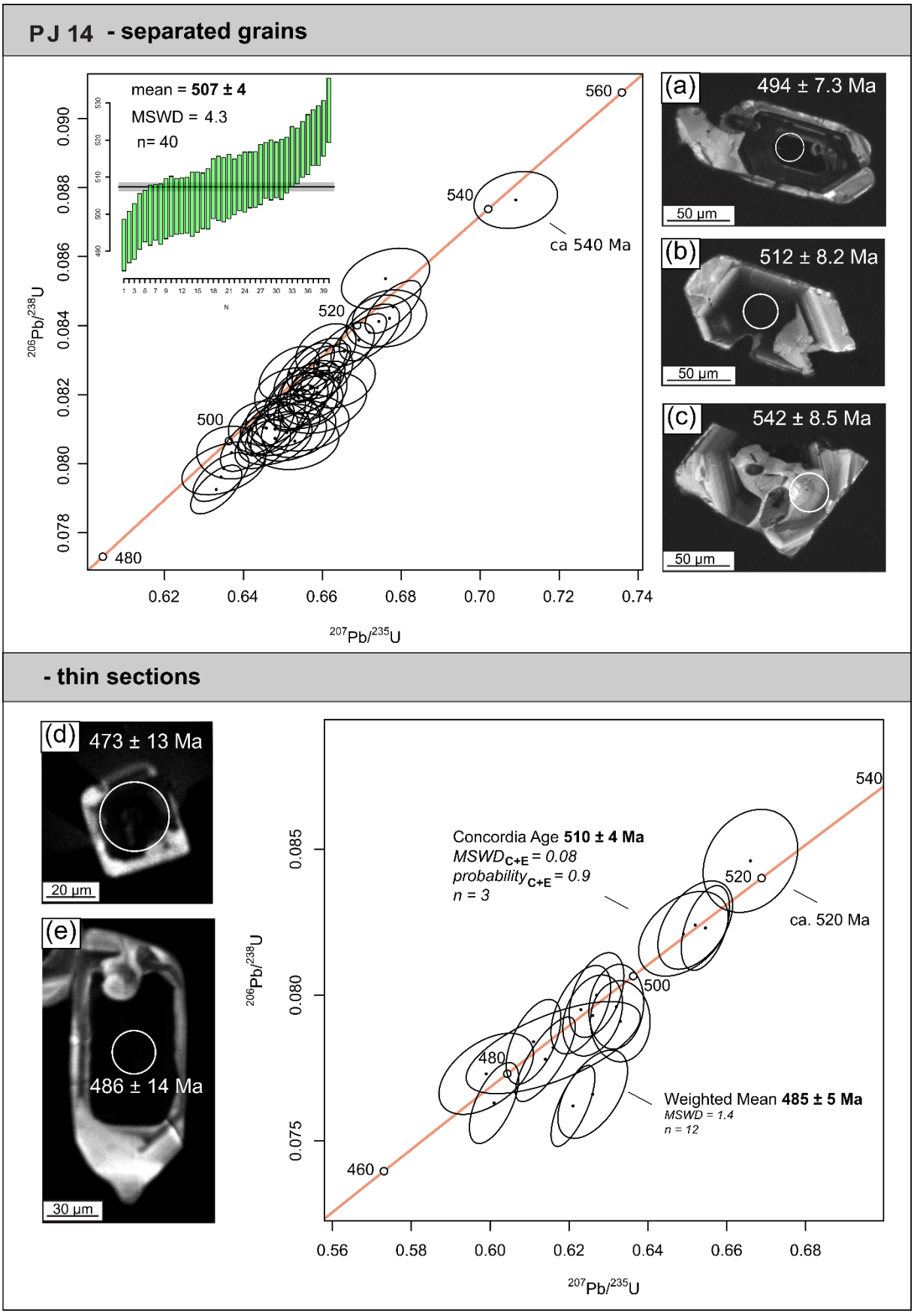

Fig. 24 Results of U-Pb zircon dating from sample PJ 14.

(a); (b); CL images of typical zircon texture with dark unzoned core wider rims with growth zones; (c) CL image of the zircon grain with intense faded or blurred domains, with the oscillatory/regular zoning preserved only as ghost area; (d); (e) CL images of dark cores of the zircon grains; Weighted mean in upper left corner is calculated for large group of analyses. ICP-MS analyses spots (25 µm) are marked with concordant $^{206}Pb/^{238}U$ ages ± 2 σ uncertainties.

Zircon grains separated from sample **PJ22** (metagabbro, NKM) revealed recrystallization, where the original euhedral zircons (~100–250 µm) with oscillatory zoning are crosscut by recrystallized domains of more homogenous compositions. Only five grains and eight spot analyses could be obtained from this sample. While two analyses located in the low-CL growth zones provided a mean age of *c.* 505 Ma (Fig. 25a), the remaining analyses yielded a concordia age of ~520 ± 4 Ma (2σ; 4 analyses; Fig. 25c, d) and an isolated age of ~537 Ma. The obtained average Th/U ratio of 0.5, see Appendix.

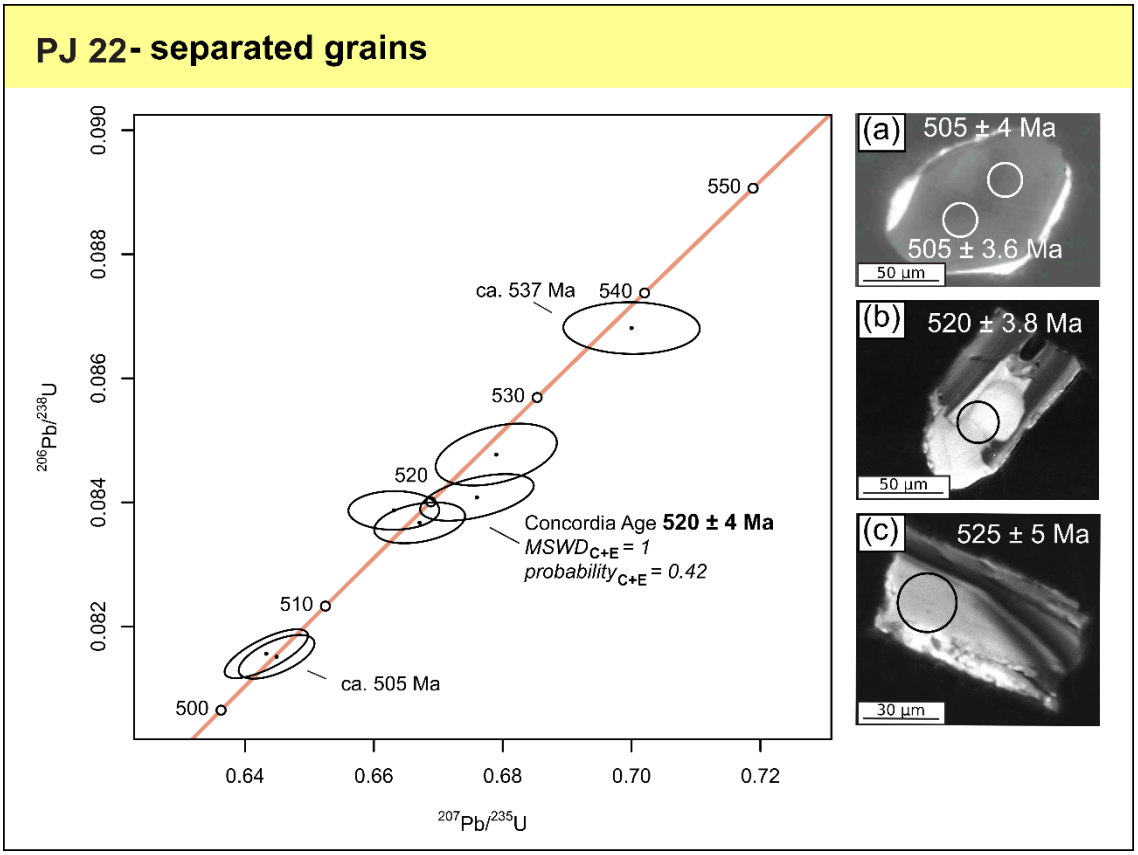

Fig. 25 Results of U-Pb zircon dating from samples PJ 22

(a) CL image of homogenous zircon with low CL domain; (b); (c) CL image of zircons with original oscillatory zonation cut by recrystallized domains with homogenous compositions. ICP-MS analyses spots (25 µm) are marked with concordant $^{206}Pb/^{238}U$ ages ± 2 σ uncertainties.

Only two zircon grains from sample **DKL** (amphibolite, DCC) were dated. Both grains (~100 and 150 µm long) exhibit euhedral crystal shapes, weakly broadly zoned with low-CL intensity(?) (Fig. 26a, b). Three spot analyses yielded a concordia age of 505 ± 3 Ma (Fig. 26) and Th/U ratio 0.3–1.0 (Appendix).

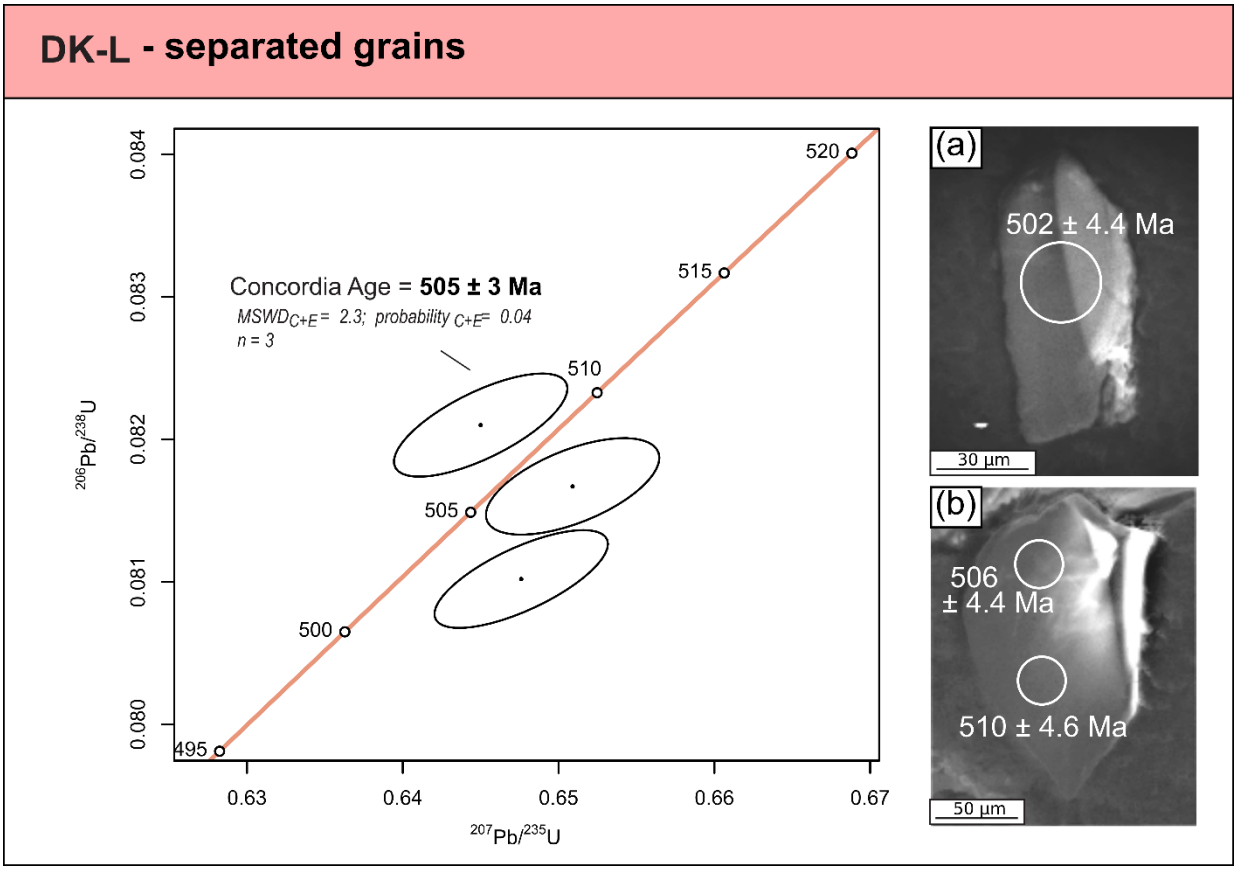

Fig. 26 Results of U-Pb zircon dating from samples DK-L

(a); (b) CL image of two analysed zircon grains, both with weak broad zonation. ICP-MS analyses spots (25 µm) are marked with concordant $^{206}Pb/^{238}U$ ages ± 2 σ uncertainties.

The results described above are plotted in two histograms for better comparison of obtained ages from both studied areas (Fig. 27). Samples from TCC-MLC area show major peak at c. 505 Ma and minor elevation between c. 480-490 Ma. Samples from DCC-KM area show the same information, but additionally the major peak has two maximums at c. 505 Ma and c. 515 Ma and it also shows lower peaks at c. 490 and 525 Ma.

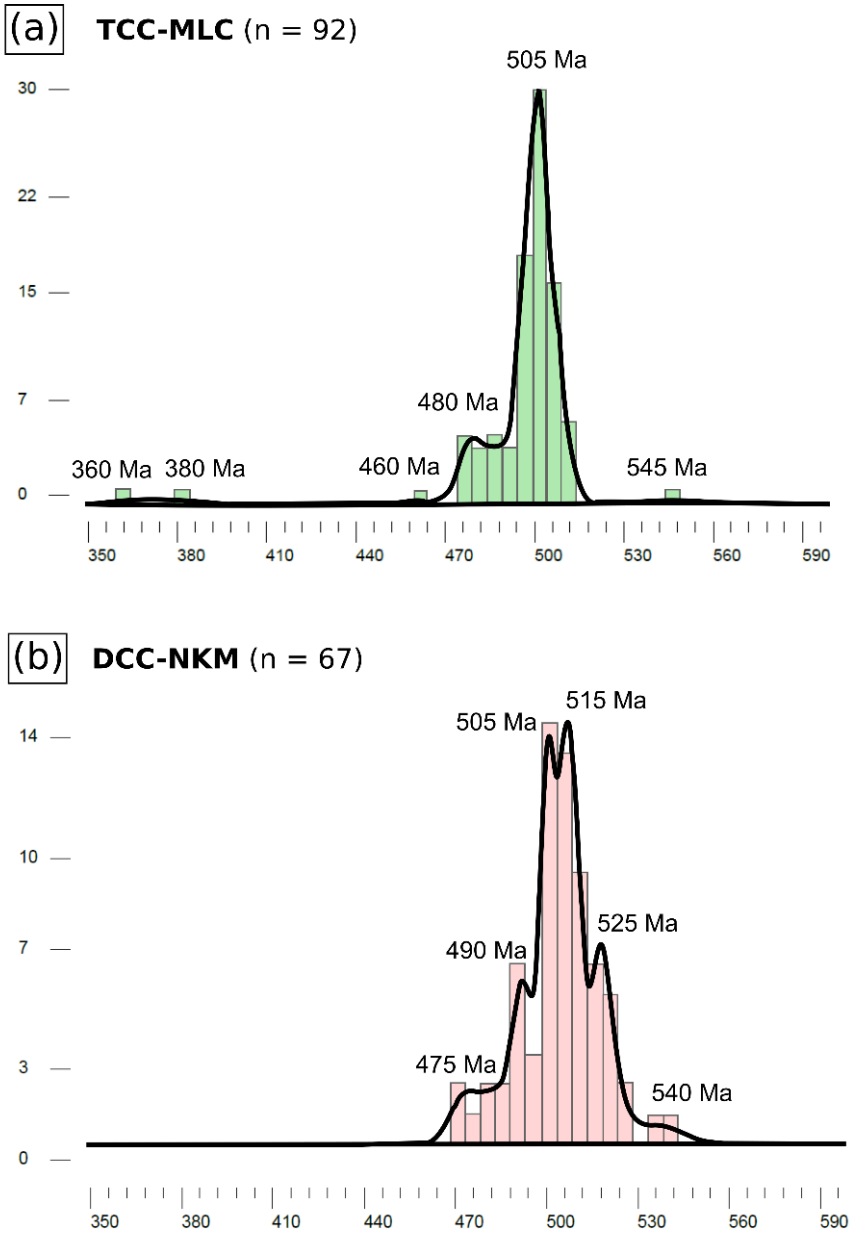

Fig. 27 Histograms and kernel density estimates (KDE) curves of the zircon ages from both studied areas.

(a)Teplá Crystalline and Marisánské Lázně Complexes (TCC-MLC) area calculated from n = 92 analyses; (b) Domažlice Crystalline Compex and Neukirchen-Kdyně Maffif (DCC-NKM) area estimated from n = 67 analyses.

2.4.2 U–Pb titanite dating

Titanite U–Pb dating was carried out on two samples: PJ5A collected from locality within TCC and DK17 collected near Kdyně (Fig. 2b). Results are plotted in Fig. 28. Both titanite grains are light brown color, have euhedral shape, 80–200 in lengths, and in BSE images show different appearance (Fig. 28). While titanite grains in sample PJ5A seem to be formed by aggregates of tiny titanite grains (1–5 μm in size, Fig. 28a), titanite grains from DK17 generally show no or very weak zonation (Fig. 28b). Titanite grains PJ5A and DK17 contain very low U content (~0.1–5 ppm) and have relatively high Th/U of 0.1–3 for sample PJ5A, whereas a range of 0.1–1 for sample DK17 (Appendix). Titanite grains from both samples contain a much higher proportion of common Pb (percentage of common 206Pb ranges from about 10% to 68% (Appendix). Regression of uncorrected data on a Tera-Wasseburg projection yield identical ages within uncertainty and give an intercept at 370 ± 6 Ma for sample PJ5A (Fig. 28a) and 371 ± 7 Ma for sample DK17 (Fig. 28b). The lower intercept age reported here for titanites represents the Devonian metamorphic event.

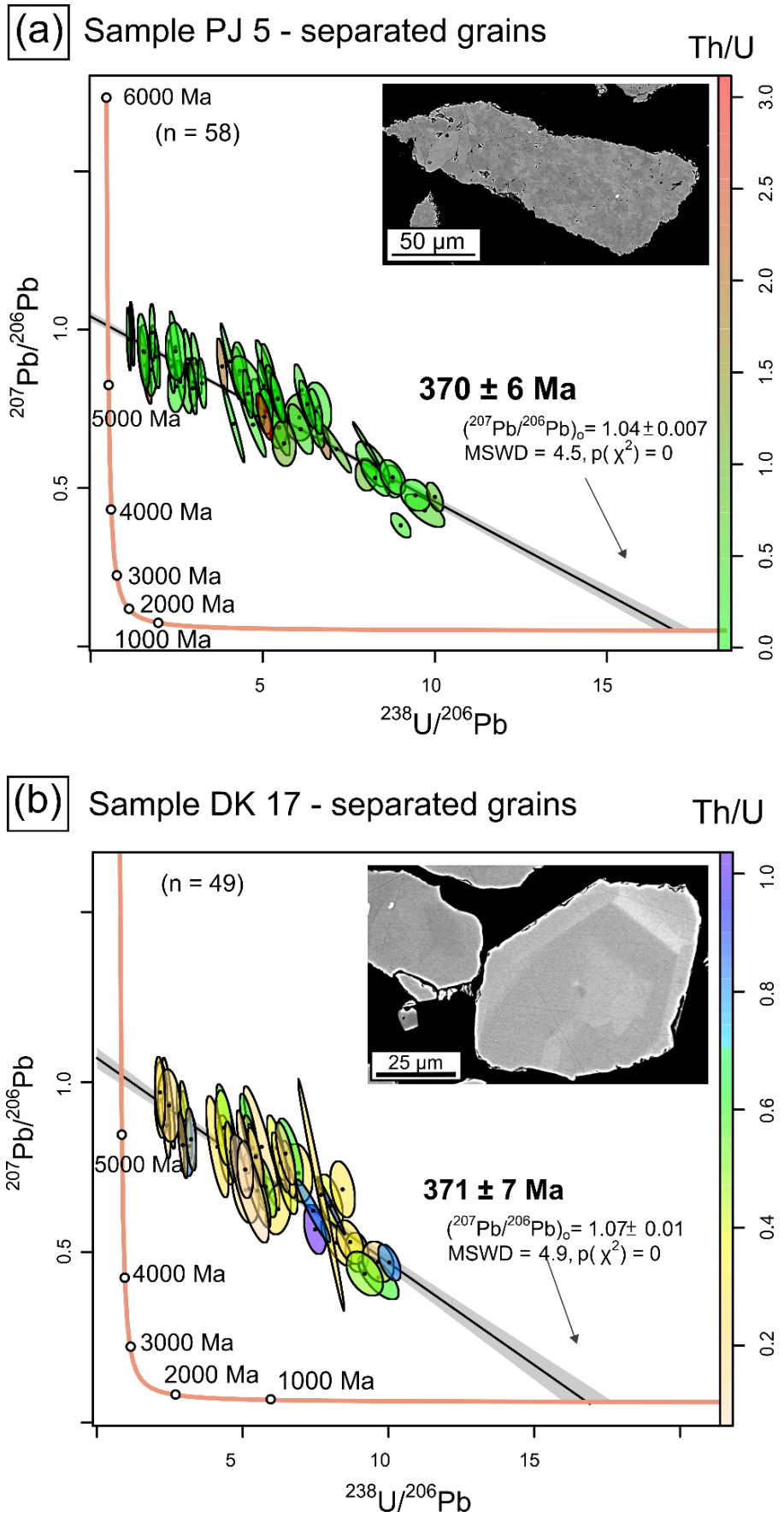

Fig. 28 Results of U-Pb titanite dating from samples PJ 5 and DK 17.

U-Pb diagram showing titanite analyses from sample PJ 5, Th/U ratio is demonstrated by different color scale, in upper left corner is detail of titanite demonstrating the aggregate texture consisting of tiny grains (b) U-Pb diagram showing titanite analyses from sample DK 17, Th/U ratio is demonstrated by different color scale, in left corner is detail of titanite with weak compositional zonation

2.5 Magmatic stage characteristics

2.5.1 Geochemistry

2.5.1.1Major and trace elements

Major and trace element concentrations for the studied samples are listed in Appendix. Since the majority of analysed samples display coronitic textures, it can be assumed that they were more or less affected by metamorphism that can potentially modify fluid-mobile element contents. Therefore, we evaluated composition using diagrams based on immobile elements to avoid possible influence of element mobility during the metamorphic process including the data for the samples collected at the MLC–TCC previously given in Jašarová et al. (2016).

Based on the trace element composition, all studied samples can be divided into three groups: the ***Group 1*** consists of metagabbroic samples from the Orlovice area and some of the surrounding ferrodiorite representing transitional type between Group 1 and Group 2. The ***Group 2*** consists of samples from the ferrodiorite body enveloping the metagabbros whereas the ***Group 3*** comprises samples from TCC-MLC area, DCC-NKM area and Poběžovice Massif. Different geochemical character of these groups is demonstrated in chondrite-normalized (Boynton, 1984) spider plots (Fig. 29a, c, e) as well as selected immobile trace element contents normalized to N-MORB (after Peaece 2014; normalizing values from Sun and McDonough, 1989; Fig. 29b, d, f). Additionally, composition of the possible parental magma for NKM (Svobodová, 1999) is plotted for comparison.

The ***Group 1*** samples (Fig. 29a) are characterized by rather flat patterns (La_N/Yb_N = 0.6–2.4; La_N/Sm_N = 0.5–1.3) with largely positive Eu anomaly (Eu/Eu*= 1.5–4.7) due to high plagioclase contents. Samples of this group show the best affinity to composition of parental magma used by Svobodová (1999) for the NKM area. In comparison, the ***Group 2*** (Fig. 29c) rocks exhibit more enriched LREE patterns (La_N/Yb_N = 2.5–4.4; La_N/Sm_N = 1.3–2.1) with either absence of only weakly negative Eu anomaly (Eu/Eu*= 0.8–1.1). Additionally, the samples exhibit an apparent U-shaped distribution of the HREE (Tb_N/Y_N = 1.3–1.6). An exception is represented by sample 06OH13 with largely positive Eu anomaly (Eu/Eu*= 3.9), La_N/Yb_N of 2.5 and La_N/Sm_N of 1.3 that mimic the composition of the ***Group 1*** samples rather than ferrodiorite of the ***Group 2***. Finally, samples of the ***Group 3*** (Fig. 29e) are characterized by pronounced LREE enrichment over HREE (La_N/Yb_N = 1.5–5.5; La_N/Sm_N = 0.8–2.4) and absence or weakly negative Eu anomaly (Eu/Eu*= 0.8–1.1). Yet, two samples are the exceptions having either negative (Eu/Eu*= 0.4; sample PJ 15) or positive (Eu/Eu*= 1.9; PJ 7) anomalies.

In terms of immobile trace elements, the ***Group 1*** and ***3*** (Fig. 29b, f) collectively display slightly decreasing pattern with significant depletion in Nb (Nb_N/Th_N = 0.1–0.9) with the exception of samples 06OH3A (Nb_N/Th_N = 1.3), PJ 20 (Nb_N/Th_N = 6.2) and DK 17E (Nb_N/Th_N = 3.4). While the majority of ***Group 1*** samples exhibit positive Ti anomaly (Ti_N/Gd_N = 0.9–5.1), the remaining ***Group 2*** and ***3*** (Fig. 29d, f) are rather Ti depleted.

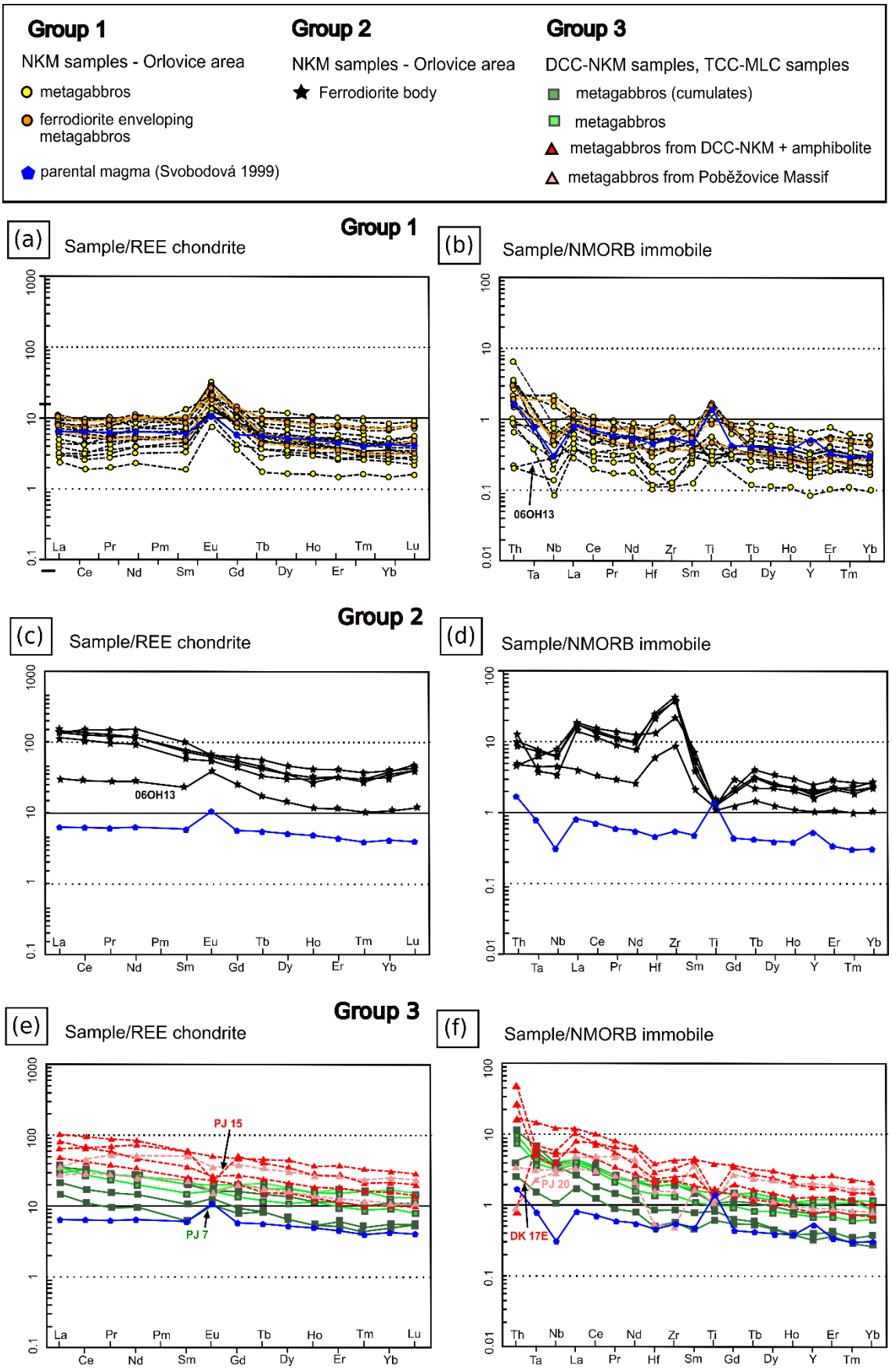

Fig. 29 Spider plots showing trace-element signatures in the studied samples.

(a) relatively immobile trace element composition of samples from Group 1 normalized to N-MORB (after Pearce 2014, normalizing values from Sun and McDonough 1989), (b) relatively immobile trace element composition of Group 2 samples normalized to N-MORB (after Pearce 2014, normalizing values from Sun and McDonough 1989); (c) REE content of Group 1 samples normalized by average chondrite composition (Boynton 1984), (d) REE content of samples from Group 2 normalized by average chondrite composition (Boynton 1984).

In the TAS classification diagram (Fig. 30a; Middlemost, 1994), most samples plot within a compositional field of gabbro and gabbroic diorite. Similarly, using Nb/Y vs. Zr/Ti classification diagram (Pearce, 1996), most of the samples plot within a compositional field of basalt with some showing composition of basaltic andesite to andesite (Fig. 30b). However, we note the ferrodiorite samples fall to the field corresponding to rhyolite or dacite due to their significantly higher Zr contents.

2.5.1.2 Sr-Nd isotopic compositions

Whole-rock Sr and Nd isotopic data are summarized in Table 6 while the initial Sr and Nd isotopic ratios recalculated back to 510 Ma are shown in Figure 30. Altogether, analysed samples have similar $^{87}Sr/^{86}Sr(i)$ values between 0.7027–0.7037 (Fig. 13a). On the other hand, initial $^{143}Nd/^{144}Nd(i)$ values more scattered values from 0.51175 to 0.51235 with corresponding ε_{Nd} values from +2.1 (sample PJ22) to +7.3 (sample PJ5; Table 6, Fig. 30). The ***Group 1*** and ***2*** samples were not analyzed during the course of this study since their Sr-Nd isotopic compositions (Fig. 30) has been already given in Svobodová (1999). In general, the analyzed ***Group 3*** rocks have overlapping Sr-Nd compositions to those from Group 1 and 2 (Fig. 30), while we note that samples from the TCC-MLC area have generally higher ε_{Nd} values compared to the DCC-NKM samples.

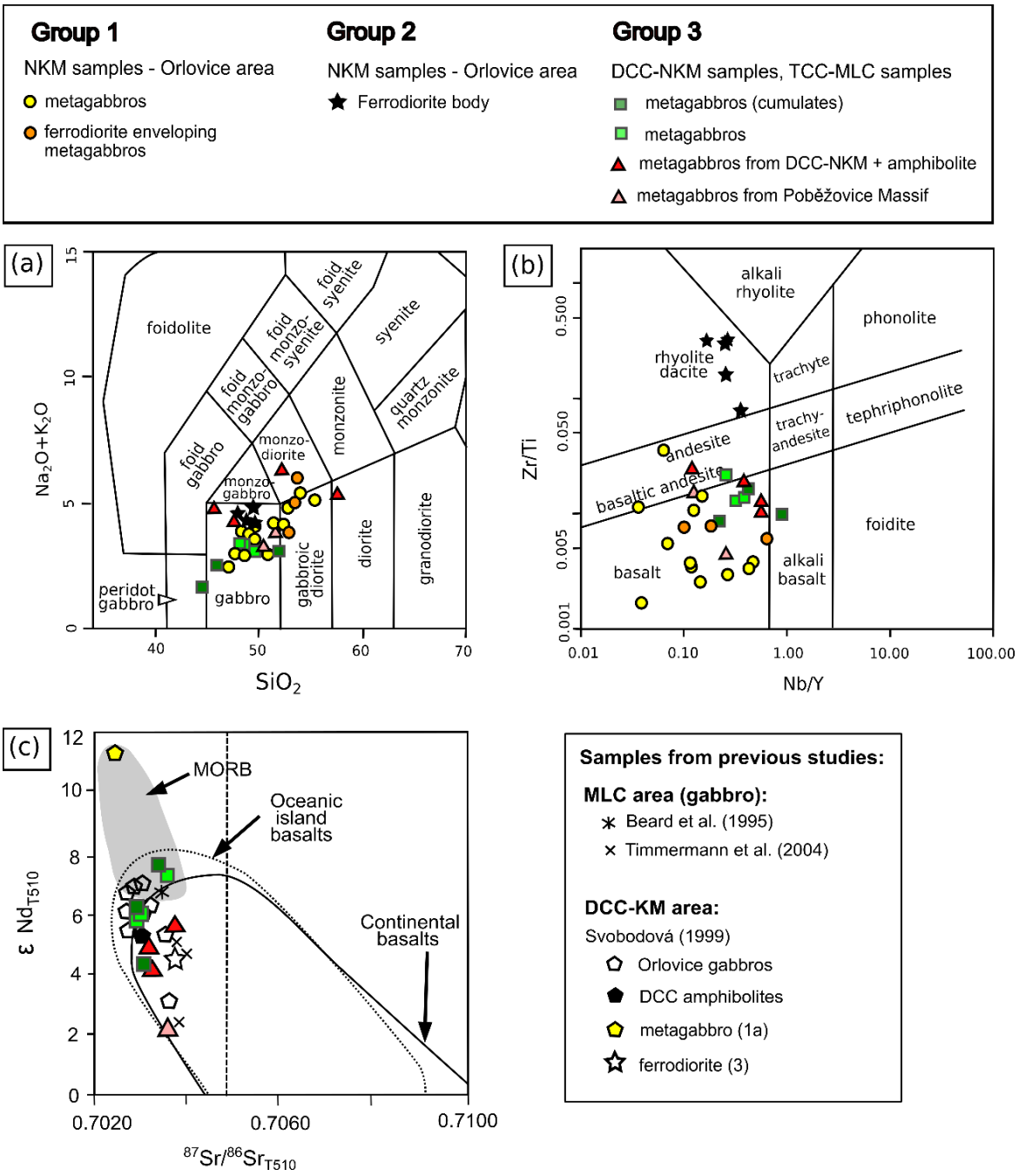

Fig. 30 Classification diagrams showing the character and isotopic composition of the studies samples. Samples of TCC-MLC samples from Jašarová et al. (2016).

(a) TAS proxy diagram of SiO_2 vs. Na_2O+K_2O (Middlemost, 1994); (b) the immobile element-based TAS proxy diagram (Pearce 1996, after Floyd and Winchester 1975); (c) ε Nd vs $^{87}Sr/^{86}Sr$ diagram show isotopic ratios of representative samples at t = 510 Ma. Schematic ocean-island basalt and continental basalt fields after White (1999). Present-day MORB field after Taylor et al. (1997) and Kempton et al. (2002). It should be noted that the MORB field was probably about 1 ε Nd unit lower at 0.5 Ga. In this section, two samples already described by Svobodová et al. (1999) as sample 1a and sample 3 are plotted for comparison

Sample	Sr (ppm)	Rb (ppm)	87Rb/86Sr	87Sr/86Sr	87Sr/86Sri	Sm (ppm)	Nd (ppm)	147Sm/144Nd	143Nd/144Nd	143Nd/144Ndi	Ɛ Nd
PJ5	192.20	4.80	0.07226	0.70408	0.70356	4.33	15.80	0.16569	0.51291	0.51235	7.28
PJ6	242.50	12.40	0.14794	0.70400	0.70292	4.03	15.20	0.16030	0.51282	0.51228	5.83
PJ7	264.60	4.50	0.04920	0.70378	0.70342	1.16	5.60	0.12524	0.51279	0.51237	7.57
PJ8	177.80	13.00	0.21156	0.70466	0.70312	3.88	15.70	0.14941	0.51270	0.51220	4.34
VP46	166.20	5.20	0.09052	0.70358	0.70292	2.00	8.50	0.14226	0.51277	0.51230	6.19
PJ9	305.50	9.80	0.09281	0.70362	0.70295	2.87	11.70	0.14831	0.51279	0.51229	6.05
PJ 15	197.30	36.90	0.54131	0.70765	0.70371	10.86	42.40	0.15486	0.51279	0.51227	5.60
PJ 20 B	271.10	10.30	0.10993	0.70436	0.70356	4.44	15.80	0.16989	0.51266	0.51209	2.13
DK 17E	579.00	9.20	0.04597	0.70353	0.70320	4.79	19.00	0.15242	0.51270	0.51219	4.18
DK 17I	214.80	5.20	0.07004	0.70367	0.70316	11.24	47.20	0.14397	0.51271	0.51223	4.87

Tab. 6 Whole rock Sm-Nd and Sr-Rb concentrations and $^{143}Nd/^{144}Nd$ and $^{87}Sr/^{86}Sr$ isotope compositions.

Initial ratio was calculated for age 510 Ma, which is considered as emplacement age (based on geochronology in this study

2.6 Re-equlibration characteristics

Since the samples from DCC-NKM area provide only limited constrains for characterization of metamorphism (M_2 mineral assemblage not suitable for P–T calculations as well as no signs of plagioclase decomposition connected to metamorphism), they are not included in following chapter.

2.6.1 Calculation of P–T conditions

Metamorphic conditions associated with formation of the corona textures have been constrained using the metamorphic assemblages in the selected samples. Only three samples were used for geobarometry, namely those containing garnet-bearing coronas (PJ5 from TCC, PJ6 from MLC near the contact with TCC, and PJ9 from MLC). The reason is that they contain the plagioclase–amphibole–garnet–kyanite assemblage suitable for both multi-equilibrium and conventional geothermobarometry.

For the characterization of metamorphic P–T conditions in the studied coronitic metagabbros (and coronitic rocks in general), the primary (magmatic) mineral assemblage is considered as metastable with respect to corona formation and thus, it has to be avoided in the calculations. Moreover, corona formation is typically associated with chemical potential gradients of the components present and therefore even the formation of two adjacent layers of corona sequence cannot be considered to represent a thermodynamic equilibrium. Considering this fact, the minerals used for P–T calculations were carefully selected so that they come exclusively from the garnet corona and occur in a close proximity to each other. Thus, the chemical composition of garnet in the vicinity of amphibole, plagioclase and kyanite inclusions was used in the calculations (see Appendix).

2.6.1.1 Multiequilibrium geothermobarometry

For the purpose of the average P–T calculations, activities of mineral end-members in phases considered for P–T estimates were calculated using the AX software (accessible at *http://www.esc.cam.ac.uk/research/research-groups/research-projects/tim-hollands-software-pages/ax*). Calculations were carried out equally for the mineral assemblage garnet–amphibole–plagioclase–kyanite in all the selected samples. First set of calculations, done with H_2O in excess, gave the following P–T conditions (Tab. 7, all errors are 2σ): sample PJ5 – 720±172 °C and 12.3 ±4.6 kbar; sample PJ6 – 765±100 °C and 14.5±2.8 kbar; sample PJ9 – 815±112 °C and 16.3±3.6 kbar.

However, the aH_2O values are expected to be generally low in the coronitic rocks; e.g., St-Onge and Ijewliw (1996) estimated water activities in similar coronitic metagabbros from Canada to values as low as 0.3–0.1. Indeed, the observed textures, represented by coronas and symplectites, indicate that the studied metamorphism occurred under H_2O-undersaturated conditions. In order, to deal with this problem, calculations with H_2O-absent equilibria were attempted, giving the following results (Tab. 7): sample PJ5 – 556±158 °C and 9.1±3.4 kbar; sample PJ6 – 679±244 °C and 12.7±5.4 kbar; sample PJ9 – 607±100 °C and 11.7±4.6 kbar. Thus, these H_2O-absent calculations led to lower mean P–T estimates, especially for samples PJ5 and PJ9, while the conditions calculated for sample PJ6 did not change significantly.

It is clear, that for our studied samples the assumed aH_2O has large effect on the average P–T calculation results. This means that at least an approximate estimate of the aH_2O values is needed in order, to obtain reasonably precise P–T results. Following the approach of Pitra et al. (2010), a series of average P–T calculations with identical mineral assemblage and varying aH_2O was performed. Examining the dependence of calculation errors and the results of the χ^2 test ("fit" value) on aH_2O, one can estimate the correct values of aH_2O. The summary of the average P–T calculations with aH_2O values ranging from 0 to 1 is given in Tab. 8. The lowest

uncertainties and the best "fit" values are obtained for very low aH_2O (~0.1) in samples PJ5 and PJ9. The sample PJ6 are also gives the lowest uncertainties for the aH_2O = 0.1, however both uncertainties and the "fit" value do not change significantly with increasing aH_2O.

It is important to note that in all cases, the results of average P–T calculations passed the statistical test for the entire range of aH_2O, which means that it is not possible to estimate the aH_2O precisely. However, based on the optimal parameters (uncertainties and the "fit" value), it can be assumed that water activity in the studied rocks was generally rather low. Thus, the aH_2O for the final average P–T calculations was set between 0.1 and 0.3. Using the plagioclase–amphibole–garnet–kyanite assemblage, the following range of temperatures and pressures was calculated for the selected samples (aH_2O = 0.1→0.3, uncertainties given as 2σ; Fig. 31): PJ5: T = 578 ± 78→640 ± 96 °C, P = 9.6 ± 2.2→10.8 ± 2.6 kbar, PJ6: T = 616 ± 72→681 ± 84 °C, P = 11.4 ± 2.0→12.7 ± 2.4 kbar and PJ9:T =659 ± 58→727 ± 70 °C, P = 12.9 ± 2.0→14.4 ± 2.4 kbar.

Sample PJ5

Phase:	Amphibole				Plagioclase		Garnet			Kyanite
Endmember:	tr	fact	ts	parg	an	ab	py	gr	alm	ky
Activity	0.240	0.000	0.004	0.018	0.710	0.570	0.017	0.017	0.150	1.000
sd(a)/a	0.156	0.996	0.700	0.482	0.050	0.055	0.498	0.497	0.198	

aH_2O = 1.0	H_2O absent
excluded endmember: spessartine	excluded endmember: spessartine
Independent set of reactions	Independent set of reactions
1) 3tr + 8gr + 24ky = 3ts + 24an + 2py	1) 3tr + 8gr + 24ky = 3ts + 24an + 2py
2) 5ts + 20an = 3tr + 8gr + 22ky + 2H_2O	2) 9tr + 6fact + 40gr + 120ky = 15ts + 120an + 10alm
3) 3fact + 8gr + 27ky = 30an + 5alm + 3H_2O	3) 9ts + 6ab + 4py + 8gr = 3tr + 6parg + 24an
4) 9ts + 6ab + 4py + 8gr = 3tr + 6parg + 24an	

For 95% confidence, fit < 1.73						For 95% confidence, fit < 1.96					
T[°C]	sd (2σ)	P[kbar]	sd (2σ)	cor	fit	T[°C]	sd (2σ)	P[kbar]	sd (2σ)	cor	fit
720	172	12.3	4.6	0.893	1.61	556	158	9.1	3.4	0.943	1.02

Sample PJ6												
Phase:	Amphibole				Plagioclase		Garnet			Kyanite		
Endmember:	tr	fact	ts	parg	an	ab	py	gr	alm	ky		
Activity	0.091	0.000	0.001	0.056	0.590	0.650	0.029	0.036	0.100	1.000		
sd(a)/a	0.293	1.119	3.900	0.316	0.050	0.050	0.432	0.404	0.258			
aH_2O = 1.0						H_2O absent						
excluded endmember: spessartine						excluded endmember: spessartine						
Independent set of reactions						Independent set of reactions						
1) 3tr + 8gr + 24ky = 3ts + 24an + 2py						1) 3tr + 8gr + 24ky = 3ts + 24an + 2py						
2) 3tr + 8gr + 27ky = 30an + 5py + $3H_2O$						2) 3fact + 5py = 3tr + 5alm						
3) 3fact + 8gr + 27ky = 30an + 5alm + $3H_2O$						3) 9ts + 6ab + 4py + 8gr = 3tr + 6parg + 24an						
4) 9ts + 6ab + 4py + 8gr = 3tr + 6parg + 24an												
For 95% confidence, fit < 1.73						For 95% confidence, fit < 1.96						
T[°C]	sd (2σ)	P[kbar]	sd (2σ)	cor	fit	T[°C]	sd (2σ)	P[kbar]	sd (2σ)	cor	fit	
765	50	14.5	1.4	0.901	0.65	679	122	12.7	2.7	0.978	0.6	

Sample PJ9												
Phase:	Amphibole				Plagioclase		Garnet			Kyanite		
Endmember:	tr	fact	ts	parg	an	ab	py	gr	alm	ky		
Activity	0.558	0.000	0.002	0.067	0.530	0.670	0.085	0.034	0.057	1.000		
sd(a)/a	0.125	1.216	1.700	0.290	0.066	0.050	0.283	0.411	0.341	0.000		
aH_2O = 1.0						H_2O absent						
excluded endmember: spessartine						excluded endmember: spessartine						
Independent set of reactions						Independent set of reactions						
1) 3tr + 8gr + 24ky = 3ts + 24an + 2py						1) 3tr + 8gr + 24ky = 3ts + 24an + 2py						
2) 5ts + 20an = 3tr + 8gr + 22ky + $2H_2O$						2) 3tr + 5alm = 3fact + 5py						
3) 3fact + 8gr + 27ky = 30an + 5alm + $3H_2O$						3) 9ts + 6ab + 4py + 8gr = 3tr + 6parg + 24an						
4) 9ts + 6ab + 4py + 8gr = 3tr + 6parg + 24an												
For 95% confidence, fit < 1.73						For 95% confidence, fit < 1.96						
T[°C]	sd (2σ)	P[kbar]	sd (2σ)	cor	fit	T[°C]	sd (2σ)	P[kbar]	sd (2σ)	cor	fit	
815	56	16.3	1.8	0.873	1.42	607	100	11.7	2.3	0.972	0.96	

Tab. 7 Results of average P–T calculations

aH2O - water activity; correlation coefficient - ; fit - result of the c2 test; endmember abbreviations: tr - tremolite; fact - Fe-actinolite; ts - tschermackite; parg – pargasite; an - anortite; ab - albite; py - pyrope; gr - grossular; alm - almandine; ky – kyanite

Sample	*aH2O*	avT [°C]	sd (2σ)	avP [kbar]	sd (2σ)	cor	fit
PJ5	*For 95% confidence, fit < 1.96*						
	0	556	158	9.1	3.4	0.943	1.02
	For 95% confidence, fit < 1.73						
	0.1	578	78	9.6	2.2	0.867	0.75
	0.3	640	96	10.8	2.6	0.88	1.07
	0.5	672	124	11.4	3.4	0.885	1.29
	0.7	695	146	11.9	4	0.889	1.44
	0.9	712	164	12.2	4.4	0.892	1.56
	1	720	172	12.3	4.6	0.893	1.61
PJ6	*For 95% confidence, fit < 1.96*						
	0	679	244	12.7	5.4	0.978	0.6
	For 95% confidence, fit < 1.73						
	0.1	616	72	11.4	2	0.875	0.6
	0.3	681	84	12.7	2.4	0.888	0.43
	0.5	715	90	13.4	2.4	0.893	0.48
	0.7	739	96	13.9	2.6	0.897	0.55
	0.9	757	98	14.3	2.6	0.9	0.62
	1	765	100	14.5	2.8	0.901	0.65
PJ9	*For 95% confidence, fit < 1.96*						
	0	607	200	11.7	4.6	0.972	0.96
	For 95% confidence, fit < 1.73						
	0.1	659	58	12.9	2	0.846	0.77
	0.3	727	70	14.4	2.4	0.86	1.04
	0.5	763	86	15.1	2.8	0.866	1.19
	0.7	787	98	15.7	3.2	0.87	1.3
	0.9	807	108	16.1	3.6	0.872	1.38
	1	815	112	16.3	3.6	0.873	1.42

Tab. 8 Results of P-T calculations using multi-equilibrium thermobarometry for range of H_2O activity from 0 to 1

aH_2O - water activity; correlation coefficient - ; fit - result of the c2 test

2.6.1.2 Conventional geothermobarometry

Using the methods of conventional thermobarometry (Kohn and Spear 1990; Ravna 2000; Tab. 7; Fig. 8), the results for the sample PJ5 from the TCC indicate P–T conditions of 585 °C and 9.4 kbar. Two sets of analyses from the MLC sample PJ6 yielded higher metamorphic conditions of 634 °C at 12.7 kbar and 711 °C at 12.9 kbar, respectively. Similarly, the sample PJ9 from the MLC gave 671 °C at 13.6 kbar and 681 °C at 12.7 kbar. Although the methods of conventional geothermobarometry do not allow determining uncertainties, which can be generally very large (e.g. Powell and Holland 2008), the comparison of the results with those obtained by the multiequilibrium geothermobarometry shows a generally good match of both approaches.

sample	T (°C)	geothermometer of Ravna (2000)	P (kbar)	geobarometer of Kohn and Spear (1990)
PJ 5	585	Grt–Hbl	09.4	Grt–Hbl–Pl
PJ6	634	Grt–Hbl	12.7	Grt–Hbl–Pl
	711	Grt–Hbl	12.9	Grt–Hbl–Pl
PJ9	671	Grt–Hbl	13.6	Grt–Hbl–Pl
	681	Grt–Hbl	12.7	Grt–Hbl–Pl

Tab. 9 Results of conventional thermobarometry

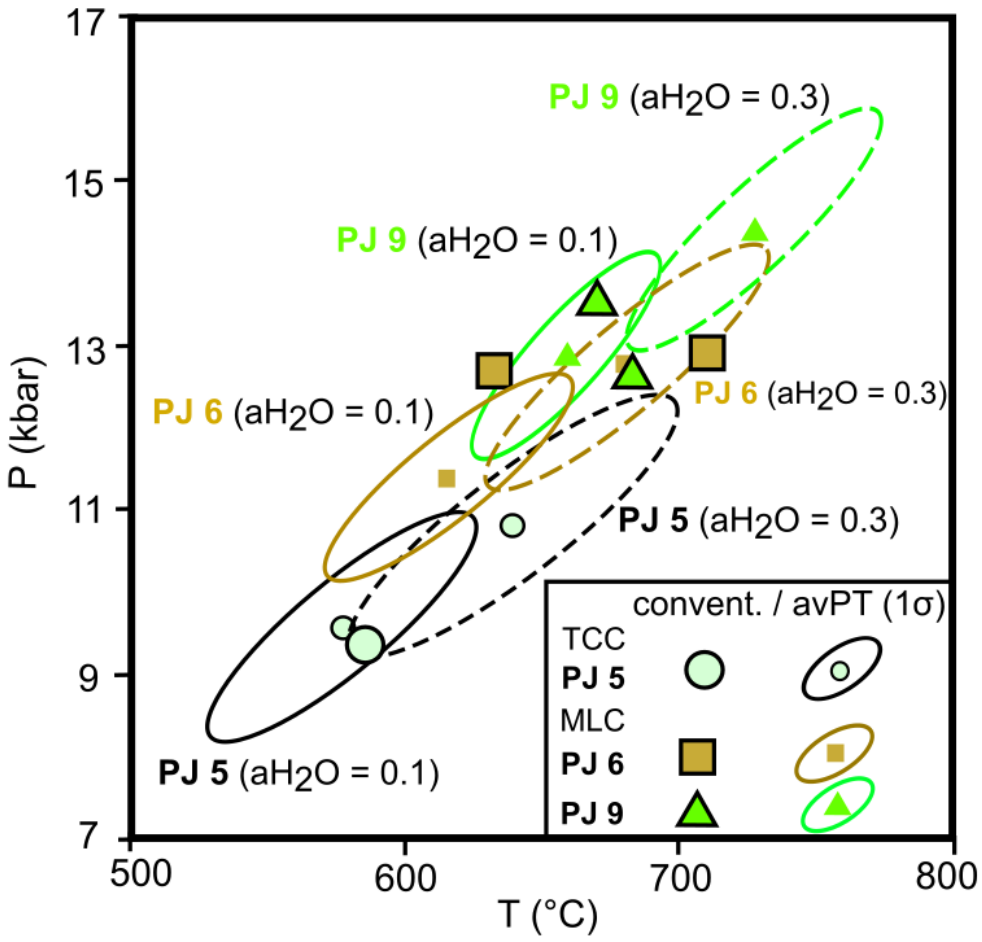

Fig. 31 P–T diagram showing correlation of the results obtained using conventional and multiequilibrium (average P–T calculations) geothermobarometry.

The results of the average P–T calculations are plotted with 1 σ uncertanities and were calculated ussuming aH_2O of 0.1 (solid line ellipse) and 0.3 (dashed ellipse)

Considering the estimated P–T conditions, it is demonstrated that the corona formation-related metamorphism near the boundary between TCC and MLC reached the upper amphibolite-facies conditions. The lowest P–T conditions were estimated for sample PJ 5 from the TCC (Fig. 31). Taking into account the spatial distribution of the selected samples, the calculated P–T conditions imply a rather continuous increase in metamorphic grade towards the structural footwall, i.e. from the east–southeast to the west–northwest.

2.6.2 Recrystallization of M_1 plagioclase

In all samples studied, the decomposition of M_1 labradorite is observed to different degrees (Fig. 32). Based on petrological observation combined with EBSD studies in selected samples, it is possible to characterize 3 stages of plagioclase recrystallization: a) the initial phase of plagioclase breakdown is demonstrated in sample PJ 8; b) the transitional phase is characterized in sample PJ 6; c) the partial recrystallization phase is described in sample PJ 9.

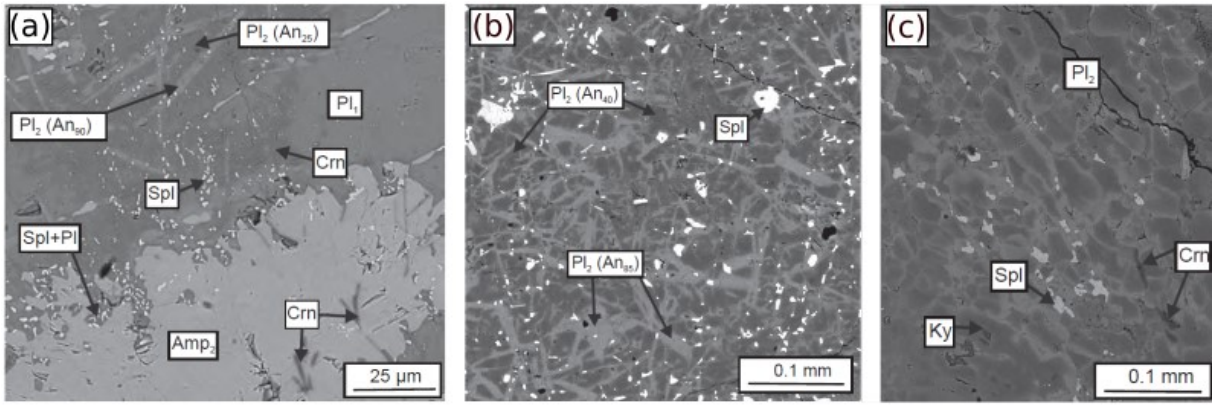

Fig. 32 BSE images of phases of decomposition of M_1 plagioclase

(a) Initial stage where the decomposition of M_1 plagioclase is observed only in some domains documented in sample PJ 8, (b) transitional stage of decomposition, where it occurs in the whole volume of plagioclase represented by sample PJ 6; (c) partial recrystallization of M_1 plagioclase in sample PJ 9.

2.6.2.1 Initial phase – sample PJ 8

In this sample, M_1 labradorite decomposition M_1 occurs in domains located in marginal parts of large grains, where the original grain is replaced by a mixture formed by thin elongated lamellae of anorthite-bytownite ($An_{83–91}$) with apparent random orientation enclosed within oligoclase-andesine ($An_{27–48}$). Additionally, in these domains, corundum lamellae of thickness bellow 1 µm with visible preferred orientation are often observed, as

well as tiny spinel grains forming chain-like texture or isolated grains are present here (Fig. 33).

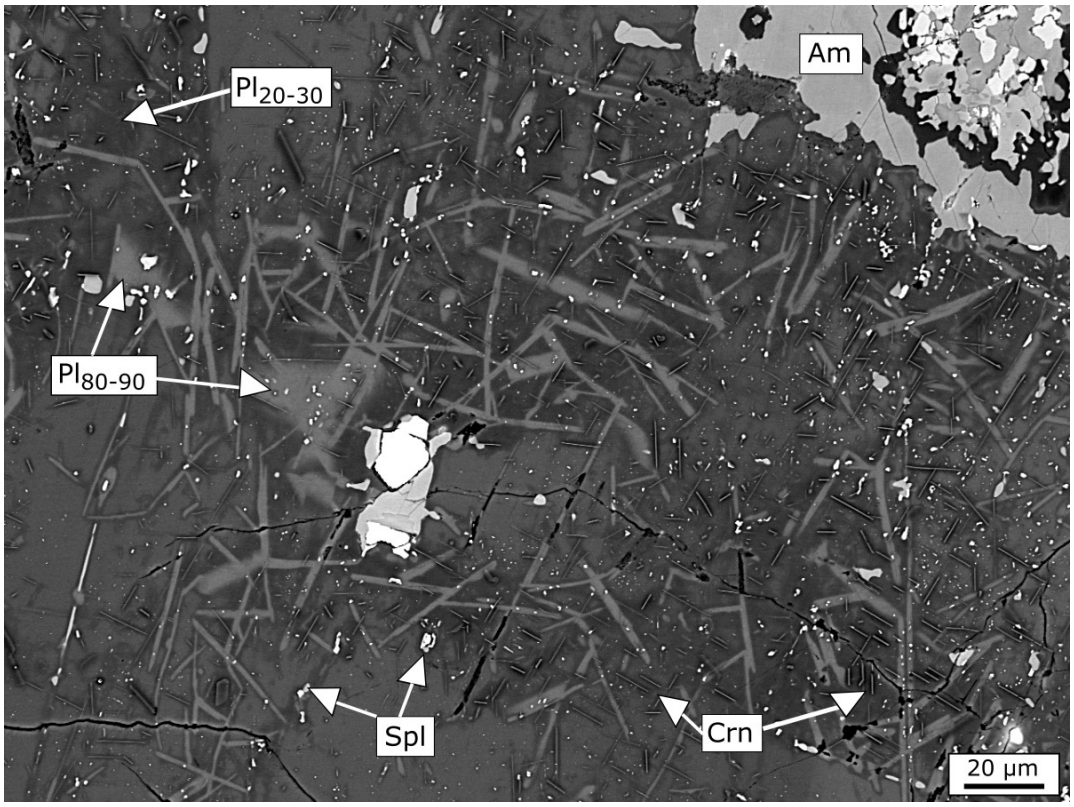

Fig. 33 Detailed BSE image of domain 01 with bytownite-anotrhite lamellae within the plagiclase-andesine matrix accompanied by spinel and corundum grains.

In order to obtain constraints on the processes responsible for such chemically and texturally complex plagioclase decomposition, the previously characterized domains were studied with the electron backscatter diffraction (EBSD) to determine the crystallographic orientation of the observed phases and examine their possible relations. Two representative domains were used for point analyses (c. 250 points for each) and in 4 domains, EBSD map analyzes were acquired. The compositional characteristics of the mineral phases in one domain are demonstrated in the compositional maps in Fig. 4. The results of crystallographic orientation measurements of the present mineral phases are characterized in Fig. 34.

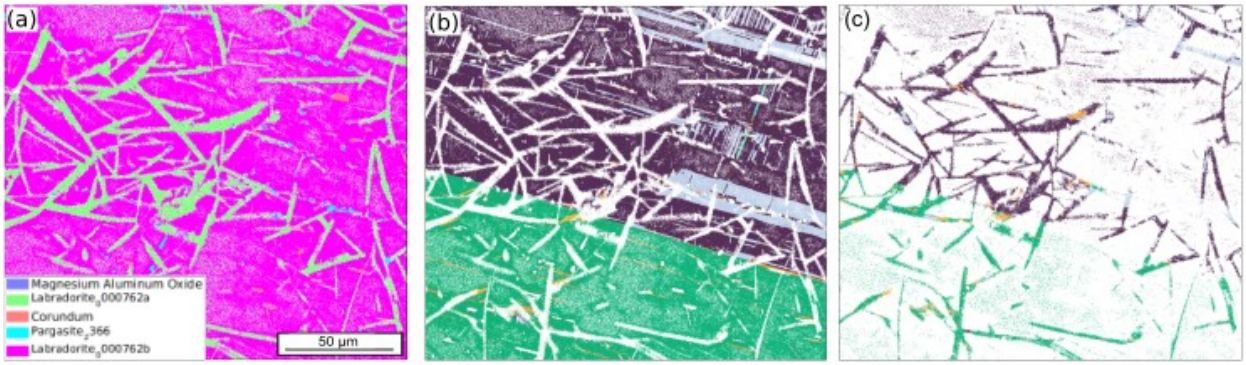

Fig. 34 Results of EBSD map analyses

(a)Orientation of different mineral phases; (b), (c) lamellae of newly formed plagioclase demonstrate relation to the orientation of magmatic twinning.

In order to distinguish orientations of acidic, intermediate, and sodic plagioclase, point analyses were used. According to the obtained measurements, all types of plagioclases show the same crystallographic orientation within one domain. However, in the main plagioclase directions (100; 010; 001), small differences in orientation are visible among single analyses (Fig. 35)

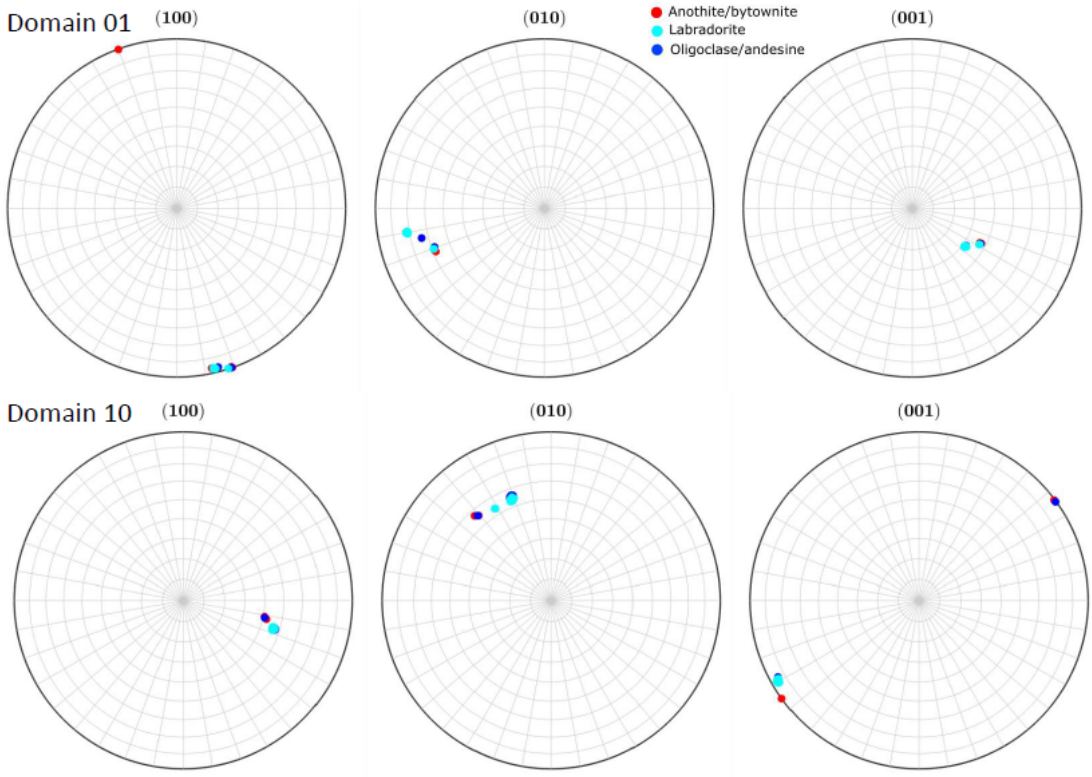

Fig. 35 Crystallographic orientations of plagioclase of different composition

In the studied domains, small spinel grains and corundum lamellas are present within the plagioclase grains. To determine the relationship between spinel and plagioclase and corundum with plagioclase, analyzes from all 6 domains were used. The results show that the spinel has the preferential orientation and, in all domains, it is characterized by the spinel (101) plane, which is parallel to the (001) plain in plagioclase (Fig. 36).

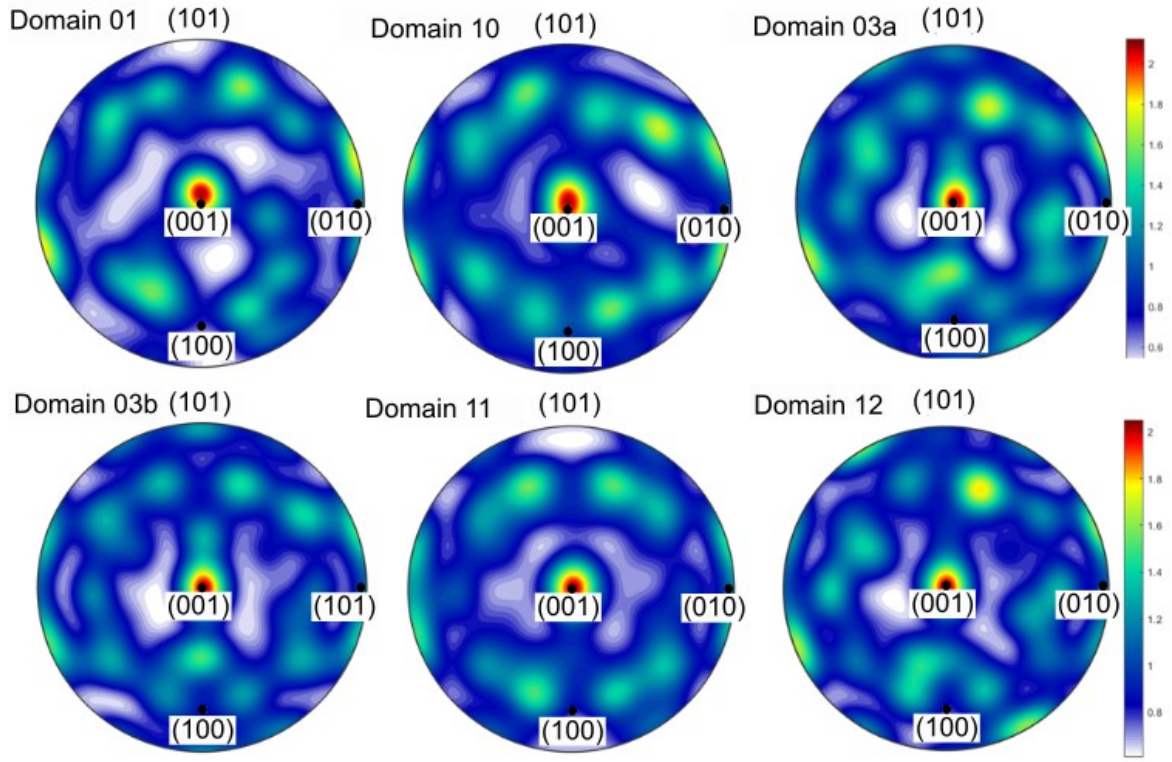

Fig. 36 Crystallographic orientation of spinel demonstrating that (101) plane of spinel is paralell to the (001) plane of plagioclase

In the case of corundum, the crystallographic orientation relation varies in different domains. The corundum plain (01-11) in domain 1 and domain 11 is close to be parallel to the (101) plain in plagioclase, in domain 3a, the corundum plain (01-11) is oriented parallel to the (100) and (-100) planes in plagioclase. In domains 10 and 12, (01-11) plane of corundum appears to be parallel to the (-100) plane in plagioclase, thus this direction occurs to be the most frequent orientation. The second plotted plane of corundum is (10-10) and it shows clear

crystallographic orientation relation in domain 3b, where this plane is parallel to the (001) plane of plagioclase. In other domains (10, 3a, 11 and 12), the corundum plane (10-10) occurs to be parallel to the (-100) plane in plagioclase.

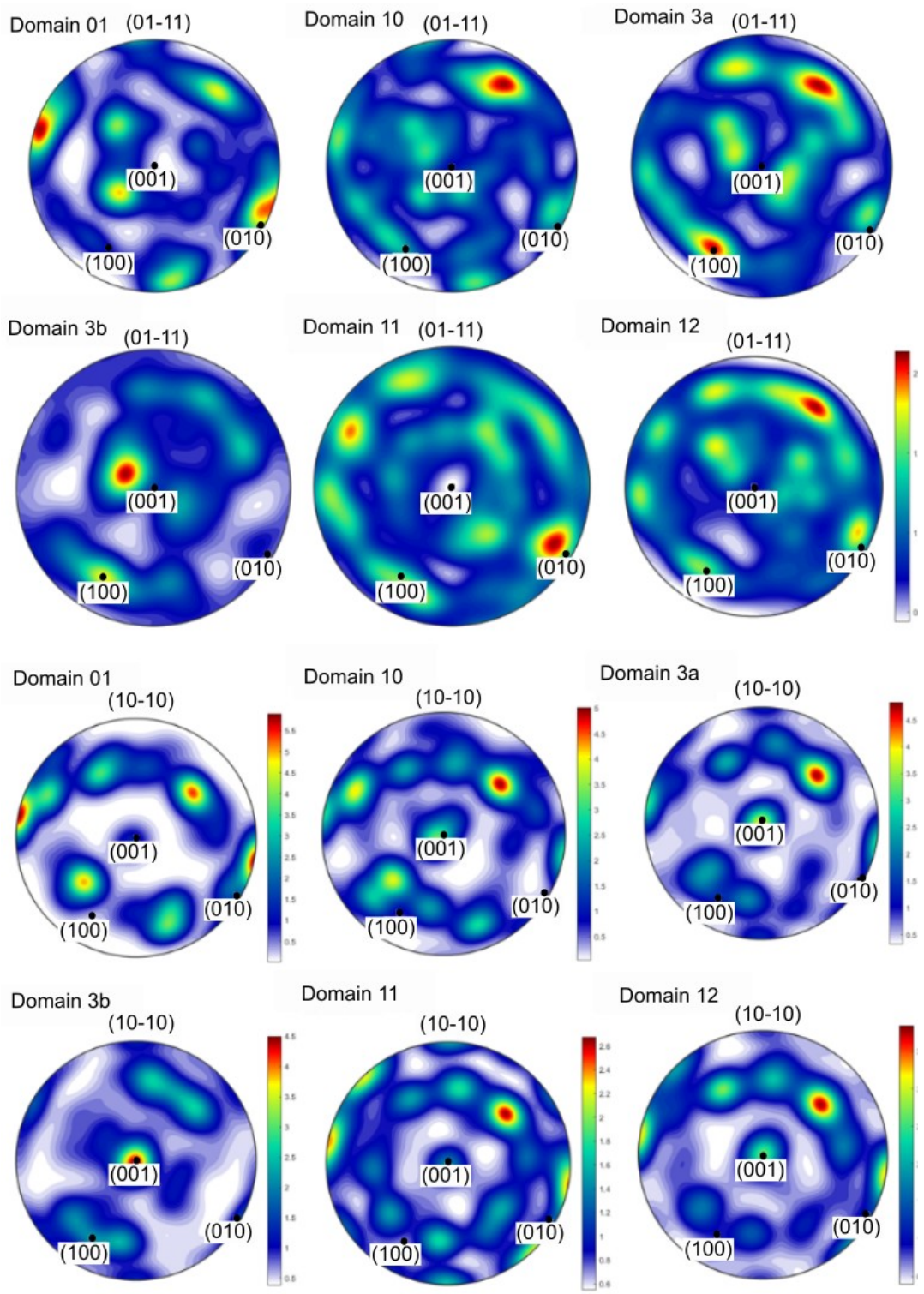

Fig. 37 Crystallographic orientation of selected corundum planes with respect to orientation of plagioclase

2.6.3.2 Transitional phase – sample PJ 6

In sample PJ 6, the decomposition of M_1 labradorite is observed in the whole volume of the sample. EBSD mapping acquired in the selected thin section (Fig. 38) revealed that partial recrystallization can be observed in the form of the appearance of new subgrain boundaries formed in the central parts of the Ca-rich lamellae. In Fig. 38 it is possible to demonstrate that low-angle boundaries begin to form in places where exsolved lamellas are present. With ongoing deformation, the angle of misorientation on the grain boundaries increases until it is transformed to high-angle boundaries of the newly formed independent grains. This points out that the process of recrystallization of M_1 plagioclase started on previously exsolved lamellas.

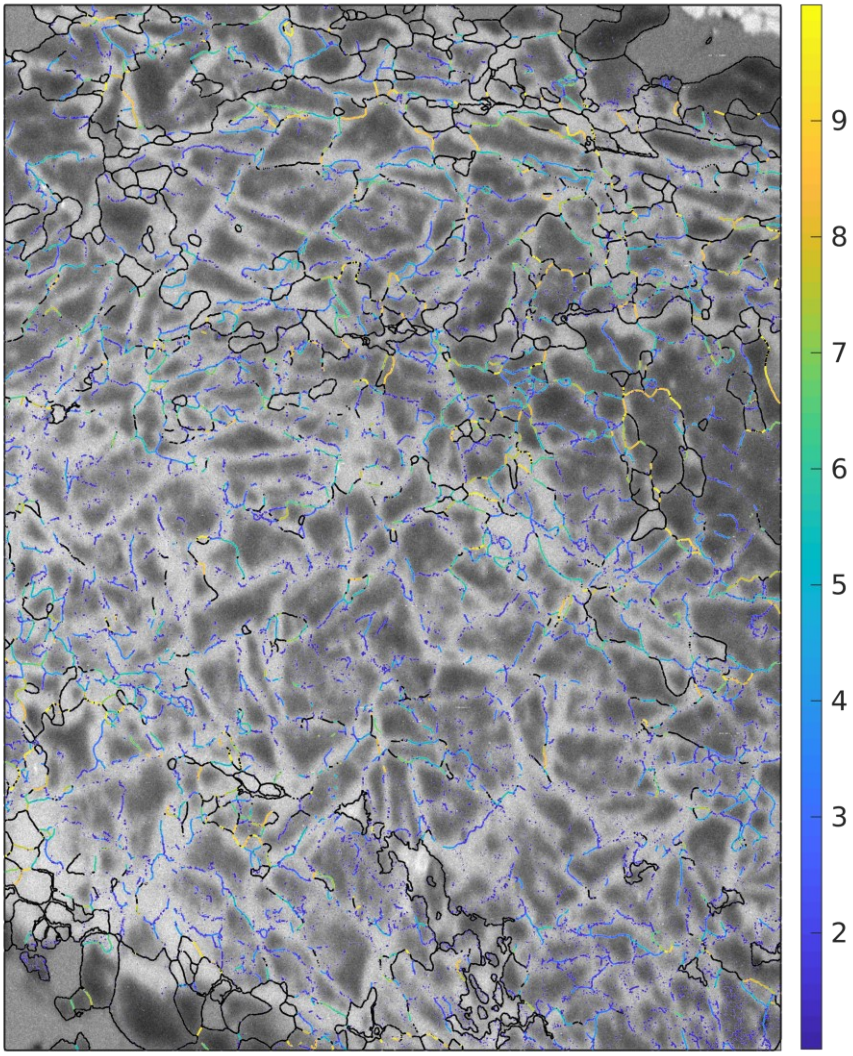

Fig. 38 Misorientation at the grain boundaries in sample PJ 6 representing the transitional stage of plagioclase recrystallization

The grain boundaries of the high-angle misorientation > 10° are marked with black color, the color scale at the right part of the image shows the low-angle (<10°) misorientation boundaries.

2.6.3.3 Partial recrystallization phase – sample PJ 9

In the sample PJ 9 metamorphism reaches higher conditions and the texture of the sample shows evidence of deformation. M_1 labradorite is changed into a fine-grained mixture of recrystallized grains with compositional zoning defined by the increase of the An content from core ($An_{35–46}$) to rim ($An_{79–94}$). The results of the EBSD mapping of the representative area (Fig. 39) demonstrate that the newly formed grains preserve the original chemistry of the lamellas, where the central parts of the grains have low Ca content, while the rims are Ca rich.

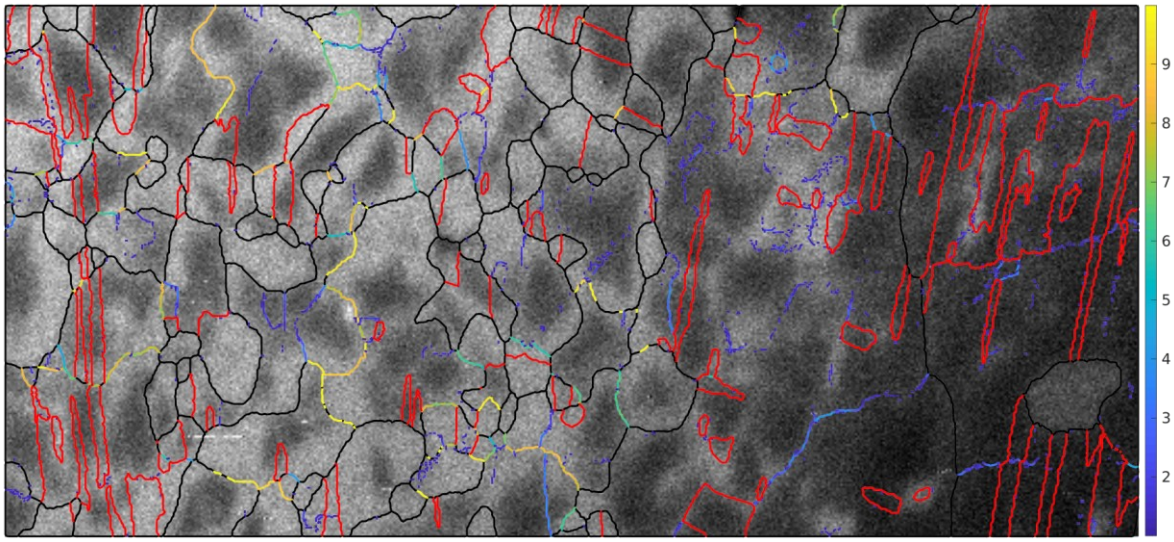

Fig. 39 Misorientation at the grain boundaries in sample PJ 9 demonstrating plagioclase recrystallization.

The red line is used for plagioclase twinning boundaries. Grain boundaries of hight angle misorientation > 10° are marked by black colour, colour scale at the right part of the image demonstrate low angle (<10°) misorientation boundaries

3. DISCUSSION

3.1 Geochronologic evaluation with respect to zircon textural position

Based on the results of U–Pb zircon and titanite dating (Fig. 21–28) combined with detailed petrological study, it was possible to define three major evolutionary stages recorded in the gabbroic rocks from the north-western and south-western corner of the TBU. Each of these events is connected with different textural position of zircon characterized above (Fig. 21a–d).

3.1.1 Cambrian magmatism

Zircon related to Cambrian magmatic event is most frequently observed as large separate crystals. The obtained ages are interpreted to reflect the magmatic stage of the gabbro evolution. The oldest ages c. 535–550 Ma obtained from samples PJ 6 (TCC-MLC), PJ 14 and PJ 22 (both from NKM) correspond to the protolith ages estimated for the MLC eclogites (e.g. Timmermann et al., 2004). It also overlaps with the ages of detrital zircons ocoming from the surrounding metasedimentary units of the Blovice accretionary complex (c. 545–526 Ma; Žák et al., 2020), which form the dominant part of the TBU. These data also include zircons from localities adjacent to NKM. Since the texture of zircon crystals described above point out to rejuvenation, it is possible that these zircons may originate from the sedimentary rocks, which were assimilated during the intrusion. Younger ages between ~520 Ma and 522 Ma that were obtained for some of the NKM samples (PJ 14 and PJ 22) are in a good agreement with the previous study by Dörr et al. (2002) who dated several types of plutonic rocks from the NKM

and concluded that zircons from Orlovice gabbro have characteristics typical of high-temperature crystallization and yield U–Pb concordant ages 524 Ma, but it there is a possibility, that these ages were obtained by method with anaccurate results. All the samples across both studied areas exhibit a dominant wide group of concordant ages 495 to 515 Ma (Fig. 10). This age was previously interpreted as the emplacement age (e. g. Bowes and Aftalion, 1991; Timmermann et al., 2004.) of the rocks from the TCC-MLC area. Based on the new data, we also consider this age to represent the intrusion age for the samples from the DCC-NKM. It is important to note, that sample PJ 14 showing wide group of ages from c. 495–527 Ma contain group of zircon grains with high concentration of the U (>100 ppm) in their cores, which probably lead to intensive metamictization followed by resetting the original age. Thus the scattered data may reflect the different stages of continuous metamictization of inherited zircon grains which is terminated by its resetting during following Cambro-Ordovitian (c. 480 Ma).

3.1.2 Cambro-Ordovician event

The group of Cambro-Ordovician zircon ages c. 480 Ma is predominantly connected to zircon forming thin rim around ilmenite which is observed only in samples of Group 3. This age in samples of Group 2 is obtained from a group of zircon grains associated with the ilmenite, but there they do not form the thin rim descried above. Additionally, several separated grains from sample PJ 6 also yield concordant ages between 480–490 Ma. This age corresponds to the data from a few metamictized zircons investigated in study by Žák et al. (2020), where it was interpreted as resetting age. It is also comparable with the age of the regional metamorphism connected to exhumation of metamorphic isograds in TCC, (U–Pb on metamorphic monazites; Peřestý et al., 2016) which is associated with gabbro intrusion. Similar ages in range of 480–470 Ma (U-Pb on zircon, monazite, Rb-Sr on muscovite; Glodný et al., 1998) was also obtained for intrusion of pegmatite located in the TCC-MLC and also in the DCC area.

Our observation in samples from TCC-MLC (Jašarová et al., 2016) as well in samples from DCC-NKM area (Fig. 2b) corroborate with the idea of (Austrheim et al., 2008), that tiny zircon grains forming thin rim around ilmenite mark the original interface of ilmenite, while rutile replace former ilmenite during metamorphism, due to its textural position suggesting it formation before rutile (Fig. 9b, 19a). In the samples investigated in our study zircon rims typically occur at the contact of ilmenite with the silicate matrix that can provide necessary Si, which together with Zr released by diffusion from ilmenite form tiny zircon grains. Since the Zr is commonly characterized as immobile, diffusion of Zr in ilmenite can be enabled by change in temperature. Formation of tiny zircons forming rim around ilmenite is proposed by Charlier et al. (2007) during postcumulus evolution or subsolidus cooling of the magma chamber, based on study fractional crystallization of Fe-Ti deposits in south-western Norway. Newly obtained results of U-Pb zircon dating (this study) systematically yielded ages c. 480 Ma for tiny zircon grains forming a rim around ilmenite, this age is consistent with decrease of temperature which followed after the peak metamorphism in TCC. Additionally, during subsequent (Variscan) amphibolite-facie metamorphism zircon rims remain resistant preserving the original ilmenite boundary, while ilmenite is partly transformed to rutile (samples PJ 9 in Fig. 9b and sample PJ 20 in Fig. 19b; Jašarová et al., 2016) and/or replacing by titanite (sample PJ 5 in Fig. 5b; samples DK 17 in Fig. 17a, c; and PJ 20 in Fig. 19b; Jašarová et al., 2016).

3.1.3 Late-stage Variscan metamorphism

Although all representative samples characterized above preserve magmatic texture, the contact of mafic minerals and adjacent plagioclase is usually marked by the development of corona layers. The formation of corona sequences is considered as a response to re-equilibration during Variscan orogenesis. In previous studies (e.g. Zulauf et al., 1997) the dominant

metamorphism in DCC-NKM are is considered of Cadomian age, thus we bring two arguments for metamorphism of Variscan age documented in our samples. First, two Variscan U–Pb zircon ages of c. 363 Ma (PJ 6) and c. 380 Ma were obtained for samples from the TCC-MLC using U–Pb dating of zircon, both analyses date the newly formed zircon corona developed at the expense of baddeleyite (Fig. 21c, d). Other Variscan ages (c. 370 Ma) were obtained from the samples PJ 5 (TCC-MLC) and DK 17 (DCC-NKM) by U–Pb dating of titanite. Occurrence of titanite is connected to the corona sequences around ilmenite indicating its metamorphic origin. This observation corroborate with the results proposed by Harlov et al. (2006) that the titanite reaction rim around ilmenite is formed due to hydration and oxidation reaction during amphibole- faceies metamorphism or subsequent green schist-facies overprint.

3.2 Geochemical data and its implications for magma source

The petrogenesis of gabbro intrusions in the TBU had been previously associated with asthenosphere upwelling connected to the crust extension preceding opening of the Rheic Ocean, while in the same time. observed ca. 20 My age gap between the TCC-MLC and DCC-NKM intrusives also allowed for connections with the delamination of subducting slab (Zulauf et al., 1997; Dörr et al., 1998, 2002; Žák et al., 2012; Hajná et al., 2017; Peřestý et al., 2017; Ackerman et al., 2019; Collett et al., 2022; Syahputra et al., 2023). In this respect, the newly obtained U–Pb ages in the course of this study significantly reduce the time gap between the TCC-MLC and DCC-NKM intrusive bodies at the expense of the older ages, thus advocating for a better connection to the opening of Rheic Ocean (Linnemann et al., 2007; Nance et al., 2010, 2012). Indeed, determined ages spanning between ~510 and 500 Ma (see above)

correspond well with the age of continental siliciclastic rocks (~515–499 Ma) deposited in the Cambrian Příbram–Jince basin, located further to the east in TBU, interpreted to reflect crustal extension related to later opening of the Rheic Ocean (Syahputra et al., 2022).

The initial magmatic stage expressed by ~507 Ma mafic NKM intrusions has a diverse major and trace element compositions (e.g., Fig. 29 and 30). Using the criteria of having MgO concentrations of ≈ 10 wt% and Ni contents ≈ 100 ppm that can be best representative for possible parental melts, three samples (PJ 12C, 06OH1B, 06OH4B) from the Orlovice area were selected to evaluate magma source with respect to geotectonic setting using Pearce (2008) approach. The Th/Yb vs. Nb/Yb (Fig. 40a) demonstrates that all selected samples as well as assumed parental magma for the NKM (Svobodová, 1999) tend to have composition of N-MORB-like melts rather than volcanic arc in agreement with previous assumptions. Yet, the observed sometimes higher Th/Yb and TiO_2/Yb indicate that even these rocks must already undregone some fractional crystallization processes (Fig. 40). Nevertheless, we conclude that parental melts for the NKM were derived from depleted source and subsequently follow tholeiitic fractionation trend. This leads to formation of a composite intrusive complex with olivine gabbro in the lower part (***Group 1*** rocks) and ferrodiorite (***Group 2***) that represents product of extensive fractionational crystallization in the upper part (Figs. 12 and 13d; see also Vejnar 1986; Svobodová et al., 1999). While the ferrodiorites of Group 2 contain higher contents of LREE and other incompatible elements such as Th expressed by the presence of abundant zircon and apatite (Fig. 29c, d), this cannot be attributed to assimilation of surrounding BAC metasediments having much higher La/Yb ratios at given Zr contents (Fig. 42c). Since also ε_{Nd} value of ferrodiorite overlaps with those obtained for the DCC-NKM gabbroic rocks, the extreme enrichment in Zr (up to ~2700 ppm; Fig. 30b, c) observed in ferrodiorite can be best explained by cumulate character of this rock type (residue after extensive fractional crystallization. This is further corroborated by extensive enrichment in Fe in ferrodiorite (up to

~20 wt. % FeO_t at MgO <5 wt. %, up to ~95 % mol. olivine fayalite; Figs. 41, 42c). Collectively, the extremely high concentration of Zr together with Fe enrichment indicate extensive fractionation of tholeiitic parental magma. This is nicely illustrated in Harker variation diagrams of selected major elements (FeO_t, Al_2O_3, MgO, TiO_2) vs. SiO_2 (Fig. 41c). Here, when the composition of parental magma evaluated by Svobodová (1999) is considered, the evolution of ***Group 1*** gabbroic rocks can be ascribed to combined effect of pyroxene ± olivine fractionation and plagioclase accumulation while olivine accumulation is expressed by predominance of either forsterite (***Group 1***) or fayalite (***Group 2***) composition. Overall, the observed composition points to generally reducing crystallization conditions which delay or prevent saturation of ferric iron-bearing phases (e.g. Osborn 1959; Vermeesch and Pease 2021). In turn, low oxygen fugacity (also calculated by Svobodová, 1999) supports MORB-like type source of the initial NKM intrusion(s) with limited role of crustal contamination during the magma evolution.

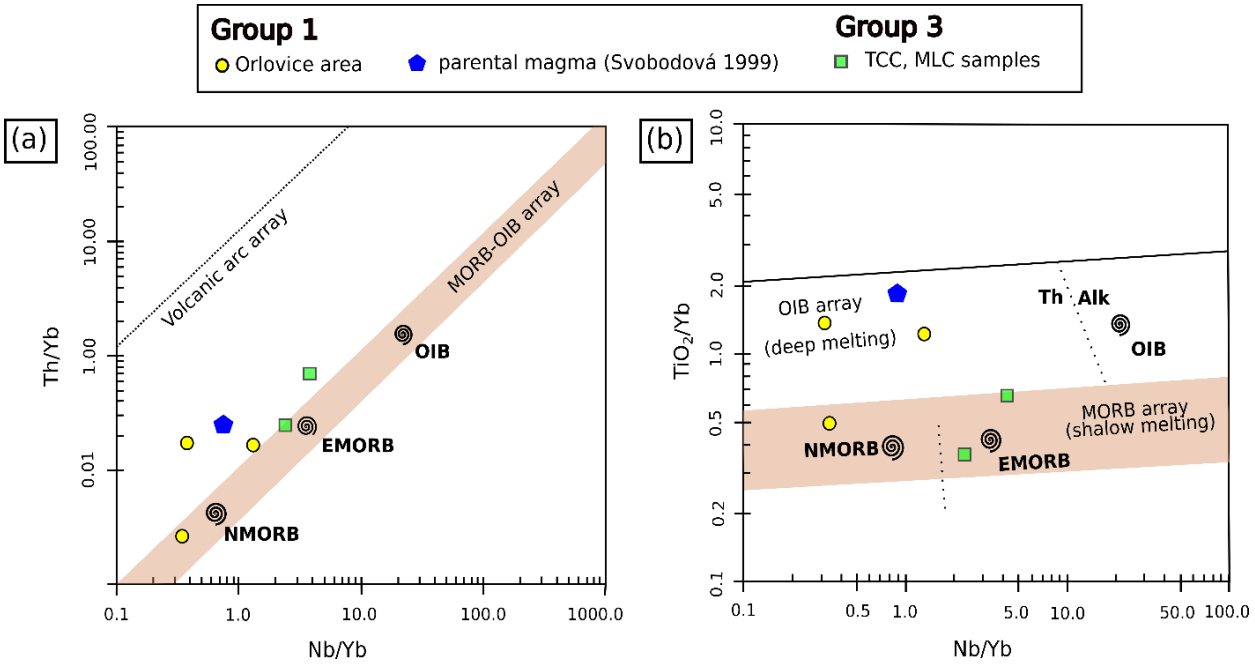

Fig. 40 Diagrams showing the geotectonic implications of seleced samples.

(a) Binary diagram Nb/Yb vs. Th/Yb (Pearce 2008, 2014). The 'MORB-OIB array' is formed by average N-MORB, E-MORB and OIB compositions taken from Sun and McDonough (1989). The Th/Nb proxy is used to distinguish suprasubduction zone from mid-ocean ridge basalts; (b) The Nb/Yb vs. TiO2/Yb

diagram to discriminate between the deep and shallow melting leading to formation of N-MORB, E-MORB and OIB (Pearce 2008, 2014)

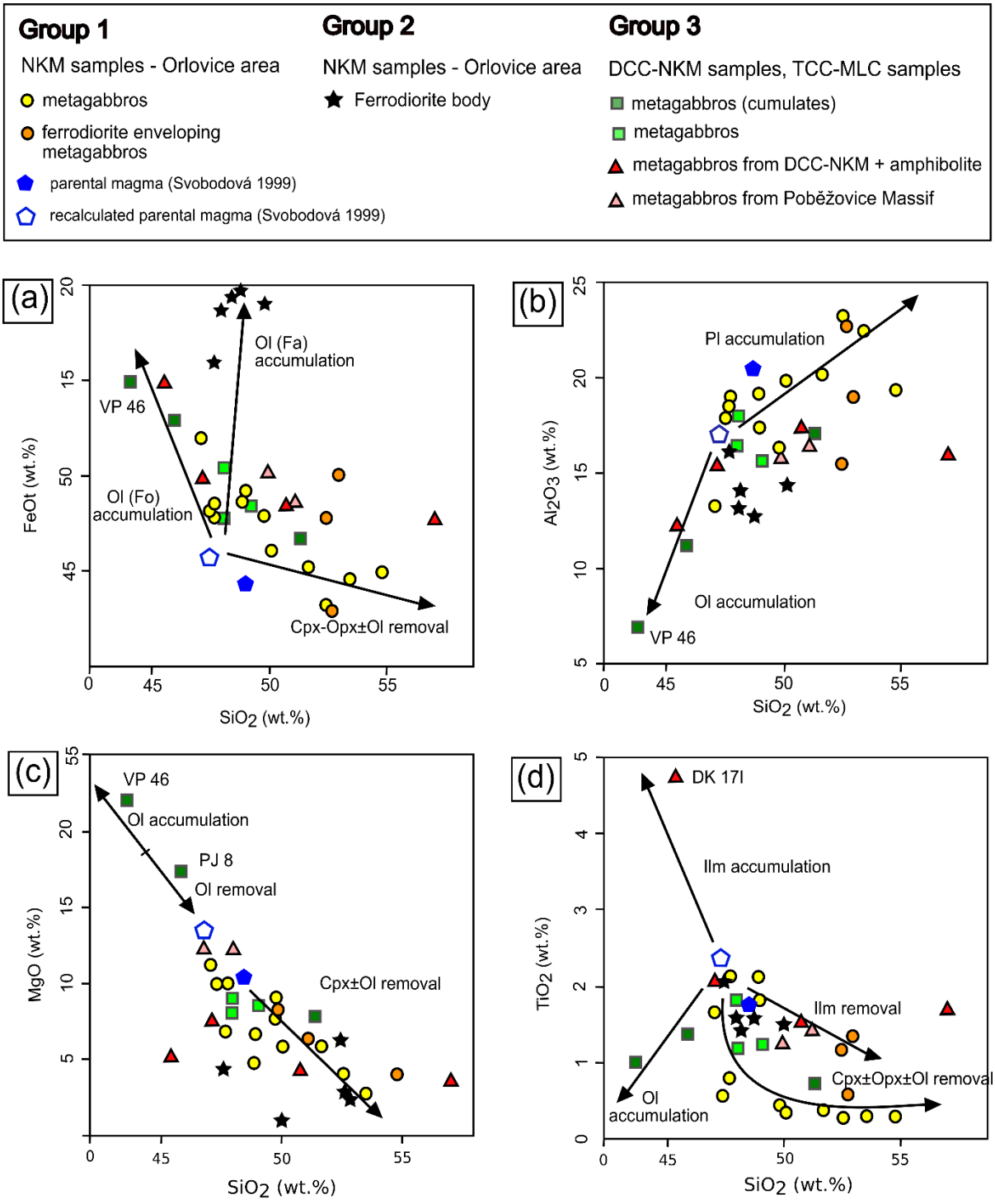

Fig. 41 Harker variation diagrams

(a) Harker variantion diagrams FeO_t vs. SiO_2 showing two trend of olivine accumulation accompanied by clinopyroxene+orthopyroxene ± olivine remuval; (b) Harker variantion diagrams Al_2O_3 vs. SiO_2 demontrating plagioclase and olivine accumulation ; (c) Harker variantion diagrams MgO vs. SiO_2

characterizing olivine accumulation and plagioclase fractionation; (d) Harker variantion diagrams TiO_2 vs. SiO_2 demonstrating ilmenite and olivine accumulation accompanied by ilmenite, clinopyroxene, orthopyroxene and olivine remuval

By contrast, subsequent mafic intrusions of ***Group 3*** gabbros dispersed both in both NKM and TCC-MLC (~502 Ma) area correspond to more evolved composition. Indeed, two samples (PJ 5 and PJ 9 from TCC-MLC) that might be best representative for parental melts have composition of E-MORB in Th/Yb vs. Nb/Yb or TiO_2/Yb vs. Nb/Yb diagrams (Fig. 40). This suggests either enriched mantle source or different evolutionary trajectory of parental melts. Several lines of evidence argue for extensive fractional crystallization of the parental melts. In the Figure 11d, the ***Group 3*** metagabbros exhibit wide range of major element contents (e.g., Al_2O_3, SiO_2, MgO) related to coupled plagioclase and olivine fractionation with those rocks with obvious cumulate texture (PJ 8, VP 46) following the trend of olivine accumulation. Similarly, the importance of ilmenite in the crystallization assemblage is demonstrated in the TiO_2 vs. SiO_2 (Fig. 41f) diagram showing predominance of ilmenite removal with one sample (DK 17I) having very high TiO_2 (4.7 wt. %) in agreement with its high ilmenite contents. At the same time, incorporation of crustal material to parental melts is evidenced by at least two signatures. First, the Group 3 samples collectively exhibit wide range of La/Yb ratios (2.7–7.4) paralleled by variable ε_{Nd} values down to ~ +2 determined for the Poběžovice Massif (Fig. 30; Fig. 42a). Second, we argued above that ***Group 3*** gabbros clearly show evidence for inherited U–Pb zircon ages that can be best related to surrounding BAC sedimentary successions.

The variable effect of combined fractional crystallization and crustal assimilation can be visualized using La/Yb vs. Zr diagram (Fig. 42b). Here, while the fractionation trend is characteristic for the ***Group 1*** and ***2*** samples accompanied by one sample from the Poběžovice Massif (PJ 21) and amphibolite from DCC-NKM area (DK-L), the composition of the majority of ***Group 3*** sampled can be explained by enhanced assimilation of adjacent metasediments of

the BAC. Similar evolutionary trends can be also seen in terms of the major element composition (Fig 42c), where the composition of other plutonic rocks from the studied areas is plotted for comparison. Apparently, the samples across the studied groups follow the tholeiitic to calc-alkaline differentiation trends. The most primitive members are represented by the diorites from the DCC-NKM area (Svobodová, 1999) whereas the samples within this study correspond to the middle section of the tholeiitic trend and the endmembers are represented by the metagranitic plutons of TCC accompanied by Mračice trondjemite located adjacent to the Poběžovice Massif (Fig. 2b).

To conclude, the assimilation of surrounding BAC sediments can account for enrichment of LREE (Figs. 29e, f and 42a) and consequently E-MORB character of the ***Group 3*** gabbros, as well as for their older zircon ages likely inherited from the BAC sediments (Fig. 29a-d). The assimilation and likely congruent melting of the BAC sediments in contact with hot mafic magmas may also explain the calc-alkaline fractionation trend (Fig. 42c) documented by widespread Cambrian calc-alkaline intrusive bodies of similar age (520-510) such as trondhjemite, tonalite, granodiorite and granite in both regions (Vejnar 1986; Zulauf et al., 1997; Dörr et al., 1998, 2002). In this case, the assimilated BAC material may promote calc-alkaline evolution of melt by increasing its alkali budget either directly or by inducing more oxidizing environment leading to earlier saturation and fractionation of Fe^{3+}-bearing phases and, in turn, to relative alkali enrichment of residual liquid. Although the clear distinction between fractionation and melting of surrounding sediments is problematic due to the fact that calc-alkaline intrusive rocks can be also produced by melting of the fore-arc sediments (e.g. Janoušek et al., 2023), we expect that both processes may equally contribute.

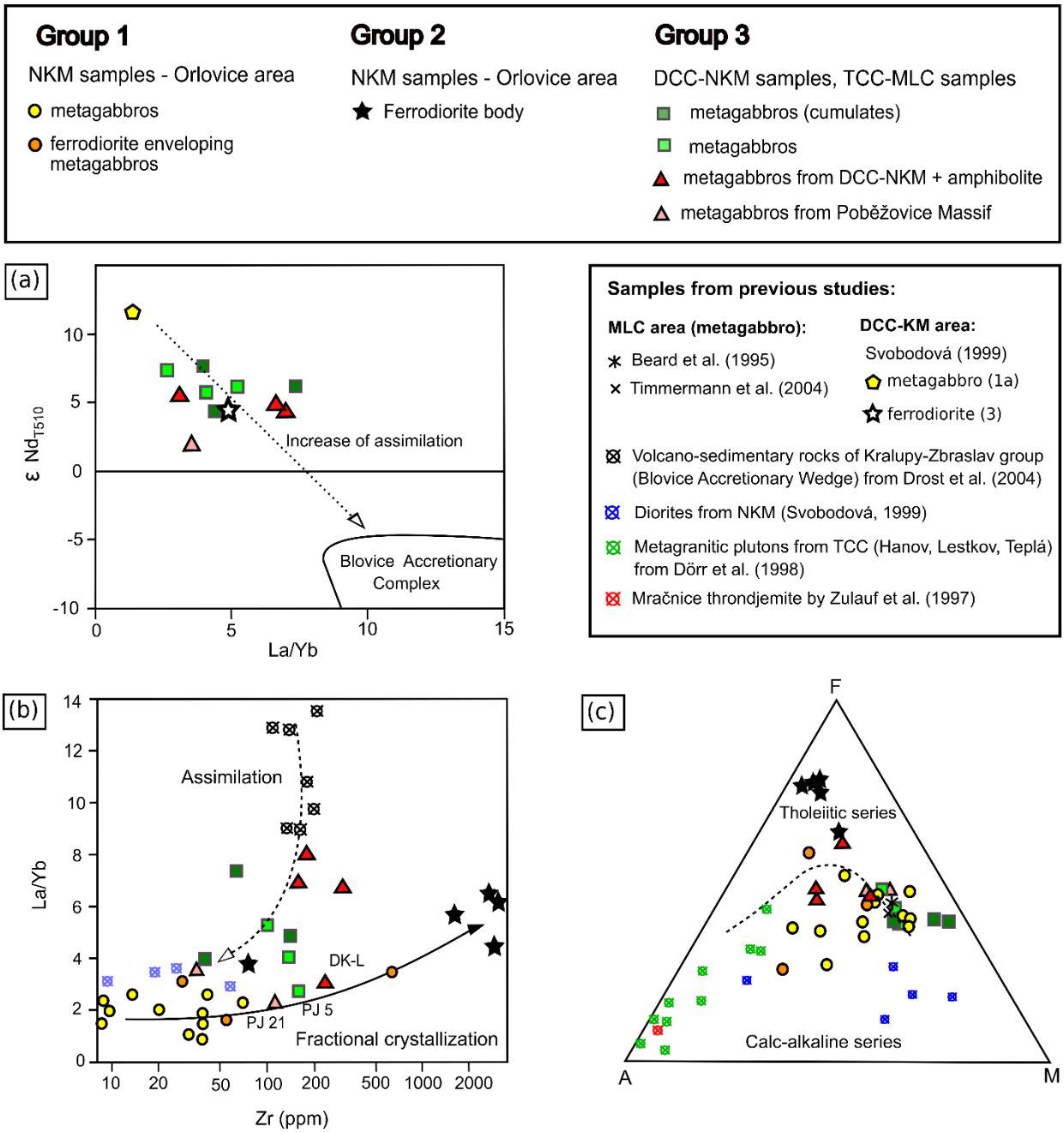

Fig. 42 Diagrams demonstrating composition of studied samples and influence of assimilation of surrounding metasedimentary rocks.

(a) diagram showing the relationship between composition of studied samples and adjacent sedimentary rock of Blovice Acretionarry Complex; (b) diagram characterizing two trends in metagabbro differenciation; (c) AFM diagram showing tholeiitic to calc-alkaline character of the studied samples. Samples from previous studies are plotted for comparison (Beard et al., 1995; Zulauf et al., 1997; Dörr et al., 1998; Svobodová, 1999; Timmermann et al., 2004, Drost et al., 2004; Drost et al., 2007).

3.3 Interpretation of re-equilibration processes

3.3.1 Implications for corona formation

Detailed petrographic study of coronitic sequences in studied samples from TCC-MLC area imply, that corona sequences observed in samples PJ 5, PJ 6 and PJ 9 were affected by later re-equilibration processes resulting in amphibolization. In samples PJ 7 and VP 46 the corona sequences have thickness below the 100 μm, which is typicall for diffusion-controlled process of its formation (Joesten, 1977). Only corona sequences in sample PJ 8 are wider than 100 μm which points out to interface reaction-controlled process (see Joesten, 1977), thus the mineral reaction was calculated for the sample PJ 8.

$$1.94\ \mathrm{Ol} + 0.07\ \mathrm{Pl} = 1.91\ \mathrm{Opx} + 0.02\ \mathrm{Hbl} + \mathrm{Sp}$$

In the case of interface reaction-controlled process there are two options for the corona formation: it was formed during linear growth (with the big jumps of chemical potencial) or non-linear, which is dominantly diffusion controlled (Abart et al., 2001).

The formation of coronitic textures in metagabbros from the MLC and TCC could reflect a prograde metamorphism (e.g. Štědrá et al. 2002; Timmermann et al. 2004), even though some of the phases present in the coronas, i.e. Ti-rich amphibole and orthopyroxene, were interpreted as late magmatic (e.g. Štědrá et al. 2002 and references therein). The gabbro bodies in TCC-MLC area intruded into relatively shallow depths as indicated by the occurrence of hornblende and pyroxene hornfelses in thermal aureoles around some of the gabbro bodies (Kachlík 1997; Štědrá et al. 2002). This contrasts with the relatively higher pressures estimated from coronas in the current study. At the same time, metamorphic P–T conditions calculated for garnet corona in TCC-MLC gabbros (Jašarová et al., 2016, this study) show very good

correlation with the record of Variscan metamorphism in the surrounding rocks. Based on these arguments, it can be concluded that the observed coronas, consisting of the M_2 metamorphic mineral assemblage, were formed by prograde metamorphism superimposed on the significantly older (~510 Ma) magmatic mineral assemblage M_1 during the regional metamorphic event of Variscan age. In studied samples from DCC-NKM area, similar corona sequences as the ones described in TCC-MLC samples are observed. Coronas around olivine in olivine-bearing samples from TCC-MLC cumulates are almost identical as coronas characterized in Orlovice gabbro (sample PJ 12B), in both cases corona sequence formed between olivine and plagioclase contain layer of amphibole followed by amphibole-spinel symplectite at the contact with plagioclase. These corona sequences correspond to coronas (type I and type II) investigated by Gallien et al. (2012), for these corona sequences authors imply a counter clockwise P–T path at gabbro-granulite transition in medium P conditions (5–6.5 kbar) and temperature below 900 °C. On the other hand, complicated corona in sample PJ 12A (Fig. 12b, c) show affinities to experimentally developed coronas by Larikova and Zaraisky (2009), especially the occurrence of gedrite within corona sequence which developed in pressure 5 kbar and temperature of 700 °C. The most significant difference between coronitic sequences from both studied areas is that most of the samples from TCC-MLC (with exception of olivine-bearing samples PJ 8 and VP 46) contain layer of garnet as a terminating layer at the contact with plagioclase. Larikova and Zaraisky (2009) concluded that garnet grown is developed at the expense of plagioclase and its formation requires salty fluid as a catalyst. In the TCC-MLC samples containing garnet layer, primary plagioclase was more, or less dissolved, so this could it release the Na to fluid needed for garnet formation as proposed by Larikova and Zaraisky (2009). Presence of the garnet layer could also reflect different P–T conditions such as higher pressures. Calculated P–T conditions for MLC-TCC samples (T = c. 600–700 °C; P = 10–13.5

kbar) were estimated for garnet layer and its inclusions and it was interpreted to reflect prograde metamorphism.

3.3.2 Decomposition of magmatic plagioclase

The coexistence of sodic (An_{17-32}) and calcic (An_{65-98}) plagioclases in amphibolite derived from metagabbro was described in Voll (1960). There, the texture is characterized as 'bush-like' without any crystallographic correlation with the plagioclase of the host. The plagioclase occurs with cloudy core domains with two plagioclases along with zoisite and inclusions-free margins of oligoclase composition. There the authors conclude that the feldspars were formed during the single exsolution phase. The same feature - elongated grains of sodic and calcic plagioclase with random orientation - was also described in O'Brien and McConnell (1999). In this paper, the authors conclude that the feldspars of these two compositions were formed during different stages of rock evolution and occur together metastable. The strongest evidence for this conclusion is the presence of zoisite or its relicts, so it is assumed that Ca-rich plagioclase represents a breakdown product of the zoisite and Na-rich plagioclase is a product of high-pressure transformation of the original magmatic plagioclase. A similar process is described also in recent studies focusing on the gabbro-to-eclogite transition (e.g., Santini-Rideout et al., 2007; Proyer and Postl, 2010; Schörn and Diener, 2016). In all of the works, the authors imply the replacement of primary plagioclase by zoisite or clinozoisite, with increasing metamorphic condition kyanite and quartz also become present. Despite the similarities in observed textures, it is important to emphasise that in any sample used in this study, no zoisite or its relict was observed during the detailed petrological description. This is the strongest argument to imply the exsolution origin of the plagioclases. Another evidence supporting this idea is due to results of EBSD measurements,

which demonstrate that all plagioclases despite their contrasting chemical compositions and apparent orientation of the lamellas in a single investigated domain show the same crystallographic orientation.

Thus, when we consider exsolution origin for the plagioclase decomposition, some information is outlined about the immiscibility of plagioclase. Smith and Brown (1988) present a study of subsolidus reactions in plagioclases, and they point out that most of plagioclases from slowly cooled rocks consist of coherent intergrowths (Fig. 1). The Boggild intergrowth is observed commonly for bulk compositions An_{43}- An_{58} and the compositions of lamellae vary between An_{39}-An_{48} and An_{53-64}. The Huttenlocher intergrowth is described in calcic plagioclases of bulk composition from An_{67} to An_{90}. In this publication, e-plagioclase is characterized as a fine-scale coherent intergrowth of regions partly related to low albite or anorthite. According to experimental results, the lattice geometry of e_2 plagioclase is typical for composition An_{30}-An_{50} and e_1 plagioclase occurs between Boggild and Huttenlocher intergrowth. The composition of the analysed plagioclases is plotted in Fig. 43, and it corresponds well to the described fields. It is important to note, that country rocks of the studied sample underwent the metamorphism of amphibolite or upper amphibolite facie conditions (e.g. Faryad, 2012; Jašarová et al., 2016; Peřestý et al. 2017), if we take it into consideration, the plagioclases lying within the e_1 and Boggild region would have the C1 symmetry in temperature around 650°C and the group of e_1 plagioclases and plagioclases lying in Huttenlocher intergrowth would have I1 symmetry around 800 °C. During the temperature around 700 °C the original labradorite probably started to exsolve the I1 plagioclase with more basic composition, and with an ongoing temperature decrease it was accompanied by more acid plagioclase of C1 symmetry.

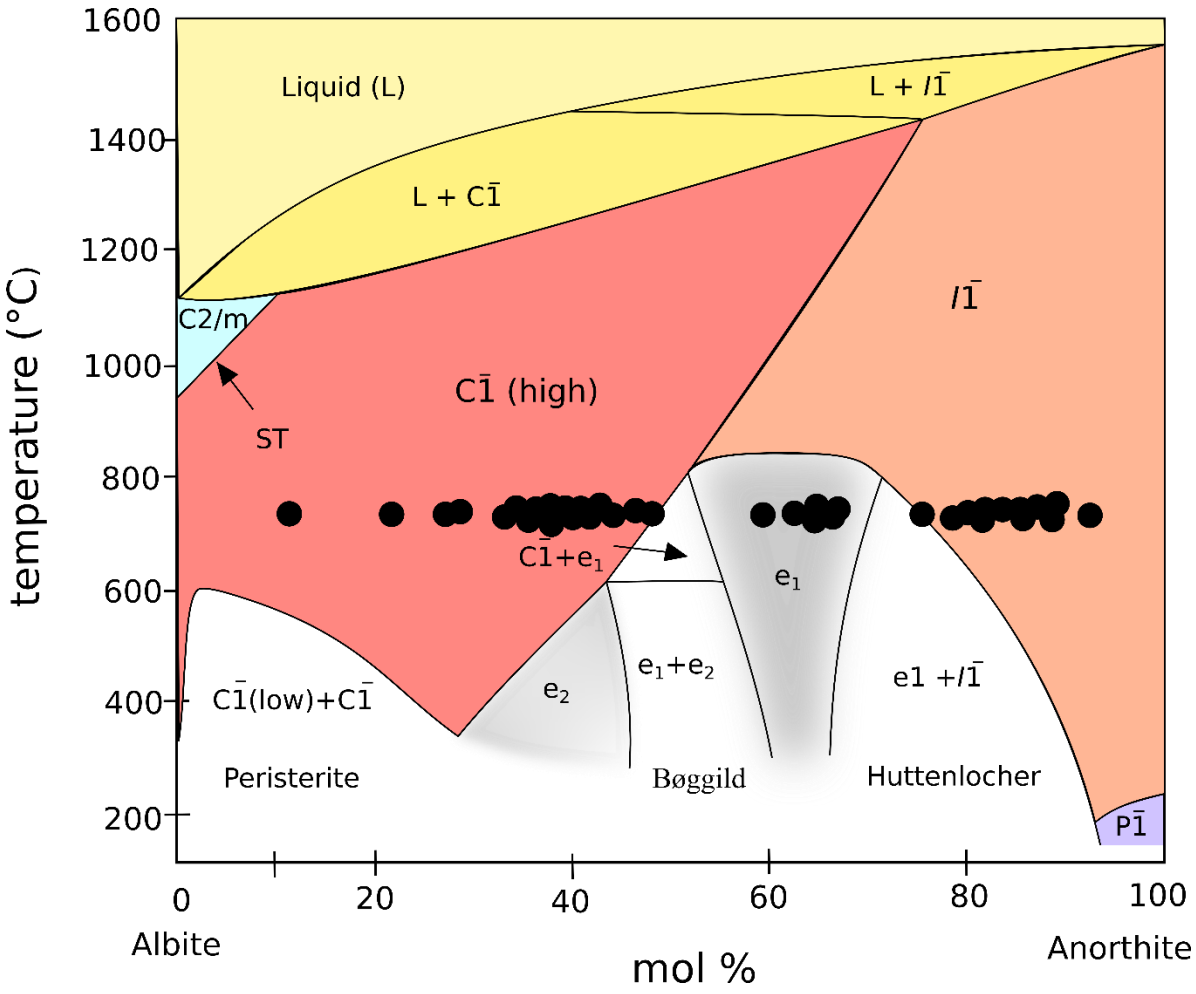

Fig. 43 Diagram of the stability field of plagioclase after Smith and Brown (1988)

The black dots demonstrate the composition of the plagioclase obtained from sample PJ 8 representing the initial stage of the decomposition of the plagioclase.

However, the timing of plagioclase decomposition is rather questionable. In plagioclase, original twinning is still well preserved in the large grains (Fig. 34), but the observed texture and distribution of the domains of plagioclase decomposition may point out that some domains (predominantly the marginal parts) probably remain metastable. With increasing metamorphic conditions, these metastable plagioclase domains were reactivated and started to exsolve acidic and sodic members. Considering all of the data mentioned above, it is question whether the initial destabilization of the M1 plagioclase is related to the Camrbo-Ordivician event

responsible for the formation of tiny zircon grains forming a rim around ilmenite due to temperature increase or the plagioclase break-down started during early stages of Variscan metamorphism. At this state of knowledge, we are not able to decide between these two obtions.

The results of the EBSD analyses of spinel, which occurs in different textural positions, show that (101) plane of spinel is in parallel position to the C axes of the plagioclase, which was obtained from all domains. The crystal lattice orientation of the spinel is restricted and apparently controlled by the crystallographic orientation of the host plagioclase. Corundum observed in all the investigated domains forms tabular-shaped grains with some preferential orientations in BSE images. The measurements of crystallographic orientations in some domains demonstrate that some corundum planes appear to be in parallel position to the main crystal axes of plagioclase (Fig. 37) which corresponds to the microprobe observation that some corundum grains occur in shape preffered orientation. The formation of spinel and corundum is interpreted as a result of variable diffusion rates of Ca and Al from the plagioclase during the corona formation. With ongoing deformation, the M_1 plagioclase started to recrystallize, whereas the recrystallization process was initiated on the exsoluted lamellae.

3.4 New data in context of evolution of western part od TBU

3.4.1 Evolution of the Cambrian magmatism

The crystallization age of gabbro intrusions along the TCC-MLC boundary inferred in this study is consistent with the previously assumed emplacement age of ca. 500 Ma (e.g., Bowes and Aftalion, 1991; Timmermann et al., 2004). On the other hand, in the DCC-NKM, the inferred crystallization of the ferrodiorite showed younger age of ~507 Ma compared to the previously reported metagabbro age of ~524 Ma (Dörr et al., 2002). Recent analysis of detrital

zircons from the DCC metasediments surrounding the NKM complex revealed maximum sedimentation age of ~525 Ma (Žák et al., 2020). Although the overlapping sedimentation/sediment incorporation into the BAC accretionary complex and intrusion of the NKM magmatic rocks had been recently interpreted as transition from subduction to slab delamination (Syahputra et al., 2023), the time span to accommodate all these processes appears to be rather tight.

In the following text, we advocate for a single magmatic event connecting the evolution of Cambrian intrusive rocks from TCC-MLC and DCC-NKM regions both spatially and temporally. First of all, it needs to be pointed out that current location of the TCC-MLC complex does not reflect its original position in the BAC but results from Variscan WNW exhumation of the previously thickened mid to lower crust of TBU along several kilometres wide detachment zone (Peřestý et al., 2020). Kinematic modelling of these authors concluded that the MLC and large portions of the TCC must be restored to greater depths towards the ESE prior to exhumation so that the current TCC-MLC boundary had been located approximately below the Tis granite (see also a correlation of Devonian deep arc magmatism in the MLC and the Čistá pluton in the vicinity of the Tis granite by Collett et al., 2022). Therefore, the TCC-MLC and DCC-NKM intrusives had originally been much closer to each other (Fig. 44) ; aligned in current coordinates along a roughly NNE-SSW striking belt.

Compared to our gabbro and ferrodiorite ages, all of these latter intrusions appear to be older (511±10 Ma Lestkov metagranite, 513±7 Ma Teplá orthogneiss, 516±10 Ma Hanov orthogneiss (Dörr et al., 1998), 505±1 Ma Tis pluton (Venera et al., 2000) in the TCC, 523±5 Ma Mračnice trondhjemite, 522±2 Ma Stod pluton (Zulauf et al., 1997), 524±3 Ma Všepadly granodiorite, 523±3 Ma Smržovice tonalite, 522±2 Ma Těšovice granite (Dörr et al., 2002) in DCC. In this regard, we express strong suspicion that large portion of these older ages is given by the BAC sediments inheritance. Since all the above cited ages come from U-Pb

measurements obtained from dissolved zircons, we cannot provide any further discussion on this topic except that the evolution from mafic to felsic intrusives is common and some intrusive contacts and mafic xenoliths suggesting the younger age of felsic rocks in both regions have been observed (Vejnar 1986).

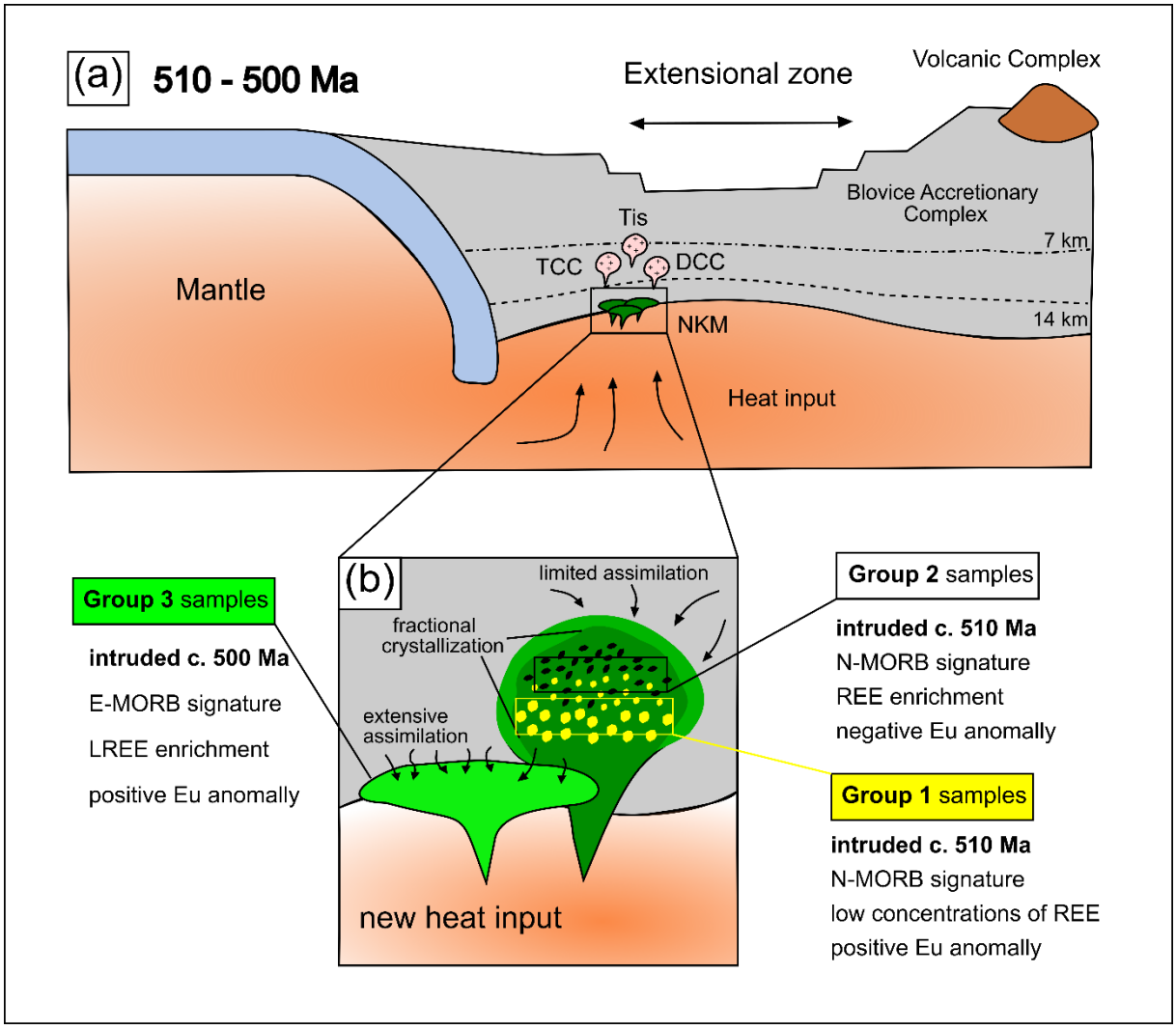

Fig. 44 Diagram summarizing the nature of parental magma of the metagabbros

(a) assumed structural position of mafic and felsic magmas and the depth of the intrusion (b) possible scenario of potions of different magmas with their characteristics

3.4.2 Devonian metamorphism

The equilibration PT conditions from coronas in several samples range between ~600–730 °C and 8–13 kbar (Štědrá, 2001; Faryad, 2012; Jašarová et al., 2016) and follow a metamorphic field gradient that is consistent with Barrovian metamorphic zones, including second generation garnets in the TCC (Žáček and Cháb 1993; Peřestý et al., 2017) and granulite facies metamorphic overprint in the MLC (Timmermann et al., 2004; Collett et al., 2018). In both complexes, this metamorphism was associated with Variscan evolution at ~375 Ma, marked by U-Pb monazite age in the TCC and Sm-Nd garnet age in the MLC (Peřestý et al., 2017; Collett et al., 2018).

It is important to note that also large number of our samples from the NKM show corona structures and replacement of the original magmatic assemblage including replacement of baddeleyite by zircon documented in sample DK 17 (Fig. 3f). Although in this case the zircon grains are unfortunately too small to be dated, the metamorphic reaction textures in our studied samples suggest that also the DCC-NKM had experienced a post Cambro-Ordovician metamorphic overprint likely of Variscan age. Indeed, our U-Pb dating of titanite replacing ilmenite or rutile (Figs. 2a, 3e, f) revealed Variscan age of ~370 Ma in both TCC-MLC metagabbro and NKM metagabbro (Fig. 9). Taking into account the error of ±6 Ma, our titanite ages are consistent with the above mentioned Variscan age of ~375 Ma. A single metamorphic event seems more likely since the replacement of baddeleyite by zircon and of ilmenite by rutile and/or titanite is spatially related to the principal corona structures in the studied metagabbros (Fig. 3g). However, based on textural relationship among ilmenite, rutile, and titanite, we are able to conclude that, during Devonian amphibolite-facie metamorphism, Cambro-Ordovician zircon rims remained resistant preserving the original ilmenite boundary, while ilmenite was partly transformed to rutile and/or replaced by titanite.

3.5 Our data and plate tectonics implications

3.5.1 Late Cambrian TBU magmatism as a result of ridge trench interaction?

The Ediacaran to Ordovician evolution of TBU is constrained by numerous subsequent evolutionary stages:

1) formation of the Davle volcanic complex in the eastern part of TBU between ~610–570 Ma (Santolík et al. 2024),

2) gradual termination of Davle volcanic arc activity followed by the deposition of post-arc laminated tuffs, black shales (Lečice Member) at ~580 and 560 Ma and deep water turbidites and conglomerates (Štěchovice Group; Ackerman et al., 2021; Hajná et al., 2018; Dorr et al. 2002; Drost 2008) and Svrchnice formation basin between ~560–530 Ma (Žák and Sláma, 2018),

3) formation of the Blovice Accretionary Complex in the forearc domain towards the west of arc between ~593–524 Ma with less volumetric accretion before ~547 Ma and accelerated accretion after (Hajná et al., 2017; Žák et al., 2020),

4) intra-arc extension associated with intrusion of juvenile trondhjemite at ~570–500? Ma (Santolík et al., 2024) and boninite dikes between ~544–524 Ma (Vítková and Kachlík, 2001),

5) Barrovian metamorphism affecting BAC sediments along the western edge of TBU prior to calc-alkaline intrusions (Zulauf et al., 1997),

6) siliciclastic sedimentation in the BAC wedge top basins and subaerial volcanism in the central and eastern TBU between ~512–499 Ma, interrupted by marine transgression at ~506–503 Ma (Drost et al., 2004; Hajná et al., 2018; Syahputra et al., 2022),

7) tholeiitic to calc-alkaline intrusions into BAC in the west of TBU between ~510–500 Ma (this study),

8) HT-LP metamorphism in the west of TBU at ~485 Ma (Peřestý et al. 2017) which coincides with

9) the onset of Ordovician marine sedimentation in the Ordovician–Devonian Prague basin in the east of TBU (Chlupáč et al., 1998).

The Ediacaran-Cambrian evolution of the TBU corresponds to that of an active margin associated with subduction of the Mirovoi ocean or its back-arc domain (Hajná et al., 2017; Ackerman et al. 2019; Žák et al., 2020; Collett et al. 2022). Soon after, in Ordovician, the TBU experienced extensional thinning related to opening of the Rheic ocean and its transformation into a passive margin (Peřestý et al., 2017; Hajná et al., 2018). The youngest forearc sediments incorporated into the accretionary prism of BAC suggest termination of subduction at ~524 Ma while the extension related HT-LP metamorphism affecting the western part of TBU and the beginning of sedimentation in the Prague basin are dated to ~485 Ma. Thus, the determined ~510–500 Ma TBU magmatism revealed in this study intruding the BAC forearc sediments fits well between these two events and agree with supposed forearc basin development at ~507–490 Ma (Hajná et al., 2018). Previously, the extensive TBU magmatism with supposed age of ~524–511 Ma (Dörr et al., 2002; Dörr et al., 1998) has been mostly explained in relation to diachronous extension culminated by opening of the Rheic Ocean (e.g. Hajná et al., 2018) assuming rather abrupt transition from subduction to rifting. On the other hand, the recent model of Syahputra et al. (2023) associated the TBU magmatism with rapid heat input following slab break off and suggested that TBU magmatism was a trigger to initiate Rheic rifting. In this respect, the depleted mantle N-MORB-like character of the NKM would be compatible with an

influx of depleted, hot asthenospheric mantle following the slab break off while the E-MORB like signature of subsequent TCC-MLC magmas indicates involvement of more evolved material. The possibility of a ridge/plume/trench interaction has been discussed in several recent studies (Hajná et al., 2017, 2018; Ackerman et al. 2019; Collett et al. 2022), from which Ackerman et al. (2019) proposed a link of such process to the TBU magmatism. Indeed, the ridge involvement may explain most of the above listed events in the TBU as well as the N-MORB character of the studied NKM intrusive rocks and associated calc-alkaline rocks similar to other areas (Maeda and Kagami 1996; Mahar et al., 2019; Tibaldi et al., 2021; Yamasaki et al., 2021).

The arc volcanism and low accretion in the forearc characterize the earlier subduction stage (>560 Ma, Fig. 45a) while the arc extinction and accelerated accretion marks the later stage (>527 Ma). This evolution is typically associated with slab flattening (e.g. Humphreys et al., 2003; Rosenbaum et al., 2005; Esprut et al., 2008; Bishop et al., 2017) which on the other hand can be induced by a positive buoyancy of young subducting slabs (Cloos 1993). The accelerated accretion in the frontal part of the prism is coeval with extension in its rear part where intra-arc and possibly back-arc basins formed and terminated by intrusions of boninite (Fig. 45b). Such situation may be explained by subduction steepening/roll-back (e.g. Scire et al. 2016) imposing a negative buoyancy in the arc domain while the younger positively buoyant part of the slab maintains a tight contact with the accretionary prism in its frontal part (Fig. 45b). In this geometry, the boninites would reflect shallow melting of the steeply dipping slab perhaps induced by the roll-back related influx of hot asthenosphere in the back-arc domain (e.g. Guivel et al. 2003; Rosenbaum et al., 2005). With the ridge approaching the trench, the positively buoyant and warm young subducting slab may have been responsible for thickening and MP-MT metamorphism of the accretionary prism reaching staurolite-kyanite grade in the westernmost part of the TBU (Fig. 45b). The next stage involves ridge subduction accompanied

by shortening in the frontal part of the prism possibly associated with a near trench exhumation of the deeper parts of the prism (Zulauf et al., 1997). Assuming that the ridge is subducted parallel to the trench, the oceanic plate across the ridge may not be dragged into the subduction and a slab window below the accretionary complex will open (e.g. Tibaldi et al. 2021; Shen and Leng 2021; Wu et al., 2022). Such geometry would induce a change from trench to transform boundary similarly to the well-known example of the Farallon trench-Pacific ridge-San Andreas transform evolution. With the continued pull/rollback of the steeply subducting plate, the subsidence migrated westward, from the arc to the forearc domain, where the Příbram-Jince (512-499 Ma) and the Skryje-Týřovice (505-499 Ma) basins formed (Fig. 45c). Meanwhile the initial gabbro bodies intruded closer to the trench followed by assimilation and anatexis of the host metasediments and terminated by andesite to rhyolite subaerial volcanism in the Skryje-Týřovice basin. The question is how much of the magmatic activity was related to the spreading ridge and how much of it was related to opening of the slab window and upflow of hot asthenosphere. The relatively large time span between the end of accretion at ~524 Ma and the initial gabbro intrusions at ~510 Ma together with the lack of extensive regional HT-LP metamorphism in the accretionary complex (e.g. Maeda and Kagami 1996), would advocate for rather slow spreading or extinct ridge with a possibility of back arc spreading as previously proposed by Ackerman et al. (2019) or Collett et al. (2022).

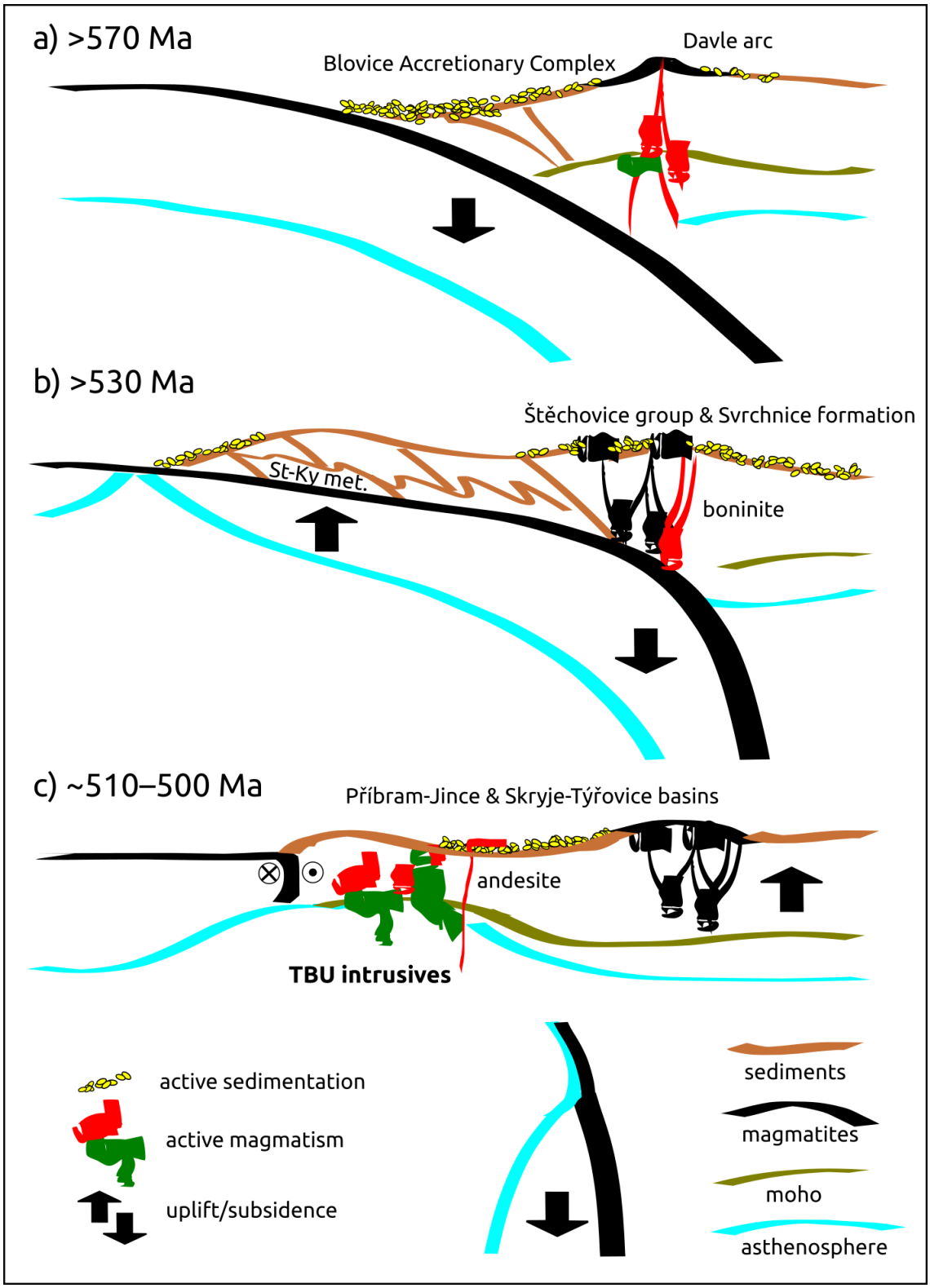

Fig. 45 Geodynamic diagram demonstrating the ridge trench interaction in TBU

(a) Davle arc volcanism and low accretion in the forearc during flat subduction; (b) steeply dipping subduction and metamorphism of the accretionary prism, boninites intrusion reflect shallow melting (c) pull/rollback of the steeply subducting plate and initial gabbro intrusion closer to the trench

4. CONCLUSIONS

- Metagabbroic rocks originate from two different portions of magma.
- The first portion of magma which includes the samples from NKM intruded c. 510 Ma and underwent fractional crystallization and crystal accumulation
- The second portion of magma represented by samples from TCC-MLC and DCC-NKM area intruded c. 500 Ma and it was significantly influenced by assimilation of surrounding metasediments
- Three events are recorded in the samples and ach of these events is related to the different textural position of analysed zircon grains.
- The oldest event is of Cambrian age c. 500 Ma, this age was obtained from isolated metamictized grains and it represents the magmatic stage of the magma evolution.
- The younger Cambo-Ordovician age (c. 480–490 Ma) is connected to tiny zircon grains forming a rim around ilmenite. These rims were formed by diffusion of Zr (released from ilmenite) combined with silica from plagioclase or amphibole.
- The youngest Devonian (c. 360–380 Ma) ages were obtained for zircon corona around baddeleyite titanite grains
- The formation of corona sequences in samples from TCC-MLC area is connected to Variscan metamorphism reaching the amphibolite-facies conditions
- Plagioclase recrystallization connected to Variscan metamorphism started on previously exsoluted lamelae and crystallization of corundum and spinel grains is interpreted due to variable diffusion rates of Al and Ca
- The magmatism in the western part of the TBU is result of ridge trench interaction
- The intrusion of mafic magmas shows affinities to slow spreading or extinct ridge

References

Abart, R., Schmud, R., & Harlov, D. (2001). Metasomatic coronas around hornblendite xenoliths in granulite facies marble, Ivrea zone, N Italy, I: constraints on component mobility. Contributions to Mineralogy and Petrology, 141(4), 473-493.

Ackerman, L., Hajná, J., Žák, J., Erban, V., Sláma, J., Polák, L., Kachlík, V., Strnad, L., Trubač, J. (2019) Architecture and composition of ocean floor subducted beneath northem Gondwana during Neoproterozoic to Cambrian: a palinspastic reconstruction based on Ocean Plate Stratigraphy (OPS). Gondwana Research 76, 77–97

Ackerman, L., Žák, K., Skála, R., Rejšek, J., Křížová, Š., Wimpenny, J., & Magna, T. (2020). Sr-Nd-Pb isotope systematics of Australasian tektites: Implications for the nature and composition of target materials and possible volatile loss of Pb. Geochimica et Cosmochimica Acta, 276, 135–150.

Ackerman, L., Pašava, J., Žák, J., Žák, K., Kachlík, V., Šebek, O., Trubač, J., Svojtka, M., Veselovský, F., Strnad, L., Santolík, V. (2021). Arc-related black shales as sedimentary archives of sea-level fluctuations and plate tectonics during the late Neoproterozoic: An example from the Bohemian Massif. Marine and Petroleum Geology, 123, 104713.

Austrheim, H., Putnis, Ch., V., Engvik, A., K., Putnis, A. (2008) Zircon coronas around Fe-Ti oxides: a physical reference frame for metamorphic and metasomatic reactions. Contrib Mineral Petrol 156: 517–527

Beackman, V., Möller, Ch. (2018) Prograde metamorphic zircon formation in gabbroic rocks: The tale of microtexture. J Metamorph Geol 2018; 36:1221–1236.

Beard, B., L., Medaris, L., G., Johnson, C., M., Jelínek, E., Tonika, J., Riciputi, L., R. (1995) Geochronology and geochemistry of eclogites from the Mariánské Lázně Complex, Czech Republic: Implications for Variscan orogenesis. Geol Rndsch 84. 552–567.

Bingen, B., Austrheim, H., Whitehouse, M. (2001) Ilmenite as a sourse for zirkonium during high-grage metamorphism? Textural evidence from Caledonides of Western Norway and implications for zircon geochronology. J Petrol 42: 355–375.

Bishop, B. T., Beck, S. L., Zandt, G., Wagner, L., Long, M., Antonijevic, S. K., ... & Tavera, H. (2017). Causes and consequences of flat-slab subduction in southern Peru. Geosphere, 13(5), 1392–1407.

Bowes, D., R., Aftalion, M. (1991) U-Pb zircon isotopic evidence for early Ordovician and late Proterozoic units in the Mariánské Lázně komplex, Central European Hercynides. N Jahrb Miner Mh 7:315–326.

Boynton, W., V. (1984) Cosmochemistry of the rare earth elements: meteorites studies. Arizona University (tuscon, USA), Dept of Planetary Sciences and Lunar and Planetary Lab.

Bues, C., Dörr, W., Fiala, J., W., Vejnar, Z., Zulauf, G. (2002) Emplacement depths and radiometric ages of Paleozoic plutons of the Neukirchen-Kdyně massif: differencial uplift and exhumation of Cadomian basement due to Carboniferous orogenic collapse (Bohemian Massif), Tectonophysics 352: 225–243.

Charlier, B., Ska°r, Ø., Korneliussen, A., Duchesne, J-C., Auwera, J., V. (2007) Ilmenite composition in the Tellnes Fe–Ti deposit, SW Norway: fractional crystallization, postcumulus evolution and ilmenite–zircon relation. Contrib Mineral Petrol 154:119–134

Cháb J., Žáček, V. (1994) Metamorphism of the Teplá crystalline komplex. KTB Rep. 94-3:33–37.

Cháb, J., Šrámek, J., Pokorný, L., Chlupáčová, M., Manová, M., Vejnar, Z., Waldhauserová, J., Žáček, V. (1997) The Teplá Barrandian Unit. In: Vrana, S. & Štědrá, V. (eds). Geological Model of Western Bohemia Related to the KTB Borehole in Germany. J. of Geol Sci, CGS Prague 47. 80–104.

Cloos, M. (1993). Lithospheric buoyancy and collisional orogenesis: Subduction of oceanic plateaus, continental margins, island arcs, spreading ridges, and seamounts. Geological Society of America Bulletin, 105(6), 715–737.

Collett, S., Štípská, P., Schulmann, K., Peřestý, V., Soldner, J., Anczkiewicz, R., Lexa, O., Kylander-Clark, A., (2018). Combined Lu-Hf and Sm-Nd geochronology of the Mariánské-Lázně Complex: New constrains on the timing of eclogite-and granulite-facies metamorphism. Lithos 304, 74–94.

Collett, S., Štípská, P., Schulmann, K., Míková, J., (2020). Chronological and geochemical contrains on the pre-variscan tectonic history of the Erzgebirge, saxothuringian Zone. Gondwana Res. 79, 27–48.

Cruciani, G., Franceschelli, M., Groppo, C., Brogioni, N., Vaselli, O., (2008). Formation of clinopyroxene + spinel and amphibole + spinel symplectites in coronitic gabbros from Sierra de San Luis (Argentina): a key to post-magmatic evolution. J Metamorphic Geol 26, 759–774.

Dallmeyer, R., D., Urban, M. (1998) Variscan vs Cadomian tectonothermal aktivity in northwestern sectors of the Teplá-Barrandian zone, Czech Republic: constraints from Ar/ Ar ages. Geol. Rundsch. 87, 94–106.

Deiller, P., Štípská, P., Ulrich, M., Schulmann, K., Collett, S., Peřestý, V., Hacker, B., Kylander-Clark, A., Whitechurch, H., Lexa, O., Pelt, E., Míková, J., (2021). Eclogite subductions wedge intruded by acr-type magma: earliest record of Variscan arc in the Bohemian Massif. Gondwana res. 99, 220–246.

Dörr, W., Fiala, J., Vejnar, Z., Zulauf, G. (1998) U-Pb zirkon ages and structural development of metagranitoids of the Teplá crystalline komplex: evidence for pervasive Cambrian plutonism within the Bohemian massif (Czech Republic). Geol Rndsch 9: 135–149.

Dörr, W., Zulauf, G., Fiala, J., Franke, W., Vejnar, Z. (2002) Neoproterozoic to Early Cambrian history of an active plate margin in the Teplá Barrandian Unit – a correlation of U-Pb isotopis-dilution-TIMS ages (Bohemia, Czech Republic). Tectonophysics 352: 65–85.

Drost, K., Linnemann, U., McNaughton, N., Fatka, O., Kraft, P., Gehmlich, M., Tonk, C., Marek, J., 2004. New data on the Neoproterozoic–Cambrian geotectonic setting of the Teplá–Barrandian volcano-sedimentary successions: geochemistry, U–Pb zircon ages, and provenance (Bohemian Massif, Czech Republic). International Journal of Earth Sciences 93, 742–757.

Drost, K., Romer, R.L., Linnemann, U., Fatka, O., Kraft, P., Marek, J., 2007. Nd-Sr-Pb isotopic signatures of Neoproterozoic - Early Paleozoic siliciclastic rocks in response to changing geotectonic regimes: A case study from the Barrandian area (Bohemian Massif, Czech Republic). In: Linnemann, U., Nance, R.D., Kraft, P., Zulauf, G. (Eds.), The Evolution of the Rheic Ocean: From Avalonian-Cadomian Active Margin to Alleghenian-Variscan Collision. Spec. Pap. Geol. Soc. Am., 423, 191–208.

Drost, K., 2008. Sources and geotectonic setting of Late Neoproterozoic–Early Paleozoic volcano-sedimentary successions of the Teplá–Barrandian unit (Bohemian Massif): evidence from petrographical, geochemical, and isotope analyses. Geologica Saxonica 54, 1–165.

Faryad, S., W. (2012) High-pressure polymetamorphic garnet growth in elogites from the Mariánské Lázně Complex (Bohemian Massif). Eur J Mineral 24: 483–497.

Franke, W., Haak, V., Onken, O., Tanner, D. (2000) Orogenic processes: quantification and modelling in the Variscan belt. In: Franke W, Altherr R., Haak V, Oncken O (eds).

Orogenic Processes: Quantification and Modelling in the Variscan Belt of Central Europe. Geological Society, London, special Publications. 179, 35–61.

Gallien, F., Mogessie, A., Hauzenberger, C., A., Bjerg, E., Delpino, S., Castro de Machuca, B. (2012) On the origin of multi-layer coronas between olivine and plagioclase at the gabbro-granulite transition, Valle Fértil-La Huerta Ranges, San Juan Province, Argentina. J. Metamorphic Geol 30: 281–301.

Gebauer, D. (1993) Geochronologische Übersicht. In: Bauberger, W. (Ed.), Geologische Karte von Bayern 1: 25 000, Erl¨auterungen zum Blatt Nr. 6439 T¨annesberg. Bayer. Geol. L.-Amt, München, pp. 10–22.

Goldsmith, J. R. (1982) Review of the behaviour of plagioclase under metamorphic conditions. Amer Miner 67: 643–652.

Grove, L. T., Ferry, M.J., Spear, F.S (1983) Phase transitions and decomposition relations in calcic plagioclase. Amer Miner 68: 41–59.

Guivel, C., Lagabrielle, Y., Bourgois, J., Martin, H., Arnaud, N., Fourcade, S., ... & Maury, R. C. (2003). Very shallow melting of oceanic crust during spreading ridge subduction: Origin of near-trench Quaternary volcanism at the Chile Triple Junction. Journal of Geophysical Research: Solid Earth, 108(B7).

Hajná, J., Žák, J., Dörr, W., (2017) Time scales and mechanisms of growth of active margins of Gondwana: a model based on detrital zircon ages from the Neoproterozoic to Cambrian Blovice accretionary complex. Bohemian Massiv. Gondwana Res. 42, 63–83.

Hajná, J., Žák, J., Dörr, W., Kachlík, V., Sláma, J. (2018) New contrains for detrital zircon ages on prolonged, multiphase transition from the Cadomian accretionary orogen to a passive margin of Gondwana. Precambrian Research, Vol. 317: 159–178.

Harlov, D., Tropper, P., Seifert, W., Nijland, T., & Förster, H. J. (2006). Formation of Al-rich titanite (CaTiSiO4O–CaAlSiO4OH) reaction rims on ilmenite in metamorphic rocks as a function of fH2O and fO2. Lithos, 88(1-4), 72-84.

Holland, T., Powel, R. (1998) An internaly consistent thermodynamic data set for phases of petrological interest. J. Metamorphic Geol., 145: 309–343.

Hrouda, F., Faryad, s., W., Chlupáčová, M., Jeřábek, P. (2014) Magneticfabric in amphibolized eclogites and serpentinized ultramafites in the Mariánské-Lázně Complex (Bohemian Massif, Czech Republic): Product of exhumation-driven retrogression? Tectonophysics 629: 260–274.

Humphreys, E., Hessler, E., Dueker, K., Farmer, G. L., Erslev, E., & Atwater, T. (2003). How Laramide-age hydration of North American lithosphere by the Farallon slab controlled subsequent activity in the western United States. International Geology Review, 45(7), 575–595.

Irvine, T.N., Baragar, W., R., A. (1971) A guide to a chemical classification of the common igneous rocks. Can J. Earth Sci 8: Pp.

Janoušek, V., Farrow, C. M., Erban, V., (2006). Interpretation of whole-rock geochemical data in igneous geochemistry: introducing Geochemical Data Toolkit (GCDkit). J. Petrol 47, 1255–1259.

Jašarová, P., Racek, M., Jeřábek, P., Holub, F.V. (2016). Metamorphic reactions and textural changes in coronitic metagabbros from the Teplá Crystalline and Mariánské-Lázně complexes, Bohemian Massif. Journal of Geosciences, 61, 193–219.

Jelínek, E., Štědrá, V., Cháb, J. (1997) The Mariánské Lázně Complex. In: Vrana S, Štědrá V (eds). Geological Model of Western Bohemia Related to the KTB Borehole in Germany. J of Geol Sci 47. 61–70.

Joesten, R. (1977). Evolution of mineral assemblage zoning in diffusion metasomatism. Geochimica et Cosmochimica Acta, 41(5), 649-670.

Joesten, R. (1986) The Role of Magmatic Reactions, Diffusion and Annealing in the Evolution of Coronitic Microstructures in Troctolitic Metagabbro from Risor, Norway. Mineral Mag Vol. 50 pp: 441–469, 474–479.

Kachlík, V. (1993) The evidence for late Variscan nappe thrusting of the Mariánské Lázně Complex over the Saxothuringian terrane (W. Bohemia). Journal of the Czech Geological Socienty 38: 46–58.

Kastl, E., Tonika, J. (1984) The Mariánské Lázně metaophiolitic komplex (West Bohemia). Krystalinikum 17. 59–76.

Kempton, P., D., Pearce, J., A., Barry, T., J., Fitton, J., G., Langmuir, C., Christie, D., M. (2002) Sr-Nd-Pb-Hf isotope results from ODP Leg 187: evidence for mantle dynamics of the Australian-Antarctic Discordance and origin of the Indian MORB source. G3: Geochemistry, Geophysics, Geosystems 3, paper number 10.1029/2002GC000320

Kohn, M., J., Spear, F., S. (1990) Two new geobarometers for garnet amphibolites, with applications for southeastern Vermont. Amer Miner Vol 75: 89–96.

Kohn, M.J., 2017. Titanite petrochronology. Reviews in Mineralogy and Geochemistry 83, 419–441.

Kretz, R. (1983) Symbols of rock-forming minerals. American Mineralogist Vol 68: 277–279

Larikova, T., L. (2000) Genesis of Drusitic (Corona) Textures around Olivine and Orthopyroxene during Metamorphism of Gabbroids in Northern Belomorie, Karelia. Petrology Vol. 8, No. 4: 384–401.

Larikova, T., L., Zaraisky, G., P. (2009) Experimental modelling of corona textures. J Metamophic Geol., Vol 27: 139–151

O´Brien, P.J., Duyster, J., Grauert, B., Schreyer, W., Stockhert, B., Weber, K. (1997) Crustal evolution of the KTB site: From oldest relics to the late Hercynian granites. In: The KTB Deep Drill Hole. J of Geophys Research 102 No. B8, AGU Washington 18203–18220.

Osborn, E. F. (1959) Role of oxygen pressure in the crystallization and differentiation of basaltic magma. American Journal of Science 257, 609–647.

Leake, B., E., Woolley, A., R., Arps, C., E., S., Birch, W., D., Gilbert, M., C., Grice, J., D., Hawthorne, F., C., Kato, A., Kisch, H., J., Krivovichev, V., G., Linthout, K., Laird, J., Mandarino, J., A., Maresch, W., V., Nickel, E., H., Rock, N., M., S., Schumacher, J., C., Smith, D., C., Stephenson, N., C., N., Ungaretti, L., Whittaker, E., J., W., Youzhi, G. (1997) Nomenclature of amphiboles: report of the subcommittee on amphiboles of the intrenatinal mineralogical association, commission on new minerals and mineral names. The Can Mineral Vol. 35: 219–246

Maeda, J. I., & Kagami, H. (1996). Interaction of a spreading ridge and an accretionary prism: Implications from MORB magmatism in the Hidaka magmatic zone, Hokkaido, Japan. Geology, 24(1), 31-34.

Matte, P., Maluski, H., Reilich, P., Franke, W. (1990) Terrane boundaries in the Bohemian Massif: results of large scale Variscan shearing. Tectonophysics 177: 151–170.

Morisset, C., E., Scoates, J., S. (2008) Origin of zircon rims around ilmenite in mafic plutonic rocks of Proterozoic anorthosite suites Canadian Mineralogist, 46, 289–304.

Middlemost (1985) Naming materials in the magma/igneous rock system. Earth-Sciences Reviews 37: 215–224.

Pearce, J., A. (1983) Role of the sub-continental lithosphere in magma genesis at active continental margins. In: Hawkesworth, C.J. and Norry, M.J. eds. Continental basalts and mantle xenoliths, Nantwich, Cheshire: Shiva Publications, pp. 230–249.

Peřestý, V. (2012) Polyphase structural evolution of superstructure and infrastructure in orogenic zones. Master thesis, Charles University in Prague (in czech).

Peřestý, V., Lexa, O., Holder, R., Jeřábek, P., Racek, M., Štípská, P., Schulmann, K., Hacker, B. (2017) Metamorphic inheritance of Rheic passive margin evolution and its early Variscan overprint in the Teplá-Barrandian Unit, Bohemian Massif. J Metamorph Geol: 35: 327–355

Peřestý, V., Lexa, O., Jeřábek, P. (2020) Restoration of early-Variscan structures exposed along the Teplá shear zone in the Bohemian Massif: contrains from kinematic modelling. International Journal of Earth Sciences 109:1189–1211

Powel, R., Holland, T. (1994) Optimal geothermometry and geobarometry. Amer Miner, Vol 79:120–133.

Powel, R., Holland, T., Worley, B. (1998) Calculating phase diagrams involving solid solutions via non-linear equations with examples using THERMOCALC. J Metamorph Geol 16: 577–588

Ravna, e., K. (2000) Distrubution of Fe2+ and Mg between coexisting garnet and hornblend in synthetic and natural systems: an empirical calibration for garnet-hornblend Fe-Mg geothermometer. Lithos 53: 267–277.

Rosenbaum, G., Giles, D., Saxon, M., Betts, P. G., Weinberg, R. F., & Duboz, C. (2005). Subduction of the Nazca Ridge and the Inca Plateau: Insights into the formation of ore deposits in Peru. Earth and Planetary Science Letters, 239(1-2), 18–32.

Santolík, V., Ackerman, L., Kachlík, V., Žák, J., Sláma, J., Strnad, L., Trubač, J. (2024). Geochemical fingerprinting of continental crust trapped in Cadomian volcanic arcs along northern Gondwana. Gondwana Research.

Salnikova, E., B., Stepanova, A., V., Azimov, P., Y., Sukhanova, M., A., Kotov, A., B., Egorova, S., V., Plotkina, Y., V., Tolmacheva, E., V., Kervinen, A., V., Rodionov, N., V., StepanovaV., S. (2022) A History of Coronitic Metagabbronorites in the Belomorian Province, Fennoscandian Shield: U-Pb (CA-ID-TIMS) Dating of Zircon–Baddeleyite Aggregates. Petrology, 2022, Vol. 30, No. 6, pp. 567–590.

Scire, A., Zandt, G., Beck, S., Long, M., Wagner, L., Minaya, E., & Tavera, H. (2016). Imaging the transition from flat to normal subduction: Variations in the structure of the Nazca slab and upper mantle under southern Peru and northwestern Bolivia. Geophysical Journal International, 204(1), 457–479.

Schulmann, K., Konopásek, J., Janoušek, V., Lexa, O., Lardeaux, J-M., Edel, J-B., Štípská, P., Ulrich, S. (2009) An Andean type Palaeozoic convergence in the Bohemian Massif. C.R. Geoscience. 341: 266–286

Schulmann, K., Lexa, O., Janoušek, V., Lardeaux, J. M., & Edel, J. B. (2014). Anatomy of a diffuse cryptic suture zone: an example from the Bohemian Massif, European Variscides. Geology, 42(4), 275–278.

Shen, X., & Leng, W. (2021). The mode of trench-parallel subduction of the middle ocean ridge. Frontiers in Earth Science, 9, 781117.

Schorn, S., & Diener, J. F. A. (2017). Details of the gabbro-to-eclogite transition determined from microtextures and calculated chemical potential relationships. Journal of Metamorphic Geology, 35(1), 55–75.

Sláma, J., Košler, J., Pedersen, R., B. (2007) Behaviour of zircon in high-grade metamorphic rocks: evidence from Hf isotopes, trace elements and textural studies. Contrib Mineral Petrol 154: 335–356.

Sláma, J., Košler, J., Condon, D.J., Crowley, J.L., Gerdes, A., Hanchar, J.M., Horstwood, M.S.A., Morris, G.A., Nasdala, L., Norberg, N., Schaltegger, U., Schoene, B., Tubrett, M.N., Whitehouse, M.J., 2008. Plešovice zircon — A new natural reference material for U–Pb and Hf isotopic microanalysis. Chemical Geology 249, 1–35

Spear, F., s., Marcussen, J. (1997) Mineral Zonig, P-T-X-M Phase Relations and Metamorphic evolution of Some Adirondack Granulites, NY, J. Petrol.Vol. 38, No. 6: pp 757–783.

Stacey, J.S., Kramers, J.D., 1975. Approximation of terrestrial lead isotope evolution by a two-stage model. Earth and Planetary Science Letters 26, 207–221.

Štědrá, V. (2001) Tectonometamorphic evolution of the Mariánské Lázně Complex, Western bohemia, based on the study of metabasic rocks. Ph.D. thesis, Charles University, Prague.

Štědrá, V., Krýza, R., Kachlík, V. (2002) Coronitic metagabbros of the Mariánské Lázně Complex and Teplá Crystalline Unit: inferences for the tectonometamorphic evolution of the western margin of the Teplá-Barrandian Unit, Bohemian Massif. In: Winchester, J. A., Pharaoh, T. C. & Verniers, J. (eds). Palaeozoic Amalgamation of Central Europe. Geological Society, London, Special Publications 201, 217–236.

St'Onge, M., R., Ijewliw, O., J. (1996) Mineral Corona Formation During High-P Retrogression of Granulitic rocks, Ungava Orogen, Canada. J Petrol, vol. 37, n. 3, 553–582

Sun, J., Yang, J., Wu, F., Xie, L., Yang, Y., Liu, Z., Li, X., 2012. In situ U-Pb dating of titanite by LA-ICPMS. Chinese Science Bulletin 57, 2506–2516.

Svobodová J. (1999) Vznik a vývoj Kdyňského Masivu, PhD. Thesis

Syahputra, R., Žák, J., Tomek, F., Kachlík, V. (2023) Hot plutonism in a cold accretionary wedge: What determined the Cadomian orogeny along the northern periphery of Gondwana? Precambrian Research 390: 107041

Taylor, S., R., McLennan, S., M. (1985) The continental crust: Its composition and evolution. Oxford, Blackwell: 312pp

Tibaldi, A., Montoya, J. A. G., Vallone, M., Goano, M., Bellotti, E., & Bertazzi, F. (2021). Modeling infrared superlattice photodetectors: From nonequilibrium Green's functions to quantum-corrected drift diffusion. Physical Review Applied, 16(4), 044024.

Timmermann, h., Štědrá, V., Gerdes, A., Noble, S., Parrish, R., R., Dörr, W. (2004) The problem of dating HP metamorphism: an U-Pb isotope and geochemical study on eclogites and related rock sof the Mariánské Lázně Complex, Czech Republic. J. Petrol 45: 1311–1338.

Timmermann, H., Dörr, W., Krenn, E., Finger, F., Zulauf, G. (2005) Conventional and in-situ Geochronology of the Teplá Crystalline Unit. Bohemian Massif: implications for the processes involving monazite formation. Int J Earth Sci 95: 629–648.

Vejnar, Z., Doležal, J., Hazdrová, M., Kříiž, J., Mrňa, F., Pokorný, L., ... & Volšan, V. (1984). Geologie domažlické oblasti. Ústřední ústav geologický.

Vejnar, Z. (1986) The Kdyně Massif, South-West Bohemia -a tectonically modified basic layered intrusion. Sborník Geological Sciences, Geology, 41, 9–67

Vermeesch, P. and Pease, A. (2021) Genetic classification of the tholeiitic and calc-alkaline magma series. Geochemical Perspectives Letters 19, 1–6.

Watson, E., B. & Baxter, E., F. (2007): Diffusion in solid-Earth systems. Earth Planet. Sci. Lett. 253, 307–327.

Whitney, P., R., McLelland, J., M. (1973) Origin of Coronas in Metagabbros of the Adirondack Mts., N. Y. Contrib Mineral Petrol No. 39: pp 81–98.

Wiedenbeck, M., Alle, P., Corfu, F., Griffin, W.L., Meier, M., Oberli, F., von Quadt, A., Roddick, J.C., Spiegel, W., 1995. Three natural zircon standards for U–Th–Pb, Lu–Hf, trace element and REE analyses. Geostandards Newsletter 19, 1–23.

Wood, D., A. (1980) The application of a Th–Hf–Ta diagram to problems of tectonomagmatic classification and to establishing the nature of crustal contamination of basaltic lavas of the British Tertiary volcanic province. Earth and Planetary Science Letters 50, 11–30.

Wu, J., Lin, Y. A., Flament, N., Wu, J. T. J., & Liu, Y. (2022). Northwest Pacific-Izanagi plate tectonics since Cretaceous times from western Pacific mantle structure. Earth and Planetary Science Letters, 583, 117445.

Yamasaki, T., Shimoda, G., Tani, K., Maeda, J., & Nanayama, F. (2021). Subduction of the Izanagi-Pacific Ridge–transform intersection at the northeastern end of the Eurasian plate. Geology, 49(8), 952–957.

Zulauf, G. (1997) Von der Anchizone bis zur Eklogit fazies: Angejippe Krustenprofile als Folge der cadomischen und variscischen Orogenese im Teplá- Barrandium (Böhmische Masse). Geotekt Forsch 89: 1–302 (in german)

Zulauf, G. (2001) Structural style, deformation mechanisms and paleostress along an exposed crustal section: constraints on the rheology of quartzofeldspathic rocks at supra- and

infrasrtuctural levels (Teplá- Barrandian unit, Bohemian Massif). Tectonophysics 332: 211–237.

Žáček, V. (1992) Garnets and metamorphic evolution of the Teplá Crystalline Komplex. Zbl. Geol. Paläontol Teil I 7/8:847–856.

Žáček, V. (1994) Garnets and metamorphic evolution of the Teplá crystalline Komplex, western Bohemia. Zentralbl. Geologie Paläontol 1: 847–856.

Žák, J., Sláma, J. (2018). How far did the Cadomian 'terranes' travel from Gondwana during early Palaeozoic? A critical reappraisal based on detrital zircon geochronology. International Geology Review, 60(3), 319–338.

Žák J., Svojtka M., Hajná J., Ackerman L. (2020) Detrital zircon geochronology and processes in accretionary wedges. Earth-Science Reviews 207, 103214

Appendix

No.	Corrected isotope ratios					Apparent ages (Ma)						U, Th and Pb content (ppm)				disc.
	$^{207}Pb/^{235}U$	±2σ	$^{206}Pb/^{238}U$	±2σ	error corr.	$^{207}Pb/^{235}U$	±2σ	$^{206}Pb/^{238}U$	±2σ	$^{207}Pb/^{206}U$	±2σ	Approx U	Approx Th	Approx Pb	Th/U	%
Zircon PJ6																
1	0.6347	0.0130	0.0797	0.0019	0.7631	499	8	494	12	530	15	1218	960	719	0.8	0.9
2	0.6350	0.0140	0.0802	0.0019	0.5052	499	9	497	11	491	23	682	1035	780	1.5	0.3
3	0.6380	0.0140	0.0802	0.0019	0.6798	501	9	497	11	526	20	762	1212	903	1.6	0.6
4	0.6348	0.0130	0.0801	0.0018	0.6451	499	8	497	11	503	18	801	289	227.4	0.4	0.5
5	0.6402	0.0140	0.0808	0.0019	0.6970	502	8	501	11	521	20	993	1359	1043.6	1.4	0.3
6	0.6530	0.0150	0.0819	0.0019	0.3935	510	9	507	11	533	30	314	239	185.2	0.8	0.5
7	0.7208	0.0160	0.0888	0.0021	0.3761	550	9	549	12	561	24	374	186	171.4	0.5	0.3
8	0.6466	0.0130	0.0812	0.0019	0.7042	506	8	503	11	516	18	1128	758	569.5	0.7	0.6
9	0.6443	0.0150	0.0807	0.0021	0.6427	505	9	500	13	543	31	550	413	315.9	0.8	0.9
10	0.6470	0.0130	0.0817	0.0020	0.6852	506	8	506	12	506	18	1590	1563	1187	1.0	0.1
11	0.6120	0.0140	0.0773	0.0019	0.2011	484	9	480	11	520	26	494	174	122.3	0.4	1.0
12	0.6432	0.0140	0.0810	0.0019	0.6634	504	9	502	11	510	22	990	371	276.3	0.4	0.4
13	0.6186	0.0130	0.0781	0.0019	0.5986	489	8	485	11	514	25	847	476	354.9	0.6	0.9
14	0.6551	0.0150	0.0825	0.0020	0.5371	511	9	511	12	514	28	461	275	207.9	0.6	0.0
15	0.6467	0.0140	0.0814	0.0020	0.7148	507	9	505	12	517	21	557	420	314.5	0.8	0.5
16	0.6158	0.0140	0.0779	0.0018	0.7191	487	9	483	11	489	21	959	1020	726	1.1	0.7
17	0.6150	0.0150	0.0786	0.0019	0.3415	487	10	488	11	496	40	315	222	160.4	0.7	-0.2
18	0.6466	0.0140	0.0813	0.0019	0.5248	506	9	504	11	532	28	551	477	361.3	0.9	0.4
19	0.6427	0.0150	0.0803	0.0019	0.4244	503	9	498	11	510	27	694	542	394.9	0.8	1.1

Tab. I Results of U-Pb zircon dating from separated grains in sample PJ 6

No.	Corrected isotope ratios					Apparent ages (Ma)						U, Th and Pb content (ppm)				disc.
	$^{207}Pb/^{235}U$	±2σ	$^{206}Pb/^{238}U$	±2σ	error corr.	$^{207}Pb/^{235}U$	±2σ	$^{206}Pb/^{238}U$	±2σ	$^{207}Pb/^{206}U$	±2σ	Approx U	Approx Th	Approx Pb	Th/U	%
Zircon PJ6																
20	0.6431	0.0130	0.0814	0.0019	0.6443	504	8	505	11	509	20	1223	1856	1352	1.5	-0.2
21	0.6444	0.0140	0.0804	0.0020	0.5018	505	9	499	12	520	28	668	628	454.3	0.9	1.3
22	0.6346	0.0130	0.0798	0.0019	0.6685	499	8	495	11	516	22	1022	1449	1025	1.4	0.7
23	0.6480	0.0150	0.0812	0.0019	0.4308	507	9	503	11	522	31	384	246	183.1	0.6	0.7
24	0.6530	0.0180	0.0817	0.0021	0.1104	509	11	506	13	515	38	500	213	162.4	0.4	0.6
25	0.6371	0.0140	0.0800	0.0019	0.6427	501	9	496	11	532	20	850	1323	945	1.6	0.9
26	0.6554	0.0150	0.0817	0.0020	0.5730	511	9	507	12	539	24	733	803	599.4	1.1	0.9
27	0.6625	0.0150	0.0826	0.0019	0.5318	516	9	511	12	518	32	530	373	294.8	0.7	0.9
28	0.6487	0.0140	0.0811	0.0020	0.5624	507	9	502	12	547	26	1022	1633	1181	1.6	0.9
29	0.6507	0.0130	0.0818	0.0019	0.6252	509	8	507	12	485	20	1269	1130	875.2	0.9	0.3
30	0.6420	0.0150	0.0801	0.0019	0.3371	504	9	497	12	492	34	355	355	267.7	1.0	1.5
31	0.6395	0.0140	0.0802	0.0018	0.5316	502	9	497	11	515	25	594	680	523.4	1.1	0.9
32	0.6167	0.0140	0.0784	0.0020	0.7007	487	9	487	12	492	24	920	1570	1139	1.7	0.1
33	0.6481	0.0140	0.0817	0.0019	0.0353	506	8	506	11	496	19	1465	1405	1040	1.0	-0.04

Tab. II Results of U-Pb zircon dating from separated grains in sample PJ 6 **(continue)**

No.	Corrected isotope ratios					Apparent ages (Ma)						U, Th and Pb content (ppm)				disc.
	$^{207}Pb/^{235}U$	±2σ	$^{206}Pb/^{238}U$	±2σ	error corr.	$^{207}Pb/^{235}U$	±2σ	$^{206}Pb/^{238}U$	±2σ	$^{207}Pb/^{206}U$	±2σ	Approx U	Approx Th	Approx Pb	Th/U	%
Zircon PJ9																
1	0.5790	0.0061	0.0747	0.0010	0.6451	464	3.9	464	6	465	17	1426	2720	528.7	1.9	-0.2
2	0.6563	0.0083	0.0822	0.0011	0.1401	512	5	509	6.6	529	26	412	403	87.7	1.0	0.6
3	0.6257	0.0079	0.0789	0.0011	0.6637	493	4.9	490	6.7	502	20	763	1107	235.4	1.5	0.7
4	0.6376	0.0097	0.0806	0.0011	0.2996	501	6.1	500	6.6	508	31	276	256	57.1	0.9	0.3
5	0.6420	0.0080	0.0806	0.0011	0.1586	504	5	500	6.6	527	27	330	298	64.85	0.9	0.8
6	0.6571	0.0083	0.0826	0.0012	0.4777	513	5.2	511	7	534	22	457	385	89.4	0.8	0.2
7	0.6560	0.0100	0.0822	0.0011	0.1822	512	6.1	509	6.8	530	29	187	164	41.78	0.9	0.4
8	0.6357	0.0079	0.0806	0.0012	0.6372	499	5	500	6.9	505	22	460	594	148	1.3	-0.1
9	0.6400	0.0082	0.0806	0.0011	0.4516	502	5.1	500	6.7	514	22	466	813	201.5	1.7	0.5
10	0.6510	0.0080	0.0828	0.0011	0.3777	509	5	513	6.7	519	24	296	360	92	1.2	-0.7
11	0.6524	0.0081	0.0818	0.0011	0.3084	510	5	507	6.6	538	23	375	731	183.1	1.9	0.6
12	0.6423	0.0077	0.0811	0.0011	0.6248	503	4.8	502	6.8	509	19	734	278	70.95	0.4	0.2
13	0.6391	0.0078	0.0804	0.0012	0.6696	501	4.8	498	6.9	527	18	691	840	201.2	1.2	0.6
14	0.6444	0.0069	0.0810	0.0011	0.6392	505	4.3	502	6.7	522	17	1156	732	157.8	0.6	0.6
15	0.6530	0.0100	0.0812	0.0012	0.1595	510	6.1	503	7	539	34	194	183	38.76	0.9	1.4
16	0.6433	0.0081	0.0810	0.0011	0.4336	504	5	502	6.7	519	23	502	322	66.04	0.6	0.4
17	0.6278	0.0079	0.0791	0.0011	0.6591	494	5	491	6.9	504	21	784	1068	218.3	1.4	0.7
18	0.6373	0.0086	0.0803	0.0011	0.4545	501	5.3	498	6.7	520	24	512	514	106.8	1.0	0.6
19	0.6455	0.0065	0.0811	0.0011	0.5030	506	4.1	502	6.6	518	17	1854	2240	487	1.2	0.6
20	0.6422	0.0063	0.0812	0.0011	0.6549	504	3.9	503	6.6	510	16	1313	1268	281.6	1.0	0.1
21	0.6274	0.0072	0.0793	0.0011	0.5798	495	4.5	492	6.8	503	20	790	1372	334.1	1.7	0.6
22	0.6329	0.0088	0.0800	0.0011	0.3260	497	5.4	496	6.5	511	27	254	150	36.63	0.6	0.3
23	0.6270	0.0080	0.0787	0.0012	0.5554	494	5	488	6.9	534	23	622	278	67.37	0.4	1.1
24	0.6390	0.0100	0.0804	0.0011	0.1617	503	6.1	498	6.7	524	36	145	125	30.3	0.9	0.8
25	0.6446	0.0066	0.0813	0.0011	0.6582	505	4.1	504	6.7	508	17	1597	1819	430.2	1.1	0.2

Tab. III Results of U-Pb zircon dating from separated grains in sample PJ 9

No.	Corrected isotope ratios					Apparent ages (Ma)						U, Th and Pb content (ppm)				disc.
	$^{207}Pb/^{235}U$	±2σ	$^{206}Pb/^{238}U$	±2σ	error corr.	$^{207}Pb/^{235}U$	±2σ	$^{206}Pb/^{238}U$	±2σ	$^{207}Pb/^{206}U$	±2σ	Approx U	Approx Th	Approx Pb	Th/U	%
Zircon PJ9																
26	0.6462	0.0090	0.0807	0.0011	0.0866	506	5.5	501	6.7	509	24	355	435	93.7	1.2	1.0
27	0.6563	0.0096	0.0820	0.0011	0.1148	512	5.8	508	6.8	527	30	289	171	36.34	0.6	0.9
28	0.6373	0.0083	0.0803	0.0011	0.5211	501	5.2	498	6.8	501	24	536	345	72.11	0.6	0.5
29	0.6568	0.0090	0.0819	0.0011	0.1820	513	5.5	507	6.7	535	29	264	153	32.49	0.6	1.2
30	0.6346	0.0076	0.0802	0.0012	0.6693	499	4.7	497	7	493	20	812	1194	240.9	1.5	0.4
31	0.6470	0.0081	0.0811	0.0011	0.4400	506	5	502	6.7	522	23	441	377	80.87	0.9	0.8
32	0.6490	0.0120	0.0812	0.0011	0.3807	509	6.8	503	6.8	511	33	151	86	26.38	0.6	1.0
33	0.6478	0.0083	0.0813	0.0011	0.2721	507	5	504	6.6	519	25	237	243	73.2	1.0	0.7
34	0.6578	0.0090	0.0822	0.0011	0.1409	513	5.5	509	6.8	516	26	222	145	46.85	0.7	0.7
35	0.6522	0.0085	0.0826	0.0011	0.3569	510	5.1	511	6.8	482	25	261	255	81.4	1.0	-0.4
36	0.6240	0.0076	0.0787	0.0012	0.6071	493	4.7	488	6.9	511	22	507	639	181.5	1.3	0.9
37	0.6421	0.0088	0.0811	0.0012	0.3975	504	5.4	503	7.2	532	25	350	465	112.3	1.3	0.3
38	0.6401	0.0082	0.0807	0.0012	0.5823	502	5	500	7.2	493	22	803	749	128.6	0.9	0.4
39	0.6491	0.0093	0.0812	0.0011	0.2215	508	5.6	503	6.7	507	30	313	205	36.23	0.7	0.8
40	0.6410	0.0085	0.0808	0.0012	0.5718	503	5.2	501	7.3	515	21	692	932	151.1	1.3	0.5
41	0.6459	0.0085	0.0809	0.0011	0.1758	506	5.2	502	6.6	523	26	372	488	85.9	1.3	0.8
42	0.6335	0.0072	0.0800	0.0011	0.6165	498	4.5	496	6.8	508	19	1033	557	96.3	0.5	0.4
43	0.6422	0.0076	0.0813	0.0012	0.3286	504	4.7	504	6.9	495	25	344	357	74.2	1.0	0.0
44	0.6578	0.0086	0.0824	0.0012	0.3210	513	5.3	511	7	518	25	430	417	92.6	1.0	0.4
45	0.6362	0.0080	0.0799	0.0011	0.4644	500	5	495	6.7	511	24	481	503	123.3	1.0	0.8
46	0.6522	0.0088	0.0818	0.0011	0.3993	509	5.4	507	6.8	516	27	334	300	76.3	0.9	0.5
47	0.6359	0.0076	0.0803	0.0012	0.6489	500	4.8	498	6.9	499	18	833	469	114.92	0.6	0.3
48	0.6403	0.0075	0.0808	0.0011	0.3991	503	4.6	501	6.8	505	23	424	303	70.39	0.7	0.4
49	0.6524	0.0087	0.0818	0.0011	0.3820	510	5.3	507	6.8	511	25	315	275	65.4	0.9	0.5

Tab. III Results of U-Pb zircon dating from separated grains in sample PJ 9 **(continue)**

No.	Corrected isotope ratios					Apparent ages (Ma)						U, Th and Pb content (ppm)				disc.
	$^{207}Pb/^{235}U$	±2σ	$^{206}Pb/^{238}U$	±2σ	error corr.	$^{207}Pb/^{235}U$	±2σ	$^{206}Pb/^{238}U$	±2σ	$^{207}Pb/^{206}U$	±2σ	Approx U	Approx Th	Approx Pb	Th/U	%
Zircon PJ9																
1	0.6080	0.0140	0.0770	0.0010	0.3627	483	8.8	478	6	508	49	259	147	121	0.6	1.0
2	0.6150	0.0120	0.0771	0.0016	0.6781	487	7.4	479	9.5	536	41	937	1140	752	1.2	1.6
3	0.6108	0.0093	0.0769	0.0009	0.5751	485	6	478	5.2	542	28	1108	1678	1073	1.5	1.4
4	0.6084	0.0081	0.0773	0.0007	0.4326	482	5.1	480	4.4	479	30	609	723	548	1.2	0.5
5	0.6412	0.0061	0.0810	0.0005	0.3674	503	3.8	502	3.2	522	22	601	543	390	0.9	0.1
6	0.4612	0.0093	0.0608	0.0010	0.4180	385	6.5	381	6.3	466	44	539	14	11.1	0.0	1.1

Tab. IV Results of U-Pb zircon dating from thin-sections in sample PJ 9

No.	Corrected isotope ratios					Apparent ages (Ma)						U, Th and Pb content (ppm)				disc.
	$^{207}Pb/^{235}U$	±2σ	$^{206}Pb/^{238}U$	±2σ	error corr.	$^{207}Pb/^{235}U$	±2σ	$^{206}Pb/^{238}U$	±2σ	$^{207}Pb/^{206}U$	±2σ	Approx U	Approx Th	Approx Pb	Th/U	%
Zircon PJ14																
1	0.6480	0.0150	0.0810	0.0013	0.1906	507	9.3	502	7.8	521	46	249.2	136.2	106.1	0.5	0.9
2	0.6498	0.0130	0.0813	0.0014	0.5955	509	7.8	504	8.1	529	34	1475	621	457	0.4	0.9
3	0.6516	0.0130	0.0826	0.0013	0.4640	509	8.1	512	7.9	513	36	535	118.9	91.1	0.2	-0.5
4	0.6587	0.0130	0.0829	0.0013	0.5493	513	8	513	7.9	519	33	661.1	535.8	414.6	0.8	0.0
5	0.6600	0.0190	0.0818	0.0015	0.3019	513	12	507	8.6	550	57	120.3	19.44	16.81	0.2	1.2
6	0.6640	0.0160	0.0824	0.0014	0.2005	516	9.7	511	8.2	515	49	209	90.7	73.1	0.4	0.9
7	0.6450	0.0150	0.0811	0.0013	0.1207	505	9	502	7.9	518	46	195	67.5	52.8	0.3	0.5
8	0.6553	0.0130	0.0818	0.0015	0.6426	512	8.1	507	8.6	536	33	4127	915	658.1	0.2	0.9
9	0.6481	0.0130	0.0811	0.0015	0.6863	507	8.3	503	8.9	517	33	831	455	356	0.5	0.8
10	0.6538	0.0130	0.0818	0.0014	0.3395	511	7.7	507	8.1	514	32	1322	1082	637	0.8	0.7
11	0.6609	0.0130	0.0833	0.0013	0.3448	515	7.9	516	7.6	510	37	373	149.5	114.5	0.4	-0.1
12	0.6743	0.0140	0.0841	0.0013	0.2755	522	8.5	521	7.7	524	37	535	418	339.9	0.8	0.3
13	0.6760	0.0190	0.0854	0.0015	0.3232	525	11	528	9	514	55	168.9	41.6	35.2	0.2	-0.7
14	0.6554	0.0130	0.0827	0.0014	0.6442	512	7.8	512	8.2	507	33	1062	618	530	0.6	0.1
15	0.6343	0.0120	0.0796	0.0012	0.6052	499	7.2	494	7.3	515	31	2989	651	521	0.2	1.0
16	0.6540	0.0190	0.0819	0.0015	0.0500	509	12	507	9.2	506	64	102.31	18.21	15.44	0.2	0.4
17	0.6770	0.0160	0.0842	0.0014	0.1343	526	9.7	521	8.4	535	44	199.1	68.5	56.5	0.3	1.0
18	0.6692	0.0120	0.0836	0.0013	0.6856	520	7.2	518	7.5	529	29	3927	1302	1042.4	0.3	0.5
19	0.6550	0.0200	0.0812	0.0014	0.1250	511	12	503	8.2	559	59	90.4	17.22	14.51	0.2	1.5
20	0.6530	0.0190	0.0807	0.0014	0.1327	511	12	501	8.5	562	59	112.8	22.04	18.39	0.2	2.0
21	0.6480	0.0160	0.0807	0.0013	0.3191	507	9.9	500	8	534	45	324.1	209.1	158.3	0.6	1.2
22	0.6418	0.0130	0.0806	0.0014	0.5948	503	7.9	500	8.5	531	34	1145	462	349	0.4	0.7
23	0.6719	0.0130	0.0838	0.0014	0.5476	522	7.9	519	8	532	33	710.4	175.5	142.1	0.2	0.4
24	0.6370	0.0150	0.0803	0.0013	0.0207	501	9.1	498	7.9	497	45	217.1	108.5	81.4	0.5	0.5
25	0.6458	0.0120	0.0810	0.0013	0.6047	507	7.6	502	7.8	534	31	1421	959	710	0.7	0.8

Tab. V Results of U-Pb zircon dating from separated grains in sample PJ 14

No.	Corrected isotope ratios					Apparent ages (Ma)						U, Th and Pb content (ppm)				disc.
	$^{207}Pb/^{235}U$	±2σ	$^{206}Pb/^{238}U$	±2σ	error corr.	$^{207}Pb/^{235}U$	±2σ	$^{206}Pb/^{238}U$	±2σ	$^{207}Pb/^{206}U$	±2σ	Approx U	Approx Th	Approx Pb	Th/U	%
Zircon PJ14																
26	0.6587	0.0120	0.0822	0.0013	0.6868	514	7.3	509	7.6	535	30	2560	691	536.9	0.3	0.9
27	0.6779	0.0120	0.0845	0.0013	0.6687	526	7.4	523	7.8	535	29	2568	1379	1130	0.5	0.5
28	0.6540	0.0160	0.0810	0.0014	0.2475	510	9.5	502	8.2	559	46	249.3	75.8	56.8	0.3	1.6
29	0.6510	0.0170	0.0809	0.0014	0.1930	509	10	501	8.4	546	49	124.5	20.4	17.14	0.2	1.5
30	0.6595	0.0130	0.0827	0.0014	0.7452	514	7.9	512	8.2	526	31	883	342	273	0.4	0.5
31	0.6500	0.0160	0.0813	0.0013	0.1543	508	9.8	504	8	531	48	146.3	55.7	43.7	0.4	0.9
32	0.6586	0.0130	0.0821	0.0013	0.3032	514	8.2	508	7.7	541	37	363.9	237.9	188.5	0.7	1.1
33	0.7090	0.0180	0.0876	0.0014	0.1897	544	10	542	8.5	556	48	154.3	55.2	56.9	0.4	0.5
34	0.6655	0.0130	0.0833	0.0014	0.5486	518	7.8	516	8.1	538	33	737	430	349.3	0.6	0.5
35	0.6449	0.0120	0.0806	0.0012	0.4010	505	7.2	500	7.4	537	29	2063	1272	935	0.6	1.1
36	0.6536	0.0140	0.0821	0.0014	0.6722	510	8.4	509	8.4	538	32	751	238	180	0.3	0.3
37	0.6331	0.0110	0.0793	0.0012	0.6359	498	6.9	492	7.2	534	29	4420	2340	1683	0.5	1.2
38	0.6600	0.0130	0.0827	0.0013	0.3287	515	8	512	7.8	530	37	386	224.1	170.2	0.6	0.5
39	0.6570	0.0130	0.0822	0.0013	0.4309	513	8.1	509	7.5	534	34	542.4	360.1	285.9	0.7	0.6
40	0.6562	0.0130	0.0819	0.0013	0.0931	513	8.2	507	8	547	38	516.4	299.1	230.3	0.6	1.1
41	0.6350	0.0180	0.0799	0.0013	0.3835	498	9.1	495	7.8	512	39	292.2	105.8	80.9	0.4	0.6

Tab. V Results of U-Pb zircon dating from separated grains in sample PJ 14 **(continue)**

No.	Corrected isotope ratios					Apparent ages (Ma)						U, Th and Pb content (ppm)				disc.
	$^{207}Pb/^{235}U$	±2s	$^{206}Pb/^{238}U$	±2s	error corr.	$^{207}Pb/^{235}U$	±2s	$^{206}Pb/^{238}U$	±2s	$^{207}Pb/^{206}U$	±2s	Approx U	Approx Th	Approx Pb	Th/U	%
Zircon PJ14 III																
1	0.6270	0.0110	0.0800	0.0023	0.4471	495	7	496	14	486	34	224	64	11.34	0.3	-0.1
2	0.6520	0.0150	0.0824	0.0024	0.4488	509	9.4	511	14	491	45	132	26	4.3	0.2	-0.3
3	0.6160	0.0350	0.0782	0.0025	0.6529	487	17	485	15	514	61	634	199	35.8	0.3	0.4
4	0.6210	0.0088	0.0762	0.0022	0.7065	490	5.5	473	13	531	20	1855	532	116	0.3	3.4
5	0.6010	0.0099	0.0763	0.0022	0.6089	477	6.1	474	13	542	23	883	206	34.1	0.2	0.6
6	0.6546	0.0097	0.0823	0.0023	0.4814	511	6.1	510	14	496	27	257	93	21.52	0.4	0.3
7	0.6140	0.0120	0.0778	0.0023	0.7692	486	7.6	483	14	518	31	221	68	15.45	0.3	0.7
8	0.6110	0.0110	0.0784	0.0023	0.5577	484	6.8	486	14	485	31	222	69	16.68	0.3	-0.4
9	0.6230	0.0120	0.0795	0.0024	0.5141	491	7.9	493	14	468	39	191	58	13.92	0.3	-0.3
10	0.6260	0.0140	0.0766	0.0024	0.5366	494	8.7	475	14	543	40	136	40	10.64	0.3	3.7
11	0.5990	0.0190	0.0773	0.0022	0.4915	476	10	480	13	470	49	235	65	14.66	0.3	-0.8
12	0.6660	0.0190	0.0846	0.0028	0.2307	521	11	523	17	461	46	147	40	11.92	0.3	-0.4
13	0.6330	0.0120	0.0791	0.0022	-0.0041	497	7.2	491	13	514	35	174	50	11.39	0.3	1.3
14	0.6320	0.0110	0.0796	0.0023	0.1146	497	7.1	494	13	481	39	107	26	6.61	0.2	0.6
15	0.6490	0.0180	0.0821	0.0023	0.4003	509	10	509	14	540	40	159	47	10.38	0.3	0.1
16	0.6260	0.0120	0.0793	0.0022	0.3073	494	7.3	492	13	528	38	116	34	7.94	0.3	0.4

Tab. VI Results of U-Pb zircon dating from thin-sections in sample PJ 14

No.	Corrected isotope ratios					Apparent ages (Ma)						U, Th and Pb content (ppm)				disc.
	$^{207}Pb/^{235}U$	±2s	$^{206}Pb/^{238}U$	±2s	error corr.	$^{207}Pb/^{235}U$	±2s	$^{206}Pb/^{238}U$	±2s	$^{207}Pb/^{206}U$	±2s	Approx U	Approx Th	Approx Pb	Th/U	%
Zircon PJ22																
1	0.6433	0.0110	0.0816	0.0007	0.7395	504	7.1	505	4	500	25	623	317	78	0.5	-0.3
2	0.6449	0.0100	0.0815	0.0006	0.6130	505	6.5	505	3.6	518	23	742	506	122.21	0.7	0.0
3	0.6671	0.0120	0.0837	0.0006	0.3371	519	7.1	518	3.3	545	28	403	293	71.54	0.7	0.1
4	0.6631	0.0120	0.0839	0.0005	0.0126	516	7.2	519	3.2	505	30	419	286	72.06	0.7	-0.6
5	0.6790	0.0160	0.0848	0.0009	0.3845	526	9.6	525	5	523	42	177	58	14.59	0.3	0.4
7	0.6760	0.0150	0.0841	0.0006	0.5065	524	8.9	520	3.8	539	36	142	43	10.94	0.3	0.6
8	0.7000	0.0180	0.0868	0.0007	-0.0244	539	11	537	4.2	548	49	75	21	5.87	0.3	0.5

Tab. VII Results of U-Pb zircon dating from separated grains in sample PJ 22

No.	Corrected isotope ratios					Apparent ages (Ma)						U, Th and Pb content (ppm)				disc.
	$^{207}Pb/^{235}U$	±2σ	$^{206}Pb/^{238}U$	±2σ	error corr.	$^{207}Pb/^{235}U$	±2σ	$^{206}Pb/^{238}U$	±2σ	$^{207}Pb/^{206}U$	±2σ	Approx U	Approx Th	Approx Pb	Th/U	%
Zircon DK-L																
1	0.6476	0.0120	0.0810	0.0007	0.7156	507	7.5	502	4.4	531	26	715	206	49.6	0.3	1.0
2	0.6509	0.0120	0.0817	0.0007	0.5928	509	7.1	506	4.4	512	27	494	476	117.9	1.0	0.5
3	0.6450	0.0120	0.0821	0.0008	0.7084	505	7.2	510	4.6	485	26	515	516	127.2	1.0	-1.0

Tab. VIII Results of U-Pb zircon dating from separated grains in sample DK-L

sample	measured			common	corrected isotope ratios								apparent ages (Ma)						aproximate concentration			Th/U
	$^{206}Pb/^{204}Pb$	$^{207}Pb/^{204}Pb$	$^{208}Pb/^{204}Pb$	^{206}Pb (%)	$^{207}Pb/^{235}U$	±2σ	$^{206}Pb/^{238}U$	±2σ	$^{207}Pb/^{206}Pb$	±2σ	6/38 vs 7/35	6/38 vs 7/35	$^{207}Pb/^{235}U$	±2σ	$^{206}Pb/^{238}U$	±2σ	$^{206}Pb/^{238}U$	±2σ	U (ppm)	Th (ppm)	Pb (ppm)	
Titanite PJ5																						
1	5	3.2	10.2	26	17.86	1.40	0.181	0.01	0.718	0.06	-0.047	0.728	2985	75	1076	37	4773	140	1.7	0.3	1.0	0.2
2	5.5	4.4	7.7	32	18.21	1.70	0.196	0.01	0.683	0.06	0.599	0.352	2970	82	1157	61	4683	150	1.6	0.4	0.8	0.2
3	6.2	4.6	10.4	28	19.50	1.70	0.177	0.01	0.810	0.11	0.245	0.886	3053	87	1042	68	3100	190	0.7	0.1	0.4	0.2
4	200	10	50	59	7.87	0.62	0.112	0.00	0.500	0.04	0.516	0.155	2205	72	686	18	4225	100	4.0	1.4	1.0	0.4
5	1	3.5	5.7	12	39.00	3.10	0.341	0.02	0.884	0.07	0.597	0.770	3717	78	1875	71	5156	160	0.6	0.2	0.6	0.4
6	6.8	5.3	12.1	27	39.30	3.10	0.328	0.01	0.871	0.06	0.547	0.524	3745	76	1849	63	5122	150	0.9	0.4	0.9	0.5
7	7.5	5.6	12.5	28	22.74	1.70	0.192	0.01	0.861	0.07	0.208	0.766	3204	73	1129	39	5100	150	1.1	0.6	0.7	0.6
8	13	5.1	22	31	10.47	0.82	0.134	0.00	0.567	0.05	0.546	0.359	2481	75	808	24	4437	120	3.3	3.2	1.1	1.0
9	2.6	3.4	6.4	22	26.10	2.10	0.225	0.01	0.874	0.07	0.272	0.758	3353	78	1307	60	5130	170	0.9	0.5	0.7	0.6
10	5.2	3.4	6.3	32	38.20	2.90	0.327	0.01	0.888	0.07	0.275	0.737	3720	78	1816	68	5150	170	0.6	0.2	0.6	0.3
11	0.4	0.8	1.4	13	51.20	4.20	0.406	0.02	0.938	0.08	0.391	0.792	4004	78	2178	100	5250	190	0.3	0.1	0.5	0.3
12	20.9	10.7	25	36	14.72	1.40	0.161	0.01	0.627	0.05	0.468	-0.196	2710	92	957	39	4542	120	4.2	1.2	1.7	0.3
13	9	8.3	8	39	15.67	1.20	0.173	0.01	0.692	0.06	0.289	0.676	2864	77	1028	37	4680	140	1.2	0.6	0.7	0.5
14	6.4	4.8	11.6	28	14.47	1.20	0.145	0.01	0.733	0.05	0.791	0.211	2759	79	867	35	4807	120	2.2	0.7	0.9	0.3
15	1.8	0.3	0.9	41	5.75	0.50	0.104	0.00	0.426	0.04	0.137	0.702	1936	74	635	26	3880	170	1.6	1.0	0.3	0.6
16	4.5	2.7	6.8	29	15.92	1.20	0.151	0.01	0.795	0.06	0.466	0.711	2854	73	902	34	4952	150	1.3	0.8	0.6	0.6
17	7.8	4.6	11.5	32	10.76	0.80	0.125	0.00	0.650	0.05	0.280	0.536	2490	69	758	23	4616	120	2.3	0.8	0.8	0.4
18	7.4	4.9	8.8	33	24.80	2.10	0.226	0.01	0.801	0.06	0.572	0.492	3285	75	1310	46	4975	140	1.2	0.4	0.9	0.3
19	6.7	1.5	6.7	38	8.40	0.65	0.122	0.00	0.528	0.04	-0.034	0.751	2274	71	738	27	4305	130	1.5	0.5	0.2	0.3
20	8.8	3.8	13.5	32	8.18	0.64	0.115	0.00	0.530	0.04	0.327	0.449	2240	71	704	22	4302	120	2.8	0.9	1.1	0.3
21	9.5	6.4	11.1	35	11.22	0.90	0.119	0.00	0.685	0.05	0.454	0.365	2532	74	722	21	4691	120	2.6	0.7	0.8	0.3
22	4	1	14	18	57.40	6.00	0.454	0.03	0.948	0.07	-0.007	0.160	4080	76	2389	120	5270	200	1.1	0.3	1.9	0.3
23	17.1	11.1	31	28	49.60	3.70	0.419	0.02	0.873	0.06	0.239	0.541	3975	72	2236	62	5126	140	1.2	0.3	2.0	0.2
24	5.6	3.5	8.5	30	14.73	1.10	0.153	0.00	0.693	0.05	0.224	0.622	2799	72	919	27	4728	120	1.8	0.7	0.7	0.4
25	2.3	1.7	0.9	41	16.40	1.40	0.182	0.01	0.681	0.07	0.127	0.801	2875	87	1067	50	4640	170	0.7	0.2	0.2	0.3

Tab. IX Results of U-Pb titanite dating from sample PJ 5

sample	measured		common	corrected isotope ratios								apparent ages (Ma)						aproximate concentration			Th/U
	$^{206}Pb/^{204}Pb$	$^{207}Pb/^{204}Pb$	$^{208}Pb/^{204}Pb$	^{206}Pb (%)	$^{207}Pb/^{235}U$	±2σ	$^{206}Pb/^{238}U$	±2σ	$^{207}Pb/^{206}Pb$	±2σ	6/38 vs 7/35	6/38 vs 7/35	$^{207}Pb/^{235}U$	±2σ	$^{206}Pb/^{238}U$	±2σ	$^{206}Pb/^{238}U$	±2σ	U (ppm)	Th (ppm)	Pb (ppm)	
Titanite PJ5																					
26	1.7	0.7	0.6	38	27.30	2.30	0.242	0.01	0.810	0.09	0.413	0.719	3366	83	1378	70	4970	220	0.5	0.2	0.2	0.3
27	27.4	19.6	48	29	36.00	3.10	0.314	0.01	0.812	0.06	0.903	-0.194	3617	81	1758	64	4990	120	2.9	2.2	2.9	0.8
28	7.9	2.6	6.2	43	6.68	0.58	0.104	0.00	0.472	0.04	0.424	0.261	2052	70	635	21	4126	110	2.5	0.5	0.4	0.2
29	1.3	1.2	3.4	19	27.50	2.30	0.230	0.01	0.866	0.07	0.538	0.363	3380	85	1330	54	5116	160	0.9	0.3	0.6	0.4
30	9.8	6.2	15.9	29	23.83	1.70	0.218	0.01	0.795	0.06	0.344	0.647	3263	69	1270	31	4948	120	1.7	0.4	1.3	0.2
31	3.8	1.2	4.4	36	6.59	0.61	0.109	0.00	0.437	0.04	0.239	0.431	2034	82	664	27	3980	160	1.5	0.8	0.3	0.5
32	6.7	2.9	8.8	35	6.49	0.47	0.100	0.00	0.470	0.03	0.092	0.557	2044	66	612	14	4150	110	4.8	4.0	1.0	0.8
33	13.8	8.7	22.2	30	15.80	1.10	0.152	0.00	0.744	0.05	0.247	0.596	2857	69	915	22	4844	120	2.5	0.5	1.2	0.2
34	7	5.9	12.9	27	17.91	1.30	0.162	0.01	0.807	0.06	0.237	0.724	2981	70	972	30	4977	140	1.5	0.5	0.7	0.4
35	7.1	3.3	6.7	38	10.33	0.80	0.125	0.00	0.637	0.05	0.170	0.986	2453	74	761	27	4580	220	1.6	1.5	0.4	0.9
36	13.2	9.9	25.6	26	53.70	6.60	0.404	0.04	0.931	0.07	0.962	0.145	3840	130	2100	170	5273	150	1.2	0.3	2.0	0.2
37	6.1	5	12	27	11.12	1.00	0.130	0.01	0.669	0.21	0.520	0.990	2509	89	785	49	4600	330	1.9	0.6	0.6	0.3
38	33	26	55	30	20.78	1.50	0.187	0.01	0.806	0.06	0.194	0.750	3129	69	1108	37	4972	140	1.3	0.3	0.8	0.2
39	10.1	7.3	16.4	29	19.76	1.40	0.183	0.01	0.785	0.06	0.128	0.812	3076	71	1084	32	4921	130	1.4	0.3	0.8	0.2
40	3.9	2.9	3.8	35	16.53	1.20	0.159	0.00	0.764	0.06	0.240	0.784	2905	72	946	27	4879	130	1.7	0.3	0.8	0.2
41	7.2	5.4	14.1	27	16.93	1.20	0.155	0.01	0.790	0.06	0.145	0.711	2924	71	924	28	4956	130	1.7	0.3	0.9	0.2
42	11.8	8.8	21.1	28	22.31	1.60	0.199	0.01	0.824	0.06	0.190	0.747	3201	67	1170	31	5014	130	1.6	0.3	1.1	0.2
43	11.1	6.7	13.5	34	19.80	1.40	0.184	0.01	0.780	0.05	0.330	0.738	3080	68	1084	31	4918	120	1.7	0.3	0.9	0.2
44	2.1	0.3	1.2	39	10.87	0.94	0.135	0.01	0.622	0.06	0.298	0.944	2481	85	811	37	4450	160	1.0	0.8	0.2	0.8
45	1.1	2.3	1.3	26	34.70	2.60	0.310	0.01	0.832	0.06	0.609	0.447	3626	74	1730	52	5032	130	1.1	0.1	1.2	0.1
46	5.8	6.3	12.4	25	37.30	2.80	0.339	0.01	0.815	0.06	0.266	0.641	3700	74	1889	58	4988	140	0.7	0.1	0.7	0.2
47	8.8	2.5	16.8	28	17.44	2.10	0.191	0.02	0.687	0.10	0.244	0.779	2985	90	1128	76	4670	310	1.1	0.1	0.7	0.1
48	20.9	17.4	42	26	62.40	6.30	0.462	0.02	0.970	0.07	0.762	0.309	4193	80	2457	93	5352	150	1.6	0.5	2.9	0.3
49	14.1	6.2	18	34	19.79	1.50	0.197	0.01	0.743	0.05	0.682	0.225	3066	76	1156	36	4832	120	1.9	0.1	1.2	0.1

Tab. IX Results of U-Pb titanite dating from sample PJ 5 **(continue)**

sample	measured			common	corrected isotope ratios								apparent ages (Ma)						aproximate concentration			Th/U
	$^{206}Pb/^{204}Pb$	$^{207}Pb/^{204}Pb$	$^{208}Pb/^{204}Pb$	^{206}Pb (%)	$^{207}Pb/^{235}U$	±2σ	$^{206}Pb/^{238}U$	±2σ	$^{207}Pb/^{206}Pb$	±2σ	6/38 vs 7/35	6/38 vs 7/35	$^{207}Pb/^{235}U$	±2σ	$^{206}Pb/^{238}U$	±2σ	$^{206}Pb/^{238}U$	±2σ	U (ppm)	Th (ppm)	Pb (ppm)	
Titanite DK17																						
1	7.4	5.2	13.6	28	21.57	1.80	0.206	0.01	0.770	0.06	0.564	0.528	3158	83	1206	39	4893	140	1.7	0.3	1.1	0.2
2	3	2	3	31	115.10	10.0	0.834	0.04	0.987	0.08	0.656	0.561	4799	85	3860	140	5381	190	0.2	0.1	0.8	0.5
3	7.2	3.8	8.5	34	20.20	2.20	0.212	0.01	0.700	0.08	0.588	0.932	3083	86	1224	74	4100	1900	1.0	0.3	0.6	0.3
4	8.3	5.9	14.3	28	21.10	1.90	0.193	0.01	0.846	0.10	0.556	0.924	3142	92	1137	65	4000	1600	1.0	0.2	0.7	0.2
5	10	6.3	17	30	13.23	1.10	0.148	0.00	0.655	0.05	0.084	0.703	2699	76	890	24	4635	130	2.4	4.8	1.2	2.0
6	350	160	380	39	8.38	0.70	0.114	0.00	0.521	0.04	0.477	0.241	2271	76	697	19	4290	120	3.7	1.3	0.9	0.4
7	2	3.1	4.6	22	41.00	3.50	0.350	0.02	0.907	0.08	0.575	0.777	3770	85	1928	77	5209	180	0.6	0.2	0.6	0.4
8	9.1	5.8	13.7	30	41.90	3.70	0.369	0.03	0.820	0.07	0.885	0.690	3800	88	1950	97	5004	160	0.9	0.4	0.9	0.5
9	7.4	5.5	12.3	28	22.96	1.80	0.193	0.01	0.867	0.07	0.210	0.769	3213	80	1136	36	5114	170	1.2	0.6	0.8	0.5
10	12	8	19.7	30	16.70	1.90	0.165	0.01	0.723	0.06	0.941	0.001	2803	98	971	55	4783	140	2.2	1.5	1.1	0.7
11	84	34	58	49	5.90	0.49	0.111	0.00	0.382	0.03	0.040	0.612	1958	73	676	19	3841	130	2.3	0.6	0.4	0.3
12	12	6.8	15.7	32	47.90	5.80	0.402	0.03	0.821	0.07	0.969	-0.094	3758	110	2090	140	5010	160	1.0	0.2	0.9	0.2
13	5.2	3.4	6.2	32	39.00	3.30	0.326	0.01	0.893	0.08	0.273	0.718	3728	82	1814	67	5160	180	0.6	0.2	0.6	0.3
14	1.3	0.2	0.2	37	51.60	4.60	0.406	0.02	0.945	0.09	0.407	0.792	4011	84	2190	110	5270	220	0.3	0.1	0.5	0.3
15	28	14.6	40	32	18.00	1.60	0.183	0.01	0.693	0.06	0.331	-0.054	2948	84	1082	37	4713	130	3.4	0.9	1.9	0.3
16	-28	-9	2	68	14.92	1.30	0.164	0.01	0.686	0.07	0.285	0.696	2796	83	976	44	4660	170	1.1	0.6	0.6	0.5
17	13	6.2	15	38	9.49	0.80	0.125	0.00	0.542	0.04	0.649	0.098	2369	78	759	21	4348	110	4.8	4.4	1.5	0.9
18	2	1.5	4.9	21	74.40	8.40	0.634	0.06	0.888	0.10	0.589	0.777	4353	120	3060	240	5130	250	0.2	0.5	0.4	2.6
19	3.3	1.2	2.4	40	9.24	0.85	0.122	0.01	0.575	0.06	0.032	0.668	2351	90	739	34	4410	170	1.4	0.5	0.3	0.4
20	18	13.5	39	25	70.20	7.80	0.562	0.04	0.874	0.07	0.943	-0.179	4256	120	2820	180	5129	160	1.1	0.2	2.4	0.2
21	5.7	4.8	5	37	15.41	1.40	0.151	0.01	0.756	0.06	0.777	0.303	2813	85	901	41	4865	150	2.1	0.6	0.9	0.3
22	1.8	0.3	0.9	41	5.79	0.54	0.103	0.00	0.429	0.04	0.133	0.704	1941	79	630	26	3890	180	1.6	1.0	0.3	0.6
23	6.7	4.6	8.5	32	27.40	2.30	0.232	0.01	0.859	0.07	0.490	0.537	3381	82	1339	46	5091	160	1.0	0.4	0.8	0.4
24	6.7	1.5	6.7	38	8.45	0.71	0.121	0.00	0.532	0.05	-0.033	0.749	2279	77	733	27	4308	140	1.5	0.5	0.2	0.3

Tab. X Results of U-Pb titanite dating from sample DK 17

sample	measured		common	corrected isotope ratios								apparent ages (Ma)						aproximate concentration			Th/U
	$^{206}Pb/^{204}Pb$	$^{207}Pb/^{204}Pb$	$^{208}Pb/^{204}Pb$	^{206}Pb (%)	$^{207}Pb/^{235}U$	±2σ	$^{206}Pb/^{238}U$	±2σ	$^{207}Pb/^{206}Pb$	±2σ	6/38 vs 7/35	6/38 vs 7/35	$^{207}Pb/^{235}U$	±2σ	$^{206}Pb/^{238}U$	±2σ	$^{206}Pb/^{238}U$	±2σ	U (ppm)	Th (ppm)	Pb (ppm)	
Titanite DK17																					
25	8.8	3.8	13.5	32	8.23	0.70	0.114	0.00	0.534	0.05	0.327	0.450	2246	77	700	22	4307	130	2.8	0.9	1.1	0.3
26	15	9.4	26	28	50.80	4.00	0.426	0.02	0.884	0.07	0.209	0.579	4003	79	2262	62	5151	160	1.1	0.3	1.9	0.2
27	5.6	3.5	8.5	30	14.80	1.20	0.153	0.00	0.696	0.06	0.223	0.623	2804	79	923	27	4737	130	1.7	0.6	0.7	0.4
28	2.5	1.8	0.9	43	16.60	1.60	0.183	0.01	0.690	0.07	0.118	0.806	2892	92	1076	51	4640	180	0.6	0.2	0.2	0.3
29	1.4	0.5	0.4	36	27.00	2.50	0.247	0.01	0.900	0.10	0.395	0.960	3365	89	1403	71	5130	240	0.4	0.2	0.2	0.4
30	29	19.4	47	30	38.60	3.30	0.334	0.01	0.835	0.06	0.880	-0.054	3705	88	1845	65	5040	140	2.4	1.6	2.8	0.7
31	6.9	2.4	5.9	42	7.00	0.63	0.106	0.00	0.477	0.04	0.395	0.262	2085	76	650	21	4140	130	2.4	0.4	0.4	0.2
32	1.3	1.2	3.4	19	27.70	2.50	0.231	0.01	0.870	0.08	0.541	0.357	3384	91	1338	54	5124	180	0.9	0.3	0.6	0.4
33	3.2	1.5	4.3	30	24.30	2.70	0.217	0.02	0.821	0.08	0.827	0.617	3154	100	1228	91	5240	330	0.6	0.2	0.5	0.4
34	9.8	6.2	15.9	29	23.92	1.90	0.219	0.01	0.798	0.06	0.343	0.648	3267	76	1276	31	4956	140	1.7	0.4	1.3	0.2
35	17	14.5	39	23	119.10	9.70	0.863	0.03	0.986	0.08	0.841	0.285	4866	82	4017	100	5381	170	0.7	0.2	2.4	0.2
36	6.7	2.9	8.8	35	6.51	0.52	0.100	0.00	0.472	0.04	0.081	0.565	2048	73	615	14	4156	120	4.8	4.0	1.0	0.8
37	15	11.5	30.4	26	83.40	9.10	0.644	0.05	0.928	0.07	0.949	0.208	4398	110	3120	190	5254	160	0.9	0.2	2.5	0.3
38	5.3	4	6.1	32	31.94	2.60	0.262	0.01	0.884	0.07	0.224	0.692	3545	81	1499	43	5148	170	0.9	1.6	0.7	1.9
39	2	1.5	4.6	23	16.20	1.70	0.178	0.01	0.641	0.06	0.727	0.129	2831	100	1050	48	4591	160	1.0	1.1	0.4	1.1
40	14	8.8	22.3	30	15.78	1.20	0.153	0.00	0.742	0.06	0.246	0.600	2859	77	920	22	4839	130	2.5	0.5	1.2	0.2
41	7	5.9	12.9	27	17.95	1.40	0.163	0.01	0.809	0.07	0.236	0.724	2984	76	973	30	4981	150	1.5	0.5	0.7	0.4
42	7.1	3.3	6.7	38	10.38	0.87	0.125	0.00	0.638	0.06	0.165	0.986	2455	80	762	27	4590	240	1.6	1.5	0.4	0.9
43	13	9.9	25.6	26	53.80	6.90	0.406	0.04	0.932	0.08	0.962	0.143	3840	130	2110	170	5276	170	1.2	0.3	2.0	0.2
44	33	26	55	30	20.85	1.70	0.188	0.01	0.807	0.07	0.196	0.749	3130	76	1111	37	4974	160	1.3	0.3	0.8	0.2
45	10	7.3	16.4	29	19.78	1.60	0.184	0.01	0.786	0.06	0.131	0.811	3077	78	1088	32	4923	150	1.4	0.3	0.8	0.2
46	3.9	2.9	3.8	35	16.55	1.30	0.159	0.00	0.765	0.06	0.242	0.783	2906	79	949	27	4881	140	1.7	0.3	0.8	0.2
47	9.9	7.7	17	28	22.63	1.80	0.199	0.01	0.823	0.07	0.257	0.731	3213	73	1173	31	5013	150	1.5	0.3	1.0	0.2

Tab. X Results of U-Pb titanite dating from sample DK 17 **(continue)**

sample	measured		common	corrected isotope ratios								apparent ages (Ma)						aproximate concentration			Th/U
	$^{206}Pb/^{204}Pb$	$^{207}Pb/^{204}Pb$	$^{208}Pb/^{204}Pb$	^{206}Pb (%)	$^{207}Pb/^{235}U$	±2σ	$^{206}Pb/^{238}U$	±2σ	$^{207}Pb/^{206}Pb$	±2σ	6/38 vs 7/35	6/38 vs 7/35	$^{207}Pb/^{235}U$	±2σ	$^{206}Pb/^{238}U$	±2σ	$^{206}Pb/^{238}U$	±2σ	U (ppm)	Th (ppm)	Pb (ppm)	
Titanite DK17																					
48	11	6.7	13.5	34	19.82	1.50	0.184	0.01	0.781	0.06	0.333	0.734	3081	75	1087	31	4919	140	1.7	0.3	0.9	0.2
49	2	0.4	0.7	42	10.96	1.00	0.140	0.01	0.623	0.06	0.318	0.935	2486	91	837	36	4440	180	1.0	0.8	0.2	0.8
50	3.4	3.3	0	48	82.80	####	0.653	0.06	0.932	0.10	0.735	0.474	4450	120	3180	240	5270	220	0.1	0.0	0.6	0.2
51	9.3	6	19.6	25	65.10	6.30	0.532	0.03	0.915	0.08	0.719	0.588	4206	86	2700	130	5230	180	0.4	0.1	0.9	0.2
52	0.9	1	1	25	34.70	2.80	0.309	0.01	0.831	0.07	0.613	0.443	3626	81	1730	52	5032	150	1.1	0.1	1.2	0.1
53	5.8	6.3	12.4	25	37.30	3.00	0.338	0.01	0.815	0.07	0.266	0.641	3700	81	1888	58	4988	160	0.7	0.1	0.7	0.2
54	5.2	3.8	12.4	24	21.10	2.20	0.241	0.02	0.703	0.10	0.234	0.967	3098	94	1379	76	2100	3200	0.6	0.0	0.6	0.1
55	21	17.9	44.3	25	78.30	6.80	0.560	0.02	0.991	0.08	0.915	0.174	4404	87	2838	93	5392	170	1.3	0.4	2.9	0.3
56	14	6.2	18	34	19.77	1.70	0.197	0.01	0.742	0.06	0.674	0.231	3065	82	1155	35	4829	140	1.9	0.1	1.2	0.1
57	2.2	1.8	0.9	40	19.30	1.50	0.198	0.01	0.725	0.06	0.221	0.756	3066	78	1161	43	4789	150	1.0	2.9	0.8	3.0
58	6.7	6.6	11.8	27	119.30	####	0.906	0.05	0.970	0.08	0.675	0.553	4835	87	4070	160	5352	180	0.2	0.0	0.7	0.1

Tab. X Results of U-Pb titanite dating from sample DK 17 **(continue)**

major elements (oxides in wt%)																
sample	PJ 5	PJ 6	PJ 7	PJ 8	PJ 9	VP 46	PJ12C	PJ13C	PJ14	PJ15	PJ20B	DK17E	DK17I	PJ21	PJ22	DK-L
SiO2	49.06	47.93	51.34	45.86	43.67	47.92	47.66	48.86	50.01	57.01	51.07	47.13	45.41	49.89	47.04	50.75
TiO2	1.26	1.82	0.75	1.39	1.03	1.21	0.81	1.83	1.50	1.71	1.41	2.08	4.73	1.27	1.70	1.52
Al2O3	15.62	16.51	17.14	11.17	7.01	17.97	18.82	17.39	14.43	15.96	16.56	15.45	12.20	15.72	13.35	17.31
Cr2O3	0.08	0.02	0.03	0.16	0.17	0.05	0.02	0.03	0.01	0.01	0.02	0.03	0.00	0.06	0.03	<0.002
Fe2O3	9.40	11.52	7.55	14.31	16.62	8.57	8.68	9.51	20.52	8.64	9.65	10.9	16.45	11.31	13.28	9.39
FeO	0.00	0.00	0.00	0	0	0.00	0.00	0.00	0.00	0.00	0	0	0.00	0.00	0.00	0.00
MnO	0.17	0.19	0.17	0.2	0.19	0.14	0.14	0.17	0.39	0.13	0.17	0.16	0.25	0.17	0.21	0.15
MgO	8.49	8.08	7.88	17.3	22.08	8.99	9.89	6.76	0.90	3.53	6.41	7.54	5.14	8.15	11.12	4.18
CaO	11.61	10.01	10.71	6.39	5.28	10.52	10.33	11.02	7.63	6.23	9.27	10.45	9.09	8.76	10.28	6.80
Na2O	2.80	2.83	2.84	1.92	1.26	2.87	2.81	3.13	4.50	3.81	2.95	3.22	3.85	2.92	2.21	3.69
K2O	0.23	0.52	0.21	0.53	0.39	0.47	0.09	0.15	0.29	1.32	0.60	0.88	0.72	0.17	0.18	2.25
P2O5	0.15	0.19	0.07	0.20	0.12	0.15	<0.01	0.01	0.40	0.24	0.15	0.29	1.07	0.16	0.05	0.44
total	99.75	99.74	99.79	99.6	99.54	99.74	99.25	98.86	100.58	98.59	98.26	98.13	98.91	98.58	99.45	96.48

Tab. XI Major element concentrations of samples from TCC-MLC and DCC-NKM area

trace elements (ppm)																
sample	PJ 5	PJ 6	PJ 7	PJ 8	PJ 9	VP 46	PJ12C	PJ13C	PJ14	PJ15	PJ20B	DK17E	DK17I	PJ21	PJ22	DK-L
Ni	119.00	55.00	42.00	601.00	565.00	136.00	111.00	74.00	29.00	<20	61.00	68.00	<20	166.00	20.00	<20
Sc	38.00	31.00	36.00	21.00	17.00	23.00	23.00	42.00	65.00	23.00	35.00	46.00	44.00	33.00	42.00	23.00
Ba	101.00	158.00	68.00	135.00	54.00	121.00	49.00	64.00	364.00	465.00	154.00	150.00	198.00	54.00	112.00	795.00
Be	<1	3.00	<1	<1	3.00	2.00	<1	1.00	<1	2.00	<1	<1	<1	1.00	<1	1.00
Co	38.10	41.90	37.00	84.40	119.60	40.80	47.10	34.50	6.40	18.60	32.60	37.10	31.50	41.50	59.70	22.00
Cs	2.30	1.20	0.70	1.20	1.10	0.80	0.20	<0.1	<0.1	1.50	<0.1	<0.1	<0.1	<0.1	0.30	0.50
Ga	15.70	17.90	16.40	13.40	10.50	15.30	14.50	16.10	18.20	19.80	15.80	17.80	21.80	22.50	14.20	20.30
Hf	4.50	3.70	1.00	3.80	1.70	2.90	0.40	1.10	49.90	5.90	1.10	4.10	7.60	3.20	1.10	4.60
Nb	7.80	9.20	2.40	8.50	8.00	7.30	0.20	1.70	7.90	8.30	6.50	12.00	28.00	7.30	2.20	13.00
Rb	4.80	12.40	4.50	13.00	5.20	9.80	0.60	1.70	0.20	36.90	10.30	9.20	5.20	1.60	3.90	41.30
Sn	2.00	<1	<1	1.00	<1	<1	<1	<1	<1	2.00	<1	<1	2.00	3.00	<1	2.00
Sr	192.20	242.50	264.60	177.80	166.20	305.50	239.50	275.90	241.20	197.30	271.10	579.00	214.80	196.60	198.50	497.20
Ta	0.60	0.60	0.20	0.90	0.70	0.50	<0.1	0.10	0.50	0.60	0.30	0.80	1.90	0.40	0.10	0.90
Th	0.90	1.20	0.30	1.30	0.50	1.10	<0.2	<0.2	1.50	3.10	<0.2	<0.2	2.00	0.40	0.40	6.10
U	0.20	0.40	0.10	0.70	0.10	0.50	<0.1	<0.1	2.30	1.50	<0.1	<0.1	0.40	0.30	0.30	3.50
V	243.00	246.00	265.00	161.00	152.00	177.00	132.00	291.00	30.00	145.00	238.00	276.00	400.00	220.00	364.00	194.00
W	<0.5	<0.5	<0.5	<0.5	<0.5	<0.5	0.70	<0.5	<0.5	<0.5	0.70	<0.5	<0.5	<0.5	<0.5	1.40
Zr	159.50	139.20	39.40	139.30	62.40	100.60	8.00	37.50	2826.80	236.80	35.50	161.00	312.40	112.90	38.00	178.80
Y	32.30	28.70	10.80	19.90	8.90	18.90	5.20	13.70	48.00	67.20	25.10	21.90	50.00	54.00	18.80	34.50
La	9.30	10.80	4.40	10.80	6.60	10.00	0.90	1.30	34.90	19.70	8.40	14.40	29.80	11.40	2.80	25.00
Ce	24.30	25.60	9.00	25.90	13.70	22.30	2.30	3.40	83.60	55.00	23.30	34.40	73.90	36.10	7.30	52.20

Tab. XII Trace element concentrations of samples from TCC-MLC and DCC-NKM area

trace elements (ppm)																
sample	PJ 5	PJ 6	PJ 7	PJ 8	PJ 9	VP 46	PJ12C	PJ13C	PJ14	PJ15	PJ20B	DK17E	DK17I	PJ21	PJ22	DK-L
Pr	3.12	3.34	1.14	3.39	1.89	2.82	0.38	0.67	11.66	8.32	3.43	4.46	10.22	6.29	1.24	6.90
Nd	15.80	15.20	5.60	15.70	8.50	11.70	2.30	4.20	55.10	42.40	15.80	19.00	47.20	30.10	4.10	27.70
Sm	4.33	4.03	1.16	3.88	2.00	2.87	0.88	1.60	10.73	10.86	4.44	4.79	11.24	9.46	2.42	6.70
Eu	1.29	1.46	0.91	1.19	0.75	1.13	0.73	1.22	3.87	1.68	1.24	1.64	3.51	2.54	1.36	1.91
Gd	5.13	5.17	1.96	4.04	2.34	3.50	1.07	2.28	10.59	12.79	5.11	4.98	12.15	9.79	3.17	7.16
Tb	0.95	0.86	0.35	0.70	0.38	0.56	0.17	0.40	1.50	2.08	0.81	0.75	1.81	1.57	0.58	1.08
Dy	5.74	5.50	2.00	4.29	2.02	3.59	1.11	2.47	9.45	13.18	5.00	4.84	10.51	9.58	3.60	6.45
Ho	1.07	1.08	0.38	0.82	0.38	0.76	0.24	0.48	2.02	2.56	0.98	0.91	1.95	1.94	0.74	1.25
Er	3.49	3.10	1.19	2.35	1.06	2.01	0.56	1.58	6.48	7.26	2.60	2.38	5.27	5.35	2.16	3.63
Tm	0.51	0.48	0.15	0.33	0.13	0.28	0.09	0.21	0.99	1.00	0.37	0.33	0.68	0.75	0.29	0.50
Yb	3.43	2.65	1.11	2.20	0.89	1.88	0.59	1.36	7.77	6.34	2.37	2.07	4.45	5.02	1.79	3.09
Lu	0.48	0.43	0.17	0.34	0.15	0.25	0.08	0.24	1.50	0.90	0.33	0.31	0.64	0.74	0.28	0.47
Mo	0.50	0.60	<0.1	0.80	0.80	0.40	0.50	0.80	2.00	0.70	0.40	0.90	1.50	<0.1	1.40	0.70
Cu	69.00	24.10	20.60	128.00	120.80	33.00	33.00	18.80	18.40	8.50	32.50	67.00	8.70	58.40	35.80	21.40
Pb	0.50	1.00	0.50	1.00	1.00	1.90	1.20	5.60	4.10	2.20	6.10	0.80	1.00	0.40	0.30	86.20
Zn	8.00	16.00	7.00	18.00	47.00	13.00	31.00	13.00	108.00	49.00	26.00	26.00	43.00	43.00	56.00	93.00
Ni	28.00	31.00	21.40	475.30	506.50	71.10	106.80	48.80	27.50	13.20	33.60	41.60	15.30	59.10	26.80	1.80
As	<0.5	1.00	0.60	2.50	<0.5	<0.5	<0.5	8.40	<0.5	4.10	<0.5	0.90	8.00	1.50	10.00	18.20
Cd	<0.1	<0.1	<0.1	<0.1	<0.1	<0.1	<0.1	<0.1	<0.1	<0.1	<0.1	<0.1	<0.1	0.20	0.20	0.20
Sb	<0.1	<0.1	<0.1	<0.1	<0.1	0.10	<0.1	0.50	<0.1	<0.1	0.40	0.10	<0.1	0.20	0.30	0.10
Bi	<0.1	<0.1	<0.1	<0.1	<0.1	<0.1	<0.1	<0.1	<0.1	<0.1	<0.1	<0.1	<0.1	<0.1	<0.1	0.50
Ag	<0.1	<0.1	<0.1	<0.1	<0.1	<0.1	<0.1	<0.1	<0.1	<0.1	<0.1	<0.1	<0.1	<0.1	<0.1	0.20
Au	3.60	1.20	0.70	2.90	0.60	0.60	<0.5	1.00	1.10	1.00	<0.5	<0.5	<0.5	1.10	2.90	0.80
Hg	0.02	0.01	<0.01	<0.01	<0.01	<0.01	<0.01	0.01	<0.01	<0.01	<0.01	<0.01	<0.01	0.02	<0.01	<0.01
Tl	<0.1	<0.1	<0.1	0.20	<0.1	<0.1	<0.1	<0.1	<0.1	0.30	<0.1	<0.1	<0.1	<0.1	<0.1	<0.1
Se	<0.5	<0.5	<0.5	<0.5	<0.5	<0.5	<0.5	<0.5	<0.5	<0.5	<0.5	<0.5	<0.5	<0.5	<0.5	<0.5

Tab. XII Trace element concentrations of samples from TCC-MLC and DCC-NKM area **(continue)**

major elements (oxides in wt%)																		
sample	06OH1B	06OH2	06OH3A	06OH4B	06OH5B	06OH6B	06OH7B	06OH8A	06OH9	06OH10B	06OH11	06OH12	06OH13	06HBK1B	06HBK2A	06MB1	06MB2	06MB3
SiO2	47.46	47.64	52.53	49.78	50.08	51.66	54.82	33.08	48.69	48.18	48.08	29.32	47.56	53.46	48.88	52.48	52.93	52.68
TiO2	0.61	2.12	0.31	0.46	0.37	0.41	0.31	0.09	1.65	1.45	1.62	2.28	2.08	0.33	2.13	1.18	1.36	0.60
Al2O3	17.87	18.38	23.21	16.23	19.74	20.13	19.31	0.45	12.68	14	13.27	2.32	16.25	22.48	19.18	15.41	18.96	22.79
Cr2O3	0.00	0.00	0.00	0.00	0.00	0.00	0.00	0.00	0.00	0.00	0.00	0.00	0.00	0.00	0.00	0.00	0.00	0.00
Fe2O3	2.28	2.02	0.52	2.44	0.55	2.28	1.63	7.04	5.67	4.89	5.98	7.95	4.43	0.97	3.30	2.33	2.59	0.93
FeO	6.10	6.67	2.76	5.77	5.55	3.18	3.55	39.35	14.79	14.67	13.28	41.55	11.37	3.76	6.27	5.67	7.71	2.14
MnO	0.13	0.14	0.06	0.13	0.09	0.09	0.11	0.73	0.42	0.41	0.38	0.77	0.26	0.09	0.15	0.17	0.17	0.07
MgO	9.92	6.79	4.12	9.03	5.74	5.83	3.87	18.41	1.61	1.58	2.26	14.27	4.49	2.66	4.68	6.25	2.53	2.80
CaO	10.05	10.04	10.79	10.67	10.46	10.86	10.02	0.41	7.85	8.27	8.71	0.51	7.29	9.81	10.32	11.83	7.48	9.90
Na2O	2.65	3.44	4.48	2.62	3.76	3.8	4.70	0.06	3.53	3.56	3.83	0.08	3.98	4.97	3.86	3.53	4.45	4.74
K2O	0.17	0.26	0.21	0.24	0.14	0.14	0.28	0.01	0.49	0.46	0.32	0.02	0.26	0.27	0.19	0.16	0.34	0.98
P2O5	0.01	0.02	0.05	0.02	0.02	0.01	0.02	0.01	0.21	0.23	0.21	0.04	0.03	0.03	0.02	0.02	0.14	0.01
total	97.25	97.52	99.04	97.39	96.50	98.39	98.62	99.64	97.59	97.70	97.94	99.11	98.00	98.83	98.98	99.03	98.66	97.64

Tab. XIII Major element concentrations of additional samples from Orlovice area

trace elements (ppm)																		
sample	06OH1B	06OH2	06OH3A	06OH4B	06OH5B	06OH6B	06OH7B	06OH8A	06OH9	06OH10B	06OH11	06OH12	06OH13	06HBK1B	06HBK2A	06MB1	06MB2	06MB3
Ni	0.00	0.00	0.00	0.00	0.00	0.00	0.00	0.00	0.00	0.00	0.00	0.00	0.00	0.00	0.00	0.00	0.00	0.00
Sc	25.66	44.20	21.30	44.80	14.68	30.37	53.68	19.19	91.13	88.68	86.98	38.02	48.33	19.81	43.18	71.08	27.10	28.49
Ba	147.51	84.71	445.51	73.11	75.61	66.51	192.91	107.66	386.51	336.51	374.41	36.75	240.26	135.81	105.41	105.31	313.61	229.66
Be	0.00	0.00	0.00	0.00	0.00	0.00	0.00	0.00	0.00	0.00	0.00	0.00	0.00	0.00	0.00	0.00	0.00	0.00
Co	45.53	43.74	19.25	42.67	42.06	30.52	14.96	147.48	12.00	12.52	14.08	119.83	33.10	14.91	29.26	27.09	18.45	13.40
Cs	0.17	0.08	0.23	0.10	0.17	0.06	0.02	0.08	0.07	0.15	0.12	0.06	0.07	0.06	0.25	0.05	0.16	0.01
Ga	0.80	1.22	0.90	1.49	0.49	1.22	2.00	0.32	14.11	14.13	18.22	0.58	1.72	1.42	1.50	2.44	6.04	1.20
Hf	0.24	1.02	0.44	0.75	0.22	0.37	1.45	0.37	48.61	42.09	26.85	1.69	1.61	0.59	1.09	1.30	12.16	0.72
Nb	0.64	1.91	0.66	0.31	1.16	0.44	0.61	0.48	13.58	12.92	17.83	5.96	4.90	0.95	3.57	1.39	9.90	1.18
Rb	2.05	4.35	2.15	3.77	7.10	0.40	1.43	0.61	3.16	3.84	2.90	0.98	2.79	0.78	0.97	0.90	4.21	5.64
Sn	0.00	0.00	0.00	0.00	0.00	0.00	0.00	0.00	0.00	0.00	0.00	0.00	0.00	0.00	0.00	0.00	0.00	0.00
Sr	232.44	279.69	338.64	226.29	225.54	287.89	331.49	6.39	252.69	257.14	233.89	8.26	268.99	357.14	291.79	256.24	335.04	449.49
Ta	0.00	0.00	0.00	0.00	0.00	0.00	0.00	0.00	0.00	0.00	0.00	0.00	0.00	0.00	0.00	0.00	0.00	0.00
Th	0.08	0.80	<0,05	<0,05	0.44	0.46	0.19	0.10	1.21	1.06	0.54	0.16	0.26	0.11	0.30	0.21	0.55	0.36
U	0.04	0.10	0.11	0.09	0.02	0.06	0.15	0.12	1.35	1.40	1.05	0.16	0.20	0.15	0.09	0.13	1.03	0.09
V	146.10	469.25	123.85	272.20	62.85	194.10	204.70	98.05	81.90	78.80	107.70	389.90	208.75	108.55	390.60	383.35	90.40	163.10
W	0.00	0.00	0.00	0.00	0.00	0.00	0.00	0.00	0.00	0.00	0.00	0.00	0.00	0.00	0.00	0.00	0.00	0.00
Zr	9.34	37.73	19.88	30.69	8.30	13.44	69.09	21.10	3115.99	2653.99	1561.99	81.09	75.34	28.69	40.66	53.14	636.04	28.13
Y	4.41	7.20	5.30	8.73	2.51	6.32	9.72	2.63	50.46	51.36	66.61	2.97	7.56	6.64	8.33	13.77	26.84	6.31
La	0.98	1.49	1.16	0.98	0.72	1.86	2.38	0.63	41.85	43.48	44.45	1.34	3.29	2.15	2.46	2.44	10.21	1.99
Ce	2.02	3.35	2.58	2.48	1.47	4.13	5.99	1.36	101.79	105.39	116.64	3.15	7.54	5.02	4.89	6.13	24.63	4.71
Pr	0.33	0.55	0.43	0.49	0.24	0.61	0.96	0.25	14.42	14.81	17.61	0.48	1.17	0.82	0.72	0.99	3.74	0.63

Tab. XIV Trace element concentrations of additional samples from Orlovice area

trace elements (ppm)																		
sample	06OH1B	06OH2	06OH3A	06OH4B	06OH5B	06OH6B	06OH7B	06OH8A	06OH9	06OH10B	06OH11	06OH12	06OH13	06HBK1B	06HBK2A	06MB1	06MB2	06MB3
Nd	1.84	2.90	2.35	2.91	1.30	3.07	5.20	1.22	69.80	72.05	88.90	2.53	6.11	4.28	3.89	5.72	18.74	3.15
Sm	0.63	0.97	0.75	1.17	0.34	0.96	1.61	0.34	13.66	14.09	18.53	0.54	1.64	1.24	1.23	1.90	5.10	0.95
Eu	0.84	0.95	1.12	0.91	0.56	1.01	2.17	0.12	4.53	4.55	4.72	0.14	2.15	2.02	1.55	1.56	2.93	1.34
Gd	0.00	0.00	0.00	0.00	0.00	0.00	0.00	0.00	0.00	0.00	0.00	0.00	0.00	0.00	0.00	0.00	0.00	0.00
Tb	0.13	0.24	0.17	0.28	0.08	0.22	0.34	0.07	1.94	2.02	2.61	0.09	0.29	0.24	0.25	0.46	0.95	0.21
Dy	0.96	1.52	1.04	1.81	0.53	1.34	2.16	0.45	10.88	11.07	14.57	0.55	1.60	1.42	1.78	2.83	5.58	1.32
Ho	0.20	0.30	0.22	0.38	0.11	0.29	0.43	0.10	2.16	2.20	2.90	0.13	0.34	0.29	0.37	0.58	1.09	0.26
Er	0.54	0.90	0.67	1.04	0.30	0.80	1.21	0.38	6.43	6.55	8.25	0.40	0.98	0.78	1.02	1.67	3.15	0.77
Tm	0.08	0.13	0.09	0.14	0.05	0.11	0.17	0.08	0.96	0.94	1.18	0.07	0.13	0.11	0.15	0.24	0.44	0.10
Yb	0.49	0.78	0.57	0.92	0.30	0.71	1.02	0.60	6.77	6.72	7.88	0.61	0.89	0.68	0.93	1.48	2.91	0.64
Lu	0.07	0.12	0.09	0.14	0.05	0.11	0.16	0.12	1.25	1.24	1.45	0.12	0.15	0.10	0.14	0.24	0.49	0.10
Mo	0.00	0.00	0.00	0.00	0.00	0.00	0.00	0.00	0.00	0.00	0.00	0.00	0.00	0.00	0.00	0.00	0.00	0.00
Cu	32.72	30.36	13.87	24.57	38.30	29.05	5.11	5.62	33.94	31.27	37.36	26.90	40.50	5.91	30.62	16.06	16.20	20.55
Pb	2.65	3.79	2.73	<0,50	1.17	<0,50	1.96	20.55	2.21	9.56	6.19	5.66	2.09	2.64	9.85	<0,50	4.27	0.50
Zn	48.65	60.65	29.53	50.80	56.25	33.22	30.70	181.70	180.70	169.45	214.55	206.15	89.85	33.13	67.50	48.80	133.95	20.32
Ni	101.60	26.74	31.43	39.93	106.60	57.00	28.64	46.10	5.89	4.47	1.06	5.72	12.31	1.56	12.58	30.51	4.26	14.53
Se	0.00	0.00	0.00	0.00	0.00	0.00	0.00	0.00	0.00	0.00	0.00	0.00	0.00	0.00	0.00	0.00	0.00	0.00
Rh	0.02	0.01	0.01	0.01	0.01	0.01	<0,005	0.01	0.01	0.00	0.01	0.01	0.01	<0,005	0.00	0.01	0.00	0.00
Pd	0.33	0.30	0.32	0.16	0.23	0.50	0.24	0.23	0.40	0.32	0.13	0.28	0.15	0.29	0.35	0.64	0.28	0.00
Ir	0.07	0.05	0.03	0.02	0.02	0.02	0.01	0.01	0.02	0.01	0.02	0.04	0.01	0.01	0.01	0.02	0.02	0.00
Pt	0.55	0.23	7.44	0.94	0.38	0.24	0.11	15.40	0.69	0.22	0.91	0.79	0.25	0.39	2.73	0.24	0.15	0.00
Cr	210.85	110.70	95.70	212.45	117.00	173.70	193.95	30.30	18.68	28.79	7.67	14.45	48.95	10.75	122.65	267.80	11.87	74.15

Tab. XIV Trace element concentrations of additional samples from Orlovice area **(continue)**

	TCC						MLC														
sample	PJ 5						PJ 6						PJ 9								
method	geoTB			av PT			geoTB			geoTB + av PT			geoTB						av PT		
mineral	Amp	Pl	Grt	Amp	Pl	Grt	Amp	Pl	Grt	Amp	Pl	Grt	Amp	Pl	Grt	Amp	Pl	Grt	Amp	Pl	Grt
SiO_2	44.80	57.08	38.32	45.09	55.68	38.42	40.80	59.50	37.56	39.51	58.07	38.61	46.51	59.39	39.48	44.80	60.05	39.01	47.97	59.78	39.19
TiO_2	0.50	b.d.	b.d.	0.35	b.d.	b.d.	0.42	b.d.	b.d.	0.41	b.d.	b.d.	1.93	b.d.	b.d.	2.10	b.d.	b.d.	0.23	b.d.	b.d.
Cr_2O_3	b.d.	b.d.	b.d.	b.d.	b.d.	b.d.	b.d.	b.d.	b.d.	b.d.	b.d.	0.12	b.d.	b.d.	b.d.	b.d.	b.d.	b.d.	b.d.	b.d.	b.d.
Al_2O_3	11.93	25.36	21.40	12.47	28.11	21.41	16.34	24.84	21.13	18.41	25.34	21.76	9.61	25.48	22.04	11.60	25.27	21.90	9.84	25.09	21.96
FeO	11.49	0.69	24.30	12.03	0.61	25.65	13.78	0.29	25.67	11.42	0.68	24.03	9.89	0.26	22.76	10.50	0.50	22.29	8.03	0.59	20.45
MnO	0.14	b.d.	1.28	0.11	b.d.	1.97	0.13	b.d.	0.89	b.d.	b.d.	0.69	0.09	b.d.	1.02	0.12	b.d.	0.85	b.d.	b.d.	b.d.
MgO	13.04	b.d.	6.15	13.16	b.d.	4.75	10.82	b.d.	5.68	11.44	b.d.	5.40	14.96	b.d.	8.41	13.95	b.d.	8.38	16.94	b.d.	8.86
CaO	11.59	7.99	7.61	11.55	10.07	7.38	10.94	6.89	7.61	11.73	7.54	9.71	11.38	7.12	6.51	11.36	6.84	6.94	11.69	6.81	8.21
Na_2O	1.30	6.80	b.d.	1.41	5.93	b.d.	2.38	7.50	b.d.	2.46	7.23	b.d.	1.87	7.46	b.d.	2.19	7.81	b.d.	1.62	7.61	b.d.
K_2O	0.66	0.23	b.d.	0.62	0.01	b.d.	0.66	0.08	b.d.	0.76	b.d.	b.d.	0.58	0.09	b.d.	0.76	0.10	b.d.	0.23	0.23	b.d.
total	95.45	98.15	99.06	96.79	100.41	99.58	96.27	99.10	98.54	96.14	98.86	100.32	96.82	99.8	100.2	97.38	100.6	99.37	96.55	100.11	99.33
cat/O	13/23	5/8	8/12	13/23	5/8	8/12	13/23	5/8	8/12	13/23	5/8	8/12	13/23	5/8	8/12	13/23	5/8	8/12	13/23	5/8	8/12
Si	6.59	2.60	3.00	6.53	2.49	3.02	6.02	2.68	2.97	5.83	2.63	2.98	6.72	2.65	3.01	6.49	2.66	3.00	6.80	2.66	2.99
Ti	0.06	0.00	0.00	0.04	0.00	0.00	0.05	0.00	0.00	0.05	0.00	0.00	0.21	0.00	0.00	0.23	0.00	0.00	0.02	0.00	0.00
Cr	0.00	0.00	0.00	0.00	0.00	0.00	0.00	0.00	0.00	0.00	0.00	0.01	0.00	0.00	0.00	0.00	0.00	0.00	b.d	0.00	0.00
Al	2.07	1.36	1.97	2.13	1.48	1.98	2.84	1.32	1.97	3.20	1.35	1.98	1.64	1.34	1.98	1.98	1.32	1.98	1.64	1.32	1.98
Fe^{2+}	1.37	0.03	1.56	1.40	0.02	1.69	1.64	0.01	1.59	1.37	0.03	1.51	1.17	0.01	1.45	1.25	0.02	1.41	0.89	0.02	1.27
Fe^{3+}	0.06	0.00	0.03	0.07	0.00	0.13	0.09	0.00	0.10	0.06	0.00	0.04	0.04	0.00	0.00	0.03	0.00	0.02	0.08	0.00	0.04
Mn	0.02	0.00	0.08	0.01	0.00	0.00	0.02	0.00	0.06	0.00	0.00	0.05	0.01	0.00	0.07	0.01	0.00	0.06	0.00	0.00	0.04
Mg	2.86	0.00	0.72	2.84	0.00	0.56	2.38	0.00	0.67	2.52	0.00	0.62	3.22	0.00	0.96	3.01	0.00	0.96	3.58	0.00	1.01
Ca	1.83	0.39	0.64	1.79	0.48	0.62	1.73	0.33	0.64	1.85	0.37	0.80	1.76	0.34	0.53	1.76	0.32	0.57	1.78	0.33	0.67
Na	0.37	0.60	0.00	0.40	0.51	0.00	0.68	0.65	0.00	0.70	0.63	0.00	0.52	0.65	0.00	0.62	0.67	0.00	0.45	0.66	0.00
K	0.12	0.01	0.00	0.11	0.00	0.00	0.12	0.00	0.00	0.14	0.00	0.00	0.11	0.01	0.00	0.14	0.01	0.00	0.04	0.01	0.00
X_{Mg}	0.67		0.31	0.66		0.25	0.58		0.28	0.64	0.37	0.29	0.73		0.40	0.70		0.40	0.79	0.33	0.44

Tab. XV. Analyses used for P-T calculation